Florida International University
FIU Digital Commons

FIU Electronic Theses and Dissertations | University Graduate School

3-21-2013

Development of Physics-based Models and Design Optimization of Power Electronic Conversion Systems

Arash Nejadpak
Florida International University, arash.nejadpak@gmail.com

DOI: 10.25148/etd.FI13042202
Follow this and additional works at: https://digitalcommons.fiu.edu/etd

Recommended Citation
Nejadpak, Arash, "Development of Physics-based Models and Design Optimization of Power Electronic Conversion Systems" (2013). *FIU Electronic Theses and Dissertations*. 824.
https://digitalcommons.fiu.edu/etd/824

This work is brought to you for free and open access by the University Graduate School at FIU Digital Commons. It has been accepted for inclusion in FIU Electronic Theses and Dissertations by an authorized administrator of FIU Digital Commons. For more information, please contact dcc@fiu.edu.

FLORIDA INTERNATIONAL UNIVERSITY

Miami, Florida

DEVELOPMENT OF PHYSICS-BASED MODELS AND DESIGN OPTIMIZATION OF POWER ELECTRONIC CONVERSION SYSTEMS

A dissertation submitted in partial fulfillment of the

requirements for the degree of

DOCTOR OF PHILOSOPHY

in

ELECTRICAL ENGINEERING

by

Arash Nejadpak

2013

To: Dean Amir Mirmiran
College of Engineering and Computing

This dissertation, written by Arash Nejadpak, and entitled Development of Physics-based Models and Design Optimization of Power Electronic Conversion Systems, is referred to you for judgment.

We have read this dissertation and recommend that it be approved.

Sakhrat Khizroev

Hai Deng

W. Kinzy Jones

H. Scott Coombe

Osama A. Mohammed, Major Professor

Date of Defense: March 21, 2013

The Dissertation of Arash Nejadpak is approved.

Dean Amir Mirmiran
College of Engineering and Computing

Dean Lakshmi N. Reddi
University Graduate School

Florida International University, 2013

© Copyright 2013 by Arash Nejadpak

All rights reserved.

DEDICATION

I dedicate this dissertation to my parents and brother, Ashkan, who I did not see them much during my Ph.D. Without their love, support and patience, this dream could never come true.

ACKNOWLEDGMENTS

I owe my deepest gratitude to my advisor, Professor Osama A. Mohammed, for his invaluable guidance and support throughout my Ph.D. studies. He has by far been the most influential and inspiring teacher and advisor I have had the privilege of working with. Indeed he has been the predominant source of the academic and professional expertise I have acquired. Throughout my Ph.D., Professor Mohammed provided me with endless support, guidance, expert assistance and significant contributions through the period of the research and dissertation development. I will always remember his belief in my abilities to work hard and to produce at a high level. I do appreciate his many constructive suggestions while the material was being developed and tested at the energy systems research laboratory. I am indebted for his willingness to accept me in his laboratory and for providing significant research facilities to develop this work in addition to his expert guidance and continued assistance, without which, I wouldn't have been able to successfully accomplish my experimental work. I am also grateful to Dr. Sakhrat Khizroev, Dr. Hai Deng, Dr. Kinzy Jones and Dr. H. Scott Coombe for serving on my dissertation advisory committee and for the many constructive discussions.

I would also such as to acknowledge the ECE department laboratory personnel and all the members and students of the Energy Systems Research Laboratory, Florida International University for their assistance during the experimental testing of this research.

I am also thankful to Professor Mohammed who provided me with financial support as a research assistant from his funded projects since I joined the PhD program at

FIU. I also thank the Florida International University for providing me with Dissertation Year Fellowship (DYF) during my last year to complete my doctoral work.

ABSTRACT OF THE DISSERTATION

DEVELOPMENT OF PHYSICS-BASED MODELS AND DESIGN

OPTIMIZATION OF POWER ELECTRONIC CONVERSION SYSTEMS

by

Arash Nejadpak

Florida International University, 2013

Miami, Florida

Professor Osama A. Mohammed, Major Professor

Increased demands for the development of new power electronic conversion systems with increased reliability, power density and controllability, require a variety of studies of their physical representations. The increase in power density of power conversion devices and the improvement of their electromagnetic characteristics require the optimization of the design while considering many of the operational parameters. A widespread need exist for the development of standardized power conversion packages for a variety of applications. The complexity of these new systems requires better methods for predicting their interactions among the power components and systems. Furthermore, effective diagnosis also presents a challenge. The physics-based modeling can play an important role in developing diagnostics strategies of the operating components.

The main objective for physics based modeling of the power converter components is to design the whole converter with respect to physical and operational constraints. Therefore, all the elements and components of the energy conversion system are modeled numerically and combined together to achieve the whole system behavioral model.

Previously proposed high frequency (HF) models of power converters are based on circuit models that are only related to the parasitic inner parameters of the power devices and the connections between the components. This dissertation aims to obtain appropriate physics-based models for power conversion systems, which not only can represent the steady state behavior of the components, but also can predict their high frequency characteristics. The developed physics-based model would represent the physical device with a high level of accuracy in predicting its operating condition.

The proposed physics-based model enables us to accurately develop components such as; effective EMI filters, switching algorithms and circuit topologies [7]. One of the applications of the developed modeling technique is design of new sets of topologies for high-frequency, high efficiency converters for variable speed drives.

The main advantage of the modeling method, presented in this dissertation, is the practical design of an inverter for high power applications with the ability to overcome the blocking voltage limitations of available power semiconductor devices. Another advantage is selection of the best matching topology with inherent reduction of switching losses which can be utilized to improve the overall efficiency.

The physics-based modeling approach, in this dissertation, makes it possible to design any power electronic conversion system to meet electromagnetic standards and design constraints. This includes physical characteristics such as; decreasing the size and weight of the package, optimized interactions with the neighboring components and higher power density. In addition, the electromagnetic behaviors and signatures can be evaluated including the study of conducted and radiated EMI interactions in addition to the design of attenuation measures and enclosures.

TABLE OF CONTENTS

TABLE OF FIGURES

FIGURE PAGE

LIST OF TABLES

TABLE PAGE

ABBREVIATIONS AND ACRONYMS

EMI	Electromagnetic Interference
EMC	Electromagnetic Compatibility
HF	High Frequency
HV	High Voltage
IGBT	Insulated Gate Bipolar Transistor
IPC	Institute of Interconnecting and Packaging Electronic Circuits
FEA	Finite Element Analysis
GA	Genetic Algorithm
Si	Silicon
SiC	Silicon Carbide
ZCS	Zero Current Switching
ZVS	Zero Voltage Switching
QRC	Quasi Resonant Converter
PCB	Printed Circuit Board
DARPA	Defense Advanced Research Projects Agency
EPRI	Electric Power Research Institute
IUT	Intelligent Universal Transformer
SSPS	Solid State Power Substations
GMRES	Generalized Minimal Residual
CG	Conjugate Gradient
SVM	Space Vector Method
SPWM	Sinusoidal Pulse Width Modulation
BJT	Bipolar Junction Transistor
FFT	Fast Furrier Transform
CM	Common Mode

DM	Differential Mode
SMPS	Switch Mode Power Supply
LTCC	Low Temperature Co-Fired Ceramic
AWG	American Wire Gauge
ZSI	Z-Source inverters
CSI	Current Source Inverter
VSI	Voltage Source Inverter
CFD	Computational Fluid Dynamics

Chapter 1 Introduction and literature review

This dissertation aims to contribute to the ongoing efforts in physics-based modeling of power electronic converters for a variety of applications. This work develops detailed and accurate model for different power system components operating in their practical environments. The physics-based model would help predict undesirable effects in the design of power conversion system and propose improvement strategies for its efficiency and reliability [1, 2].

The interaction of power electronic conversion system with other connected devices may raise many issues such as electromagnetic interference (EMI), overvoltage transients that threaten the lifetime of devices, current spikes and increased power loss [3-11].

Modern power semiconductor devices operate at higher power ratings in shorter switching times. The most popular static switches, such as MOSFETs and IGBTs, have switching times in nanoseconds. The new trends in power semiconductor devices, such as Silicon Carbide (SiC) based devices, can further increase voltage edge rates due to shorter minority carrier lifetimes and higher operating voltages. Furthermore, higher switching frequencies increase switching losses. To reduce switching losses, usually the switching frequency is fixed in the range of tens of kHz or other soft switching techniques are being used. Increased voltage edge rates, switching frequencies and voltage magnitudes have led to the problem of EMI and overvoltage in power electronic converters [11].

In order to design a converter that can deal well with the mentioned issues, detailed and accurate computer models of the power electronic converters are essential to evaluate

the overall system performance and observe the effects of applied control algorithms to the system, before any actual hardware is implemented. Evaluation of the control algorithm performance is usually important at lower frequencies [12-14].

So far, the models presented for power electronic converters are mainly designed to represent the low frequency behavior of the system and fail to predict the high-frequency phenomenon that arises during the operation of these devices. These high-frequency behaviors may cause many failures in the converter package. The high-frequency models available in the literature are based on experimental measurements of the component's parameters. Very few are based on the computational design. There are some problems associated with experimental measurements and subsequent parameter identification. Measurement devices that are more often needed for carrying out experiments to determine the model parameters are not available during the development stages. Therefore, to overcome this limit, a computational design is coming into perspective [15, 16].

Computational design is a standard procedure in the design of power electronic systems. In this method, all the constitutive components of a system are designed with the exact size and geometry of the actual device and with the identical material properties. To consider the geometric complexity, nonlinearity, induced eddy currents and electric circuits, the FE field analysis needs to be coupled with the electric circuit analysis. This is because the physical quantities governing electromagnetic systems are often interrelated through magnetic, electric, mechanical and thermal variables. A change in one of these variables causes a change in other parameters. The coupled field circuit model can accurately represent this interdependence considering all involved variables. It also helps to analyze the entire system behavior without losing flexibility [16, 17].

With this technique, one can test new concepts immediately without the need to order components and assembling, which might be time-consuming and expensive. If something fails, there is no destruction, but information about too high voltages and/or currents. Critical operating states just before failure can be exactly reproduced and currents, voltages and junction temperatures can be easily monitored, which makes it comparably easy to identify problematic designs. Expensive equipment for measurement, power supply and load, which is essential for testing prototypes, is not needed in a first design stage. Further advantages of simulation are the ability to easily visualize fields, flows and distributions of physical properties and the ability of automated parameter optimization or analysis with statistical techniques [17-26].

Due to these advantages, it would be desirable to replace designing prototypes by their corresponding physics-based models obtained through computational efforts, in order to reduce development time, save development cost and detect reliability issues. Unfortunately, practical simulation will never fully map reality. The power electronic system under investigation must be simplified in order to be able to handle the model with a computer. Numerical simulation will always give a result, but it is up to experience and knowledge of the designer to verify the usefulness or accuracy [17], [28].

A physics-based simulation model, in order to be useful for utilization in a design procedure, must have specific requirements. The requirements of the simulation physics-based model and new trends modeling and simulation of the power electronic converters are briefly described in the next section.

Requirement for the simulation model

Figure 1.1 describes the new trends and requirements in power electronics converter design. In order to increase efficiency and performance, these requirements must be considered during the design process of converters [11].

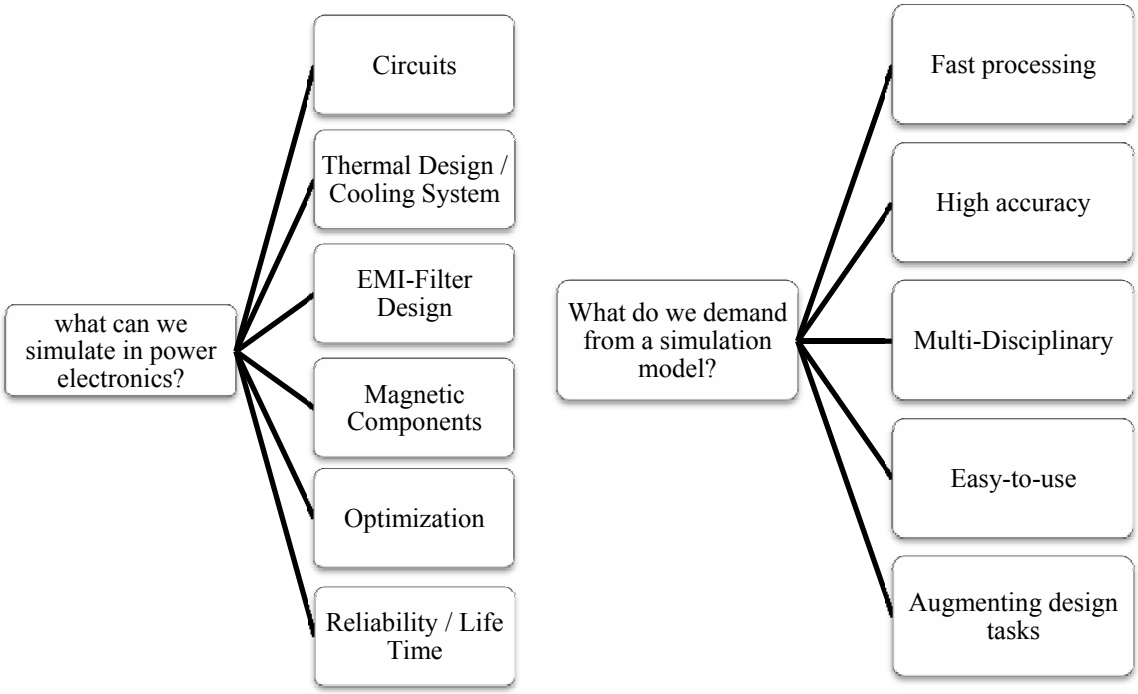

Figure 1.1 Trends and requirements

Power electronic converter simulation requirements

The goals which are necessary to achieve in a simulation are mainly as follows [11], [27]:

Circuits: The voltage and current waveforms of different nodes and branches of a circuit need to be measured to verify their proper functionality. All component voltage and current levels have to remain within safe ranges.

Thermal Design: The thermal management of electronic products is always a headache to the high power electronics design engineer. Since all electronic components

are assembled on the PCB, it's important to develop a good solution to dissipate the heat from PCB to the chassis with the conduction method.

EMI-Filter Design: It would be desirable to be able to calculate the common mode (CM) and differential mode (DM) noises propagated in the converter system's simplified models of the semiconductor switches, before building and testing an EMI filter.

Magnetic Components: Magnetic components such as inductors and transformers are the inseparable components in most of the power electronic systems. They significantly contribute to the system losses, volume and weight. In order to optimize the system's size and efficiency and power rating, more realistic magnetic component models is needed in the circuit simulation. These models must be able to consider iron losses, eddy-currents, skin- and proximity-effects and thermal behavior [11].

Optimization: Nowadays, with the increasing demand for power electronic converters, power electronic systems should be optimized in terms of costs, volume and weight. Also, some other examples are: to minimize the heat-sink volume, to minimize the EMI filters weight, to maximize the reliability of the power module, or to maximize the converter's robustness for a given range of operating conditions. Several techniques for optimization have been proposed so far, which all can be useful in design optimization of a power electronic conversion system [11].

Reliability: A high percentage of all failures in power electronic systems are related to improper thermal management in power converter design procedure. Therefore, calculating the converter system reliability based on transient temperature rises is an important feature of power electronics simulation models [11].

Software requirements

Related to demand from simulation models, the following requirements are essential: Fast processing: The simulation time should be limited to a couple of minutes, because often a large number of simulations are needed to investigate and verify a design before building a prototype [11], [28-32].

High accuracy: The models which are used in the simulation software should be accurate enough that can well represent the behavior of the actual device. Poor modeling of the component will lead the simulated results to have nothing in common with reality. By the means of physics-based modeling of the power electronic converters, a detailed model of each of the constitutive components is considered with the exact geometry and material properties as reality. Therefore, the converter's behavior from low to high frequency can be well represented by the physics-based model of the converter. Note that there is always a tradeoff between the accuracy and simulation time of the models, the more accurate the models are the more they will take to accomplish the simulation.

Multi-Disciplinary: Power electronics converters usually operate at a wide range of frequencies (DC to MHz), dimensions (μm to m), temperatures (0°C to 275°C) and power ratings (mW to MW). Therefore, they require design tools with extremely broad numerical capabilities. Power electronics is located at the intersection of various engineering disciplines such as circuit design, thermal design, electromagnetics, digital electronics, control theory, material science, especially with focus on packaging and reliability engineering. This multi-disciplinary aspect of power electronics becomes significant with rising switching frequencies, need for higher power densities and demand for higher reliability and robustness in wide parameter ranges. Therefore, the simulation

model must be capable of operation at different operating conditions and environments and should provide the ability to perform coupled simulations. Because temperature has a major impact on reliability, a multi-physics model, such as electro-thermal issues should be considered [11].

Easy to use: Because of the multi-disciplinary character of power electronics, a design procedure for the power electronics converter could be complicated. The models obtained for each of the components are based on the physical properties of the actual component. Utilizing such a model in circuit simulation software requires a link to electromagnetic field simulator software that can solve a coupled electromagnetic field problem. This procedure is not only time consuming but also, requires understanding of both electromagnetic field propagation and finite-element methods (FEM), which makes it more complicated. Therefore, simulation software for performing specialized calculations needs to have a user interface that is simple enough to be handled by an engineer who is not a specialist in this field, but should still be powerful enough to give useful simulation results. Furthermore, such software needs interfaces so that data can be exchanged easily between different programs. For example, the thermal simulator giving a thermal network model of a power module must provide the ability to directly export this network into a circuit simulator so that transient junction temperatures can be calculated [11-27].

Augmenting design tasks: In the physics-based modeling algorithm, the geometry and the material properties of each components and the overall system must be in the parametric order that can be modified throughout the optimization procedure. As an example, optimizing a heat sink for minimum volume at a given thermal resistance is a

challenging task but essential if the converter system must be designed for maximum power density. This provides an example of a design task that can be aided by software with an easy-to-use graphical user interface [11].

Literature review

System-level simulation of power electronics may be conducted at several resolution levels, e.g. steady-state characterization, average-value modeling, switch-level waveforms, etc. This simulation process usually takes place in two main categories: 1) electromagnetic and 2) Thermal. A detailed and complete physics-based model of the converter should be able to predict the electromagnetic behavior of the converter as well as the temperature distribution throughout the converter. By obtaining such a compressive model of the power electronics converter, one can predict and improve the problems that arise in an ill-conditioned system, at early development stages. Therefore, the first step is to have an understanding of those problems. Due to this fact, this literature review is basically focused mainly on the electromagnetic and thermal behavior of the power electronic converters and their coupling to the other systems [3-48].

Issues involved in the high frequency power converter's operation

There are a number of issues involved in the high frequency power converter's operation and load interactions. Increased voltage rates associated with power semiconductor devices have undesirable effects, including increased common mode currents leading to electromagnetic compatibility (EMC) problems, insulation breakdown due to inverter induced overvoltage at the converter output terminals, increased losses

and high frequency noises. In this dissertation, efforts have been made to predict some of these problems, which include electromagnetic interference and thermal behavior of the converter package. These problems are described briefly as follows [49]:

Electromagnetic interference (EMI)

Electromagnetic compatibility (EMC) is becoming an important issue in the design of modern power electronics systems [1, 2]. In conventional design methodologies, EMC issues are addressed only after a prototype is built. At that stage, the traditional EMC remedies are confined to adding extra components, metal shields, metal planes, or even redesigning the entire system. This leads to a potentially significant impact both on the cost and on the time-to-market of the products. Therefore, it is commonly recognized that EMC must instead be addressed during the design phase and not after [2, 50].

A numerical prediction of EMI/EMC has the potential to address EMI issues at the design stage and before prototyping. It provides significant benefits by avoiding late re-design and modifications of the converter implementation, leading to shorted design times and reduced post-prototype EMC costs. Such models can also be used to help find low cost solutions to reduce EMI suitable for the high-volume, low-priced power electronics conversion systems.

Several issues are the main contributor to EMI and noise propagation in the converter's circuit. The fast-switching speed of semiconductor devices in power converters leads to self-inflicted voltage transients due to the stray parasitic inductance and capacitance in the converter [3]. EMI created by the switching action is studied in [22-26]. In [25], a method based on utilizing DC-link decoupling capacitors is proposed.

Therefore, the proposed technique is acted such as an EMI filter to control the voltage overshoot of the switching devices, as well as suppressing the EMI effects. One well-known method in controlling the propagated electromagnetic noises in switching devices is through the control of switching modulation techniques. In [26] effects of different pulse with modulation and soft switching techniques on the conducted EMI propagation in the power converter circuit are discussed. In [22], the effects of nonlinear phenomenon of the semiconductor switch on the high-frequency EMI source are presented. Also [23] presents an EMI reduction for the power semiconductor switches, using a modified drive circuit to control the rise/fall time of the switching device.

The other contributor to the common-mode (CM) electromagnetic interference noise in power electronics systems is the parasitic capacitances between high dv/dt nodes and the ground [24]. Several studies are dedicated to the modeling these parasitic effects of converter's components. Magnetic components are other major contributors to the CM noise propagation. Due to the voltage gradients in inductor windings, there is always an electric field distributed between turns, between windings and between windings and cores. Reference [19], or example, deals with the inductor windings parasitic cancellation methods. In those studies, basically, two methods of cancelling parasitic capacitances are proposed. One is to use mutual capacitance theory and the other is implemented with the help of mutual inductance.

Furthermore, poor layout of the converter's PC boards is another reason for noise propagation. Previously, methods based on the parallel-plate waveguide and FEM analyses were introduced to solve the PCB unwanted coupling problems [34-35], [51]. In

[44], multilayer power printed structures are proposed to control the EMI noises generated in power converters.

All components and interconnections contain unwanted (parasitic) circuit elements. Often a combination of these elements can make a change in the operating condition of the power converter. This makes the EMI issues more complicated [23]. Therefore, in this study, attention is given towards modeling and characterization of different power system components EMI behavior. Special attention is given to the power converter's model since it plays an important role in the EMI evaluation and analysis.

Overvoltage

The voltage stress caused by converter's switching algorithm, such as pulse width modulation or frequency modulation, is considerably higher than that caused by sinusoidal waveform. The PWM waveform with high rate of dv/dt and fast switching often leads to deteriorating of the voltage enduring capability of the conductor. High switching frequencies are often utilized in modern switching devices to obtain low switching losses. The shorter switching times in modern semiconductor devices, increase dv/dt at the motor's terminals, significantly. The sharp rise of wave-fronts in the PWM voltage waveform has high frequency contents in the MHz range. The high frequency operation excites the stray capacitances between various parts of the components causing each wave-front to see the distributed parameters of the converter [2], [52, 53].

The overvoltage problem is compounded when the converter is connected to the load through a cable. The cable is an inherent part of the system. Due to the impedance mismatch between the cable and the load impedance, the voltage pulse generated at

converter terminals is reflected at the load's terminals. Because of the repeated voltage reflections, the load terminal voltage can reach twice the voltage of the dc bus value of the converter.

Many methods exist for mitigating the EMI or voltage spikes in the power electronics converters. In order to verify the performance of the power converter and the mitigation techniques at the design stage, the simulation software should have specific characteristics, which are essential to reach accurate results [2].

Computational Developments

For evaluation of the electromagnetic fields propagation within a power electronics circuit, what is missing is an efficient coupling in order to take into account the multi-disciplinary aspects of power electronics [11].

Transient power electronics circuit simulations for the PWM rectifiers typically run over a few periods lasting for tens of milliseconds. Nowadays, switching frequencies are typically in the range of hundreds of kilo-Hertz with the tendency to rise due to improved semiconductor devices. Numerical time steps should be smaller than the smallest time constant in the system, resulting in a numerical time step width smaller than 100 ns for 100 kHz switching frequency. Therefore, over one period (20ms) there is a minimum number of 200,200 numerical time steps required. In the case, one would such as to take into account the semiconductor switching behavior, which takes typically several tens of nanoseconds, the numerical step width should be reduced further. As an example, if the finite element method (FEM) is employs to calculate the electromagnetic field propagation within the 3D-model, one single FEM simulation takes typically a few

minutes up to a few hours. Theoretically, this must be done at every time step of the numerical circuit simulation to achieve true coupling. Assuming 10min calculation time for one FEM-simulation, the total time of the coupled simulation would be 200,000 × 10min = 3.8 years. Similar problems arise in the case of coupling the circuit simulation directly to a 3D-FEM solver [11].

One possible strategy of performing numerically efficient coupled simulations is to extract equivalent circuit models from 3D-FEM simulations, which are typically represented by small networks that can be integrated easily into the circuit simulator. The insertion of such small equivalent circuit network models will increase the computational effort of the circuit simulation, however the total effort will still be comparably small and could be handled easily [33], [36, 37], [45], .

Each component of the power circuit is described by an equation. Linearizing the equations within one time step of the circuit simulation, results in a system of linear equations that can be solved in matrix form.

Thermal Simulation

With thermal capacitance C_P [Ws/(K.kg)], material density ρ [kg/m^3], temperature dependent thermal conductivity λ [W/Km], thermal flow density w [W/m3] and temperature T [K], the thermal conduction inside a solid structure is described by the heat conduction equation as follows [11]:

$$C_p(T).\rho\frac{\partial T}{\partial t} = \nabla[\lambda(T).\nabla T] + w(\bar{x},t) \tag{1-1}$$

Considering thermal convection, which is the main cooling mechanism in case of water cooling or air-cooled heat sinks, there are two additional coupled differential equations, one is in scalar form and the other one is in vector format [11]. Therefore, considering convection directly will increase the computational effort of the computational fluid dynamics (CFD) problem, significantly. A significant improvement provides the strategy to define convection in form of a boundary condition via a heat transfer coefficient and calculate the remaining solid structure employing only heat conduction with no need of CDF simulations. This strategy is described in detail in reference [30].

Modeling of Thermal Coupling

Power semiconductors, which are usually placed on heat sinks, will heat up neighbor semiconductors by rising the heat sink temperature. Inside power modules the same effect takes place between dies and is generally known as 'thermal coupling'. This effect can be significant and must be considered in thermal equivalent network models. A general modeling procedure called Impedance Matrix Method [36] is very effective.

The modeling process with emphasis on the accuracy of the 3D-FEM simulations of the thermal step responses is discussed in detail in [30]. Software implementation, scaling issues, coupling with a circuit simulator and numerical simulation are discussed in [29-32]. Not only for a problem as large as the multi-chip power module, but also for much smaller problems. A careful software implementation of the whole modeling process of the "Impedance Matrix" method is the best solution in order to handle the the issues associate with the problem at hand.

IGBT Module Design Optimization

Relevant design objectives for IGBT modules are high current capabilities of power terminals, low stray inductance in commutation path, uniform current and loss distribution between paralleled chips. Combining EM field calculations with circuit simulation is an efficient means to optimizing these parameters. The field vectors allow identifying critical chip placements and substrate layouts, where strong magnetic fields might induce unwanted voltages in the gate signal loops. Transient simulations using extracted impedance matrices and accurate IGBT and diode models show how these induced voltages affect the dynamic current sharing [7], [15], [40-42].

Switching- and Conduction Losses

Simulation of conduction losses can be simply performed by defining a resistor and a voltage source in series with an ideal switch, where the resistor might be defined as temperature-dependent in order to model the general temperature-dependency of semiconductor losses. For switching losses, there are basically two strategies available. One strategy is to try to model the switching process in the time domain with extremely high accuracy and calculate the resulting switching losses. The problem with this approach is that the numerical time steps during the switching action should be set to very small values. This might cause problems with the numerical stability and increase the simulation time, significantly [11].

A different strategy is preferable especially for switched system simulations. Here one would implement a counter that injects an energy pulse containing the switching loss energy as given in a datasheet or derived from measurements any time an ideal switch is

turned on or off. This will not slow down the simulation speed because the ideal switching action occurs within one numerical time step, the simulation will remain numerically stable and the accuracy will be very high. Such a simple loss counter scheme is described in detail in references [11], [32], [40-42].

Transient Junction Temperatures Considering Temperature-Dependency of Semiconductor Losses

The critical aspect of the coupling is to make the switching and conduction losses dependent not only on voltage and current, but also on the transient junction temperatures of the semiconductors. The temperature-dependent loss characteristics given by datasheet or measurement of the power module's semiconductors can be defined via dialog and attached to the IGBT and diode symbols of the power circuit. The power module is set up as a 3D structure including the heat sink and the thermal solver will automatically build the full thermal model via impedance matrix that can be inserted into the circuit solver. The transient semiconductor losses are also calculated [11].

Electromagnetic Simulation

The numerical techniques for the solution of field problems can be classified into two groups. One group is based on the differential formulation of the Maxwell equations (FDM, FEM) or integral equation (IE) based techniques (Method of Moments). A good choice of the appropriate method seriously affects the modeling and simulation effort and the accuracy of the results. The solution variables of FDM and FEM are the field variables E and H, whereas IE based techniques are formulated in circuit variables

(currents and voltages). Bearing in mind a tight integration of the electromagnetics simulation within a circuit solver, IE-based techniques fit better to the concept of multidisciplinary simulations. Furthermore, for IE-based techniques the model handling is more convenient, because only the involved conductor geometries needs a discretization in contrast to FDM or FEM, where the whole space including vacuum must be taken into account. MoM has the huge drawback that it is a high frequency approximation. Low frequency to DC cannot be handled correctly by MoM.

In the FE model of a power converter circuit, a current source is often used as an excitation. However, in actual operating conditions, a voltage source is often used as an exciter. To calculate current in the circuit, combined solution of the field and circuit equations must be solved. To tackle this situation, time harmonic formulations using complex variables were presented for sinusoidal supply. To simulate arbitrary voltage waveforms or transients, time-stepping simulations were developed. Direct coupling between the field and circuit equations was used to solve electrical machines simulations [33]. To solve coupled field circuit analysis, many authors have presented general methods. The circuit can be a network of resistors, inductors, capacitors, diodes or other semiconductors. The circuit equations are usually solved by loop currents or nodal voltages. However, most of the formulations combine both approaches to result in minimum number of unknowns [1, 2].

The models, proposed for each component allows us to have a flexible multi-purpose simulation tool, which enables us to use the same model for frequency domain as well as for time domain simulations. Solving a full wave Maxwell equation enables us to maps the electromagnetic behavior of arbitrary 3D layouts and geometries into an equivalent

network of lumped circuit components. Theoretically, this method gives an accurate result from DC up to the highest frequencies [1, 2].

In the used FEM method, all regions of conductors are discretized into many partial elements. The proposed method creates matrices of inductances L_{ij}, coefficients of potential P_{ij} and node resistances Rm. The individual matrices are responsible for the magnetic and electric field couplings and material conductivity, respectively. The generated lumped circuit network can then be excited by current and voltage sources and the frequency or time domain response is then calculated by a circuit simulator. The simulation corresponds to a solution of a matrix equation, which is generated from the element matrices.

Inductive Component Modeling, Optimization and Augmenting Design Tasks

In order to perform more realistic numerical simulations of power electronic systems, detailed models of inductive components would be very helpful. In [14] and [38], it is shown for a typical DC/DC converter how one would achieve larger power densities than by employing an optimization loop with an internal simulation that takes into account detailed inductive component models including iron losses, skin and proximity effect in addition to detailed thermal models. Making such models available to circuit simulation via component databases would increase the efficiency of the simulation platform significantly [11].

In comparison, designing prototypes based on trial and error would be extremely time-consuming. Compared with measurements that were performed on the optimized prototype, the accuracy of the simulation may prove to be very good.

Algorithms for complex tasks such as EMI-filter optimization are discussed in [3], [8]. Realizing the software implementing the algorithms and providing an easy-to-use interface would be of great benefit because EMI-filter design and optimization is essential in many applications.

Generally, integrating such tools into a power electronic simulation environment will increase the designer's productivity and the usefulness of the simulations significantly, [11].

Simulating Conducted EM Noise

The design of differential mode (DM) and common mode (CM) EMC input filters is a fundamental issue of converter design. The filter strongly influences the converter performance concerning power density or control dynamics. The filter design must ensure the compliance to EMC standards, so that the converter can operate in a non-ideal environment with external disturbances and does not interfere with neighboring electronic equipment. The conventional design procedure is to physically build a converter system, to measure the EM noise and conducted emission levels and to perform design iterations for the input filter until its noise measurements fulfill the required EMC standard [8]. An alternative method of designing a filter is to simulate the converter behavior. This method permits noise prediction without the need to build hardware. However, this method must include all relevant parameters in the system model, which

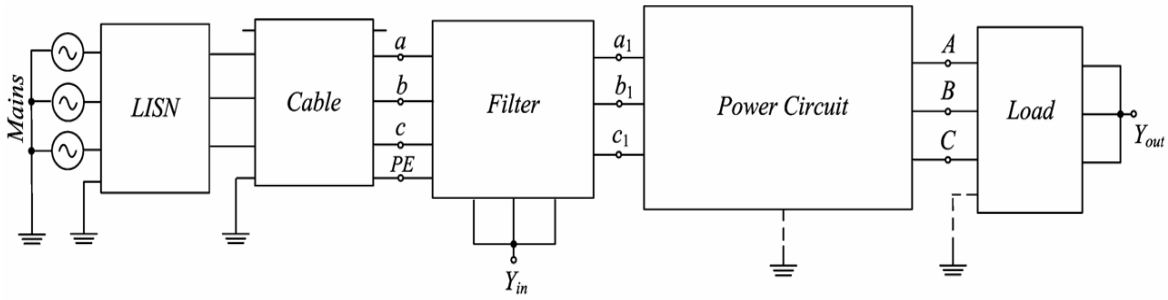

Figure 1.2 Block diagram of the power train prototype and model. The DM and CM noise measurements are performed with front end Line Impedance Stabilization Network (*LISN*). The source for EMI noise is the Power Circuit. The DM noise propagates through the filter and the cable towards the LISN, while the CM noise is caused by step voltage changes and propagates mainly through parasitic impedances to protective earth (indicated by dashed lines) [11]

may lead to an extraordinary complex simulation. This complexity and the lack of a combined tool for exact stray parameter extraction and circuit simulation is the reason why EMC simulation was mainly neglected in the converter design process.

Figure 1.2 shows the block diagram of a complete power conversion system, where each block is constituted of a more detailed circuit sub-model. The converter topology shows a high complexity and is a good demonstration object to show that EMI prediction is possible, even for complex systems. For evaluation of the converter control system, this modeling level of the power circuit would be adequate. However, for an EMI simulation which should be accurate up to 30 MHz, the model must include a transistor model that depicts the switching transient accurately as well as its parasitic depletion layer capacitances. In this study a physics-based IGBT model proposed in [21, 22], [48] is used and shown in Figure 1.3.

Similarly, the main model of the other building blocks of EMI filter, cables and load are included in the complete model, to construct a physics-based model of the overall

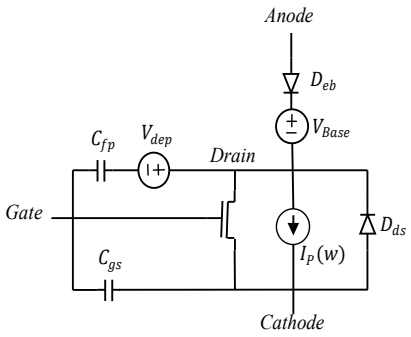

Figure 1.3 Physics-based IGBT model, details see [21]

converter. More details about the hardware setup and simulation can be found in in references [47], [48].

In general one should consider a frequency domain simulation for an EMI prediction, but due to the complex control scheme of the power conversion system and the inclusion of the finite switching transient, this would result in severe modeling problems. Therefore, a time domain circuit simulation of few periods was performed using a numerical step width of 10ns to achieve the necessary frequency resolution. The overall simulation time took several hours on a common 3 GHz personal computer. Following the time-domain simulation, a CM noise level spectrum was calculated by Fourier transform of the noise voltages at the Line Impedance Stabilization Network (LISN).

Improvement in reliability, power density and controllability of such systems require a variety of studies of their physical representations. The increase in power density and the improvement in electromagnetic and thermal characteristics require the optimization of the design [11], [54].

The complexity of these new systems requires better methods for predicting their interactions among the power components and systems. Furthermore, effective diagnosis also presents a challenge. The physics based modeling can play an important role in developing diagnostics strategies of the operating components.

Physics based modeling is essential to mimic actual hardware and minimization of hardware design iterations. Dynamic models are required to study the large signal time-domain transients as well as small-signal frequency-domain stability and controller design [17].

Fundamental obstacles to the modeling and simulation are a lack of high-fidelity models, an exhaustive computational burden and rigid simulation platforms. Automated order-reduction techniques facilitate efficient physics-based component models and flexible simulation environments that help designers synthesize dynamic behavior of the original system within a design cycle. A candidate for efficient simulation frameworks is shown in Figure 1.4. The first physics-based descriptions of components provide highly accurate models. Then, order reduction facilitates system-level integration of physics-based component models in a switching power converter and consequently, provide a fast computational environment [17].

Problem statement

A physics based high frequency model for power converters is proposed based on finite element analysis. It consists of the low frequency model developed earlier [1-16] with a lumped high frequency branch connected in parallel. The parameters required for modeling the low frequency model are calculated by nonlinear finite element solutions.

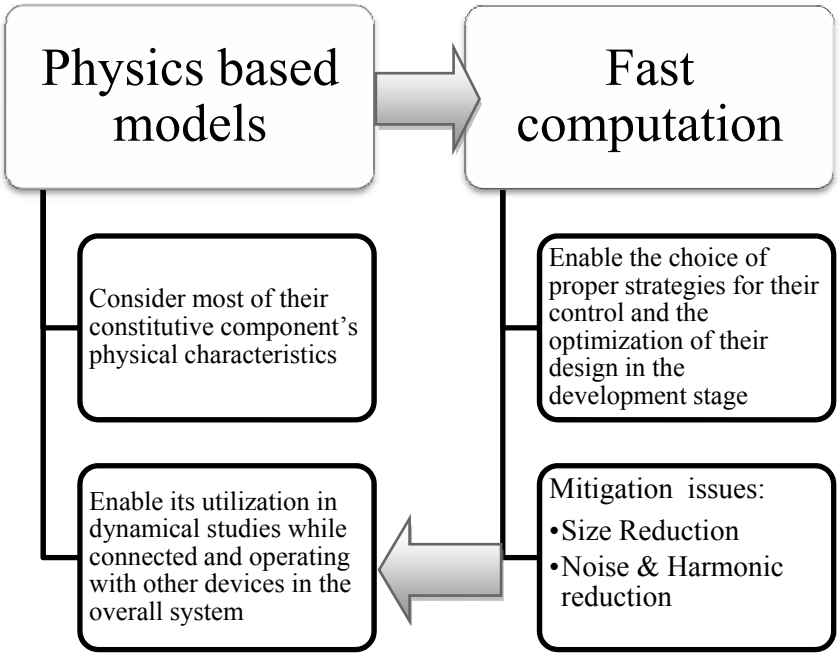

Figure 1.4 Efficient simulation framework for switching power converters

The low frequency converter model captures the low frequency dynamics and the high frequency branch considers the distributed effects converter component's parameters.

The resistance and inductance of each individual element were calculated by a 2D magneto-dynamic FE analysis. The frequency dependent resistance and inductance were calculated by applying currents to each component with a set of frequency values to provide a set of curves. The self-capacitance of each individual component and the mutual capacitances between them were evaluated by a 2D electrostatic FE analysis. By using the circuit parameters corresponding to the applied switching frequency and their actual arrangement, a distributed parameter winding circuit was formed. The Kron matrix

reduction technique was applied to the distributed-parameter circuit to obtain the lumped high frequency branch.

The developed model was used to evaluate the power electronic converter high frequency behavior. This includes the converter output terminal overvoltage, EMI, effect of switching frequencies on the operational behavior of the converter. The simulation results show the ability of the developed model to represent the converter low and high frequency behavior under various dynamic operating conditions. Simulations were performed on different types of converter applications. The experimental verification is also provided.

In addition, a motor and drive model was also developed for EMI analysis and evaluation. This consists of the lumped parameter models of different system components such as cable, inverter in addition to the motor. The lumped parameter models were used to enable faster simulations. The results obtained were verified by experimental measurements and excellent agreements were obtained.

A study was conducted on changes in the components arrangement design to investigate its influence on the converter high frequency behavior. This was shown to have a little effect on the parameter values.

Different software packages were utilized to solve the entire problem. Infolytica 3D was used to solve the coupled field circuit problem for the calculation of low frequency parameters such as flux linkage and Magnetic Flux Density. It is also used to calculate the resistance and inductance at high frequency operation. Infolytica/ElecNet was used to solve an electrostatic analysis for the calculation of capacitances. Matlab/Simulink is used to design the filter, which is used in series with the high frequency branch to block

the fundamental frequency component. Matlab matrix reduction toolbox is used to reduce the order of the distributed parameter model. Simulink is used to test the high frequency converter model in an integrated motor drive system. The dSpace controller development environment was used in the experimental verification of the developed model.

Originality and significance

In this dissertation, several issues involved in the high frequency PWM operation were investigated particularly critical issues such as overvoltage, current spikes and EMI, which are of great importance.

The novelty of the proposed model and its implementation is that a high frequency physical model of the power electronic converter was derived based on the actual geometrical and other physical information of the converter. The goal here is to obtain the high frequency converter parameters. This is the first attempt to develop such a model to obtain these parameters without using experimental procedures. The developed model has the potential to be used instead of expensive testing procedures of obtaining these high frequency parameters by experiments.

Since the physical modeling of the converter was performed, its use in the simulation would lead to high quality improvement of final design. This enhances the designer's ability to virtually prototype any converter using simulation and estimating its performance before any actual hardware is manufactured.

It is often desirable to have an estimate of the overvoltage at the design stage itself and accordingly provide adequate insulation for the loads and other appliances connected to the power converter. In addition, the correct estimation of EMI would lead to follow

the EMC compliance procedures in the design stages. It would also reduce time-to-market for the manufacturer saving significant development cost.

New or the available control algorithms can be tested with the developed model. In addition, it is helpful for selecting the range of operating switching frequencies with which a tradeoff between switching losses and the converter's harmonics can be decided. The developed model will be useful in the dynamic simulation of overall system.

The main contribution of this dissertation is the physics-based modeling of the whole converter package. This approach enables to design any power electronic conversion system to meet electromagnetic standards and design constraints. This includes physical characteristics such as; decreasing the size and weight of the package, optimized interactions with the neighboring components and higher power density. In addition, the electromagnetic behaviors and signatures can be evaluated including the study of conducted and radiated EMI interactions in addition to the design of attenuation measures and enclosures.

Moreover, in this study the effect of the switching action on the conduction EMI as well as the radiated EMI is being considered for the first time. Also, a novel model has been proposed for the switching devices, especially power IGBT, that can be used to study the high-frequency behavior of the system.

Dissertation Outline

This dissertation is organized as follows: Chapter 2 covers the fundamentals of order reduction techniques and the tools used in the remaining chapters. In chapter 3, calculation of components parameters are discussed. In Chapter 4, physics based

modeling approach for modeling the power electronics component is introduced. Chapter 5 is dedicated to modeling the PC board connections. Chapter 6 introduces a physics based modeling approach for power semiconductor devices. In chapter 7, the application of the Silicon Carbide (SiC) devices in power electronic converters is discussed. Chapter 8 introduces the application of the physics-based modeling approach in power electronics. Chapter 9 is dedicated to the experimental setup and verification of the power electronic converter's models and their design optimizations.

Parts of this work are published as number of journal and conference technical papers which are listed at the end of this dissertation.

Chapter 2 Electromagnetic Field and circuit coupling

This chapter is prepared based on the studies in electromagnetic field and circuit coupling analysis accomplished in the previous works by Abed [1] and Ganu [2], et. al. This chapter describes the field and circuit equations, which are used in solving the coupled field circuit problem. Electromagnetic field equations are usually solved by numerical computations such as finite element (FE). This is due to the capability of the finite element method (FEM) in handling complex geometries and local nonlinearities of variables. To achieve a precise system level simulation, the FE equations must be coupled with the external circuit and control equations. The coupling can be achieved using either the direct or the indirect method. In the direct method, the simulation in the FE software and circuit simulation tools were performed simultaneously. In the indirect coupling method, the FE and circuit simulation tool were performed one after each the other and the results of one was used by the other. The time constants involved in the field and circuit domain and the complexity of the model, dictate which method should be used for coupled field circuit simulation [2] and [55].

Overview

In this dissertation, the electromagnetic field circuit coupled method was utilized to simulate the power electronic conversion system. The methods are implemented in the FE software and the Simulink environment. To perform the electromagnetic field circuit simulation, one approach is a direct method where a functional block representing the FE model of the converter's components are directly coupled with other components of the

circuit and the control system using Magnet-Simulink link. The input to the block is voltage while the outputs are the currents and the electromagnetic fields. The same time step was used to solve the field and circuit together. This method is very popular due to the ease of model construction and simulation, flexible options for post processing and the possibility of extending the FEA to experts in power electronics or control systems. This method was mainly used for the verification of the electrical and electromagnetic behavior of the power electronic converter.

Another approach is to initially simulate the FE model and obtain an equivalent circuit representation for the converter model. Subsequently, this model can be used in circuit simulation software to analyze the electric behavior of the converter. This process can be performed repeatedly to optimize the design and reach the best configuration of the converter or control algorithm applied to the converter. To obtain the equivalent circuit model, coupled field and circuit equations for electromagnetic conductors are solved. Once each of the component's models are obtained then the system simulation involving power electronics and control equations are solved together with the same time step.

In the following sections, the field and circuit equations are reviewed. The coupling of field and circuit equations has utilized references [56-60]. This formulation was implemented in Infolytica-Magnet/Elecnet software.

Maxwell's and parametric equations

This section is restated from [61]. It is repeated here for continuity. In this study, Maxwell's electromagnetic field equations are the basis of all the developments. As a review, these equations can be summarized as follows:

$$\nabla \times \overline{E} = -\frac{\partial \overline{B}}{\partial t} \tag{2-1}$$

$$\nabla \times \overline{H} = \overline{J}_e + \overline{J} + \frac{\partial \overline{D}}{\partial t} \tag{2-2}$$

$$\nabla \cdot \overline{D} = \rho_e \tag{2-3}$$

$$\nabla \cdot \overline{B} = 0 \tag{2-4}$$

where, $\overline{E}$ is the electric field intensity vector [V/m]

$\overline{B}$ is the magnetic flux density (induction) vector $[Wb/m^2]$

$\overline{H}$ is the magnetic field intensity vector $[A/m]$

$\overline{J}_e$ is the excitation (external) current density vector $[A/m^2]$

$\overline{J}$ is the induced current density vector $[A/m^2]$

$\overline{D}$ is the electric flux density (displacement) vector $[C/m^2]$

ρ_e is the external charge density $[C/m^3]$

The displacement term in (2-2) is neglected. Therefore, (2-2) can be rewritten as follows:

$$\nabla \times \overline{H} = \overline{J}_e + \overline{J} \tag{2-5}$$

In addition to Maxwell's equations, there are other important parametric equations, as follows, which relate the various field variables as affected by the surrounding media.

$$\overline{H} = \nu \overline{B} \tag{2-6}$$

$$\overline{B} = \mu \overline{H} \tag{2-7}$$

where, ν is the magnetic reluctivity of the medium.

μ is the magnetic permeability of the medium.

Both ν and μ are functions of the B-H magnetization characteristic of a magnetic material as well as the operating point.

$$\nu = 1/\mu \tag{2-8}$$

The other parametric relationships are as follows:

$$\bar{J} = \sigma \bar{E} \tag{2-9}$$

$$\bar{D} = \varepsilon \bar{E} \tag{2-10}$$

where, σ is the electrical conductivity of the medium.

ε is the permittivity of the medium $[F/m]$.

The current density term $\bar{J}$ in (2-9) represents the induced current density component and not the external (or source) component. In addition to equations (2-1) through (2-10) a key variable, namely the magnetic vector potential (M.V.P) $\bar{A}$ can be defined as follows:

$$\bar{B} = \nabla \times \bar{A} \tag{2-11}$$

This is somewhat analogous to the electrostatic scalar potential V where the electric field vector $\bar{E}$ can be defined as a gradient of an electrostatic scalar potential V. That is, one can write:

$$\bar{E} = -\nabla V \tag{2-12}$$

Based on above equations, the magnetic vector potential field formulation is developed. In this formulation, the flux density is the curl of a magnetic vector potential and the relationship between the current density and the field variable is in a curl-curl

form. This is similar to the Poissonian relationship that relates electrostatic scalar potential to charge densities in electrostatic fields [2].

Vector field formulation

Using the Maxwell equations mentioned in (2-1) to (2-4), the electromagnetic field inside the object is governed by the following set of nonlinear partial differential equations:

$$\nabla \times \overline{E} = -\frac{\partial}{\partial t}\left(\nabla \times \overline{A}\right) \tag{2-13}$$

The operators $(\partial/\partial t)$ and $(\nabla\times)$ are interchangeable. Therefore, one can write (2-1) as follows:

$$\nabla \times \overline{E} = -\nabla \times \left(\frac{\partial \overline{A}}{\partial t}\right) \tag{2-14}$$

Therefore, we have the following:

$$\nabla \times \left(\overline{E} + \frac{\partial \overline{A}}{\partial t}\right) = 0 \tag{2-15}$$

Hence, one can define a scalar potential function V as follows:

$$\overline{E} + \frac{\partial \overline{A}}{\partial t} = -\nabla V \tag{2-16}$$

Rearranging (2-16), one can write that

$$\overline{E} = -\left(\frac{\partial \overline{A}}{\partial t} + \nabla V\right) \tag{2-17}$$

Therefore, from (2-17) and (2-9) one can write the following:

$$\overline{J} = -\sigma\left(\frac{\partial \overline{A}}{\partial t} + \nabla V\right) \tag{2-18}$$

Also, from (2-11) and (2-6) we have:

$$\overline{H} = \nu\overline{B} = \nu\left(\nabla \times \overline{A}\right) \tag{2-19}$$

Hence,

$$\nabla \times \overline{H} = \nabla \times \left(\nu\left(\nabla \times \overline{A}\right)\right) \tag{2-20}$$

From (2-20) and (2-5) one obtains the following:

$$\nabla \times \left(\nu\left(\nabla \times \overline{A}\right)\right) = \overline{J}_e + \overline{J} \tag{2-21}$$

Substituting (2-18) into (2-21) yields the following key equation:

$$\nabla \times \left(\nu\left(\nabla \times \overline{A}\right)\right) = \overline{J}_e - \sigma\frac{\partial \overline{A}}{\partial t} - \sigma\left(\nabla V\right) \tag{2-22}$$

Taking the divergence of both side of (2-18) and then using the fact that the divergence of the curl of any vector field is zero, we get

$$\nabla.(\sigma(\frac{\partial A}{\partial t} + \nabla V) = 0 \tag{2-23}$$

Equations (2-22) and (2-23) represent the fundamental equations of the vector potential formulation for electromagnetic field.

To derive the time harmonic equation this physics interface solves, magnetic and electric interface, the analysis is started with Maxwell-Ampere's law including displacement current. This does not involve any extra computational cost in the frequency domain. Firstly a time-harmonic field is assumed as (2-24).

$$\nabla \times H = J = \sigma(E + \upsilon \times B) + j\omega D + J^e \tag{2-24}$$

Using the definitions of the fields $B = \Delta \times A$ and $E = -\nabla V - j\omega A$ and combine them with the constitutive relationships $B = \mu_0(H + M)$ and $D = \varepsilon_0 E$, (2-25) is obtained.

$$(j\omega\sigma - \omega^2\varepsilon_0)A + \nabla\times(\mu_0^{-1}\nabla\times A - M) - \sigma v\times(\nabla\times A) + (\sigma + j\omega\varepsilon_0)\nabla V = J^e \quad (2\text{-}25)$$

The equation of continuity is again obtained by taking the divergence of Ampere's law. It is the equation solved for the electric potential. Thus the following equations for V and A is achieved.

$$-\nabla.\left(\left(j\omega\sigma - \omega^2\varepsilon_0\right)A - \sigma v\times(\nabla\times A) + (\sigma + j\omega\varepsilon_0)\nabla V - \left(J^e + j\omega P\right)\right) = 0 \quad (2\text{-}26)$$

$$\left(j\omega\sigma - \omega^2\varepsilon_0\right)A - \sigma v\times(\nabla\times A) + (\sigma + j\omega\varepsilon_0)\nabla V + \nabla\times\left(\mu_0^{-1}\nabla\times A - M\right) = J^e \quad (2\text{-}27)$$

where A is magnetic potential , J^e is external current density, M is magnetization and $\boldsymbol{v}$ is the motion speed which here, it is equal to zero [2].

To perform the finite element analysis, initially, the geometry is meshed by finite elements, consisting of first or second order triangular elements. If possible, the cross section of the electromagnetic device is divided into symmetry sectors, from which only one is modeled using FE and symmetry constraints are set to the periodic boundary [2].

In the FEA, the magnetic vector potential and electric scalar potential can be expressed as follows:

$$A = \sum_{j=1}^{N_n} \lambda_j a_j \quad (2\text{-}24)$$

$$V = \sum_{i=1}^{N_m} \lambda_i v_i \quad (2\text{-}25)$$

where, N_n , N_m are the total number of free nodes in the finite element mesh, λ_j and λ_i are the classical approximation functions of edge and nodal elements, a_j and v_i are the magnetic vector potential and electric scalar potential at node j.

Equations (2-22) and (2-23) can be written in the following matrix form:

$$\begin{bmatrix} S & C \\ 0 & T \end{bmatrix}\begin{bmatrix} a \\ v \end{bmatrix}+\begin{bmatrix} G & 0 \\ C^T & 0 \end{bmatrix}\frac{d}{dt}\begin{bmatrix} a \\ v \end{bmatrix}=\begin{bmatrix} F \\ P \end{bmatrix} \tag{2-26}$$

By solving (2-26), the vector and scalar potential which satisfies (2-22) and (2-23), is obtained.

Electric circuit equations

The FE equations are coupled to circuit equations. This external circuit coupling allows us to simulate the operating conditions of the electromagnetic device with the real power supply connections.

Generally, any electric circuit can be represented by the following integral-differential matrix equation:

$$[E_k]=[r_k][I_k]+[L_k]\frac{\mathrm{d}}{\mathrm{dt}}[I_k]+\left[\frac{1}{C_k}\right]\int[I_k]dt+[\gamma_k]+\frac{d}{dt}[\psi_k] \tag{2-27}$$

Where, E_k is the vector of voltage sources in each electric mesh k.

r_k is the matrix of resistances (symmetric).

L_k is the matrix of inductances (symmetric).

I_k is the vector of electric current in each mesh.

γ_k is the vector of non-linear voltage drop each electric mesh k.

C_k is the matrix of capacitances.

ψ_k is the vector of flux linkages in the coil.

In matrix r_k, elements $r_{ij}\,(k\times k)$ are calculated by,

$\mathrm{r_{ii}}$ is obtained by addition of resistances in the mesh i.

r_{ij} is obtained by addition of resistances which belong to the meshes i and j with the sign + if the currents of meshes i and j are in the same direction, with the sign – otherwise.

$L_{ij}\left(k\times k\right)$ is formed the same way as the resistance matrix.

$C_{ij}\left(k\times k\right)$ is formed the same way as the resistance matrix.

k is the number of electric meshes

Now, we can put the equations together to obtain the coupling system. Equation (2-27) can be written in the following form:

$$[E_m]=[X_0]\int[i]dt+[X_1][i]+[X_2]\frac{\mathrm{d}}{\mathrm{dt}}[i]+\frac{d}{dt}[\psi]+[\gamma] \tag{2-28}$$

Relation between magnetic and electric circuit equations

In a magnetic component, for a conductor, the current density can be expressed by (2-18). To characterize the current density, the vector of turns density N (with $J_0 = Ni$) is defined. The relation between the winding voltage V_0 and the current is obtained by the projection of vector N on J_0 and by an integration on the whole winding volume Ω_o. Under these conditions, the winding voltage is given by [1]:

$$V_o = r_o i + \frac{d}{dt}\int_{\Omega_o} A.N\ d\Omega \tag{2-29}$$

In this expression, the integral term represents the flux linkage ψ of (2-27). ψ is a non-linear function of the current due to the magnetic material properties.

Coupling of field and circuit equations

In most of the cases, magnetic and electric equations are solved simultaneously. The electromagnetic field equations are solved using a formulation with magnetic vector potential. The coupling is obtained by the conductor current expressed in terms of current density and the flux linkage expressed from the vector potential. Two approaches can be can be used to perform this task. In the first approach, the coupled equation system is only expressed in terms of the vector potential and scalar potential. In the second approach, the magnetic variables and the currents are kept as unknowns. The second approach is utilized throughout this dissertation.

The current density in the last term of (2-26) is expressed as a function of the current with help of vector N, F can be written as follows:

$$[F] = [D][i] + [F'] \tag{2-30}$$

The elements of matrix D depends on vector N and functions given by (2-24) and (2-25). The flux ψ can also be expressed from the integral of (2-18) and the vector potential circulation a. For a system with several conductors, we can show that the vector $[\psi]$ takes the form:

$$[\psi] = [D]^T [a] \tag{2-31}$$

From (2-26), (2-29), (2-30) and (2-31) we obtain:

$$\begin{bmatrix} S & Q & -D \\ 0 & G & 0 \\ 0 & 0 & r_m \end{bmatrix} \begin{bmatrix} a \\ v \\ i \end{bmatrix} + \begin{bmatrix} T & 0 & 0 \\ Q^T & 0 & 0 \\ D^T & 0 & L_m \end{bmatrix} \frac{d}{dt} \begin{bmatrix} a \\ v \\ i \end{bmatrix} + \begin{bmatrix} 0 \\ 0 \\ C_m^{-1} \int i dt \end{bmatrix} + \begin{bmatrix} 0 \\ 0 \\ \gamma_m \end{bmatrix} = \begin{bmatrix} F' \\ P \\ E_m \end{bmatrix} \tag{2-32}$$

Equation (2-32) represents the coupled circuit-field system. In this equation, the unknowns are the vector potential, the scalar potential for the magnetic domain and the mesh current for the electric circuit and all equations are solved simultaneously.

FE is coupled with Simulink to perform system simulations studies through an S-function functional block. The S-function functional block schematic is shown in Figure 2.1. A constant time step Δt is used for the coupled FEM computation. The sampling time of the FEM block is set to that value and the same time step sizes are used elsewhere in the model [1].

Naturally, this also requires careful analysis and knowledge of the physical system on the part of the user. The input and output variables are defined as stated above and are updated discretely at the major steps as set for the finite element analysis. The average of the input voltage from two adjacent steps is replaced by a single value taken from the middle point between the steps. This is not equivalent to the selected trapezoidal integration method, but it has not caused any problems with accuracy or convergence [1].

The state variables are not required because the vector potential and current are solved inside the FEM block. The data transfer between the FEM block and Simulink is illustrated in Figure Figure 2.1. Before the simulation, the initialization parameters are stored in a file, from which the FEM reads the parameters before the first time step. During the time-stepping simulation, the variables are passed directly back and forth between the FEM block and Simulink. After the simulation, the field solution is stored in a file with the same format as the one with the initial field. The simulation variables can be stored in MATLAB's workspace or in a separate file [1]. This task was performed by Nagy et. al [1] and was re-implemented here in this dissertation.

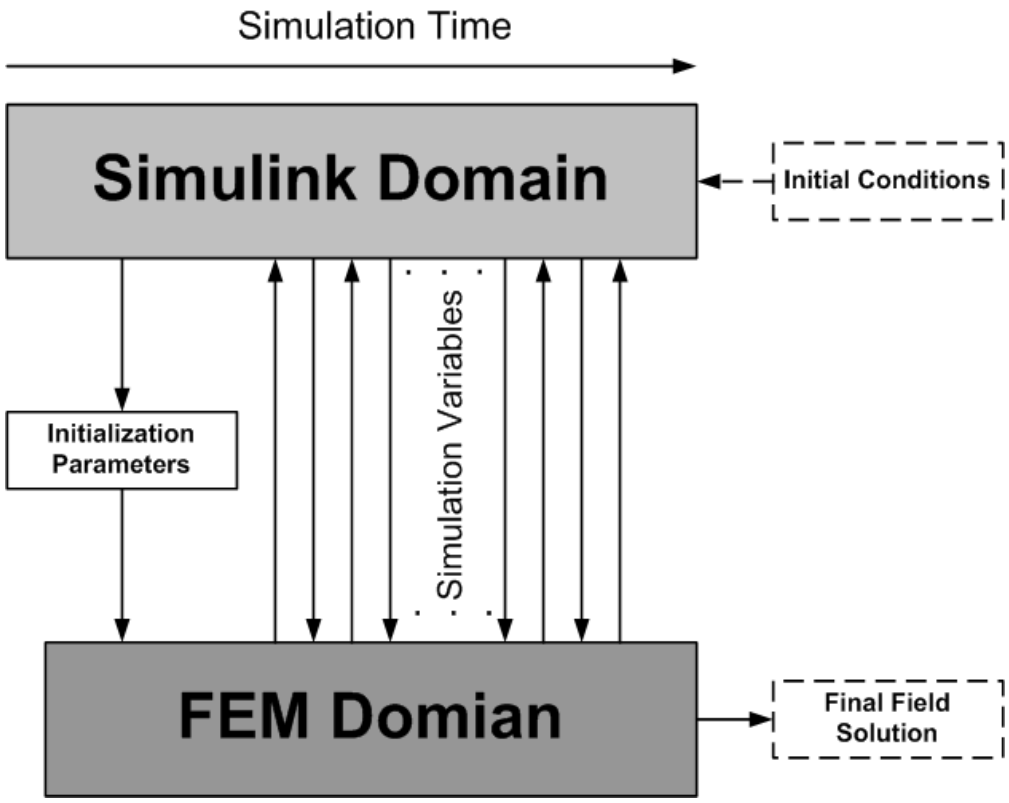

Figure 2.1 Schematic of the coupling between the FEM and SIMULINK, [1]

Conductor representation in coupled-FE method

In the solid conductors, or massive conductors, eddy currents represent a significant part of the total excitation and they cannot be omitted from the analysis. Neglecting the source current density component from analysis, rearranging (2-22)

$$\nabla\times(\nu\nabla\times A)+\sigma\frac{\partial A}{\partial t}+\sigma\nabla V=0 \tag{2-33}$$

In the two dimensional model, the magnetic vector potential and the current density are reduced to their z components. It follows that the value of the electric scalar potential is constant on the cross section of a two dimensional conductor. Its value is a linear function of the z coordinate. If L is the length of the solid conductor (along the z

coordinate), $L\nabla V$ represents the potential difference ΔV induced between the ends of the conductor. Equation (2-24) can be integrated on each solid conductor region k where ΔV is constant. We obtain:

$$\int_{S_k} J ds_k = I_k = \int_{S_k} \sigma \frac{\partial A}{\partial t} ds_k - (\nabla V_k) \int_{S_k} \sigma ds_k \tag{2-34}$$

Where I_k is the total current through solid conductor k. If we consider that:

$$\Delta V_k = L_k \nabla V_k \tag{2-35}$$

$$R_k = \frac{L_k}{\int_{S_k} \sigma_k ds_k} \tag{2-36}$$

Where, L_k is the length of the kth solid conductor, R_k is the conductor DC resistance, σ_k is the conductivity of the solid conductor

We can deduce the relation between the total current I_k and the potential difference ∇V_k of the kth solid conductor

$$\Delta V_k = R_k I_k + R_k \int_S \sigma \frac{\partial A}{\partial t} ds_k \tag{2-37}$$

Using the Galerkin method, we can discretize (2-22) and (2-34):

$$[S][A] - [G]\frac{d[A]}{dt} - [C][\Delta V] = [0] \tag{2-38}$$

$$[\Delta V] = [R][I] + [R][C]^T \frac{d[A]}{dt} \tag{2-39}$$

Where A, ΔV and I represent the vector potential at each node (of N nodes), the potential difference for each solid conductor (of M solid conductors) and the global current respectively. The matrices are defined by:

$$S_{ij}\left(N\times N\right)=\int_{S}\left(\nu\nabla\lambda_i\nabla\lambda_j\right)L\mathrm{d}s \tag{2-40}$$

$$G_{ik}\left(N\times N\right)=\int_{S}\sigma\lambda_i\lambda_j L\ \mathrm{dS} \tag{2-41}$$

$$C_{ik}\left(N\times M\right)=\int_{S}\sigma\lambda_i\mathrm{dS} \tag{2-42}$$

$$R_{kk}\left(M\times M\right)=R_k \tag{2-43}$$

Where, R_k = the resistance of the kth conductor

ν =the reluctivity of the problem being studied

σ = the conductivity of the problem being studied

L =the length of the problem being studied

Coupling with conductors

We have to put (2-40) in (2-38) so as to take into account the solid conductor in the electric circuit. The potential difference ΔV is kept as unknown. The system to solve is:

$$[S][A]-[G]\frac{d[A]}{dt}-[C][\Delta V]=[0] \tag{2-44}$$

$$[R][C]^T\frac{d[A]}{dt}-[\Delta V]+[R][I]=[0] \tag{2-45}$$

$$[D][\Delta V]+\left[Z_m^{'}\right][I_m]+[L_m]\frac{d[I_m]}{dt}=[E_m] \tag{2-46}$$

where the matrix $[D]$ is defined by the relation:

$$[I]=[D]^T[I_m] \tag{2-47}$$

The value of $D_{ij}\left(K\times M\right)$ becomes

+1, if conductor i belongs to mesh j with right way

-1, if conductor i belongs to mesh j with wrong way

0, if conductor i does not belong to mesh j

$\left[Z_m^{'}\right]$ is the matrix of impedances

$Z_{ii}^{'}$ is the addition of impedances in the electric mesh i without the resistances of solid conductors.

The system comprising of equations (2-65), (2-66),(2-67) can be symmetrical:

$$[S][A]-[G]\frac{d[A]}{dt}-[C][\Delta V]=[0] \tag{2-48}$$

$$-[C]^T\frac{d[A]}{dt}+\left[R^{-1}\right][\Delta V]-[D]^T[I_m]=[0] \tag{2-49}$$

$$-[D][\Delta V]-\left[Z_m^{'}\right][I_m]-[L_m]\frac{d[I_m]}{dt}=-[E_m] \tag{2-50}$$

The matrix $[R]$ is diagonal and strictly positive by definition.

Calculation of components parameters using electromagnetic field computations

In every power electronic converters, the constitutive components contain the parasitic components, which their effects come into perspective at different frequency ranges. Therefore, to design converters that have the desired behavior at all the frequency ranges, it is necessary to have an understanding of the parasitic component's values. In this chapter we are focusing on calculation of the values of those components and their corresponding parasitics. This chapter is mainly taken from [61], which is restated in [1].

Calculation of low frequency parameters

In this part, one of the famous methods of inductance calculation is discussed. The Infolytica software package is utilized to solve the coupled field circuit problem to obtain the low frequency parameters. The details of calculating parameters for the low frequency magnetic component's model are given below.

Inductance calculation by energy perturbation method

The inductance is a complicated function of the conductor's current and the saturation characteristics of the electromagnetic device. The energy perturbation method is used to compute the self and mutual inductances of the winding. The method detail is as follows [1]:

For a lossless (conservative) magnetic field with n-coupled conductors, the instantaneous terminal power of the j^{th} conductor can be written as:

$$P_j = R_j i_j^2 + i_j L_{j1} \frac{di_1}{dt} + i_j L_{j2} \frac{di_2}{dt} + ... + i_j L_{jn} \frac{di_n}{dt} \qquad (2\text{-}51)$$

where V_j is the terminal voltage of conductor j.

i_j is the current in conductor j.

λ_j is the total flux linkage.

L_{jk} is the incremental inductance which is the partial derivative of flux linkage.

$\partial\lambda_j$ with respect to current i_k where k=1, 2, 3… n.

The first term represents the instantaneous power dissipated and the remaining terms represent the instantaneous reactive power associated with the flux linkage of the j^{th} coil.

The total energy W of the system,

$$W = \sum_{j=1}^{n} W_j \tag{2-52}$$

where:

$$W_j = \sum_{j=1}^{n}\sum_{k=1}^{n} \int_{i_k(0)}^{i_k(t)} \left(L_{jk} i_j\right) di_k \tag{2-53}$$

If we disturb the n currents by small increments, $\Delta i_1, \Delta i_2, —, \Delta i_n$, L_{jk} remain constant, so the energy increment Δw is given by:

$$\Delta w = \sum_{j=1}^{n}\sum_{k=1}^{n} L_{jk} \int_{i_k}^{i_k+\Delta i_k} i_j di_k \tag{2-54}$$

Performing the integration and using difference equation to express the partial derivatives of the global energy with respect to the incremental change in currents. The inductances can be found by using the following equations.

$$L_{jj} = \frac{\left[w\left(i_j + \Delta i_j\right) - 2w\left(i_j\right) + w\left(i_j - \Delta i_j\right)\right]}{\left(\Delta i_j\right)^2} \tag{2-55}$$

$$\begin{aligned} \frac{\left(L_{jk} + L_{kj}\right)}{2} = [&w\left(i_j + \Delta i_j, i_k + \Delta i_k\right) - w\left(i_j - \Delta i_j, i_k + \Delta i_k\right) \\ &- w\left(i_j + \Delta i_j, i_k - \Delta i_k\right) + w\left(i_j - \Delta i_j, i_k - \Delta i_k\right)] / \left(4 \cdot \Delta i_j \Delta i_k\right) \end{aligned} \tag{2-56}$$

where, $w\left(i_j \pm \Delta i_j, i_k \pm \Delta i_k\right) = w\left(i_j, i_k\right) + \Delta w\left(\pm \Delta i_j, \pm \Delta i_k\right)$

Model solving procedure

The components analysis can be performed either in magneto-dynamic or in transient operation. The inherent assumption in magneto-dynamic analysis is that the voltage, current and field quantities vary sinusoidal with time. Therefore, each element can take

only a single value though the flux density varies throughout the time cycle. This results in the saturation harmonics being neglected. Since there is no motion in the model, time stepping transient analysis is considered to solve the problem.

The transient analysis consists of electromagnetic field formulation, electric circuit formulation and motion equations. Each formulation provides different matrices. These are coupled, discretized in time domain and solved simultaneously at every time solution. A converged solution is obtained at each time step solution.

$$\nabla\times\left(\frac{1}{\mu}\nabla\times\bar{A}\right)+\sigma\left(\frac{\partial\bar{A}}{\partial t}-\bar{v}\times\left(\nabla\times\bar{A}\right)\right)=\bar{J}_0 \tag{2-57}$$

$\bar{A}$ is the magnetic vector potential.

$\bar{v}$ is the velocity.

$\bar{J}_0$ is the source current density.

The velocity term is eliminated since there is no movement in the model's structure. In doing this, the velocity becomes zero and (2-57) has the following general form:

$$\nabla\times\left(\frac{1}{\mu}\nabla\times\bar{A}\right)+\sigma\left(\frac{\partial\bar{A}}{\partial t}\right)=\bar{J}_0 \tag{2-58}$$

The method of weighted residuals is applied to the above field equation to obtain finite element matrix equations.

The components modeled in finite-element can be modeled as a current source driven or voltage fed in the time step analysis. It is necessary to simulate the actual operating conditions of each component in a converter under consideration

Therefore, component's currents must be calculated from the value of the voltage source and other circuit parameters. So the external circuit should be modeled to helps us connect voltage supply to the converter.

In the upcoming sections more details about the modeling of such devices are discussed.

Calculation of parameters at high frequency operation

This chapter describes the procedure of calculating the parameters required for the formation of a high frequency model of typical power converter equipment [18-27]. Magnetic components of different rating and winding arrangement are used as example. The Infolytica/Magnet software package is used for computing the resistance and inductance matrices. The Elecnet software package is used to calculate the capacitance matrices.

Review of parameter calculations

Many methods have been proposed to calculate the parameters of the magnetic components and transformer winding. Some researchers have provided significant advances in the analytical calculation of self and mutual inductances in transformers [62, 63]. However, that effort leads to ill-conditioned set of equations. In order to avoid this problem, F. De Leon et al. has proposed the image method to calculate leakage inductances and charge simulation approach to calculate capacitances [64]. A frequency dependent and distributed effects model of the magnetic components was obtained by some procedures based on software simulation or analytical algorithms [64-67]. These procedures mainly depend on computational approach of finite element analysis. They do

not need the magnetic component to be actually built. There was an effort to obtain the model parameter values for the magnetic components from actual measurements [68]. The main drawback of this procedure is that actual magnetic component and its measurement apparatus should be available.

Analytical models for round conductors without considering proximity effects were proposed earlier [68, 69]. Analytical models for rectangular conductors with approximate proximity effects were also proposed [70-72]. The analytical model for round Litz wire windings with a more exact expression of effective resistance of losses was proposed [73]. The repeat cell concept was utilized to analyze the high frequency magnetic field and losses in a volume of multi-turn winding with periodic arrangement of conductors in its cross section [74]. Very few researchers have dealt with high frequency behavioral modeling of power converters by the computational approach.

The electromagnetic field effects in the winding conductor

The power converter high frequency behavior depends on the frequency of operation due to both magnetic and electrical field effects in different components of the converter. The converter's model must consider these effects. These effects can be represented by passive elements such as the leakage inductance and resistance of each winding, the stray capacitances and the losses in the core due to eddy currents. These effects are described in the following section.

Magnetic field effects

The current distribution in a conductor region is affected by the time changing magnetic field. According to Faraday's law, when a conductor is subjected to a time

changing magnetic field, a voltage is induced inside the conductor. This alters its current distribution. The frequency of the magnetic field determines current distribution inside a conductor. At high frequencies, the current shows tendency to flow towards surface causing the resistance of the conductor to increase compared to its low frequency value. Also, the flux penetration depth inside the lamination core is minimal at high frequencies. Therefore, accurate modeling of eddy current effects is very important for predicting the high frequency behavior of the converter. The time changing magnetic field is produced either by the conductor current itself (skin effect) or by a neighboring conductor's current (proximity effect). Furthermore, geometric effects such as air gap and end effects also alter the magnetic field distribution. These effects are discussed in the following section.

1) Skin effect: When a time varying current flows through a conductor, a time harmonic magnetic field is created around it. It affects current flowing in the conductor causing it to move towards the conductor surface.

2) Proximity effect: The current distribution in one component is affected by magnetic field created by neighboring components. Proximity effects are prominent than skin effects while calculating the resistance values at high frequency operation.

These two phenomena are usually calculated together. The overall non-uniform distribution of current in the winding conductors is called the eddy current effect.

3) Geometric effect: The geometric parameters such as air gap and end effects change the distribution of magnetic field. Fringing flux around gap regions affects the current distribution of the conductors. The end effect comes into existence when there is a ferromagnetic material close to the winding. A ferromagnetic material offers a low

reluctance path to the magnetic flux thus changing the original magnetic field distribution. This affects both the resistance and the inductance of the conductors.

Electric field effect

In magnetic components of any power electronic conversion system, dielectric materials separate the conductors. This arrangement forms stray capacitances. The capacitance value depends on the geometry, properties of dielectric materials and frequency. In this study, it is assumed that both electrical permittivity and electric field energy are constant in the considered frequency range and, therefore, the value of the stray capacitances is constant with frequency. Stray capacitances play a major role in high frequency behavior of the power converter.

In this dissertation, the aforementioned effects of skin, proximity, geometry and electrical field are included in the computation of the resistance, inductance and capacitance matrices of high frequency winding branch.

Chapter 3 Modeling Passive components

This chapter deals with modeling of different electromagnetic power devices using coupled-FEM. This approach was described in chapter 2 and simulation results will allow us to optimize, to find out the response of the different devices under different operating conditions and to evaluate their operational parameters during the design process. Different power components which are widely used in the power electronic converters are modeled using FEM, to show the effectiveness of the physics-based modeling in design and optimization of power electronic converters. In this chapter, different types of magnetic components will be modeled as well as power inductors, transformers and planar inductors. Also, Ceramic capacitors which have a wide application in power electronics converter have been modeled. After solving the electromagnetic equation for each of these components finally, the equivalent circuit models have been obtained for each of these components. These equivalent circuit models can later be used in any circuit simulation tool to study the high-frequency behavior of the converter. Three dimensional electromagnetic equations have been solved in FE to obtain the circuit model. Infolytica/Magnet+Elecnet have been used as a FE tool. The circuit equivalent model can be implemented in Simulink or Pspice.

Inductors

Inductors are one of the main constitutive components of power electronic converters. In electronic power equipment, inductors are used to smooth out ripple voltage in dc supplies, an application where they carry direct current in the coils. Most practical designs include an air gap in the magnetic core to prevent magnetic saturation and

therefore control the inductance value under a wide range of operating conditions. The definition of the number of turns, geometry of the magnetic core and length of the air gap must take into account the following interrelated factors: desired inductance value, direct current in the winding and ac voltage across the winding.

Inductors are usually built at different switching frequencies and power ratings. One of the most important factors in the high frequency behavior of such devices is the geometry of the inductors windings. Moreover, the core and winding materials can also affect the high frequency behavior of the switching inductors. In this section, some types of the power inductors are modeled and their high frequency model is obtained.

Example 1, magnetic-core wire wounded inductors

The basic configuration of the inductor used in the study consists of a single coil or busbar wound around the central limb of a rectangular magnetic core. The main geometrical dimensions are shown in Figure figure 3.1. The size of each window is 20.0 cm by 20.0 cm and the busbar is placed in a rectangular region of 12.0 cm height and 6.0 cm width. A non-magnetic insulating layer of 4.0 cm separates the conductor from the magnetic core. The depth of the device is 7.5 cm.

The finite element model includes several regions that allow extra flexibility for altering material properties, changing the placement of the winding and facilitate the analysis of the results. The light gray area that appears in the right side limb of the core, for instance, is a union of artificial material boundaries that enables the inclusion of air gaps with different lengths. Several air layers in the core window and around the right side limb permit to quantify the energy storage of the leakage fields.

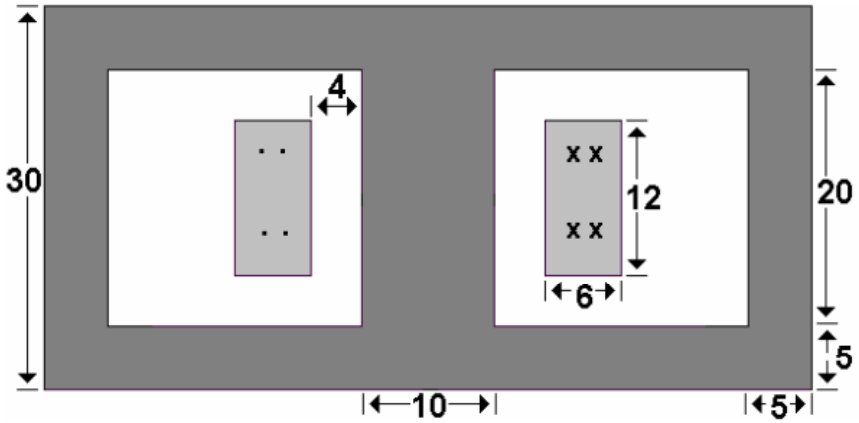

Figure 3.1 Sketch of the inductor, dimensions in centimeter.

The magnetic core is an isotropic non-linear magnetic material defined by analytic saturation curve shown in Figure 3.2. The finite element mesh of the inductor consisting of 125227814 elements is illustrated in Figure 3.3. Dirichlet boundary condition was adopted on the external circle of infinite region surrounding the inductor. The FEM parameters are all shown in Table 3.1. We performed different studies to evaluate the inductor operational characteristics and to obtain its operational parameters.

A three dimensional finite element study is performed on this component in order to calculate the parasitic elements of these components which can affect the operating condition of the converter.

The electromagnetic field inside the inductor and capacitor is governed by the following set of nonlinear partial differential equations [10]:

$$\nabla \times \left((\upsilon) \vec{\nabla} \times \vec{A} \right) = \vec{J} \tag{3-1}$$

$$\nabla . \sigma \left(\frac{\partial \vec{A}}{\partial t} + \nabla V \right) = 0 \tag{3-2}$$

where $\vec{A}$ is the magnetic vector potential, $\vec{J}$ is the total current density, v is the magnetic reluctivity, V is the electric scalar potential and σ is the electric conductivity. By solving these equations, the resistance and inductance of the inductor are calculated as a function of frequency.

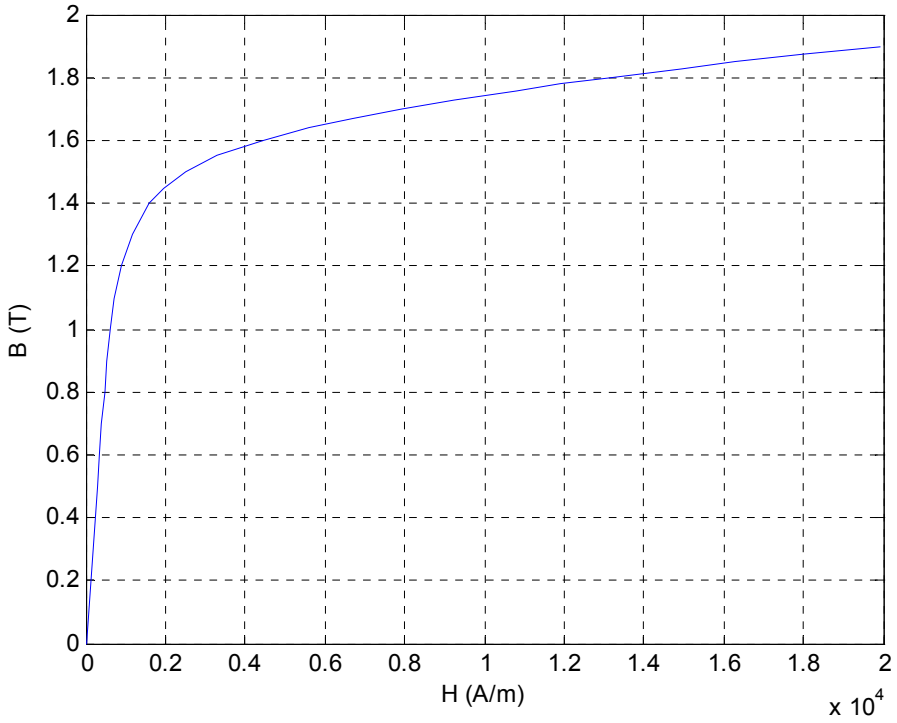

Figure 3.2 Ferrite core magnetizing curve [1]

Table 3.1 Numerical simulation parameters

Parameter	Nodes	Edges	Faces	Tetrahedra	CG Steps	Allocated Memory	Simulation Time
Value	10585360	74183824	125227814	57889978	731	19.59 GB	18:26':14''

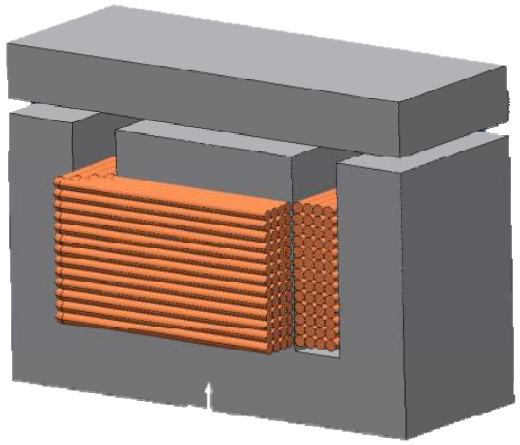

(a)

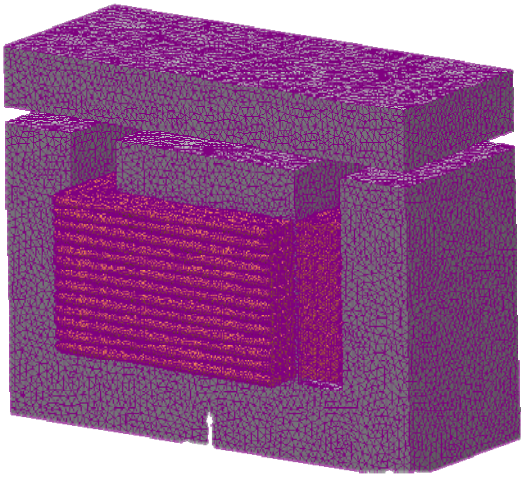

(b)

Figure 3.3 Finite element analysis model, a) inductor model, b) Inductor finite element mesh details.

Also, the electrostatic problem was solved for the calculation of capacitances matrix as capacitances are a function of geometry rather than frequency. An electrostatic analysis is assumed to be a linear analysis which means that the electric field is

proportional to the applied voltage. The analysis determines the electric scalar potential distribution caused by the applied voltage. The following Maxwell equation is solved during electrostatic analysis.

$$\nabla.(\varepsilon \nabla V) = -\rho \tag{3-3}$$

where ρ is surface charge density, ε is permittivity, V is electric scalar potential. By coupling electric and magnetic analyses, electromagnetic analysis for frequency response analysis based on (3-4) are applied in this simulation.

$$-\nabla.\left(\left(j\omega\sigma - \omega^2\varepsilon_0\right)A - \sigma v \times (\nabla \times A) + (\sigma + j\omega\varepsilon_0)\nabla V - \left(J^e + j\omega P\right)\right) = 0 \tag{3-4}$$

For the numerical analysis of this problem, the coupling of FE and circuit based analysis is utilized. The amount of energy and magnetic and electric field are estimated from the FE model and for the connecting sources, loads coupling between the FE model and the circuit-based software (SPICE) is implemented.

Following the solution of the FE model, the inductance, capacitance and resistive matrices were obtained via calculation of the energy matrix in the FE model. The magnetic energy is calculated by:

$$W = \frac{1}{2}\iiint_V \mu.Re\left(H_1.H_1^*\right)dv + \frac{1}{2}\iiint_V \mu.Re\left(H_2.H_2^*\right)dv + \frac{1}{2}\iiint_V \mu.Re\left(H_1.H_2^*\right)dv \tag{3-5}$$

where $\boldsymbol{H}_i, i = 1,2$ is the magnetic field intensity inside the model and μ is the permeability of the model.

Following the calculation of the magnetic energy in the FE model, equation (3-5), all self and mutual inductances were estimated based on magnetic energy value, see equation (3-6).

$$L_{ij} = \frac{1}{I^2} \iiint_V \mu_0 . Re\left(H_i . H_j^*\right) dv \tag{3-6}$$

The electrostatic energy is used to obtain the capacitance matrix of the model. The electrostatic is calculated as:

$$W = \frac{1}{2} \iiint_V \varepsilon . \left(D_1 . E_1\right) dv + \frac{1}{2} \iiint_V \varepsilon . \left(D_2 . E_2\right) dv + \frac{1}{2} \iiint_V \varepsilon . \left(D_1 . E_2\right) dv \tag{3-7}$$

where $\boldsymbol{D_i}$ is the electric displacement and $\boldsymbol{E_i}$ is the electric field inside the model. Self and mutual capacitances are calculated based on electrostatic energy value as (4-8).

$$C_{ij} = \frac{1}{V^2} \iiint_V \varepsilon_0 . \left(D_i . E_j\right) dv \tag{3-8}$$

The resistance matrix of the model is calculated based on the current density in the model's conductors as in equation (4-9) below. The resistance between different layers of the model is calculated as:

$$P = \iiint_V \frac{Re\left(J_1 . J_1^*\right)}{\sigma} dv + \iiint_V \frac{Re\left(J_2 . J_2^*\right)}{\sigma} dv + 2 \iiint_V \frac{Re\left(J_1 . J_2^*\right)}{\sigma} dv \tag{3-9}$$

$$R_{ij} = \frac{1}{I^2} \iiint_V \frac{Re\left(J_i . J_j^*\right)}{\sigma} dv \tag{3-10}$$

where J_i is the current density and σ shows the electric conductivity.

A numerical technique based on adaptive MEI-FEM (magnetic-electric interface finite element method) is used. This method has much more accurate result in comparison with quasi-static electromagnetic finite element method, electrostatic finite element method and magnetostatic finite element method. All experiments are performed on a x5677 dual core 3.47 GHz CPU and 192GB RAM. The iteration process is terminated when the normalized backward error (tolerance) is reduced by 10^{-3}. The result of FEA is illustrated in Figure 3.4.

In the implementation of the MEI-FEM, the adaptive grouping method is used to reduce the memory consumption and captures the fine details of the structure. The simulation time for the analysis of the inductor with ten million degrees of freedom and 10^{-3} percent tolerance of energy was 18 hours. The analysis method which is used in this analysis is GMRES with SOR and SORU pre and post smothers.

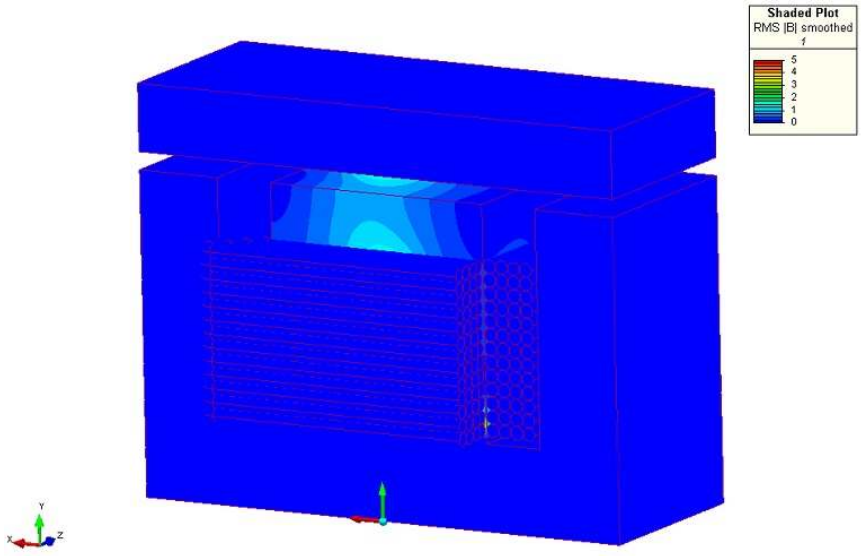

Figure 3.4 Magnetic field density illustration in the magnetic core.

Development of lumped-parameter model

The capacitive reactance is increased by increasing the switching frequency. Therefore, very small capacitive reactance has effect in input transfer function in higher frequencies. Besides, mutual inductances between elements at far distances are more significant in the transfer function in high frequencies. So a model which considers all these reactances is essential. The distributed-parameter model considers almost of the tiny capacitive reactances and mutual inductances for the high frequency analysis.

Following the calculation of all required parameters for the distributed model, these parameters are located in the model and the model evaluation procedure starts. As in the lumped parameter model the evaluation procedure from the distributed parameter nature of the problem at hand, we start at a location x and moving an infinitesimal distance Δx toward the lower end of the winding, the potential difference ΔV is calculated as:

$$\begin{bmatrix} \Delta V_1(x,s) \\ \Delta V_2(x,s) \end{bmatrix} = \begin{bmatrix} Z_1(s)\Delta x & Z_m(s)\Delta x \\ Z_m(s)\Delta x & Z_2(s)\Delta x \end{bmatrix} \begin{bmatrix} \hat{I}_1(x,s) \\ \hat{I}_2(x,s) \end{bmatrix} \tag{3-11}$$

where $\hat{I}_1(x,s)$ and $\hat{I}_2(x,s)$ are the current following in Z_1 and Z_2, respectively. The indices 1 and 2, indicates the first and the second layer of the inductor's model. A detailed description of this method is presented in reference [75]. By transferring the modal domain into a phase domain, the voltages of the top terminal in two layers are calculated as:

$$\begin{bmatrix} V_{s1}(s) \\ V_{s2}(s) \end{bmatrix} = \begin{bmatrix} M_{11}(s) & M_{12}(s) \\ M_{21}(s) & M_{22}(s) \end{bmatrix} \begin{bmatrix} I_{s1}(s) \\ I_{s2}(s) \end{bmatrix} \tag{3-12}$$

where $M_{ij}(s)$ are elements of impedance matrix in s-domain.

To determine the frequency characteristics of the inductor we set $s = j\omega$ in the related equations. The input impedance is given by:

$$Z_{in}(j\omega) = \frac{V_{s1}(j\omega)}{I_{s1}(j\omega)} \tag{3-13}$$

Using the above equations, input impedance on the component is calculated as the following:

$$Z_{in}(j\omega) = M_{11}(j\omega) \tag{3-14}$$

The rational function given by (3-14) can be represented by an equivalent electrical network as shown in Figure 3.5. Note that, the circuit model in figure 3.5 is not unique and can be shown in various configurations. This network reflects the frequency dependence of the inductor resistance inductance and capacitance. Using $Z_{in}(j\omega)$, the natural frequencies are determined.

The distributed model parameters of the inductor, for the example at hand, from the finite element analysis were; R_1= 0.4568 Ω, R_2=0.4568 Ω, L_1=0.984 μH, L_2=0.984 μH, L_m=0.567 μH, C_{s1}=6 pF, C_{s2}=6 pF, C_{g1}=0.13 pF, C_{g2}=0.13 pF, C_m=3.2 pF.

As we mentioned earlier, the indices 1 and 2 in the inductor parameters stand for the first and the second layers of the inductor, respectively. Note that the neutral-end terminal point of the first layer is connected to the line-end terminal of the second layer.

As stated previously, an advantage of the distributed-parameter model is to reveal the high frequency behavior of the model. figure 3.6 shows the distributed model of the inductor.

Utilizing the distributed parameter model developed in this study, a realistic picture emerges. The number of resonances becomes more practical and representative of the real device. Accounting for parasitic resonances in higher frequencies will enable a realistic inclusion of EMC issues in the design stage.

The proposed algorithm for designing a physics based model of the component is summarized as follows:

- Step 1: Design the planar inductor in the FE software.

- Step 2: Calculate the magnetic and electric fields based on equations (3-1) and (3-2).
- Step 3: Calculate resistances, self and mutual inductances and capacitances based on equations (3-6)-(3-8) and (3-10).
- Step 4: Substituting the obtained parameters into the circuit shown in figure 3.5.

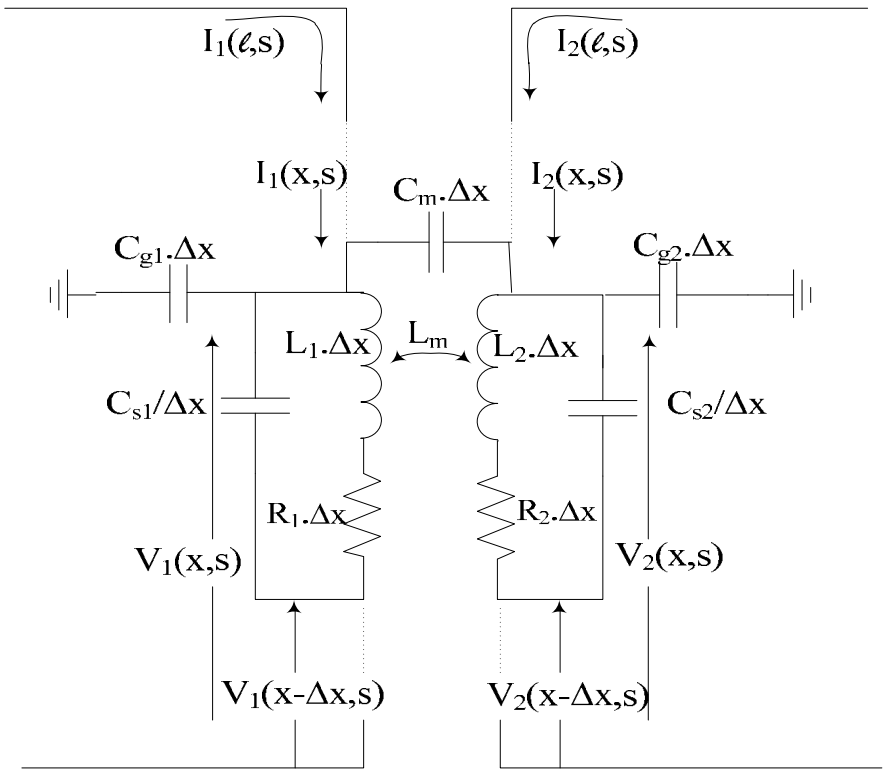

Figure 3.5 Infinitesimal section of a multi-layer winding of inductors.

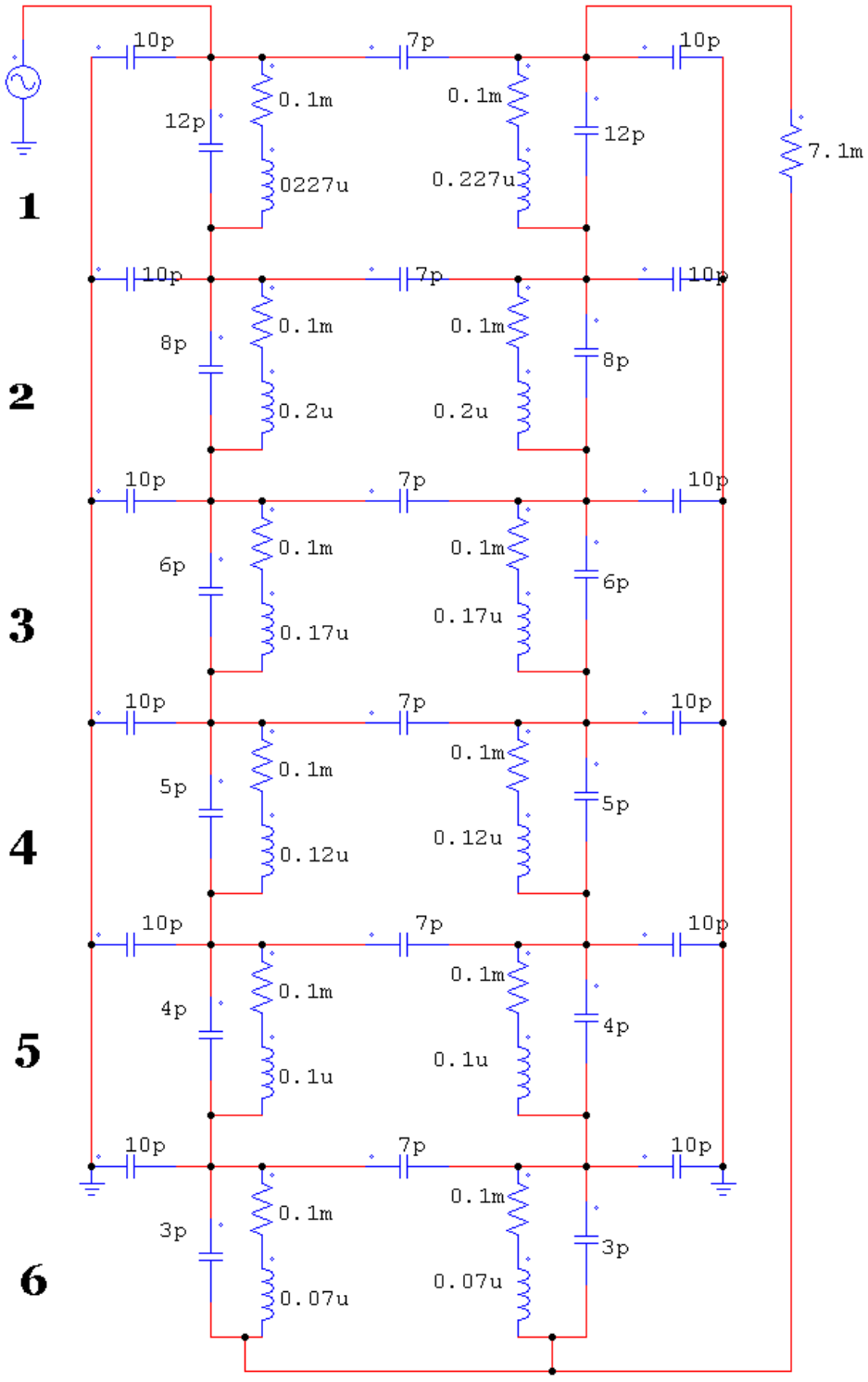

Figure 3.6 High-frequency model for inductor

Example 2, Toroidal inductors

The other sort of components also can be modeled in a same way, following figures show the FE model of Toroidal inductor used in a power converter. After solving the FE model of the device the High frequency model of the component can be obtain through the same process as we discussed in example 1. Table 3.2 and 3.3 show the material properties and FE results of Toroidal inductor.

Note that, in all these models, the nonlinear properties of the material are derived from the manufacturer datasheet. Figure 3.8 shows the magnetic flux density in the Toroidal inductor obtained from FEM simulation.

To obtain the high frequency physics-based model of the system the same approach as it was described in the last section is used. The parameters of inductances and resistances are all replaced in the circuit shown in figure 3.5.

The distributed model parameters of the inductor, from the finite element analysis were; R_i= 0.7321 Ω, L_i=1.278 μH, L_m=1.157 μH, C_{si}=17.2 pF, C_{gi}=0.98 pF, C_{mi}=3.2 pF, $i=1,2,\ldots, n$.where n stands for number of turns in this type of inductor.

Table 3.2 Material Properties

Material	Initial permeability	Saturation magnetic flux density	Remanent flux density	Coercive force	Core loss (100kHz)	Electrical Resistivity	Magnetostriction
Ferrite 31	1500	270mT	290mT	18 A/m	480 kW/m^3	6.5 Ω-m	-0.6 ×10^{-6}

Table 3.3 FEA results

Tetrahedra	Nodes	Edges	CG tolerance	Allocated memory	CG steps
1209155	207791	1417965	0.01%	1.05 GB	238

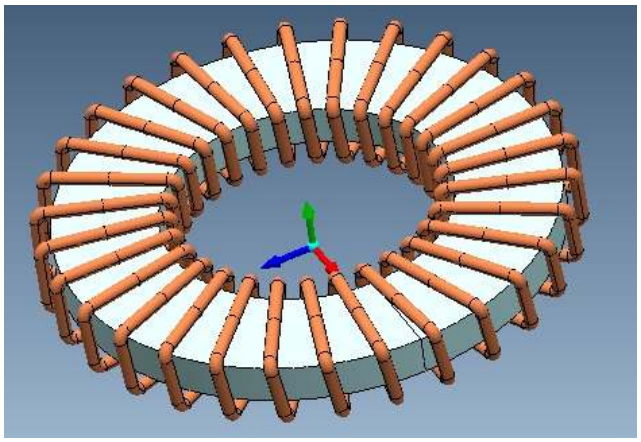

(a)

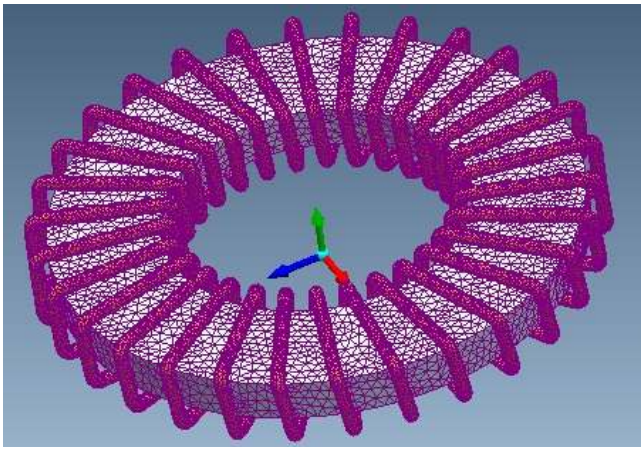

(b)

Figure 3.7 Finite element analysis model, a) Toroidal inductor model, b) Toroidal inductor finite-element mesh details.

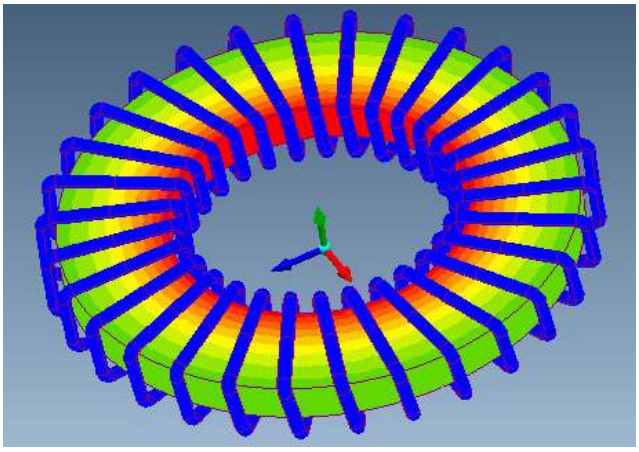

Figure3.8 Magnetic field density illustration in the magnetic core.

Example 3, Planar Inductor

Planar magnetic based design technologies have been widely applied to power design for better cooling and ease of fabrication. The planar inductor, is a low profile device that covers a large area, whereas, the conventional inductors would be more cubical in volume. Planar inductors are designed the same way as the conventional inductors. Planar inductors use the same planar cores and PC winding board techniques. It is normal to operate planar magnetic at a little higher temperature than conventional designs. It is important to check the maximum operating flux level at maximum operating temperature.

The other design is for planar magnetic, there is no bobbin for the planar magnetic core so for this reason we have to calculate that due to the current which is passing through the inductor how many turns can a planar core contain, the track which can sustain in handling a 7 ampere current should have at least 2 *mm* width so with this assumption we start our design, first we select the core PC90EL25X8.6-Z this core cross sectional area is 85.6 mm^2.

In the geometry which is shown in figure above the cross sectional area has the width of, $\frac{E}{2} - \frac{F_1}{2} = 7.25\ mm\ (285.43\ mil)$ and the height of the core is: D=2 *mm* (78.74 mil), therefore if we aim to use the wire size AWG12 with diameter of 2.05 *mm* (80.7 mil) then we conclude that this core can contain around 3 turns in each layer with the clearance of 0.27 *mm* (10.83 mil), therefore in order to make 20 number of turns we have to realize our design in 7 layers.

For calculating the width of external and internal traces on PCB ANSI / IPC-2221/IPC-2221A design standards for PCB trace width can be used which approximate the traces width as follows:

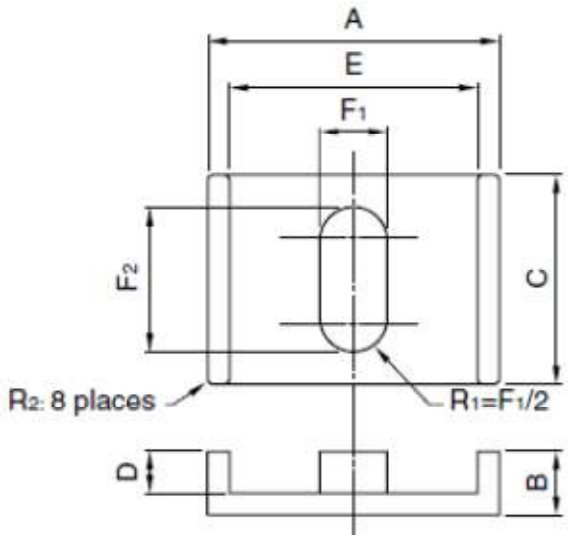

Figure 3.9 Planar EI core.

PCB material FR-4

- Board thickness=1.6mm (0.063")
- Trace thickness=35μm (1 oz)

$$A[mils^2] = \left(1/KT^b\right)^{\frac{1}{c}} \text{ (PCB Trace area)} \tag{3-15}$$

$$l[mils] = \frac{A}{my} \text{ (PCB Trace width)} \tag{3-16}$$

where, I [A] *(Current),* T [°C] *(Temperature rise),* m [oz] *(Mass of PCB trace)*

Constants: y = 1.378 *[mils/oz] for copper,* b = 0.44, c = 0.725, k = 0.048 *(for outer layers),* k = 0.024 *(for inner layers)*

Also the clearance value between the tracks is calculated by the following equation:

$$\text{Clearance in inches} = 0.023" + (0.0002" \times V) \tag{3-17}$$

where, V is the voltage peak across traces.

Therefore, a trace which can pass current of 5 amperes should be at least 50 mils for internal and 20 mils for external traces, with 40 mils of clearance. The finite element model is demonstrated in figure 3.10.

Table 3.4 Material Properties

Material	Initial permeability	Saturation magnetic flux density	Remanent flux density	Coercive force	Core loss (100kHz)	Electrical Resistivity	Magneto-striction
PC95	3300	410mT	85mT	9.5A/m	290kW/m^3	6 Ω-m	-0.6×10^{-6}

Table 3.5 FEA results

Tetrahedra	Nodes	Edges	CG tolerance	Allocated memory	CG steps
52309	9148	61734	0.01%	124 MB	109

The material properties and finite element results are all illustrated in Tables 3.4 and 3.5, respectively.

The other example of the planar inductor is the air-core planar inductor which is widely used in the power electronic conversion systems.

To design the planar inductor, the first step is to calculate the trace width. For calculating the width of external and internal traces, on PCB ANSI/IPC-2221/IPC-2221A design standards for calculation of trace width can be used which approximate the traces width as equations (3-15) and (3-16).

The other design for inductor is the air core planar inductor. In this part, an air core spiral winding inductor is designed. For this design, it is assumed that the inductor must

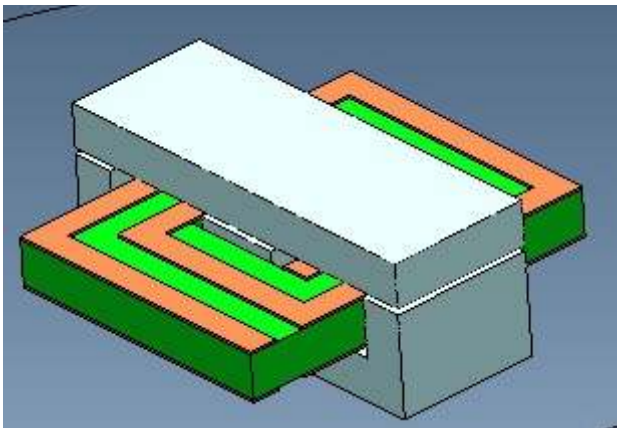

(a)

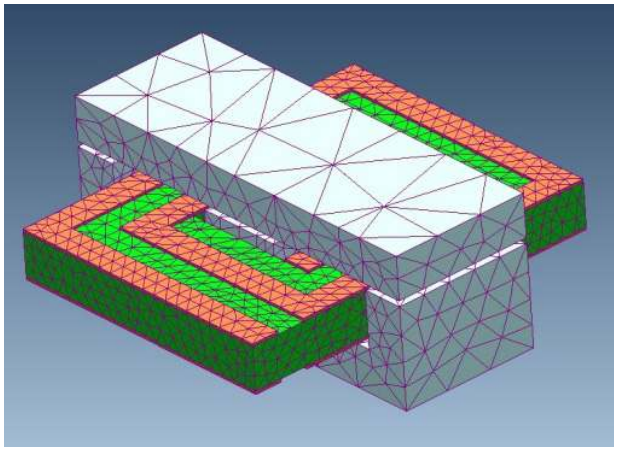

(b)

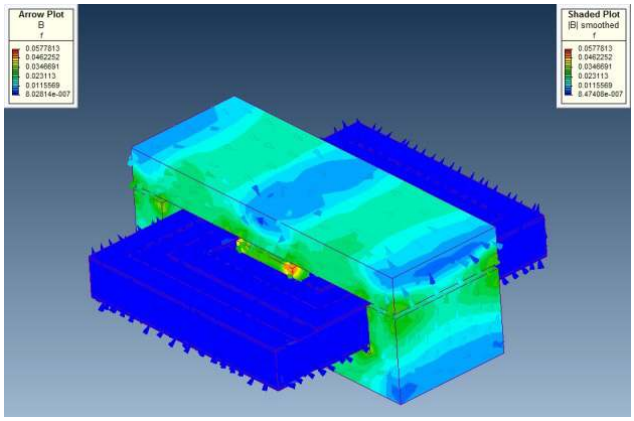

(c)

Figure 3.10 Finite element analysis model, a) planar inductor's model, b) planar inductor's finite-element mesh details, c) Magnetic field density illustration in the magnetic core.

pass a current of 6 RMS amps. Hence, the trace needs to have a width of 1.783 mm according to equations (3-15) and (3-16).Therefore, to obtain an inductor of 20 μH we can use equation (3-18);

$$L = \frac{\mu_0 N^2 D_{AVG} C_1}{2} \cdot \left(Ln\left(\frac{C_2}{\rho}\right) + C_3\rho + C_4\rho^2 \right) \tag{3-18}$$

$$\rho = \frac{D_{out} - D_{in}}{D + D_{in}} \tag{3-19}$$

$$D_{AVG} = \frac{D_{out} + D_{in}}{2} \tag{3-20}$$

And $C_1 \sim C_4$ depending on the layout, in which for the square type of winding are as follows: $C_1 = 1.27, C_2 = 2.07,\ C_3 = 0.18, C_4 = 0.13$. D_{out} is calculated such as (3-21);

$$D_{out} = D_{in} + 2W + (W + S) \times (2N - 1) \tag{3-21}$$

where D_{in} is the internal diameter, W is the trace width and S is the distance between two adjacent trace, (trace clearance).

For a multiple layer inductor the total inductance is $L_{total} = L_1 + L_2 \pm 2M$ where $M = 2K_c\sqrt{L_1 L_2}$ .The coupling factor K_c in this equation is a function of distance between layers and winding style, which is calculated by (3-22):

$$K_C = \frac{N^2}{(Ax^3 + Bx^2 + Cx + D)(1.67N^2 - 5.84N + 65) \times 0.64} \tag{3-22}$$

where, A=0.184, B=-0.525, C=1.038, D=1.001.

These calculations were carried out on a 2 layer winding and the following data was obtained. When 14 turns were completed in each winding and a distance of 0.2 mm

between the layers was achieved, an inductance of 20 μH was obtained. (In this case W=1.78mm, S=0.5mm and the distance between each layer is 0.2 mm)

In a design with more than two layers, there would be more coupling factors. The same method can be used to obtain each coupling factor and the total inductance per the mutual-inductance connection formulas could be used. Figure 3.11 shows the finite element model of the air-core planar inductor and its corresponding magnetic and electric field is shown in figure 3.12.

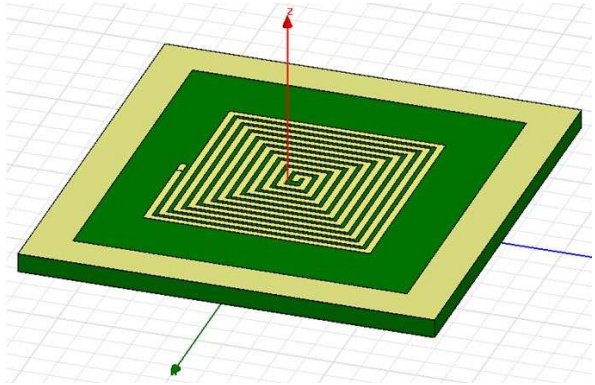

(a)

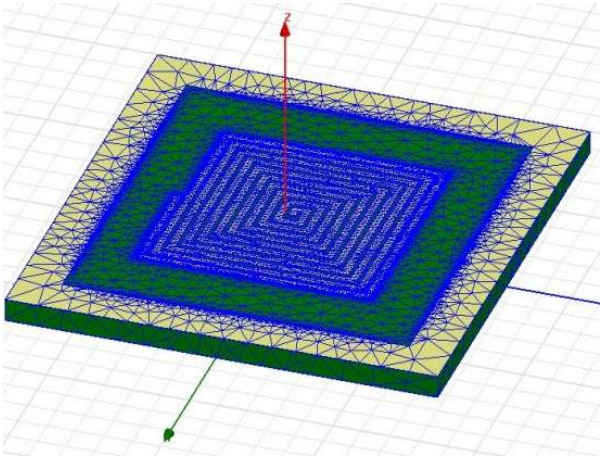

(b)

Figure 3.11 Finite element analysis model, a) air-core planar inductor's model, b) air-core planar inductor's finite-element mesh details,

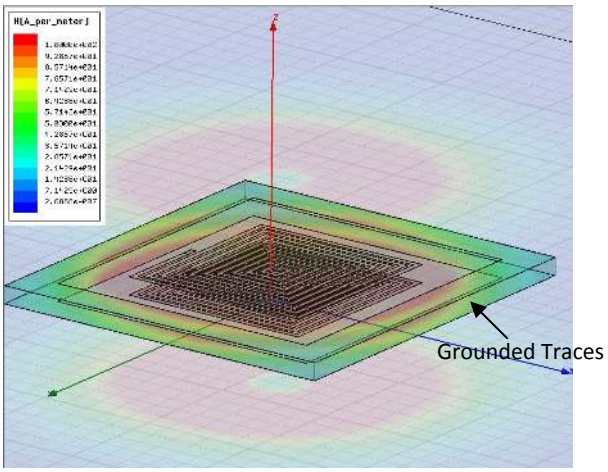

(a)

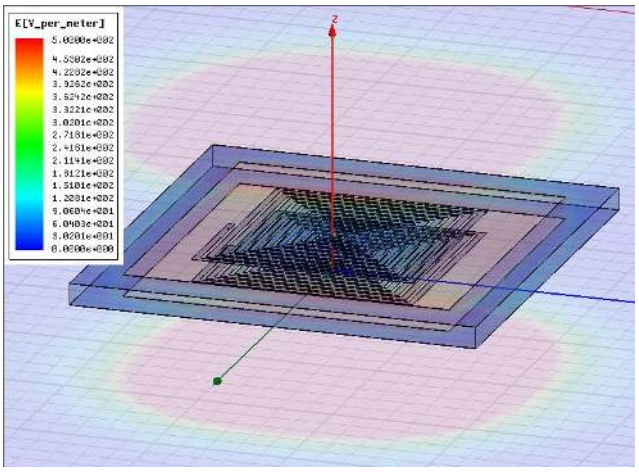

(b)

Figure 3.12 a) Magnetic field density illustration, b) Electric field in air-core planar inductor.

The distributed model parameters of the inductor, for the example at hand, from the finite element analysis were; R_1= 0.2713 Ω, R_2=0.2713 Ω, L_1=0.557 µH, L_2=0.557 µH, L_m=0.307 µH, C_{s1}=8 pF, C_{s2}=8 pF, C_{g1}=0.33 pF, C_{g2}=0.33 pF, C_m=6.7 pF, which these results are replaced in the high-frequency model illustrated in figure 3.5.

Transformers

A single-phase, 120/12 V, 60 Hz, transformer was modeled using the coupled FE method. The transformer geometry is shown in figure 3.13. High voltage and low voltage windings are concentric cylinders surrounding a vertical core leg of rectangular cross section. The conductors have constant conductivities. The primary and the secondary windings are represented by rectangles of corresponding materials in the FE domain. The magnetic core is an isotropic non-linear magnetic material defined by analytic saturation curve shown in figure 3.14. The finite element analysis results of the transformer are illustrated in table 3.6. The Dirichlet boundary condition was adopted on the external circle of infinite region surrounding the transformer.

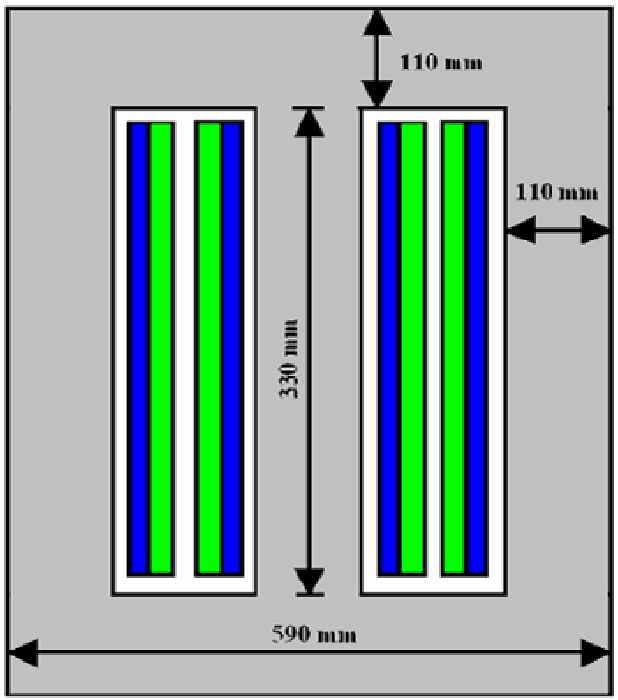

Figure 3.13 Sketch of the transformer, dimensions in millimeter [1].

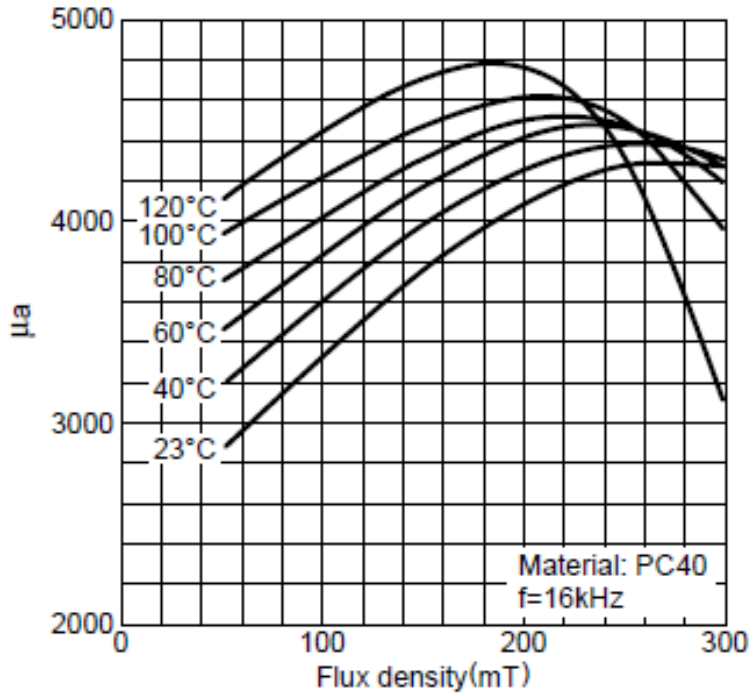

Figure 3.14 Nonlinear properties of the material, derived from the manufacturer's datasheet

Table 3.6 Material properties.

Material	Initial permeability	Saturation magnetic flux density	Remnant flux density	Coercive force	Core loss(100kHz)	Electrical Resistivity	Magnetostriction
PC40	2300	380mT	140mT	15A/m	420 kW/m^3	6.5 Ω-m	-0.6 ×10^{-6}

Table 3.7 FEA results

Tetrahedra	Nodes	Edges	CG tolerance	Allocated memory	CG steps
1312302	228548	1541396	0.01%	1.328 GB	159

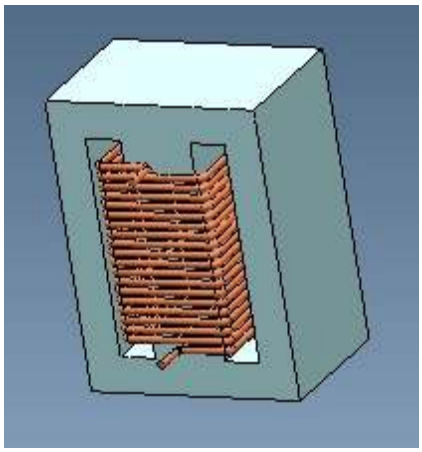

(a)

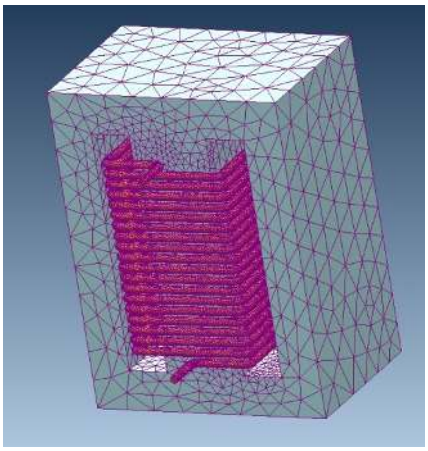

(b)

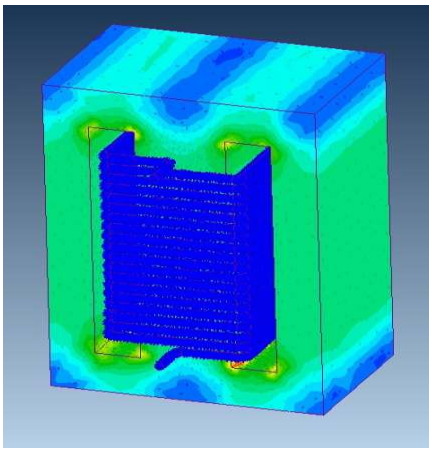

(c)

Figure 3.14 Finite element analysis model, a) Transformer's model, b) Transformer's finite-element mesh details, c) Magnetic field density illustration.

Capacitors

In this part we want to model a capacitor in a Finite Element Analysis (FEA) tool. Figure 3.15 shows the capacitor geometry which is modeled in software, in this geometry capacitor is loaded with dielectric material; dielectric material is selected as Glass (Soda Lime) which has the permittivity constant of 6.25. In this problem we have used the electric charge density of -1 and 1 C/M^3 on the two electrodes respectively, applied as line charges. The benefit of this material is that its behavior at the range of frequency and voltage which we are studying is constant.

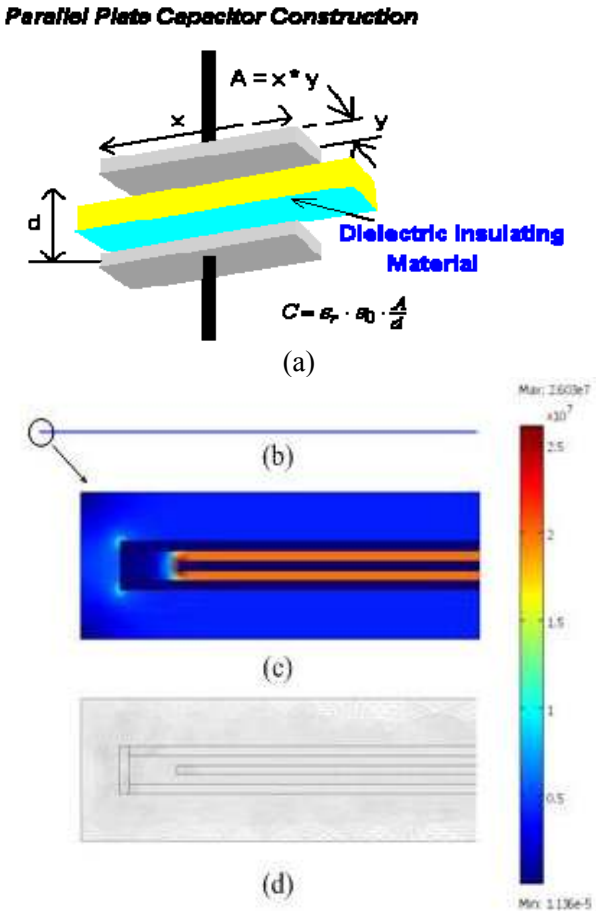

Figure 3.15 Field spectrum from the finite element electric analysis for the calculation of high frequency model of this component. (a) Geometry of the capacitor (b) capacitor (c) field in small part of the capacitor (d) mesh in capacitor.

To obtain the capacitor high-frequency model, the same approach was used, as it was discussed in the previous section. The following parameters are obtained finally after solving the electro-static and magneto-static equations. The distributed model parameters of the capacitor, for the example at hand, from the finite element analysis were; $R_{c1,2,3}$= 0.006725 Ω, R_{cm}=10 kΩ, $L_{c1,2,3}$=5 pH, $C_{s1,2,3}$= 0.49 pF, $C_{g1,2,3}$=4.42 pF, C_m=177 nF. As we mentioned earlier, the indices 1, 2 and 3 stand for the number of layers of the capacitor which is shown in figure 3.15(b). Figure 3.16 shows the equivalent high-frequency model of the capacitor. This circuit can replace the ideal capacitors in the circuit simulation software. Therefore, a more realistic model of the component will be used.

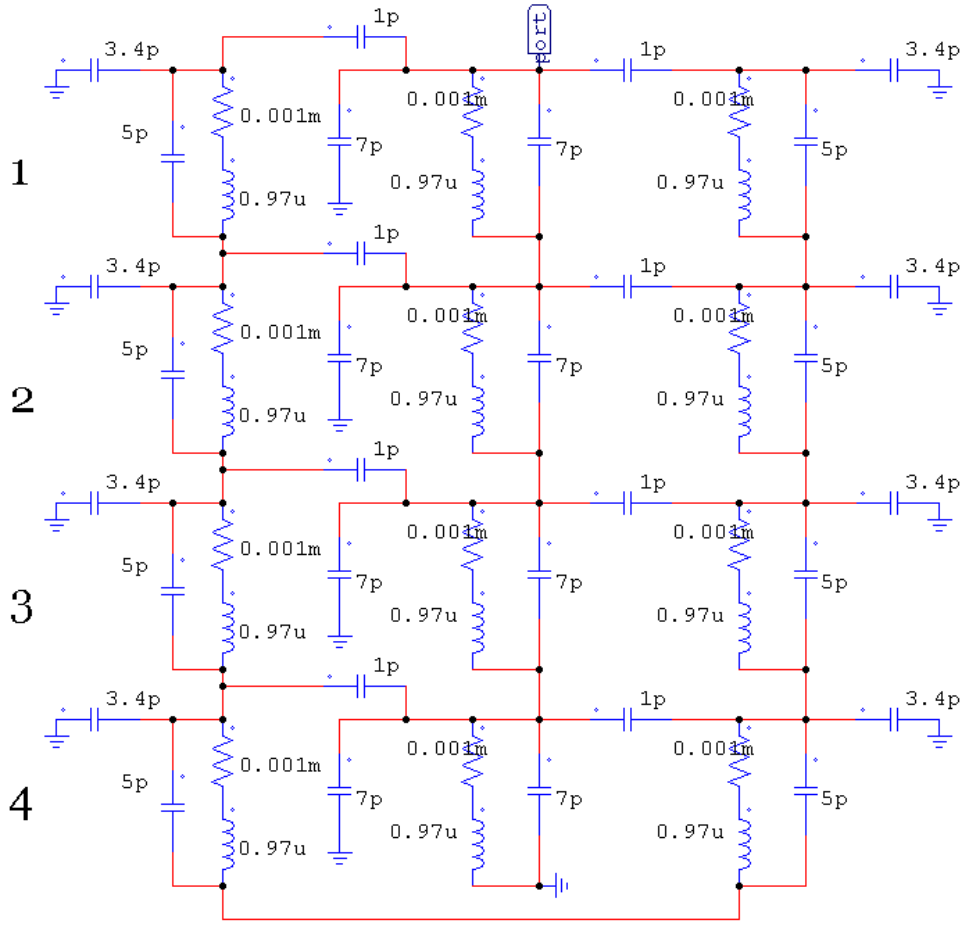

Figure 3.16 Circuit model for high-frequency representation of the capacitors.

In this chapter, some of the most common component used in the power electronic conversion systems was modeled. A method for the high frequency model of the converter's components was presented using coupled circuit/ electromagnetic FE computations. FE analysis was performed to obtain the frequency behavioral model of the converter. In order, to obtain the physics-based model of the whole converter package, it is necessary to first obtain the physics-based model of all individual components and then replace the entire constitutive components by their corresponding acquired model.

Chapter 4 Modeling Connections on Printed Circuit Boards and Copper Traces

This section presents a practical approach to design a power converter's circuit board. The proposed algorithm is based on modeling the electromagnetic behavior of a power converter fabricated on a printed circuit board (PCB) using finite elements (FE) analysis. In this method all components on the circuit board, including copper traces, are modeled as a 3-dimentional netted sheet with specific voltage nodes and current meshes. An electrical circuit was then created for the finite element models. These models were then placed in a schematic to graphically and electrically represent the power converter PC board. Moreover, in this study, a circuit model is built for the trace, in which the model parameters variations versus frequency and geometry of are calculated. The obtained model can be used to distinguish the effects of parasitic elements of PCB traces on EMI/Cross-talk between the traces. The equivalent circuit model for the system is acquired and the results are compared with the corresponding analytical results.

Transmission of the signal through the conductive traces on a PCB can create an electromagnetic field in the area around the trace, which it can induces voltage to the surrounding traces, correspondingly. Therefore, there is a need to measure the electromagnetic phenomenon on circuit boards. This issue becomes more important when the board is so compact, where the signal traces is passing a high power, high frequency signal. This unwanted electromagnetic coupling between the conductors can seriously affect signal quality and reduce noise margin in the high frequency systems. Such a coupling manifests itself in the form of cross-talk, which is an electric or magnetic coupling between the circuits [76-78].

This section concentrates more on the circuital modeling of crosstalk in order to understand the parameters that affect the crosstalk phenomenon. With full understanding of the contribution of each parameter to the crosstalk response, one can identify the optimum value of the parameters that should be utilized for the reduction of crosstalk. The modeling approach will be based on capacitive and inductive coupling for the adjacent traces**.** The **FE** analysis is used to measure the parasitic elements of the PCB traces with respect to the surrounding traces.

The modeled system is composed of three parallel copper traces on the FR-4 epoxy material which is covered by a 1 Oz copper plate on the bottom as shown in figure 4.1. In this model, the traces width and clearance between the traces is considered to have a constant value of 20 mils on a standard 1.6 mm PCB. To reduce the effects of the crosstalk phenomenon on the PCB traces, which is caused by the electromagnetic fields, one need to use the simplified system to analyze and study the electromagnetic behavior of the system.

In this study, the predefined PCB structure is modeled and electromagnetic fields produced by the current carrying trace are modeled. Subsequently, the values of the parasitic components of the traces are calculated. An equivalent circuit model is derived for the system and the results obtained from the system's cross-talk phenomena are compared and verified by its mathematical model.

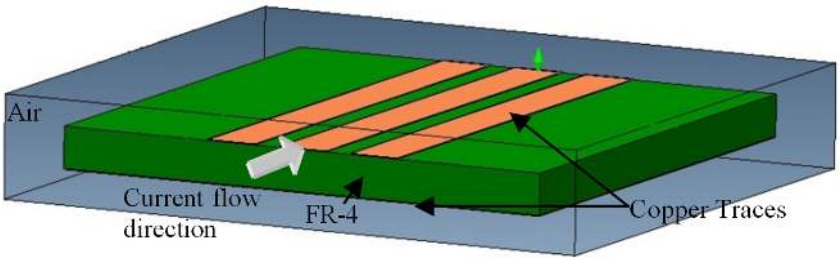

Figure 4.1 Schematic of PCB traces on FR-4 board

Design considerations for PCB traces

One important criterion in PCB design is the capability of the traces to handle the amount of current which they are supposed to pass. Passing high amount of current from a conductor may cause overheating of the trace, which may lead the conductor to melt down and failure of the whole circuit.

For calculating the width of external and internal traces, on PCB ANSI/IPC-2221/IPC-2221A design standards for calculation of trace width can be used. According to IPC standards, the current carrying capacity of PCB traces represents the maximum electrical current that can be carried continuously by a trace without causing an objectionable degradation of electrical or mechanical properties of the product. Using this standard the traces widths are approximated as follows.

$$A[mils^2] = \left(\frac{I}{KT^b}\right)^{\frac{1}{C}} \quad \text{(PCB Trace area)} \tag{4-1}$$

$$l[mils] = \frac{A}{my} \quad \text{(PCB Trace width)} \tag{4-2}$$

where, I [A] is the current which passes through the trace, T [°C] is the temperature rise and m [oz] is mass of copper. Y, b, c and k are constants which their values are shown in table 4.1.

The other issue in the traces is the skin effect, which increases the current density in the edges of the trace. This effect will eventually lead to trace overheating. This phenomenon is basically modeled as following equation:

$$\delta = \sqrt{\frac{\rho}{\pi f \mu_0}} \tag{4-3}$$

PC boards are mainly made of FR-4 material which its physical characteristics are shown in table 4.2.

In the round copper wires maximum current density can vary from 4A/mm^2 for a wire isolated from free air to 6A/mm^2 for a wire in free air. In the case of PCB copper traces, for TOP and BOTTOM layers, maximum current density can be as high as 35A/mm^2 with a copper thickness of 35 µm. Copper traces are usually used in 0.5, 1, 2 and 3 oz. 1 oz of copper thickness is about 1.4 Mils, which is approximately 35 µm.

Table 4.1 Constants

y *[mils/oz]*	b	c	k	
1.378	0.44	0.725	0.048 external layer	0.024 internal layer

Table 4.2 Physical characteristics of FR-4

mass density $\left(\frac{kg}{m^3}\right)$	dielectric constant	permeability	heat capacity $(\frac{J}{Kg.K})$	thermal conductivity $(\frac{W}{m.K})$
1900	4.7	1	840	1.06

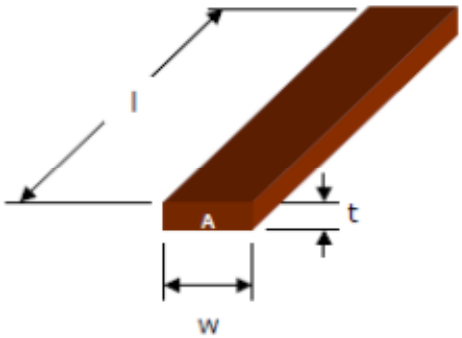

Figure 4.2 Copper trace geometry

Electrical Equivalent Models for Crosstalk Prediction

A test setup for the measurement of crosstalk effects is depicted in figure 4.3(a). In this setup, a signal which is passing through the conductors is modeled as a voltage source $V_S(t)$, with internal resistance R_S. As our goal is to model the crosstalk effect on the PCB, the load is considered as a pure resistive shown as R_L. A receptor circuit shares the same reference conductor and connects two terminations R_{NE} and R_{FE} by a receptor conductor, [79].

Figure 4.3(b) shows the equivalent π-model for the system. In this model, *Lm* represents the mutual inductance between conductors, *Lg* is the self-inductance of generator conductor, *Lr* is the self-inductance of the receptor conductor. Also, *Cm* is the mutual capacitance between conductors, *Cr* is the capacitance of receptor conductor, *Cg* is the capacitance of generator conductor. This model is used to determine the electromagnetic behavior of the copper strips which represent the copper traces on FR4 material. This model enables us to model the conducted noise propagated through the copper traces.

The parameters in this model are consisting of the capacitance matrix and inductance matrix, defined in (4-4) and (4-5), respectively. This model's matrices are defined based on [80], as follows:

$$C = \begin{bmatrix} C_g + C_m & -C_m \\ -C_m & C_r + C_m \end{bmatrix} \tag{4-4}$$

$$L = \begin{bmatrix} L_r & L_m \\ L_m & L_g \end{bmatrix} \tag{4-5}$$

In the next section, the calculation procedure to obtain the impedance matrices is explained. Consequently, this model can be used to simulate the mentioned electrical equivalent models.

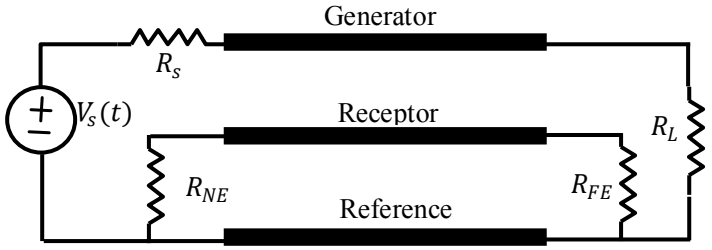

(a)

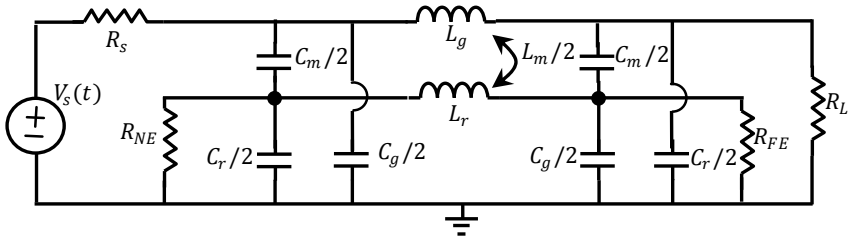

(b)

Figure 4.3 a) Copper traces model for illustrating crosstalk, b) π –model

Physics Based Modeling

To evaluate electrical and magnetic characteristics and also to acquire values of the circuit parameters described in chapter 2, a 2D electromagnetic FE analysis is performed to obtain resistances, self and mutual inductances and capacitances between the traces on different layers in the system's structure [81].

The electrostatic problem is solved for the calculation of the capacitances. The electrostatic analysis determines the electric scalar potential distribution caused by the applied voltage in different layers then capacitances are calculated based on the energy

principle. By applying voltage on the middle trace, considering the surrounding traces as a ground, the capacitance matrix is calculated from the stored static energy. To obtain the self and mutual inductances the following magnetic equation is solved in FE:

$$\nabla \times \left((\upsilon) \vec{\nabla} \times \vec{A} \right) = \vec{J} \qquad (4\text{-}6)$$

Also the electrostatic problem is solved for the calculation of capacitances matrix as capacitances are a function of geometry rather than frequency. An electrostatic analysis is assumed to be a linear analysis which means that the electric field is proportional to the applied voltage. The analysis determines the electric scalar potential distribution caused by the applied voltage. Equation (4-7) is solved during electrostatic analysis.

$$\nabla . \left(\varepsilon \nabla V \right) = -\rho \qquad (4\text{-}7)$$

where ρ is surface charge density, ε is permittivity, V is electric scalar potential.

Figures 4.4 and 4.5, show the behavior of these elements versus the change in the geometry, (i.e. trace width and thickness) and amplitude of the current passing through the conductor. In these figures, the values of the IPC-2221A design standards are compared with the results obtained from FEA. It is noticed that some error exist in the results obtained from the standard equation and FEA results. Figure 4.4 shows the change in the trace temperature when a RMS current of 10 (A) is passing through the trace. Figure 4.5 shows the current handling capability of the traces, while keeping the trace's temperature below 50 ℃.

After solving the FE model, the inductance, capacitance and resistive matrices are obtained via calculating the energy matrix in the FE model.

The inductance matrix is calculated based on the magnetic energy calculated by (4-8). Self and mutual inductances between the traces are calculated by (4-9)

$$w = \frac{1}{2}\iiint_V \mu . Re\left(H_1 . H_1^*\right)dv + \frac{1}{2}\iiint_V \mu . Re\left(H_2 . H_2^*\right)dv + \frac{1}{2}\iiint_V \mu . Re\left(H_1 . H_2^*\right)dv \tag{4-8}$$

$$L_{ij} = \frac{1}{I^2}\iiint_V \mu_0 . Re\left(H_i . H_j^*\right)dv \tag{4-9}$$

where $\boldsymbol{H}_i, i = 1,2$ is the magnetic field intensity inside the model and μ is the permeability of the model.

The value of the magnetic energy is changed with the change in the current amplitude, therefore, the inductance values calculated by (4-9), is varied by change in the frequency. Figure 4.4, shows the change in trace's stray inductance versus trace width and frequency. This figure is showing that by increasing the trace width the operating temperature on the copper traces will decrease; therefore the copper traces can handle more current at any instant. Figure 4.5 is showing the current handling capability of the copper traces versus trace width, which is in agreement with the results of Figure 4.4. in these figures the results obtained from the IPC standard is compared with the FE simulation results.

The resistance matrix inside the model is calculated based on the current density in the model conductors such as (4-6). Resistance between different layers of the model is calculated by (4-11).

$$P = \iiint_V \frac{Re\left(J_1 . J_1^*\right)}{\sigma}dv + \iiint_V \frac{Re\left(J_2 . J_2^*\right)}{\sigma}dv + 2\iiint_V \frac{Re\left(J_1 . J_2^*\right)}{\sigma}dv \tag{4-10}$$

$$R_{ij} = \frac{1}{I^2}\iiint_V \frac{Re\left(J_i . J_j^*\right)}{\sigma}dv \tag{4-11}$$

where $\boldsymbol{J}_i$ is the current density and σ shows the electric conductivity.

Change in the frequency of injected signal may cause into skin effect in the conductor, which increases the current density in the edges of the trace. Consequently, the resistance of the conducting part of the trace will be higher. Figure 4.6 Change in trace's stray inductance versus trace width and frequency. It is observed that the inductance value is increased with the increase in the operating frequency of the system. Also, by decreasing the width of the traces the inductance value will increase as well. This is due to the fact that at higher frequencies, the flux surrounding the copper traces will close their path in a smaller area. This will consequently leads to increasing level of the inductance Figure 4.7, shows the change in the trace resistances versus the change in the trace width and signal frequency.

Electrostatic energy, shown in (4-7), is used to obtain the capacitance matrix of the model.

$$w = \frac{1}{2}\iiint_V \varepsilon.Re(D_1.E_1)dv + \frac{1}{2}\iiint_V \varepsilon.Re(D_2.E_{21})dv + \frac{1}{2}\iiint_V \varepsilon.Re(D_1.E_2)dv \tag{4-12}$$

where $\boldsymbol{D}_i$ is the electric displacement and $\boldsymbol{E}_i$ is the electric field inside the model. Self and mutual capacitances are calculated based on electrostatic energy value as (4-7).

$$C_{ij} = \frac{1}{V^2}\iiint_V \varepsilon_0.Re(D_i.E_j)dv \tag{4-13}$$

The capacitances are a function of geometry rather than frequency. Therefore, the capacitance values are not changing with the change in the frequency of the injected signal to the traces.

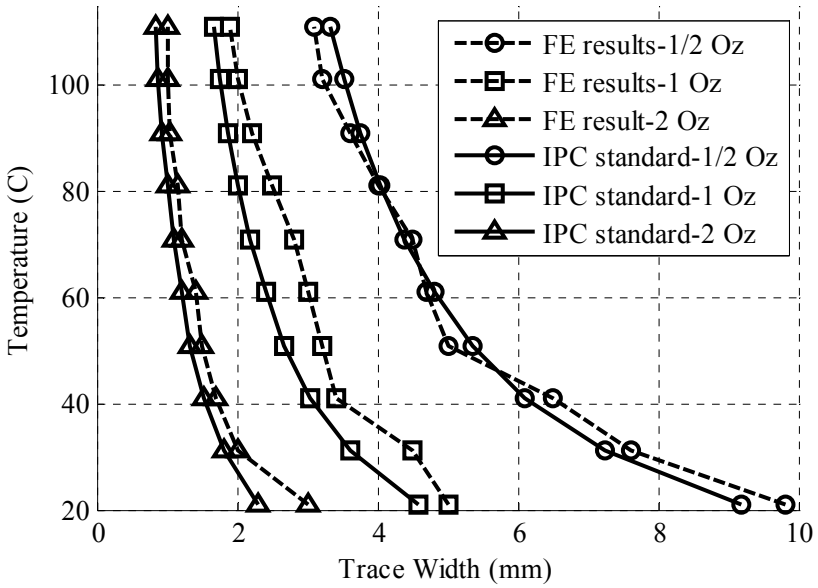

Figure 4.4 Change in the trace's temperature versus trace width and thickness

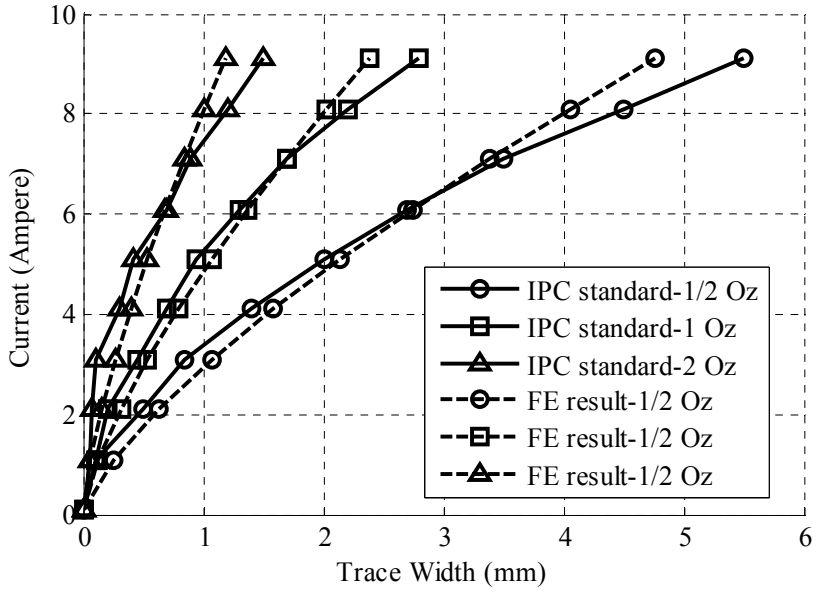

Figure 4.5 Change in current handling capability versus trace width and thickness.

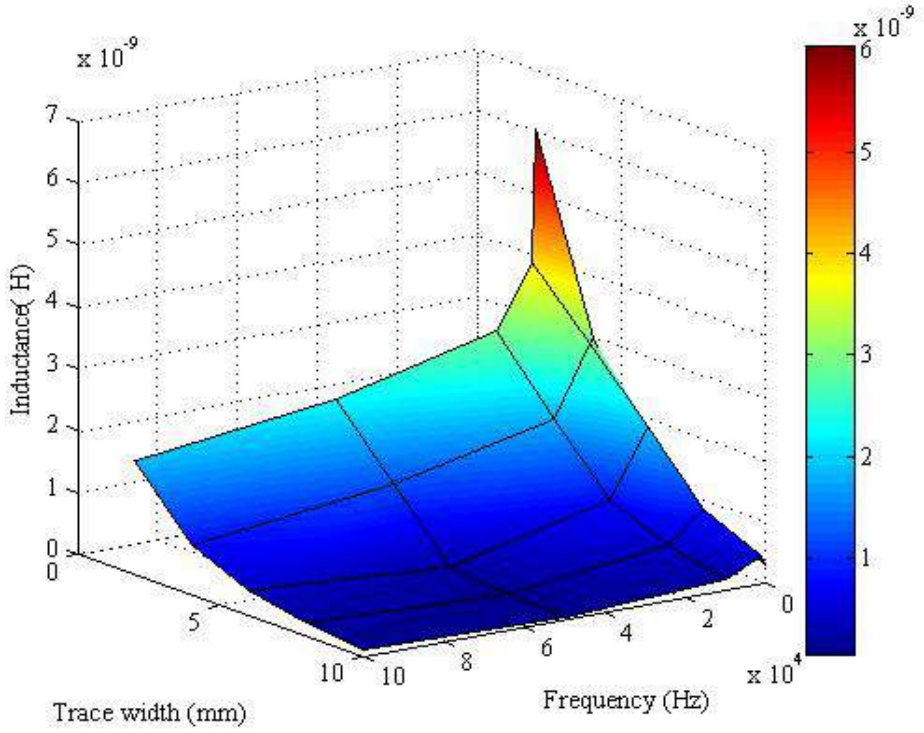

Figure 4.6 Change in trace's stray inductance versus trace width and frequency.

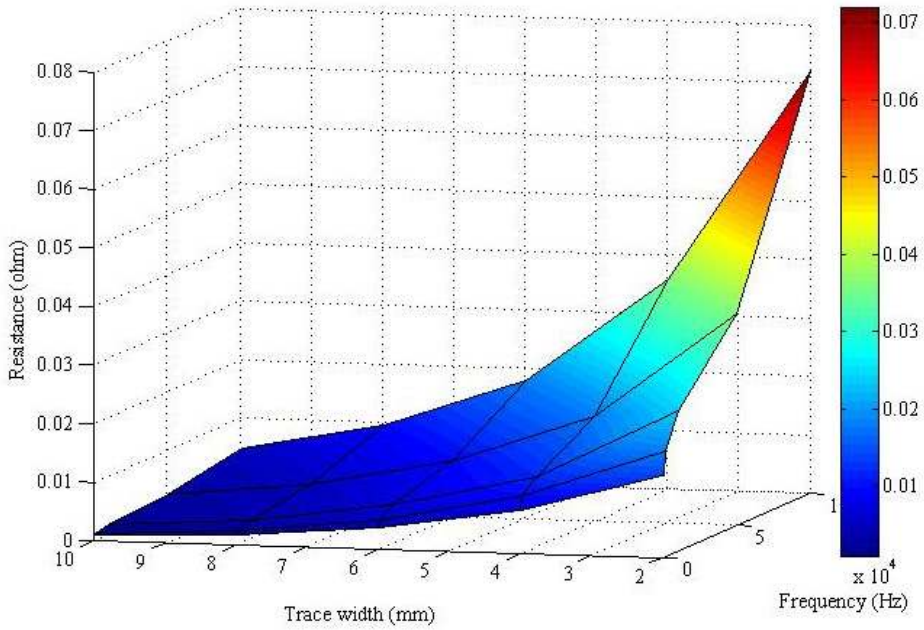

Figure 4.7 Change in the trace resistances versus the change in the trace width and signal frequency.

Figure 4.8, shows the change in the capacitance between two adjacent trace versus change in the width of the trace. It is observed that the capacitance value will increase linearly with the increase in the trace width. This is due to the fact that with increase in the trace width more area is provided between die-electric surfaces, therefore will lead to increasing kevel of capacitance. Figure 4.9 shows the change in the capacitance between two adjacent trace versus traces distance. After calculating all required parameters, these parameters are located in the model and the model evaluation procedure starts.

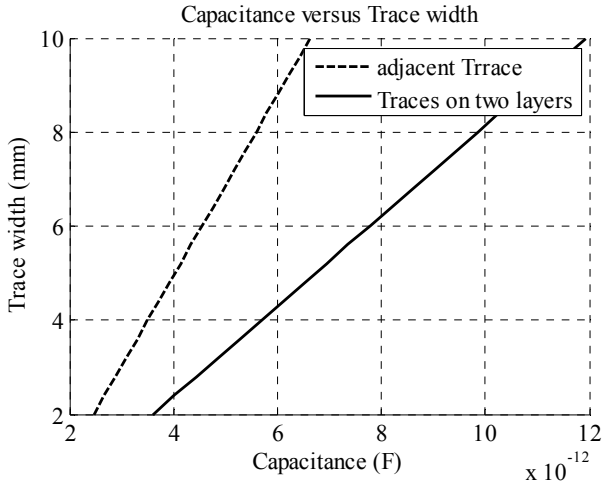

Figure 4.8 Change in the capacitance between two adjacent trace versus change in the width of the trace.

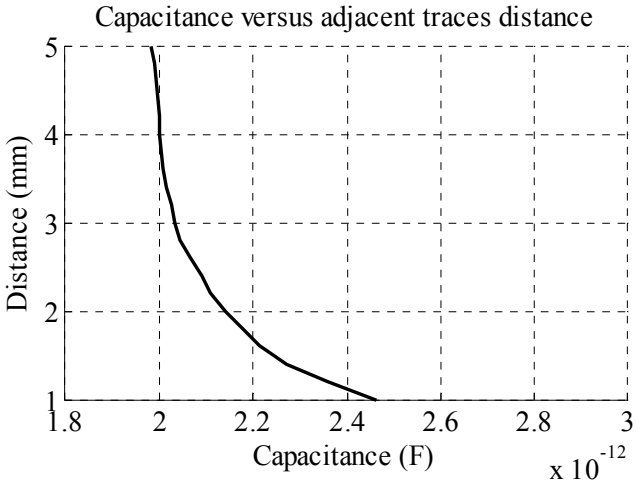

Figure 4.9 Change in the capacitance between two adjacent trace versus traces distance.

Calculation of Crosstalk

The cross-talk effect between the traces in the aforementioned system is calculated based on the algorithm introduced in [80]. In this method the cross-talk can be measured as a function between the input $V_S(t)$ and the outputs V_{NE} .

$$\frac{V_{NE}}{V_S} = j\omega\left(M_{NE}^{IND} + M_{NE}^{CAP}\right) + M_{NE}^{CI} \tag{4-14}$$

where $\omega = 2\pi f$, M_{NE}^{IND} shows the Inductive coupling, M_{NE}^{CAP} shows the Capacitive coupling and M_{NE}^{CI} shows the Common impedance coupling in the near-end crosstalk. Their values are calculated based on equations (4-15)-(4-17), respectively.

$$M_{NE}^{IND} = \frac{R_{NE}}{R_{NE} + R_{FE}} \times \frac{L_M}{R_S + R_L} \tag{4-15}$$

$$M_{NE}^{CAP} = \frac{R_{NE} \times R_{FE}}{R_{NE} + R_{FE}} \times \frac{R_L \times C_M}{R_S + R_L} \tag{4-16}$$

$$M_{NE}^{CI} = \frac{R_{NE}}{R_{NE} + R_{FE}} \times \frac{R_L}{R_S + R_L} \tag{4-17}$$

These equations are implemented in Matlab. Figure 4.10, describes the near-end crosstalk variation versus frequency for electric equivalent model for R_s=R_{NE}=R_{FE}=50 Ω. This figure is showing that using the equivalent electrical model which is obtained through the physics-based modeling approach, some frequencies and oscillations are observed which the conventional analytical models fails to predict them. In figure 4.11, the near-end cross talk of the analytical model is compared with that of electric equivalent circuit model obtained by FE. As it can be seen, these two models are equal up to the frequency of 40 kHz.

In order to reduce the cross-talk in this system, two approaches have been utilized. One is based on changing the position of the reference line and the other one is based on the proper shielding of the signal carrying traces. To test these two algorithms different structure topologies are constructed in FE. Therefore the aim of the study is to minimize the amplitude of electromagnetic field produced by the conducting traces.

Figure 4.12 and 4.13; show the magnetic field $|B|$ and electric field $|E|$ around the copper trace, respectively. In these figures a DC current of 5 ampere is passing through the middle trace. It is observed that the magnetic and electric fields produced by the conducting trace surround the adjacent trace. Therefore, our goal is to limit the boundaries of these electromagnetic fields. It is noticed that increasing the frequency of the signal will limit the magnetic field produced by the current carrying conductor, while the electric field remains almost constant. Figures 4.14 and 4.15, also, confirm the results shown in figures 4.12and 4.13. In figure 4.14 and 4.15, the magnetic and electric fields values are plotted in different frequencies. In all these figures it is observed that with the increase in the operating frequency the magnetic and electric field propagation will decrease. This fact can be used to control or mitigate the level of noise propagation through the PC board in a power conversion system. Figure 4.14 and 4.15; show the change in electric and magnetic field versus the length on the copper traces. Also, it can be observed that the small amount of change is taking place in the electric field. This is due to the fact that the permittivity of the materials is constant with the change in frequency.

After calculation of the crosstalk for the configuration shown in figure 4.1, where the outer wire is the reference wire, now, it is intended to reduce these unwanted phenomena, the proposed algorithm is described as follows:

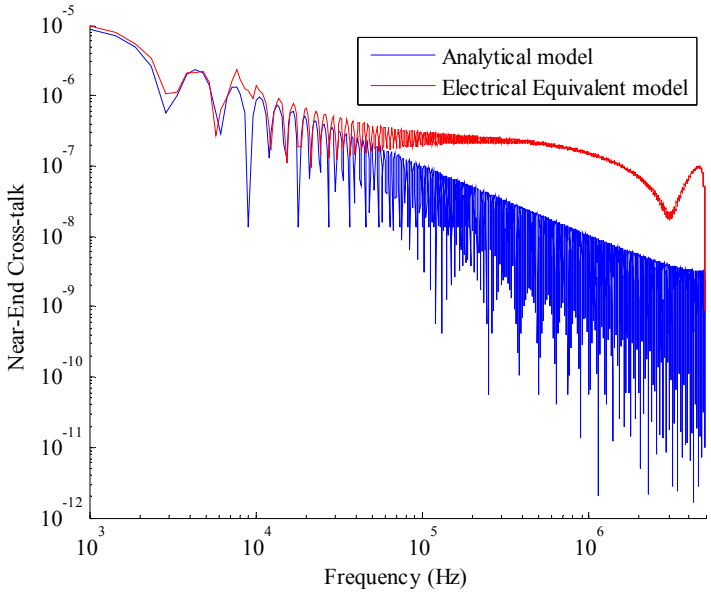

Figure 4.10 Near-end crosstalk variation versus frequency for the model shown in figure 2.

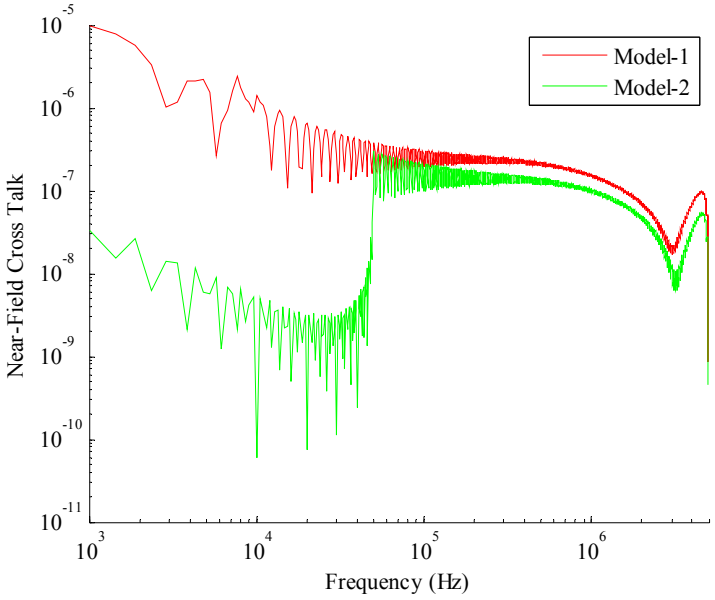

Figure 4.11 Comparison of near-end crosstalk variation between two arrangements of three microstrip

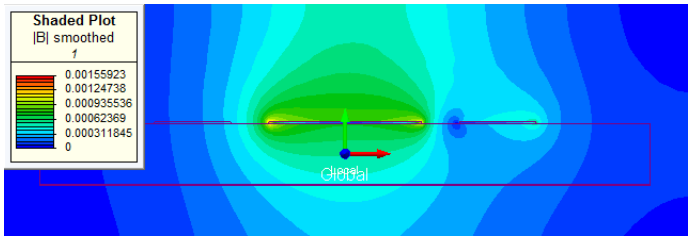

(a)

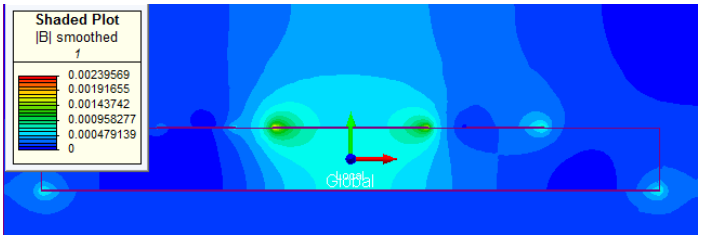

(b)

Figure 4.12 Magnetic field |B| around the copper traces in different switching frequencies, a) Frequency of 100 Hz, b) Frequency of 500 kHz

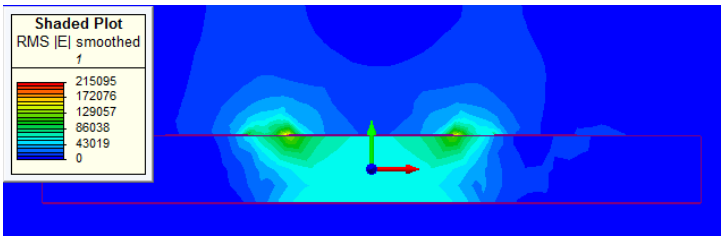

(a)

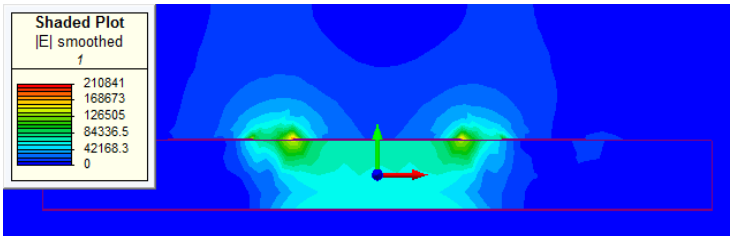

(b)

Figure 4.13 Electric field $|E|$ around the copper trace at different switching frequencies, a) Frequency of 100 Hz, b) Frequency of 500 kHz

1- Suppose that instead of choosing the outer wire as the reference conductor, we choose the middle wire as the reference wire. One of the outer wires is the generator; the other outer wire is the receptor trace. Therefore, the structure of the system is changed. This change may leads to decrease in the values of the parasitic components in the system.

2- In open, or partly open structures electric-and magnetic fields are localized mainly between the traces, but some of the fields are widened from sides and above the traces. In order to limit the electromagnetic field on the PCB board area, all the traces are surrounded by the plates of copper which are grounded [82].

These two methods are applied and the result is shown in figure 4.10. In this figure, decrease in the amplitude of the cross talk is observable.

The behavior of the copper traces and their parasitic performances with respect to the structure and geometry were analyzed in this chapter, using a finite element physics-based representation of the system.

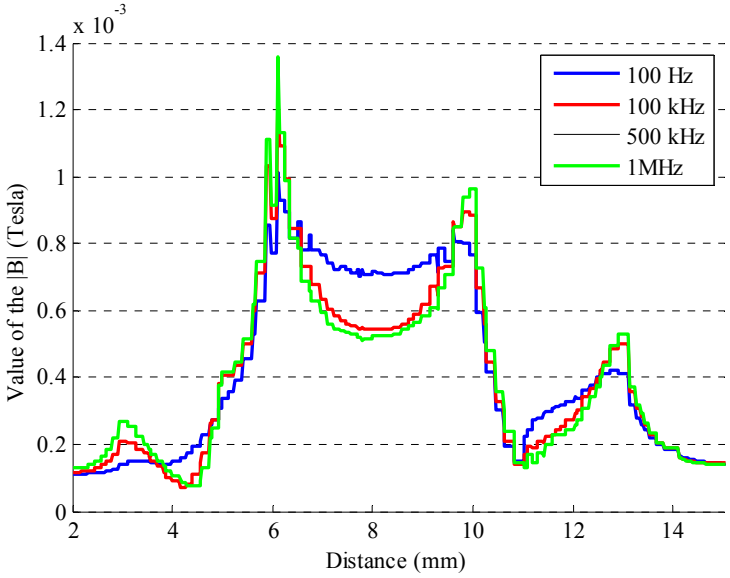

Figure 4.14 Magnetic field in the s PCB model area with respect to different frequencies.

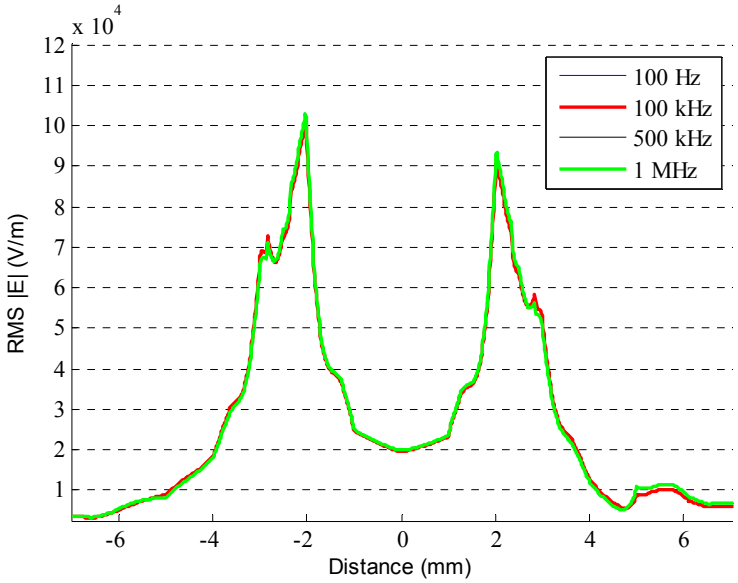

Figure 4.15 Electric field in the s PCB model area with respect to different frequencies.

The equivalent electrical model is presented to calculate crosstalk. Theoretical investigations of near-end crosstalk were also detailed to validate these presented models. We demonstrated that the effects of crosstalk are changed when we change the structure of the system. This was verified in this paper by changing the place of the reference conductor position. The obtained theoretical results and simulations data, demonstrated that crosstalk decreases of *5dB*. This technique is very practical and it can be applied to reduce coupling effects on interconnects in the initial design stages.

Chapter 5 Modeling of the Active components

Electromagnetic interference (EMI) is a challenging problem for systems involving switching power converters. One of the demanding issues in the design of adjustable speed drives is identifying and modeling sources of EMI emission. The EMI noise in these systems produces undesirable effects the control system such as communication errors, degraded equipment performance and malfunction or non-operation [50]. Along with the sizeable market for motor-drives, obtaining an accurate model to predict the system's high frequency behavior is necessary. Availability of such an accurate and detailed HF model is a crucial factor in designing an efficient EMI filter for attenuating the noise emitted or conducted by the system. So far, many studies have been specified on the EMI modeling of motor-drives. The HF model of different types of motor-drives for the investigation and prediction of EMI were discussed in [84-101]. In [84-93], analytical and numerical approaches were presented which proposes a simulation model for a complete drive system based on the frequency domain. References [94-101] present ideas to develop HF model for motor drive system based on the circuit measurements. In these techniques, the frequency responses of the component's characteristics and their corresponding input impedances were obtained experimentally and suitable models were developed to match the experimental results. In the case of using numerical and mathematical approaches, a methodology to obtain the system's high frequency parameters is through using Finite Element Analysis (FEA). Application of FEA in power electronics and drive systems was discussed in [85-90]. This methodology is privileged over the LCR meter measures because: 1) take into account different

geometric configurations of system components and 2) eliminate costly and complicated procedures of testing the system's components and measurement [85].

Previous studies were more concentrating on the cable's or motor's models to study EMC issues and little or no effort was done on acquiring a HF model for power converter part, (i.e. the inverter circuit in this system). For instance, to model the power converter, only the capacitive or resistive elements in the conductors or between the devices and ground were considered [85], [87], [91], [95], [98] and [107]. However, in such systems the power devices transitions are the main sources of EMI [50] and [87]. This modeling approach, although useful, but fails to identify the high frequency behavior of the power conversion system. In [85], [90], [97] a method based on the circuit parameter extraction was proposed, which yields a circuit equivalent model for the power semiconductor devices (IGBT). This model is combined with the other power train components to construct a comprehensive model for the whole motor-drive system. Also, a time domain model for the inverter circuit in the motor-drive system was presented in [86] and [100]. In this method a basic structure of the Hefner's model was used to model the power IGBT which is utilized in the inverter's circuit. The two former methods are a step forward to achieve a model to describe the HF behavior of the power converters. However, these methods overlook some parasitic braches which exist in the power conversion system's layout and can provide a conductive path for the flow of HF current.

The HF models of the converter containing the power semiconductor devices such as IGBTs are based on circuit models. These models are not only related to the parasitic inner parameters of the power devices, but also the connections between these devices.

The main objective of this paper is to obtain a high-frequency physics-based model of IGBT-based power converters. The developed model should acts exactly as the physical device with a high level of accuracy and with little or no compromise.

In a motor-drive system, there are several components, such as the inverter, cable and motor, which need to be modeled for a comprehensive high-frequency investigation. Previous studies such as those in [102],[110], [103] and [111], the HF physics-based model for the armored power cable and PM synchronous motor (PMSM) were obtained. This paper is primarily concentrating on the HF physics-based model of active devices. The developed individual models for these active elements and the HF model of PCB copper traces in addition to other connections are used in combination to construct the whole power converter model.

Modeling of the IGBT

Nowadays, so many different methods of Modeling for IGBTs exist among all the most famous ones are the Hefner's method and Kraus' method. These algorithms are all based on the analytical algorithms that can predict the behavior of the IGBT from low frequency up to the switching frequency. In this section two novel methods are introduced that can predict the high-frequency behavior of the IGBTs, as well. The first one is physics-based modeling of the IGBT which is based on combination of the Hefner's method and FE analysis of the device and the second one is behavioral modeling which is through the circuit measurements.

Physics-based modeling of the IGBT

This section focuses on modeling the semiconductor devices specifically IGBT and its joined components in an inverter circuit with magnetic dependent features. In [108] and [113], a method based on the semiconductor device I-V characteristics measurement was introduced, which demonstrate a good accuracy in predicting the turn-on and turn-off transients of the device. This model also provides the noise source for excitation of system parasitics so that later can be used to predict the EMC/EMI problems in the power converters.

The model used in this study, utilized the device model which is defined in [104] or [113] and enhance the model accuracy by considering the parasitic components, which are ignored in these previous models. In this study, the object's structure and geometry was modeled using finite element analysis to evaluate their electromagnetic characteristics. The proposed modeling method is based on coupling the analytical model of the IGBT with FEM.

Model Structure

In this part, the physics-based model for the IGBT is described. The proposed model for IGBT is composed of the analytical model combined with the circuit model derived from FEM. The analytical model used for the IGBT is based on the Hefner's algorithm [104]. Figure 5.1 shows the main circuit model proposed in [104] for the power IGBT. The diode D_{eb} represents the anode side p-n junction forward voltage drop while the voltage source V_{base} accounts for the voltage drop in the drift region which is the base of the pnp transistor.

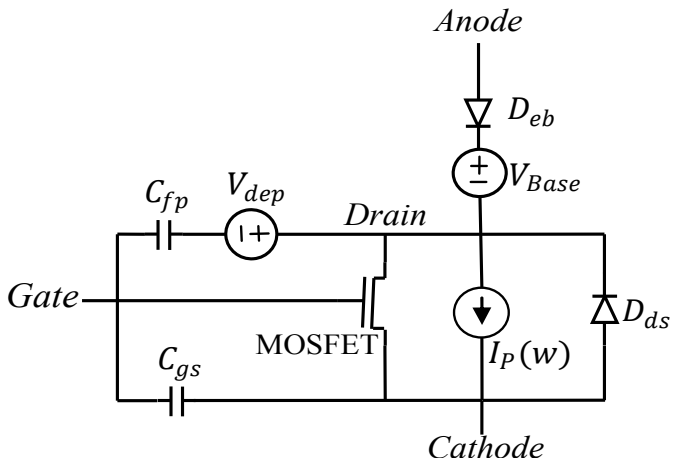

Figure 5.1 Conventional Hefner's model for the IGBT, representing a low frequency model for the device.

The $I_N(W)$ represents the base electron current of the IGBT. The hole current at the cathode is represented by the current source $I_P(W)$, where W stands for the IGBT base width. The diode D_{ds} models the drain to the source capacitance due to the junction at the collector.

The capacitance between the gate and drain of the switch, $C_{gd,}$ is defined as the series connection of a voltage source V_{dep} and a capacitor C_{fp}, which represent a voltage source dependent to the drain-gate voltage and the gate field plate capacitance, respectively. In this model, C_{gs} represents the gate to source capacitance.

The model shown in figure 5.1 is based on the Hefner's analytical model that can describe the steady-state and transient condition during the switching actions. But, this model ignores most of the parasitic elements that exist in the IGBT's layer's structure. These parasitic elements have significant impact on the propagation of noise in the circuit. To compensate this limitation, the effects of the parasitic elements should be considered. The model proposed in this paper, incorporate the model shown in figure 5.1.

Subsequently, this model is expanded by adding the parasitic components that exist in the structure of the IGBT including the stray and mutual impedances in or between the Gate, Drain and Source terminals of the device.

The parameters and function blocks shown in figure 5.1 were implemented in Matlab/Simulink using the equations introduced in [104] and [105]. To model the IGBT's interlayer impedances, FE analysis is used. Next subsection explains the procedure which is followed to estimate the value of these impedances. The total hole current at the collector is the addition of the steady-state current and transient current.

$$I_P(W) = I_{P_{SS}}(W) + I_{TRN} \tag{5-1}$$

The steady-state hole current at the cathode is calculated as:

$$I_{P_{SS}}(W) = \frac{P_0^2}{bn_i^2} I_{sne} + \frac{qAD}{L}\left[P_0\left(\frac{\coth\left(\frac{W}{L}\right)}{b} + \frac{1}{\sinh\left(\frac{W}{L}\right)} \right) - P_W\left(\coth\left(\frac{W}{L}\right) + \frac{1}{b\sinh\left(\frac{W}{L}\right)} \right) \right] \tag{5-2}$$

$$I_{TRN} = -qAp(W)\frac{\partial W}{\partial t} \tag{5-3}$$

where, I_{sne} is the electron reverse saturation current at the emitter/base junction. Undepleted base width (W) is given by:

$$W = W_B - (W_{fp-dep} + W_{pn-dep}) \tag{5-4}$$

where W_B is the total base width, the gate field plate depletion width (W_{fp-dep}) is calculated as follows:

$$W_{fp-dep} = \begin{cases} \frac{w_{fp}}{V_{fp}} V_{ds} & 0 \le V_{ds} \le V_{fp} \\ W_{fp} & V_{ds} > V_{fp} \end{cases} \tag{5-5}$$

Also the normal p-n junction depletion width is given by:

$$W_{pn-dep} = W_{inc}\sqrt{2\varepsilon_{si}(V_{ds} + V_{bi})/qN_{scl}} \tag{5-6}$$

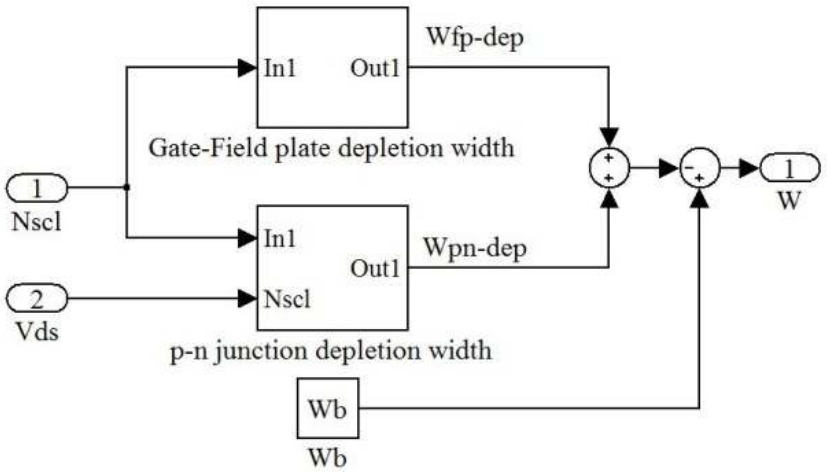

Figure 5.2 Block Diagram for calculation of undepleted base width

Undepleted base width calculation is implemented in Simulink based on (5-4). Figure 5.2 shows block diagram for calculation of undepleted base width of IGBT.

N_{scl} in (5-6), represents the effective doping factor and is given by:

$$N_{scl} = N_B + I_P(W)/(qA\upsilon_{psat}) \tag{5-7}$$

p(W) used in (6-2), (6-3) is the carrier concentration in the base that can be expressed as:

$$p(w) = \frac{P_0 \sinh\left[\frac{W_B - W}{L}\right] + pw_{ratio} \times P_0 \sinh\left(\frac{W}{L}\right)}{\sinh\left(\frac{W}{L}\right)} \tag{5-8}$$

In model illustrated in figure 5.1, the voltage drop across the base (V_{base}), is calculated as:

$$V_{base} = \frac{I_T W}{(1+1/b)\mu_n A q n_{eff}} - \frac{D}{\mu_n}\log\left(\frac{P_0 + N_B}{P_w + N_B}\right) \tag{5-9}$$

where n_{eff} has an analytical solution and is described in [112]. The carrier concentration(P_w), is a function of the pnp transistor gain and is given by (5-10),

$$P_W = \begin{cases} pw - ratio * p_0 & V_{gs} \geq V_{th} \\ 0 & V_{gs} < V_{th} \end{cases} \tag{5-10}$$

In this model the capacitance between the IGBT's gate and drain can be implemented in the form of connecting C_{fp} in series with a voltage source, which is given by:

$$V_{dep} = f(V_{dg}) = V_{dg} - V_n\sqrt{\frac{2V_{dg}}{V_n}} + V_n \log\left[1+\sqrt{\frac{2V_{dg}}{V_n}}\right] \tag{5-11}$$

The drain to cathode capacitance is represented by a reverse biased diode D_{ds} connected between the drain and cathode.

Figure 5.3, shows the block diagram of $I_P(W)$, $p(W)$ and W calculations, which is implemented in Matlab/Simulink. In this block diagram $I_P(W)$ is calculated based on (5-1), effective doping (N_{scl}) is implemented based on (5-7) and carrier concentration block is implemented based on (5-8). Block diagram shown in figure 5.3 is demonstrated in figure 5.4 as analytical calculation block. Voltage drop across the base (V_{base}) and depletion layer voltage (V_{dep}) is also calculated based on (5-9) and (5-11), respectively. In this model the MOSFET model block is a Level 1 MOSFET, which is being used in Simulink. Table 5.1, describes the complete parameter sets, which are used in the IGBT model.

In order to obtain an accurate analytical model for the semiconductor switches that represent the actual device the first step is to calculate the unknown parameters. In [117], a method based on electrical measurement is introduced to calculate the IGBT parameters which are described in Table 5.1. The values of these parameters are given in Table 5.2.

The performance of the IGBT which is modeled in this section, is limited to the frequency of 5MHz, and our model fails to predict the behavior higher than this frequency.

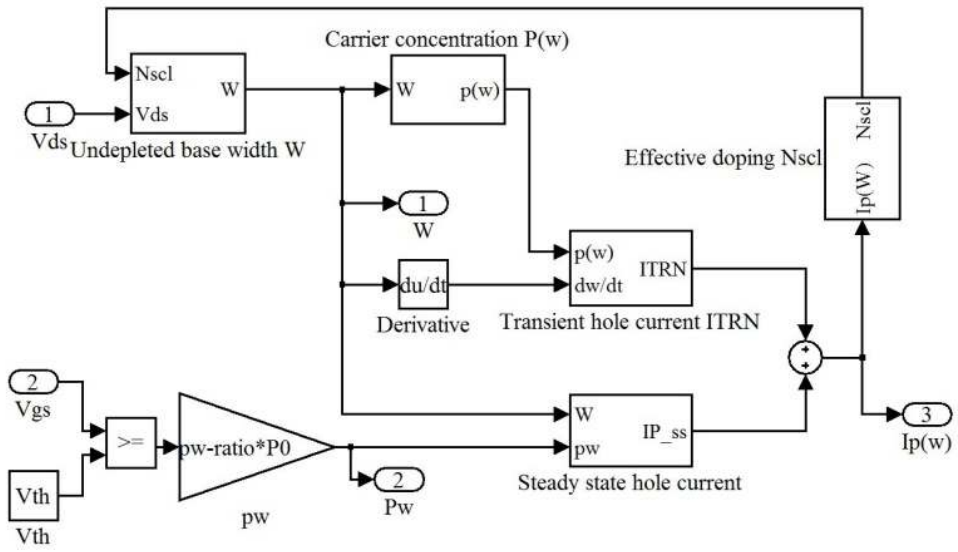

Figure 5.3 Implementation of IGBT model in simulink/Matlab

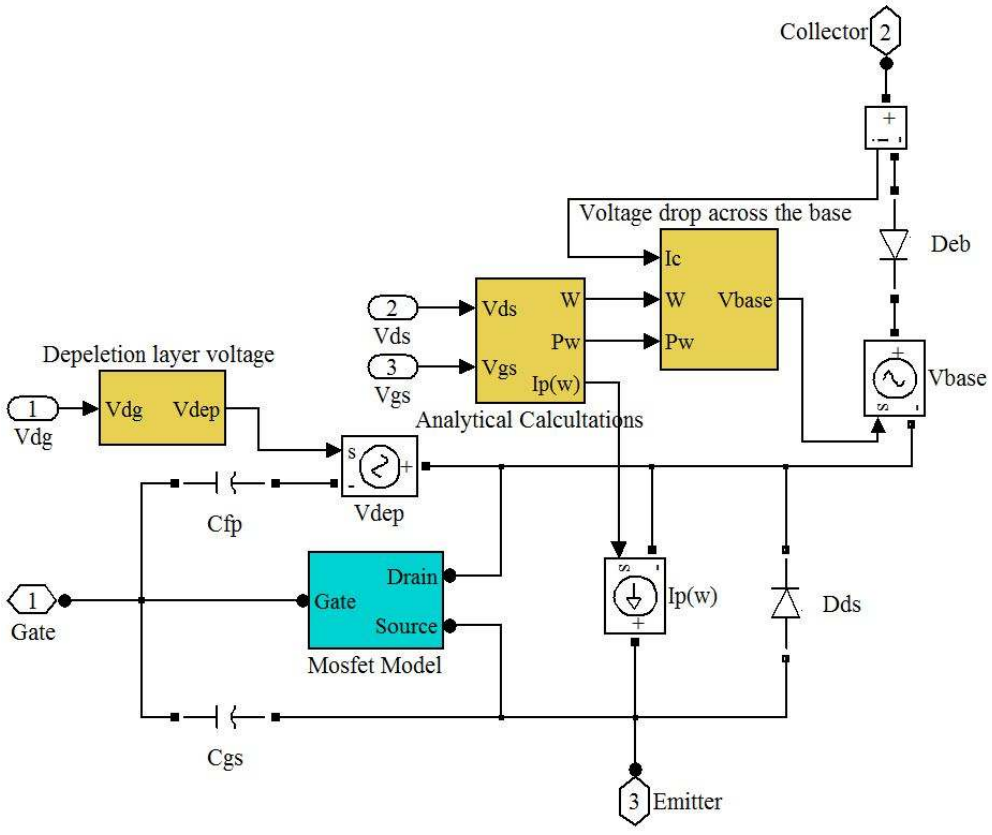

Figure 5.4 Implementation of IGBT model in simulink/Matlab

Table 5.1 Sequence of parameters used in the Hefner model

Static measurement		Dynamic measurement	
Symbol	Description	Symbol	Description
V_T	Threshold voltage	C_{GS}	Gate-source capacitance
N_B	Doping concentration	C_{fp}	Gate-drain overlap oxide capacitance
W_B	Base width	A	Active area
K_P	Transconductance factor	Pw_ratio	Carrier concentration gain
K_F	Triode region factor	I_{SNE}	Emitter electron saturation current
Thetha	Transverse field transconductance factor	V_{TD}	1.02

Table 5.2 Extracted parameters

Static measurement		Dynamic measurement	
Symbol	Value	Symbol	Value
V_T	1.62 V	C_{GS}	2.25e-10 F
N_B	4.5e15 cm^{-3}	C_{fp}	1.63e-10 F
W_B	51e-4 cm	A	1.36e-4 cm^2
K_P	0.62 AV^{-1}	Pw_ratio	0.33
K_F	0.2	I_{SNE}	1.91e-16 A
Thetha	0.07 V^{-1}	V_{TD}	1.02 V

The IGBT model shown in figure 5.4, is one of the IGBT model which contain many of the IGBT details. This model can explain many details related to the IGBT behavior during its operation. This model is based on the IGBT physical equations.

In the next section, a novel method based on the circuit measurement is used to obtain a new IGBT behavioral model. The obtained functional model will be compared to the

analytical model described in this section, the conventional IGBT model which is provided in Simulink/Matlab and also the PSIM IGBT model.

Modeling the parasitic components

To obtain the Physics-based model, the geometry of the actual IGBT is modeled by finite elements. A 3D quasi-static FE analysis was performed to obtain parasitic resistances and inductances of different layers in the semiconductor structure.

In FE method, one approach to calculate the inductance, capacitance and resistive matrices is through calculating the energy matrix in the FE model.

Figure 5.5(a) shows an IGBT cell model in its FE mesh. This model consists of several layers attached together to produce an n-channel IGBT cell. In this structure, the n+ layer at the top is the source or emitter and the p+ layer is the collector. Other layers arrangements are shown in figure 5.5(a) include the substrate, n and p channels. Also, channel's material is silicon (Si) and the pad's material is SiO_2. The structure and layout of the system shown in figure 5.5, is explained in [111].

To achieve the circuit model of each unit cells, the magnetostatic and electrostatic analysis were separately performed on the IGBT model. In the magnetostatic analysis, to obtain the inductance and resistance values, six different current directions were defined within the IGBT model [110]. These current directions were defined in the form of coils in the contacts of the IGBT's collector, emitter and gate. Other coils were defined as the routes between the collector-gate, gate-emitter and collector-emitter. The current directions are defined in figure 5.5(b). For further illustration, in this figure the IGBT layer's structure are depicted in 2D format. The direction of these currents was defined as

follows: When the device is on, the collector is at a higher voltage than the emitter and therefore, minority carriers are injected from the collector p+ region into the collector n region. The charges reduce the collector bulk region resistance and thus create a conductive path from collector to emitter. When a positive gate voltage is applied, gate current flows until the gate capacitance is charged and the gate voltage rises to the "on" level, thus a conductive path is created from gate-emitter. A positive voltage on the gate attracts electrons from the "p" gate region towards the silicon surface under the gate. These electrons invert the "p" directly under the gate to form an "n" region, thus creating a path for charge flow between the "n" collector region and the "n" emitter region. Therefore, a conductive path between the collector and gate is created which can be considered in modeling the parasitic components of the device [114].

The electromagnetic field inside this device is governed by the following nonlinear partial differential equations:

$$\nabla\times\left(\mu_0^{-1}\nabla\times A-M\right)-\sigma v\times\left(\nabla\times A\right)+\sigma\nabla V=J^e \tag{5-12}$$

where A is magnetic vector potential , J^e is external current density, M is magnetization, V is the electric scalar potential, σ is the electric conductivity and $\boldsymbol{v}$ is the motion speed which in this case, it is equal to zero. Note that, the magnetization curve was considered in several points in the hysteresis curve.

Also, the electrostatic problem is solved for the calculation of capacitances matrix as capacitances are a function of geometry. The analysis determines the electric scalar potential distribution caused by the applied voltage.

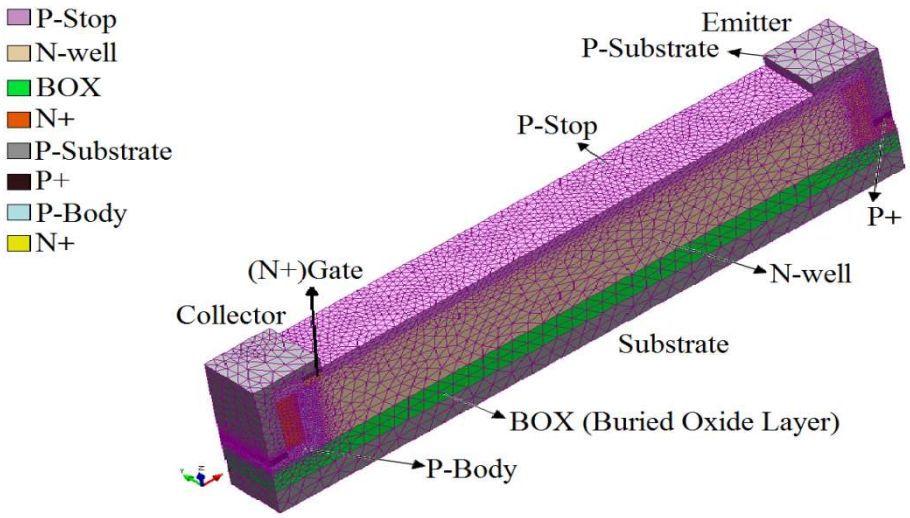

(a)

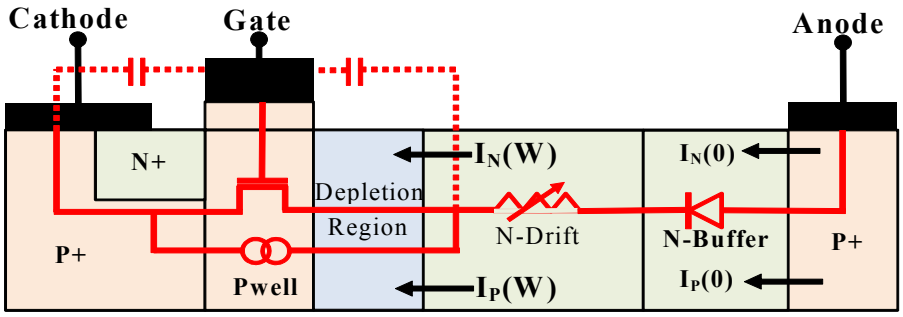

(b)

Figure 5.5 IGBT cell model, (a) 3D FEM model, (b) 2D model for illustration of the current direction in the IGBT structure.

The following set of equations was solved during the electrostatic analysis, note that, $\widetilde{A} = A + \nabla\psi$:

$$E = -\frac{\partial A}{\partial t} - \nabla V = -\frac{\partial\left(\widetilde{A} - \nabla\psi\right)}{\partial t} - \nabla\left(\widetilde{V} + \frac{\partial\psi}{\partial t}\right) = -\frac{\partial\widetilde{A}}{\partial t} - \nabla\widetilde{V} \tag{5-13}$$

$$\widetilde{V} = V - \frac{\partial \psi}{\partial t} \tag{5-14}$$

where Ψ is magnetic flux and V is electric scalar potential.

As stated above, the parameter calculation is based on the magnetostatic and electrostatic fields. In addition to considering all electric and magnetic fields in (5-12) and (5-13), deviation of electric and magnetic fields versus time was also considered. This assumption is crucial for parameter estimation in the frequency response analysis (FRA). Since inductances and resistances change at higher frequencies, the deviation of fields should be considered for accurate results.

The power IGBT was created by paralleling several of those unit cells (figure 5.6 (a, b)). Figure 5.6(a) shows the layout of the IGBT cells, paralleled together on the silicon wafer. Therefore, to obtain the power IGBT model, the model of each of the unit cells must be connected together, as shown in figure 5.6 (b). Consequently, an electric network was obtained which can characterize the IGBT high-frequency behavior (figure 5.6(c)).

After solving the FE model, the inductance, capacitance and resistive matrices are obtained via calculating the energy matrix in the FE model. The magnetic energy is calculated as:

$$W = \frac{1}{2}\iiint_V \mu . Re\left(H_1 . H_1^*\right) dv + \frac{1}{2}\iiint_V \mu . Re\left(H_2 . H_2^*\right) dv + \frac{1}{2}\iiint_V \mu . Re\left(H_1 . H_2^*\right) dv \tag{5-15}$$

where $\boldsymbol{H}_i, i = 1,2$ is the magnetic field intensity inside the model and μ is the permeability of the model.

After calculating the magnetic energy inside the FE model, using equation (5-15), all self and mutual inductances are estimated based on magnetic energy value as:

$$L_{ij} = \frac{1}{I^2} \iiint_V \mu_0 . Re\left(H_i . H_j^*\right) dv \tag{5-16}$$

The electrostatic energy was used to obtain the capacitance matrix of the model. The electrostatic is calculated by:

$$W = \frac{1}{2} \iiint_V \varepsilon . \left(D_1 . E_1\right) dv + \frac{1}{2} \iiint_V \varepsilon . \left(D_2 . E_2\right) dv + \frac{1}{2} \iiint_V \varepsilon . \left(D_1 . E_2\right) dv \tag{5-17}$$

where $\boldsymbol{D}_i$ is the electric displacement and $\boldsymbol{E}_i$ is the electric field inside the model. Self and mutual capacitances are calculated based on electrostatic energy value as (5-18).

$$C_{ij} = \frac{1}{V^2} \iiint_V \varepsilon_0 . \left(D_i . E_j\right) dv \tag{5-18}$$

The resistance matrix inside the model is calculated based on the current density in the model conductors as equation (5-19). The resistance between different the layers of the model is calculated by (5-20).

$$P = \iiint_V \frac{Re\left(J_1 . J_1^*\right)}{\sigma} dv + \iiint_V \frac{Re\left(J_2 . J_2^*\right)}{\sigma} dv + 2 \iiint_V \frac{Re\left(J_1 . J_2^*\right)}{\sigma} dv \tag{5-19}$$

$$R_{ij} = \frac{1}{I^2} \iiint_V \frac{Re\left(J_i . J_j^*\right)}{\sigma} dv \tag{5-20}$$

where J_i is the current density and σ shows the electric conductivity.

Following the calculation of all required parameters for the distributed model, these parameters were utilized in the model.

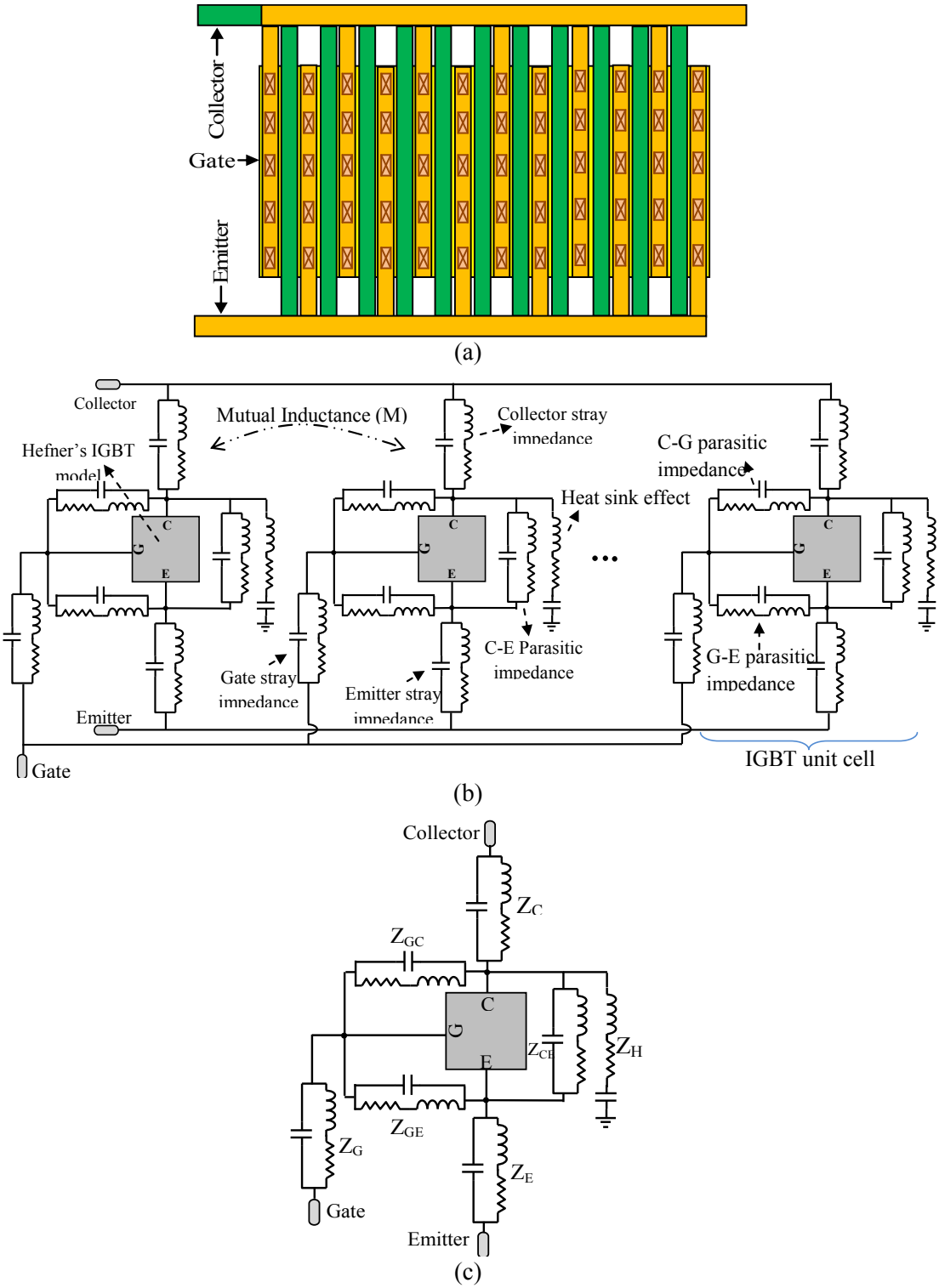

Figure 5.6 Implementation of a unit IGBT cell in FE domain,(a) geometrical demonstration of the unit, (b) IGBT distributed equivalent circuit network from 3DFE, (c) Lumped model reduced equivalent electrical circuit.

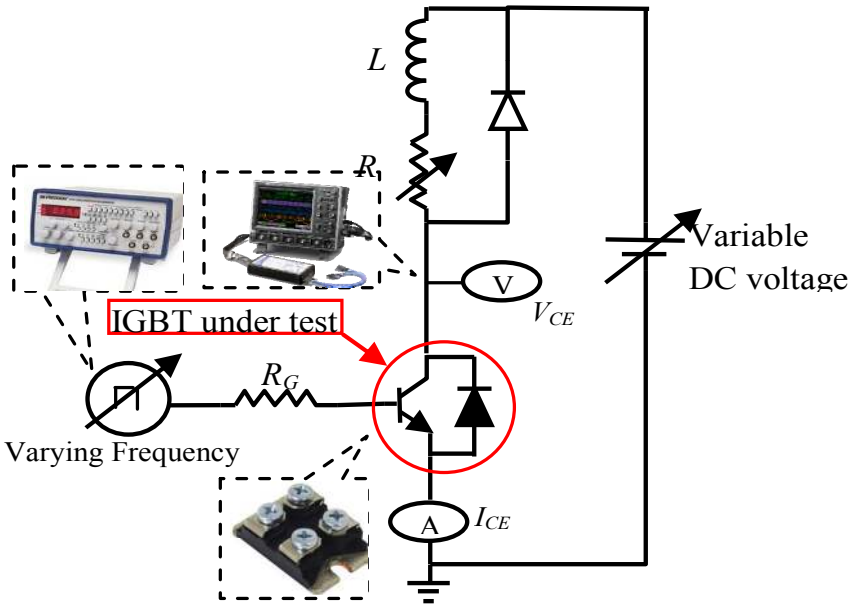

Figure 5.7 Experimental test setup.

Figure 5.6(b) shows the electric circuit obtained from the FE model, for a single unit IGBT cell. In this model, all the resistors and inductors represent built-in resistances and parasitic inductances of an IGBT module. The IGBT cell within the IGBT module, shown in figure 5.6(a), has the width of 36 μm. Therefore, in a device with a width of 560x4 μm, it is considered that 62 of these unit cells are in parallel (see figure 5.6(b)).

The Hefner's model, shown in figure 5.1, was utilized as a block in the IGBT model illustrated in figure 5.6(c). This model is composed of parasitic elements, which are calculated using FEM and Hefner's analytical model. This model has the capability to represent the IGBT dynamic and static behaviors.

The model for the analysis of the IGBT in FEM contained 4.6×10^5 degrees of freedom and 1×10^{-3} percent tolerance of energy. The analysis method used here is generalized minimum residual method (GMRES), which was used to solve

nonsymmetrical systems. Since the geometry of the elements are non-uniform (The length of some elements are much bigger than the width of them), geometric multi-grid method was chosen as the pre-conditioner and F-cycle as multi-grid cycle.

To verify the accuracy of the IGBT model, a test setup, as shown in figure 5.7 was assembled. In this test, the IGBT was switched under different PWM switching frequencies. Subsequently, the voltage waveforms were recorded to compare the switching behavior of the proposed IGBT model with the measurement.

Figures 5.8 and 5.9 show the results of this comparison. As it is shown in these figures, the proposed method can estimate the high frequency oscillations during the turn on and turn off transition of the semiconductor switching. It is noticed that at lower frequencies, the parasitic elements are resonating due to the excitation by the switching actions. At higher frequencies, higher damping which is due to higher resistance and lower inductance lead to smaller oscillations. Therefore, the error between the measured waveforms and the model are reduced.

In figure 5.8 and 5.9, switching waveforms of the semiconductor device are illustrated (these figures include the Gate-Emitter voltage and Collector-Emitter voltage during the turn off and turn on transition). In these figures, the actual switching waveforms were recorded by TPS2014B Tektronix digital oscilloscope (100 MHz, 1 GS/s). Finally, the measured waveforms are compared to the waveforms which are obtained using the simulation of the proposed model for the semiconductor devices. It is noticed that the proposed model can estimate the high frequency oscillation in the switching action, which the conventional models fails to present.

Figures 5.8(a) and 5.8(b) show the Gate-Emitter voltage waveform in two different switching frequencies (2 and 10 kHz) during the off time transition. While figure 5.8(c) shows the Gate-Emitter voltage in the on time transition. Also, figure 5.9(a) and 5.9(b), show the Collector-Emitter voltage waveform in switching frequencies of 2 and 10 kHz, during the off time transition. Figure 5.9(c) shows the Gate-Emitter voltage in the on time transition.

Figures 5.10 and 5.11, compare the frequency spectrum and harmonic order of the two modeling approaches vs. the measurement. Figure 5.10(a) shows the frequency spectrum of the switching action in frequency of 2 kHz. It can be noticed that there is less difference between the frequency spectrum of the proposed model and actual measurement of the system. The harmonic diagram shown in Figure 5.10(b), confirms the higher accuracy in the proposed approach, to model the high frequency behavior in switching action.

Figure 5.11(a) shows the frequency spectrum of the switching action in frequency of 10 kHz. As shown in figure 5.9(c), the proposed model can well represent the high frequency behavior of the switching action in frequency of 10 kHz and above. This phenomenon is confirmed in the frequency domain in figures 5.11(a) and 5.11(b). The harmonic order of the switching at frequency of 10 kHz is shown in figure 5.11(b). This figure compares the harmonic order of the proposed model, Hefner's method and measurement data.

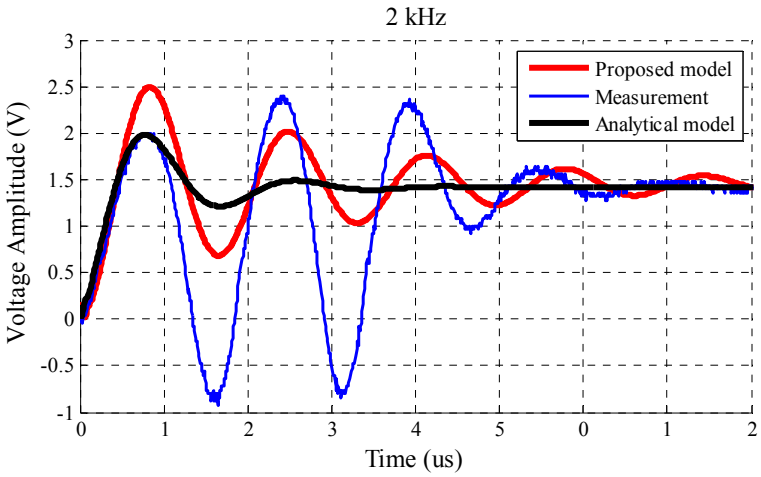

(a)

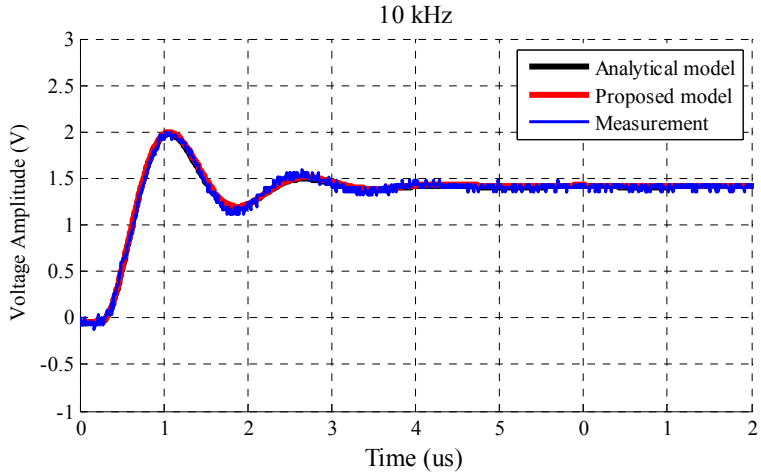

(b)

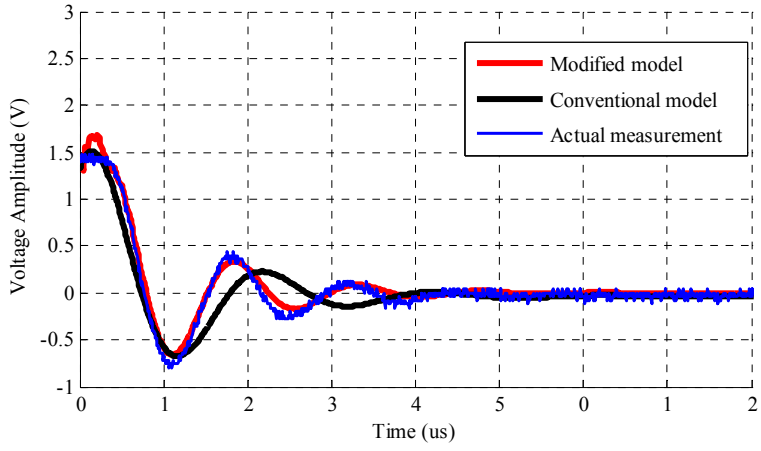

(c)

Figure 5.8 Comparison of the Gate-Emitter switching resonances in the three modeling approach in different switching frequencies, (a) 2 KHz, (b) 10 KHz, (c) switching resonances in turning on transition.

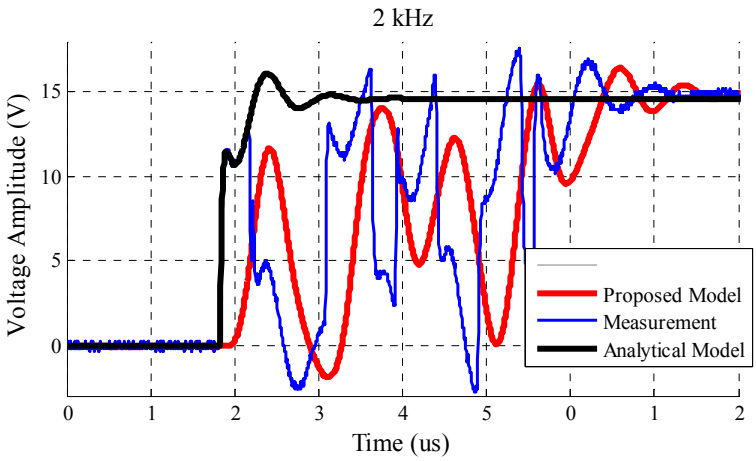

(a)

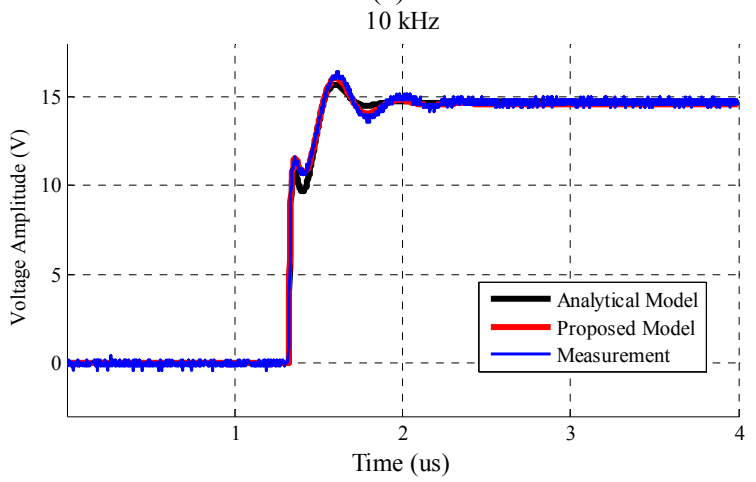

(b)

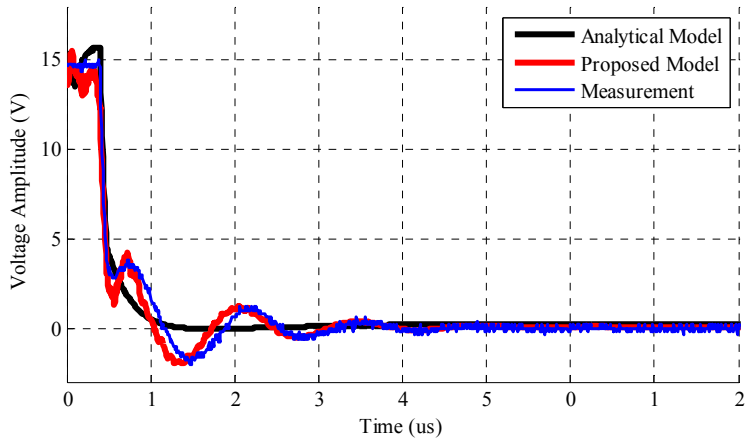

(c)

Figure 5.9 Comparison of the Collector-Emitter switching resonances in the three modeling approach in different switching frequencies, (a) 2 KHz, (b) 10 KHz, (c) switching resonances in turning on transition.

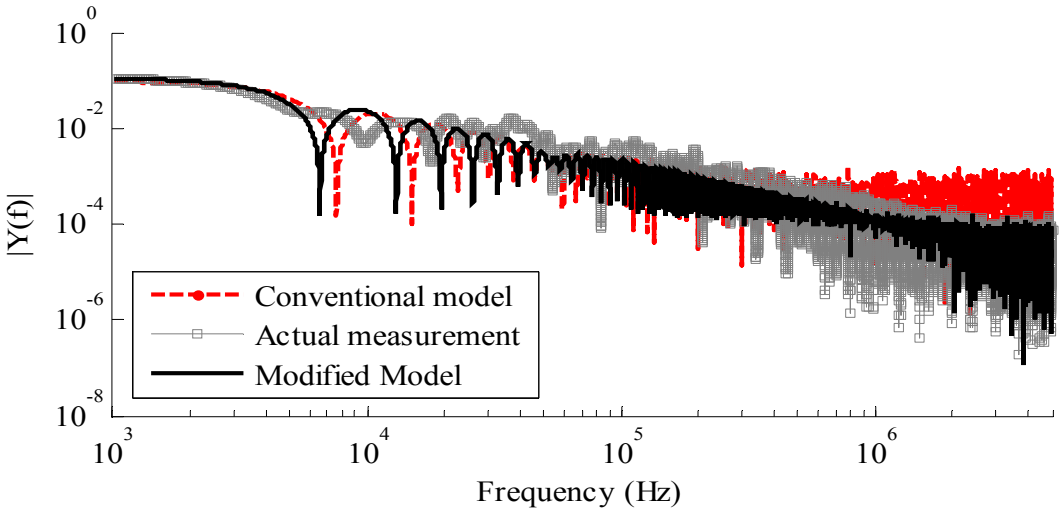

(a)

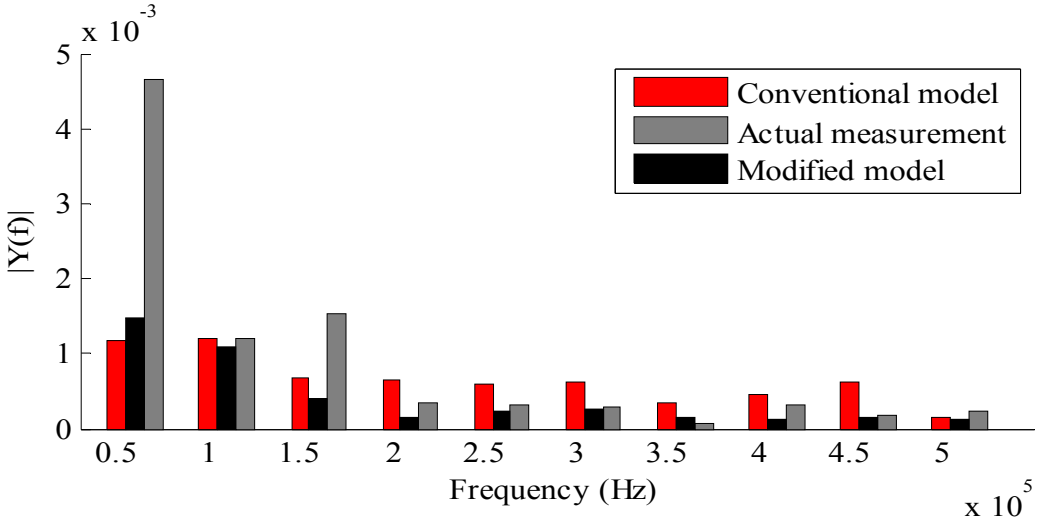

(b)

Figure 5.10 (a) frequency spectrum of the switching transition in 2 kHz, (b) comparison of the harmonic order in two modeling approach vs. measurement.

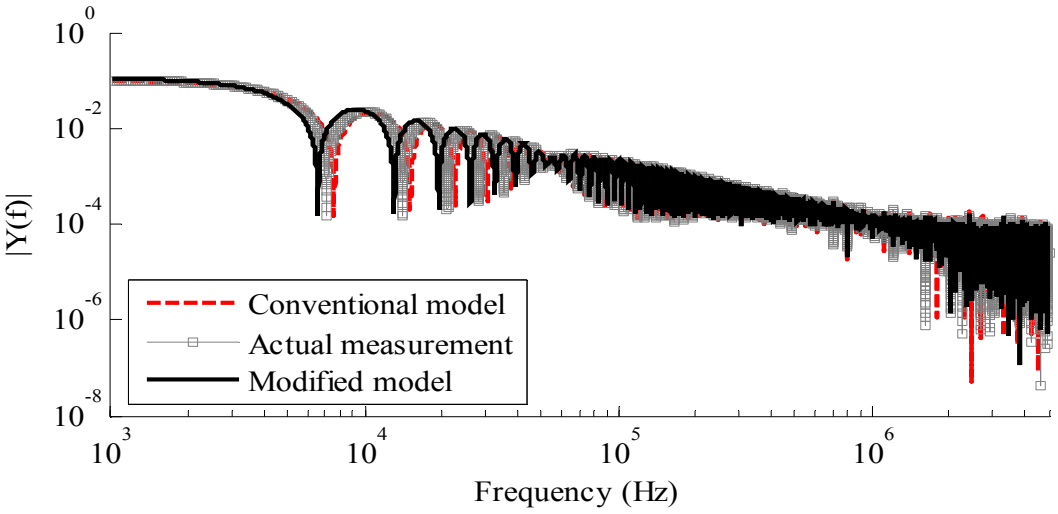

(a)

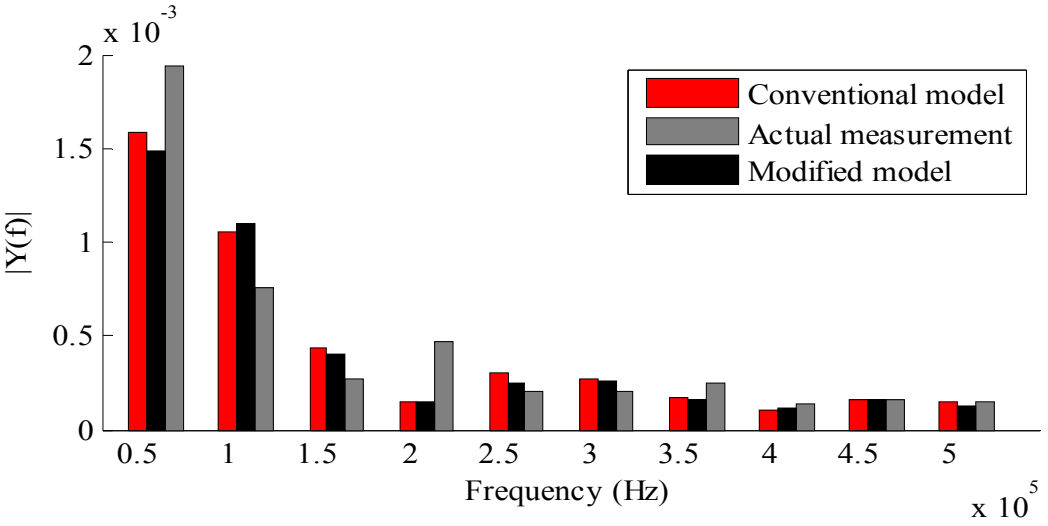

(b)

Figure 5.11 (a) frequency spectrum of the switching transition in 2 kHz, (b) comparison of the harmonic order in two modeling approach vs. measurement.

Functional ON/OFF Behavioral Modeling of Power IGBT

In this section, a method based on the step response of a linear system is being used to obtain a model of power IGBTs. The IGBT voltages and currents are measured at

different power ratings and switching frequencies. Using a system identification algorithm, a state-space model is obtained for the system which represents a matching step response. Finally, acquired individual models are combined, using fuzzy description of the system. This model can predict the behavior of the switch over a wide range of frequencies. The current and voltage waveforms of the proposed model in switching action are compared with the actual IGBT. This model can be used in designing the power converters circuit and study the high frequency behavior of the switches.

Due to the increased focus on the behavior of power IGBT devices in power converter designs, detailed physics based models are required. Many published studies present works which have been oriented to develop IGBT models for different simulator packages [112], [118] and [119]. Among them, the IGBT model developed by Hefner is one of the most used in several commercial circuit simulation programs [118]. This modeling approach, although useful, but fails to identify the high frequency behavior of semiconductor devices.

The Hefner's model and other related algorithms are all based on the switch parameters, which most of such parameters are not provided in the datasheets of the product. Therefore, in order to use this algorithm, there is a need to extract the switch parameters. In [120]-[123] some parameter extraction algorithms for power IGBTs were introduced. To achieve the IGBT's parameters, several testing circuits must be built. Subsequently, by performing circuit measurements, the switch parameters are evaluated. Utilizing the analytical models for IGBTs in the simulation software needs solution of a series of nonlinear differential equation, which increase the complication and required

solution time. Therefore, a model is needed, which can present a good tradeoff between convergence, simulation time, accuracy, simplicity and comprehensibility.

The aim of this part is to propose a method to model the power IGBTs based on the circuit measurements. The proposed algorithm is based on system identification, by performing an analysis of the step response of a linear system. Performing such an evaluation over a specific range of frequencies and power ratings, the state-space models for the system are obtained. These individual models can be stored as a multi-dimensional data table. Finally, using a fuzzy description of the system, a model is obtained which can well predict the behavior of the device in a wide range of operating conditions. The accuracy of the proposed model was verified by comparing measurements with the existing IGBT analytical model such as Hefner's model. These models are implemented in MATLAB/Simulink and can be used as a substitution for the conventional IGBT models.

System Identification

To obtain a numerical and mathematical model which can well represent the behavior of the IGBT during the on and off time period, an algorithm based on the system identification is applied. System identification is a methodology for building mathematical models of dynamic systems using measurements of the system's input and output signals in time or frequency domain [124], [125]. In this study the identification process is based on obtaining the Markov parameters from input-output data by frequency domain approaches. Once the Markov parameters are determined, they become entries in the Hankel matrix for state-space identification [126].

To obtain the Markov parameters, the step response of the dynamical system is used (in this case, IGBT under a switching action). To obtain the step response of the IGBT the circuit shown in figure 5.7 is assembled to measure the current and voltage waveforms of the IGBT under test. The switching frequency of the system is changed using a signal generator. The time domain step response of the IGBT was recorded by a 1 Gs/second TDS2014B Tektronix Oscilloscope. The result of identification process is a n-degree state-space model for the system, where n is dependent on the best matching model to represent the system's behavior, which is given by:

$$\dot{x}(t) = A_i x(t) + B_i u(t); \qquad i = 1, 2, ..., r \tag{5-21}$$
$$y(t) = Cx(t) + Du(t)$$

where the parameters, *A, B, C* and *D* used in the state-space models estimated using Hankel matrices which are calculated by identified Markov parameters.

The summary of the utilized algorithm to determine the state-space realization of the system is as follows:

1) Least-square identification method is used to find a multi-variable transfer function:

$$G(\lambda(s)) = D_L^{-1}(\lambda) N_L(\lambda) = \sum_{k=0}^{\infty} G_k \lambda^k \tag{5-22}$$

where $D_L(\lambda), N_L(\lambda)$ denotes the polynomial matrices obtained by means of some identification method such as linear regression.

2) Solving for the transformed Markov parameters yields:

$$G_k = N_k - \sum_{j=1}^{k} D_j G_{k-j} \quad k = 0, \cdots, n \tag{5-23}$$

$$G_k = -\sum_{j=1}^{k} D_j G_{k-j} \quad k = n+1, \cdots, N \tag{5-24}$$

3) Arranging the Markov parameters in the Hankel matrix results in the following matrix:

$$G_{r,s}^{q}=\begin{bmatrix} G_{q+1} & G_{q+2} & \cdots & G_{q+s} \\ G_{q+2} & G_{q+3} & \cdots & G_{q+s+1} \\ \vdots & \vdots & \ddots & \vdots \\ G_{q+r} & G_{q+r+1} & \cdots & G_{q+r+s+1} \end{bmatrix} \tag{5-25}$$

4) Finally the system matrices will be as follows:

$$G_{r,s}^{0}=U\Sigma V^{T} \tag{5-26}$$

$$E_{y}^{T}=\begin{bmatrix} I_{p\times p} & 0_{p\times(r-1)p} \end{bmatrix} \tag{5-27}$$

$$E_{u}^{T}=\begin{bmatrix} I_{m\times m} & 0_{m\times(s-1)m} \end{bmatrix} \tag{5-28}$$

$$\Sigma_{n}=diag\{\sigma_{1},\sigma_{2},\cdots,\sigma_{n}\} \tag{5-29}$$

U_n is the matrix of first n columns of U

V_n is the matrix of first n columns of V

where the matrices U and V are calculated based on [127]. Consequently, the state-space matrices are calculated as:

$$A_{n}=\sum\nolimits_{n}^{-1/2}U_{n}^{T}G_{r,s}^{(1)}V_{n}\Sigma_{n}^{-1/2} \quad \overline{A}=\frac{1}{\tau}(A_{n}-I) \tag{5-30}$$

$$B_{n}=\sum\nolimits_{n}^{1/2}V_{n}^{T}E_{u} \quad \overline{B}=\frac{1}{\tau}B_{n} \tag{5-31}$$

$$C_{n}=E_{y}^{T}U_{n}\Sigma_{n}^{1/2} \quad \overline{C}=C_{n} \tag{5-32}$$

$$D_{n}=G_{0} \quad \overline{D}=D_{n} \tag{5-33}$$

which yields the *n*th-order state-space realization as (5-21). The main advantages of state-space models include reasonable flexibility for data that is not too complicated.

Figures 5.12, 5.13 and 5.14 show the step response of state-space model of the system in a specific switching frequency and power rating that was identified through the described algorithm. In this figure, the IGBT is operated at the switching frequency of 2, 6 and 10 kHz; the switch's Drain-Source voltage is measured and recorded. The switching transition, shown in figure 5.12, is also compared with the Hefner's model. It is noticed that

the proposed model, which is based on the circuit measurements, can present a better approximation of the actual system when it is used in a circuit. In this study the state-space model order is 8. The zero-pole plots of the system are also shown. To keep the stability of the system all the poles of the system should be placed inside the unit circle.

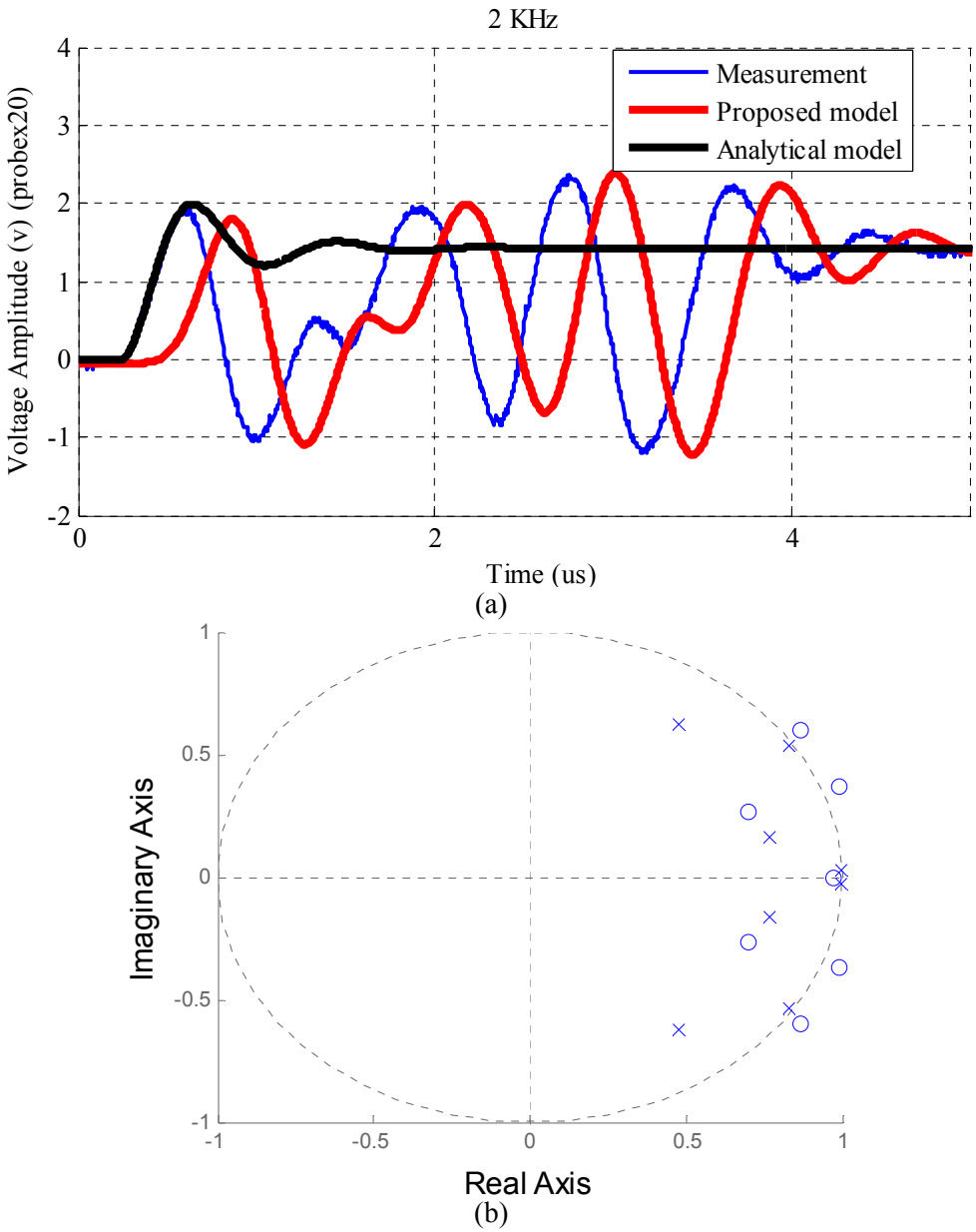

Figure 5.12 a) Estimated state-space model of the system vs. switch's measured Drain-Source voltage at 2kHz, b) Zero-pole map of the estimated state-space model of for the system

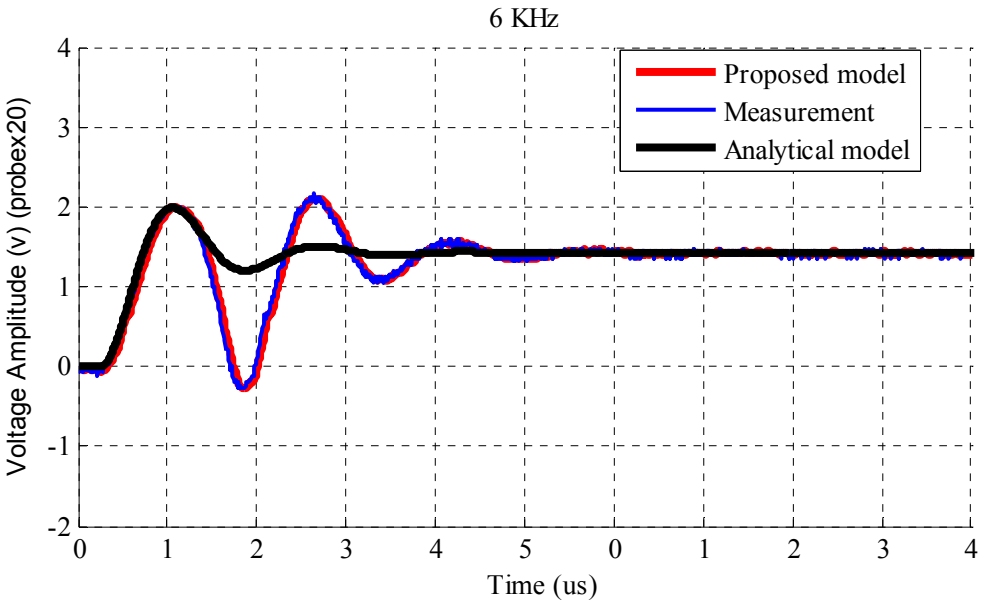

(a)

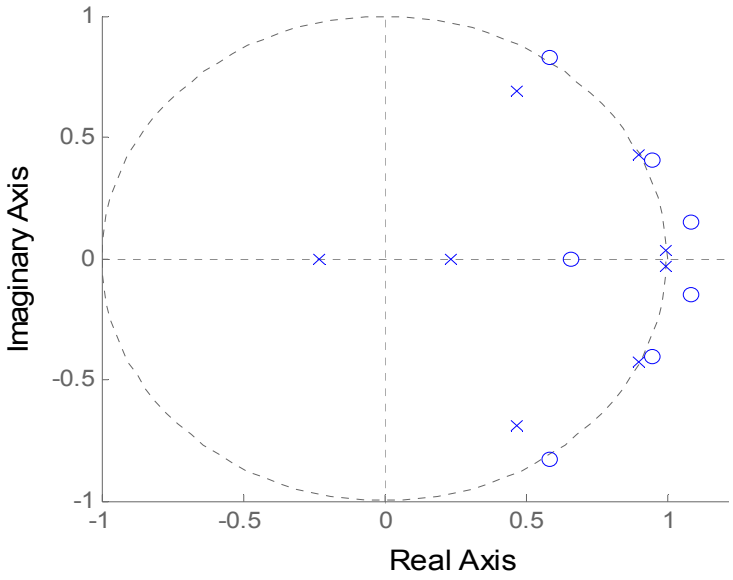

(b)

Figure 5.13 a) Estimated state-space model of the system vs. switch's measured Drain-Source voltage at 6KHz, b) Zero-pole map of the estimated state-space model of for the system

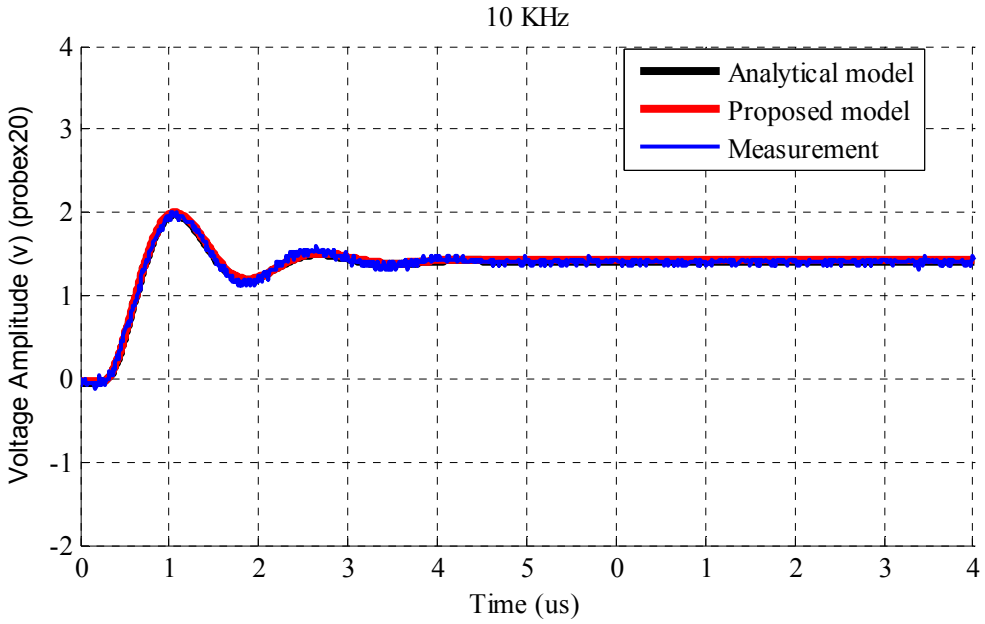

(a)

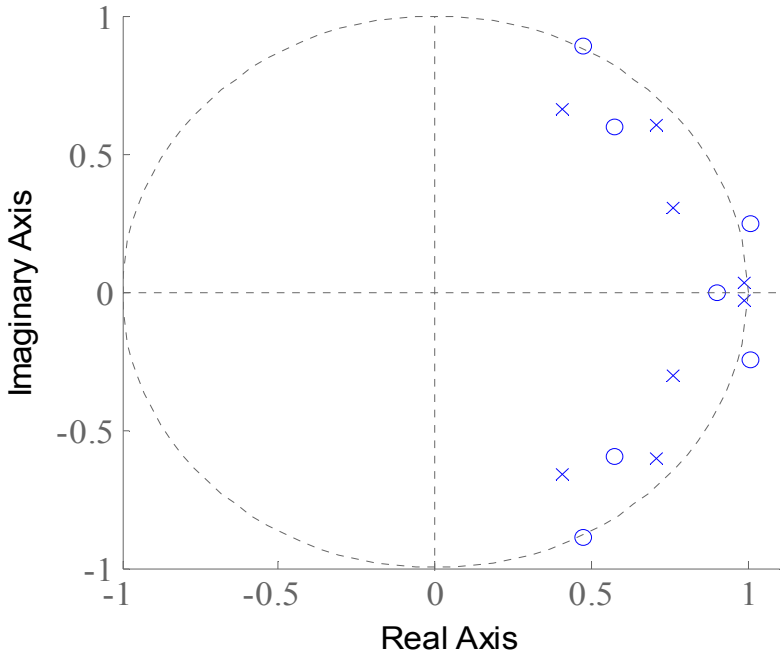

(b)

Figure 5.14 a) Estimated state-space model of the system vs. switch's measured Drain-Source voltage at 10KHz, b) Zero-pole map of the estimated state-space model of for the system

Acquiring the IGBT Functional Model

Our aim is to achieve a unit model which can predict the IGBT behavior, at the measured operating points, with the capability of interpolating the performance of the device in the range of between those points. Hence, calculated individual state-space equations for each operating points are combined together using a fuzzy weighting function as follows:

$$\begin{aligned} &\dot{x}(t) = A_i x(t) + B_i u(t); \qquad i = 1,2,...,r \\ &y(t) = Cx(t) + Du(t) \end{aligned} \tag{5-34}$$

Takagi and Sugeno method [128] was used to combine the local description of the dynamical system and presents a fuzzy model with the available IF–THEN rules where the ith rule can have the form:

$$\begin{aligned} &IF\ x_i(t)\ is\ F_1^i\ AND,...,AND\ x_n(t)\ is\ F_n^i \\ &THEN\ \dot{x} = A_i x + B_i u \end{aligned}$$

where $F_j^i\,;\, j = 1,2,...,n$, is the jth fuzzy set of the ith rule. The fuzzy model of the system was obtained using weighted averaging of local linear models:

$$\dot{x} = \sum_{i=1}^{r} \alpha_i \left(A_i + B_i u\right) \ \ where\ \ \alpha_i = \frac{w_i}{\sum_{i=1}^{r} w_i} \tag{5-35}$$

where w_i represents a membership function of the fuzzy system.

Using Gaussian membership function the fuzzy description of the whole system is described as follows:

$$Y = \sum_{i=1}^{r} G_i \times EXP\left(\frac{-\left(f - f_i\right)^2 - \left(P - P_i\right)^2}{\alpha.\sigma^2}\right) \tag{5-36}$$

where G_i stands for the system transfer function which is calculated based on:

$$G_i = C \times (S.I - A)^{-1} \times B + D \tag{5-37}$$

This equivalent model can predict the behavioral characteristics of the IGBT during the turn on and off period of the IGBT switching operation. In this circuit, the IGBT is turned on and off at a specific frequency, voltage and current rating. Figures 5.12, 5.13 and 5.14 show the voltage of the collector emitter of the IGBT at different switching frequencies, during ON and OFF time transition. In these figures, the proposed model was compared to actual measurement of the switch waveforms and the Hefner's model. It is noticed that the proposed model can give a better estimation of the IGBT switching behavior as compared to the analytical algorithm.

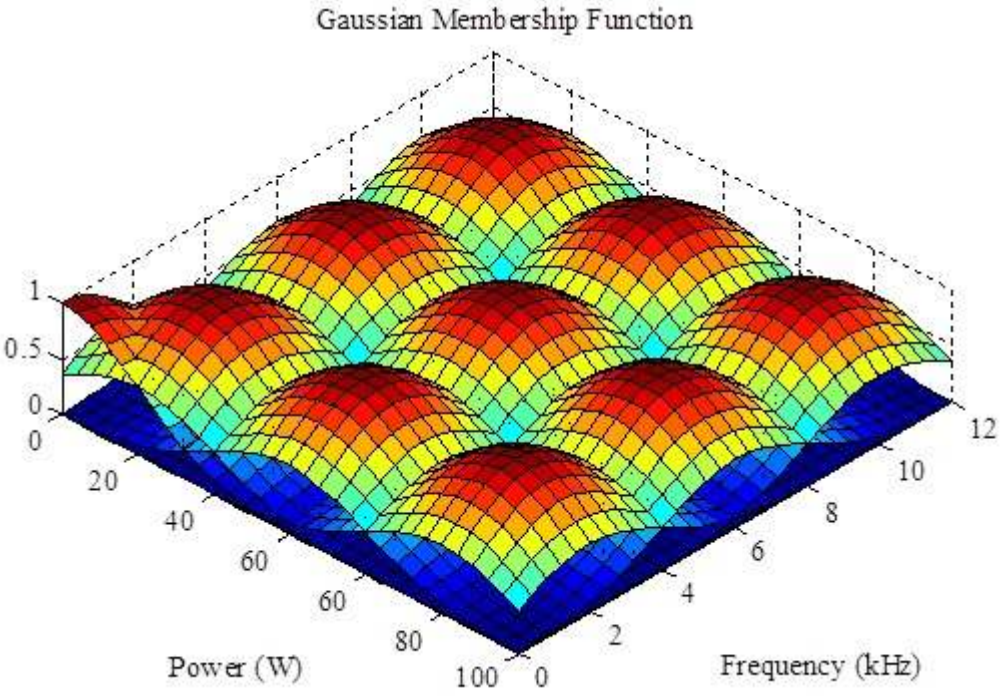

Figure 5.15 Applied fuzzy weighting function (w_i).

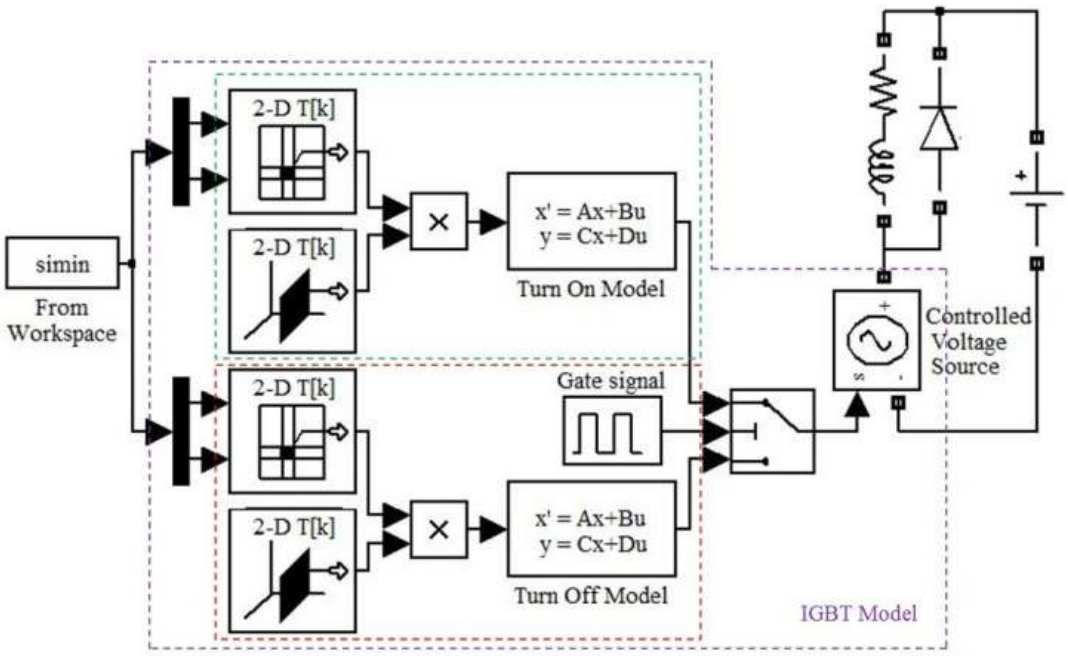

Figure 5.16 Implementation of IGBT behavioral model in Simulink.

Figure 5.16 shows the IGBT behavioral model implemented in Matlab/Simulink. In this configuration, two separate state-space model is considered for the switch, in which one is modeling the turn on transient behavior and the other one, models the turn off transition. Each model is weighted using Gaussian membership function. Consequently, all the models combines together to constitute a model that can characterize the behavior of the actual switching action in a circuit. In this model the Gate-Emitter command is considered to be a square-wave signal with constant amplitude of 15 volts.

In order to simulate the analytical model for the semiconductor switches that represent the actual device the first step is to calculate the unknown parameters. In [117], a method based on electrical measurement is introduced to calculate the IGBT parameters. The values of these parameters are given in Table 5.1.

As stated before, in this modeling approach the inner states, which are not modeled via system identification approach, are estimated using the Fuzzy modeling of the system. Therefore, the response of the system can be an average of the adjacent states.

The FFT spectrum of the proposed model and measurement data are compared in figure 5.17 and 5.18, to verify the accuracy of the proposed model in estimating the HF behavior of the device.

By examining the switching transition in different switching frequencies, more oscillations are detected at lower switching frequencies. It can be because of the parasitic elements which are resonating due to the excitation by the switching actions. At higher frequencies, higher damping which is due to higher resistance and lower inductance lead to smaller oscillations. Therefore, the error between the measured waveforms and the model are reduced.

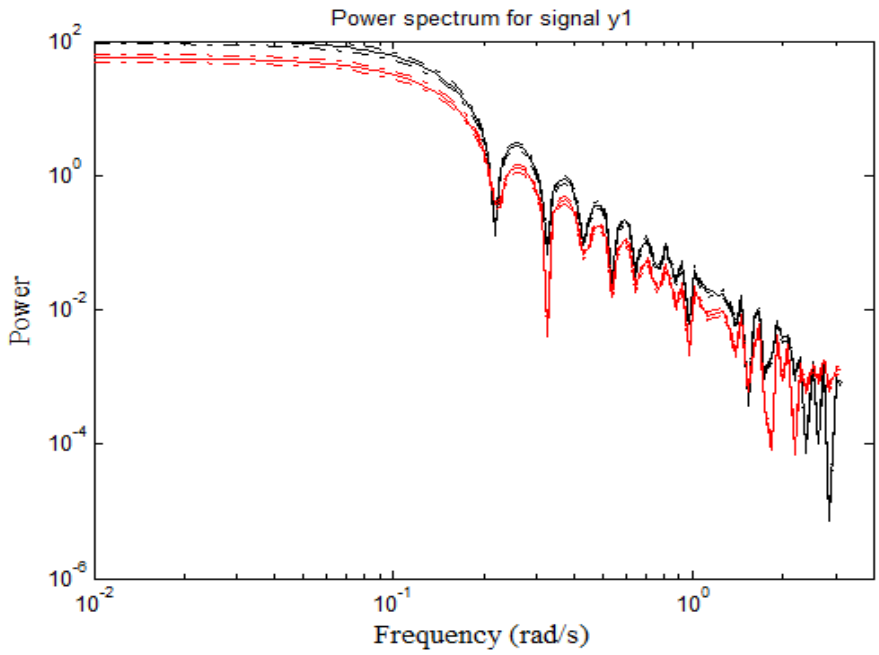

Figure 5.17 Frequency spectrum of the Drain-source voltage in the frequency of 4 kHz

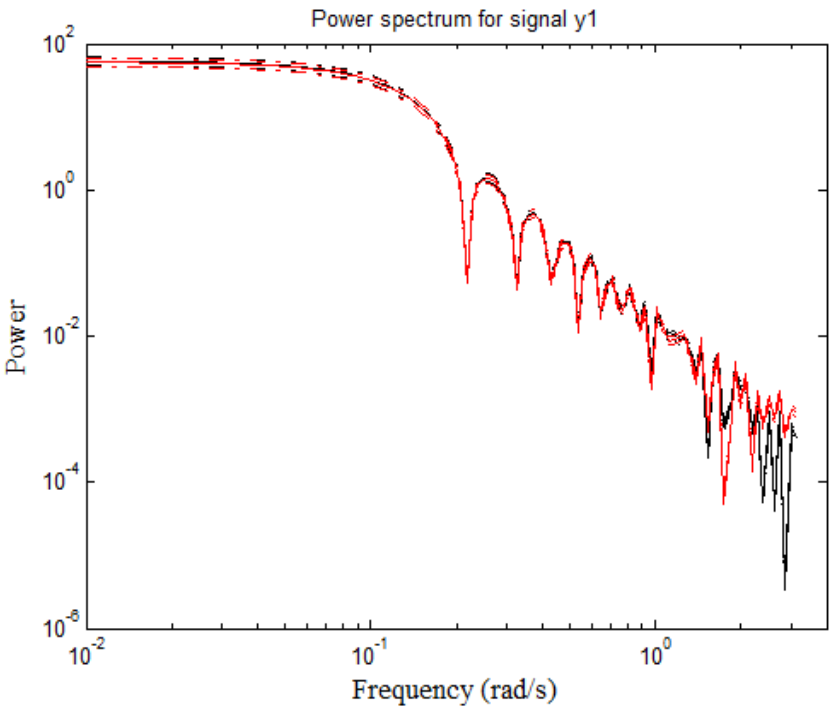

Figure 5.18 Frequency spectrum of the Drain-source voltage in the frequency of 12 kHz

Figure 5.18 shows the FFT spectrum of the converter output voltage. It is noticed that by considering the proposed model, the system accuracy in estimating the actual power system's high-frequency behavior is improved.

Dynamic Electro-Thermal Model of Power IGBT Devices

This section presents an algorithm to model the temperature dependent characteristics of SiC IGBT devices. In this method the electro-thermal behavior of the device is modeled using a numerical model. The proposed electro-thermal model is based on the Kraus IGBT electrical model coupled with the Elmore thermal model, which represents the propagation delay of the heat flux through the physical geometry of each layer. This model is used to evaluate the electro-thermal behavior and heat transfer performance of

the device package. The parameters of the model are extracted from the three-dimensional finite element (FE) for computation of the transient thermal impedance. The accuracy of the developed model is verified by comparing the obtained results with those resulting from an analytical simulation and experimental results**.**

In this part, initially, the proposed electro-thermal model of the device is described and the obtained results are compared with experimental data. The effects of temperature rise on the high frequency phenomenon during the switching actions of the device are evaluated as well as the power loss of the device. We have verified that a detailed SiC IGBT model is capable of accurately describing the static and dynamic electro-thermal performance of the device.

Principle of electro-thermal modeling of IGBT modules

In this section, the analytical electro-thermal model for the IGBT is briefly described. This model is based on the Hefner's algorithm. The proposed model can predict the IGBT behavior for both steady-state and transient cases. With the electrical model specifications of the IGBT, this model was used to construct the thermal equivalent circuit, which was used to predict the temperature rise of the IGBT in switching action.

Electrical Model

The IGBT basic structure is shown in figure 5.19. This structure consists of a Darlington pair of MOSFET and a BJT. Based on the algorithm described in [129], to model the IGBT electrical model, the BJT, which is considered as the output stage of the IGBT, is considered to operate in the active region and the MOSFET is considered to be

operating in both the linear and the saturation regions. In figure 5.19(a), the collector current I_c can be expressed as:

$$I_C = (\beta + 1) I_D \tag{5-38}$$

where I_D is the drain current of the MOSFET and β is the current gain of the BJT.

The saturation voltage of the MOSFET is determined as follows:

$$V_{DS}(sat) = V_{GE} - V_{th} \tag{5-39}$$

where V_{th} is the threshold voltage of the MOSFET.

For $V_{DS} < V_{DS}(sat)$, the MOSFET part of the IGBT operates in the linear region and for $V_{DS} > V_{DS}(sat)$, the MOSFET is in saturation mode. Therefore, (5-40) and (5-41) describe the drain current of the MOSFET in the linear and saturation region, respectively.

$$I_D = k_p \left[(V_{GE} - V_{th}) V_{DS} - \frac{V_{DS}^2}{2} \right] \tag{5-40}$$

$$I_D = k_p (V_{GE} - V_{th})^2 \tag{5-41}$$

Combining equations (5-38) and (5-40) yields:

$$I_C = (1 + \beta) k_p \left[(V_{GE} - V_{th}) V_{DS} - \frac{V_{DS}^2}{2} \right] \tag{5-42}$$

By considering the voltage drop between the emitter-base of the BJT as $V_{BE} = V_{CE} - V_{DS}$, it yields:

$$I_C = (1 + \beta) k_p \left[(V_{GE} - V_{th})(V_{CE} - V_{BE}) - \frac{(V_{CE} - V_{BE})^2}{2} \right] \tag{5-43}$$

For $V_{CE} < V_{GE} + V_{BE} - V_{th}$. Similarly, in the saturation mode, which is expressed as $V_{CE} > V_{GE} + V_{BE} - V_{th}$, the collector current is expressed as:

$$I_C = (1+\beta)k_p(V_{GE} - V_{th})^2 \tag{5-44}$$

Equations (5-43) and (5-44) describe the steady state current characteristics for an IGBT that is modeled using figure 5.19. However, this model, cannot predict the high level injection or voltage drop in the IGBT. This model can be used to predict the temperature rise in the IGBT switching action.

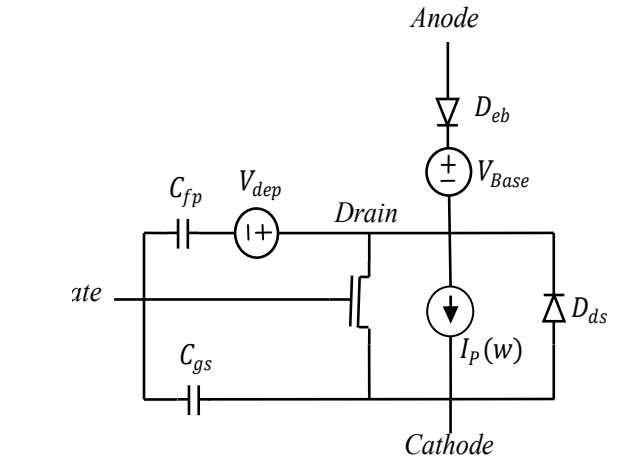

(a)

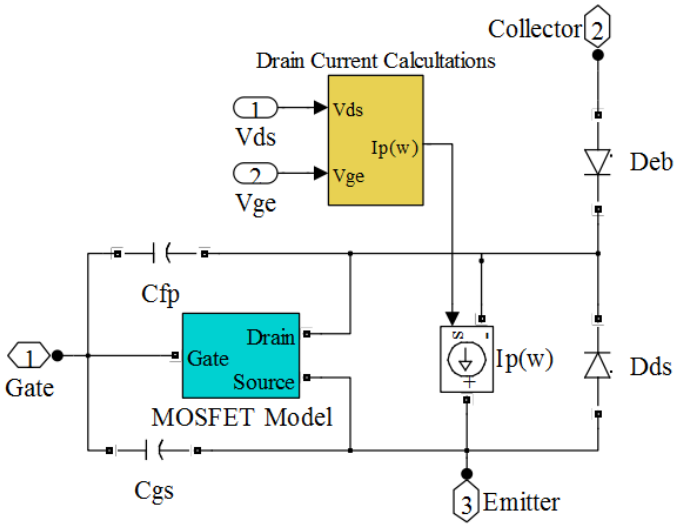

(b)

Figure 5.19 a) Darlington representation of IGBT, b) Implementation of the IGBT model in MATLAB.

Figure 5.20, shows the I-V characteristics of the SiC IGBT. The results show acceptable similarity between the simulation results and the measured data obtained from datasheet. It can be noticed that this model cannot predict the IGBT behavior at higher temperatures. This error is due to neglecting the thermal behavior of the device. In the next section, the thermal model of the IGBT is obtained. Therefore, the model was modified in a way to comply with the change in the temperature.

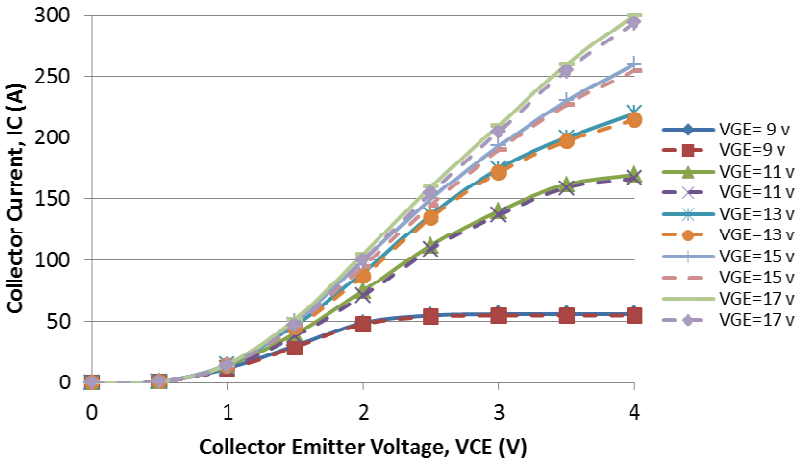

(a)

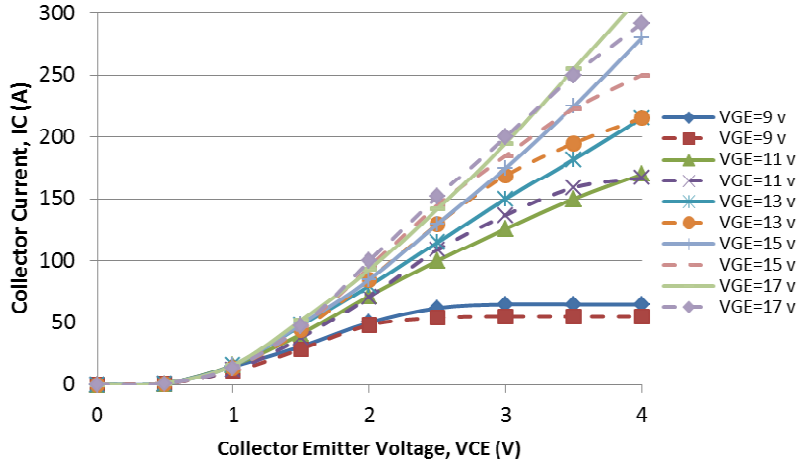

(b)

Figure 5.20 Typical output characteristic at a) 25 ℃ and b) 150 ℃

Thermal model

The geometry of the die and the substrate of the SiC IGBT device and the heat transfer path are illustrated in figure 5.21. This geometry was used to determine the thermal resistance of each layer to predict the temperature of each layer including the junction temperature. Subsequently, the model shown in figure 5.19(b) was enhanced by adding the thermal circuit.

The model demonstrated in figure 5.19 was used to determine the power loss in the SiC IGBT module. The calculated power loss was then used to indicate the temperature rise in each layer.

To obtain a dynamic electro-thermal model of device, the device model should be enhanced by adding a dynamic thermal network to the model as well as considering the device's temperature dependent parameters [118], [129]. The proposed thermal network is composed of an RC components model to extract the thermal resistances and time constants.

The parameters of this network are introduced based on the Elmore delay [130], [131], which represents the propagation delay of the heat flux through the physical geometry of each layer. To obtain the values of the RC network, a 3D-FE analysis is performed. Subsequently, the following steps are taken to obtain these values:

1) Calculation of the components of impedance temperature profile, using 3D-FEM, as follows:

$$Z_i^{th}(t) = \frac{\left(T_i(t) - T_{i+1}(t)\right)}{P_0} = R_i f_i^{th}(t) \tag{5-45}$$

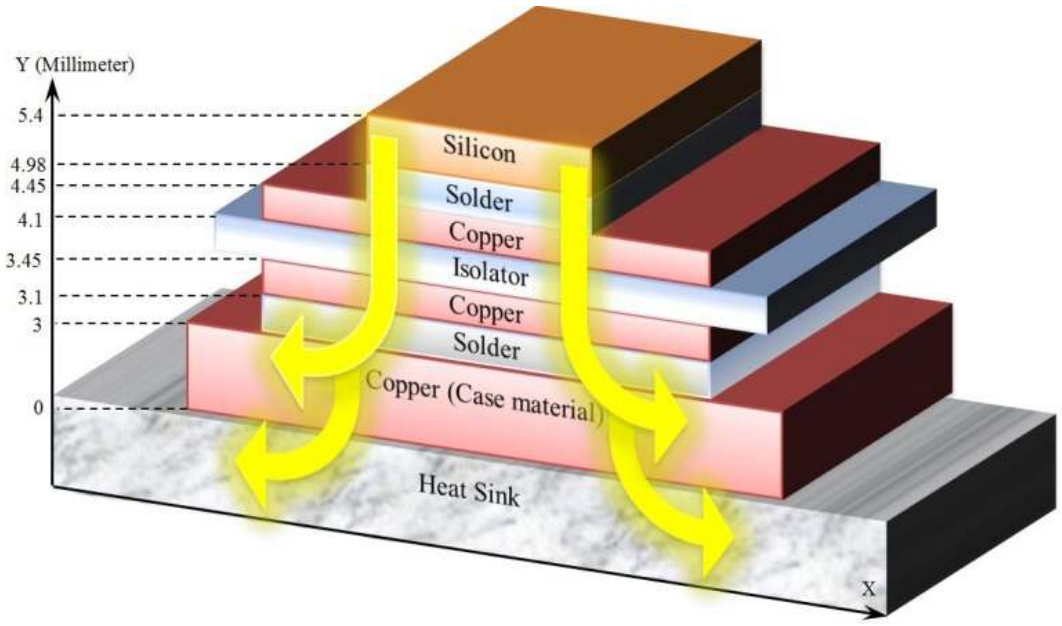

Figure 5.21 Geometry of the studied power module

2) Evaluation of dynamic response function, $f_i^{th}(t)$, to extract the propagation delay time of heat flux:

$$f_i^{th}(t) = \frac{Z_i^{th}(t)}{R_i} \tag{5-46}$$

3) The Elmore delay is introduced in $f_i^{th}(t)$, for calculating the propagation delay time, as in (5-47),

$$t_{elm,i}^{th} = \int_0^{\infty} \left[1 - f_i^{th}(t) \right] dt \tag{5-47}$$

4) Time constants of elementary components are calculated with propagation delay times, as (5-48),

$$\tau_i = t_{elm,i}^{th} - t_{elm,i-1}^{th} \tag{6-48}$$

5) Finally, The thermal capacitances of component layers were obtained, $C_i = \frac{\tau_i}{R_{i0}}$

Accordingly, the model shown in figure 5.19(b) is enhanced by adding the thermal circuit. The model demonstrated in figure 5.19 is used to determine the power loss of the SiC IGBT module (figure 5.21). The calculated power loss is then used to indicate the temperature rise in each layer. This process is shown in figure 5.23. According to the power dissipation, the temperature change can be obtained from (5-49).

$$\Delta T(t) = \int_0^t P(\tau).\frac{dZ_{th}(t-\tau)}{dt}d\tau \tag{5-49}$$

where ΔT is the temperature change, $P(t)$ is the dissipated power at the top surface of the device. The concept of equation (5-49) can be used to correlate the junction temperature rise at any instant.

Also, in the model shown in figure 5.22, to consider the effects of the temperature rise on the electrical behavior of the device, the current gain of the BJT (β) and the trans-conductance factor k_p, are assumed to be linear functions of temperature. The following equations show this function:

$$\beta = \beta_{ref}\left(1+\alpha_1(T-T_0)\right) \tag{5-50}$$

$$k_p = k_{p_{ref}}\left(1+\alpha_2(T-T_0)\right) \tag{5-51}$$

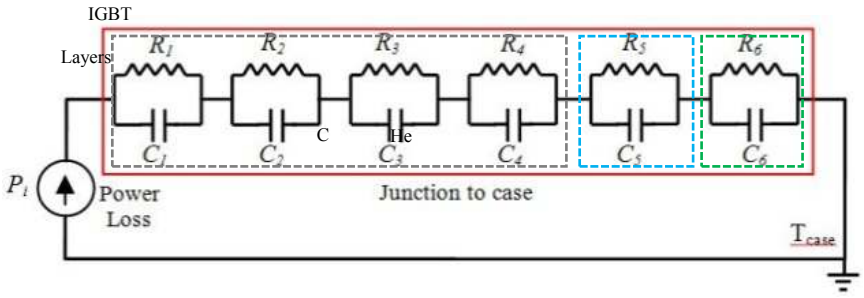

Figure 5.22 Equivalent diagram of the thermal impedance between junction and case layer.

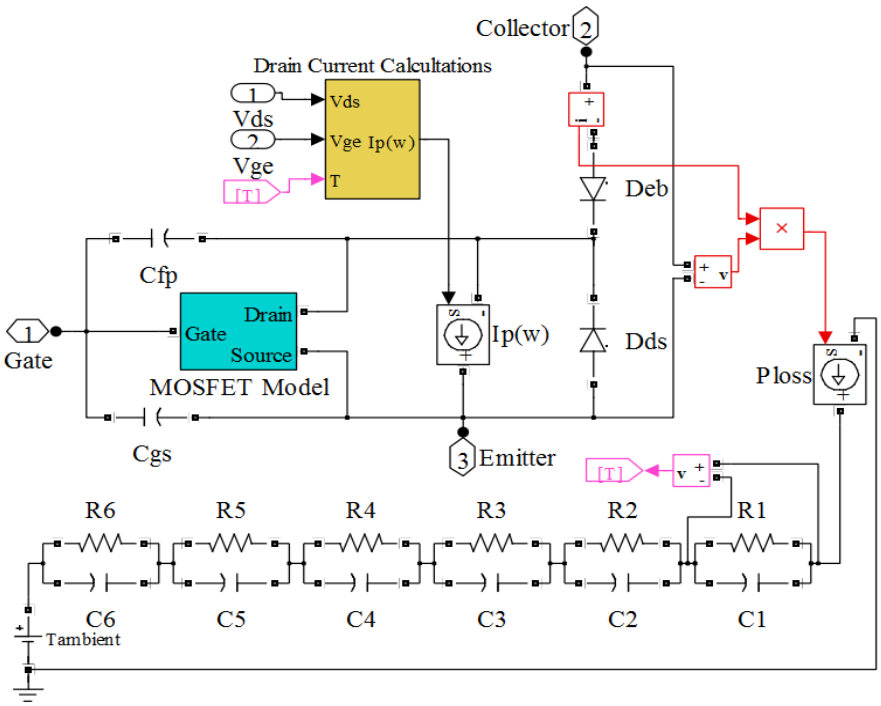

Figure 5.23 IGBT electro-thermal model in Matlab.

Also, the SiC thermal conductivity is given by:

$$K(T) = K_0 \left(\frac{300}{T} \right)^{4/3} \tag{5-52}$$

Table 5.3 shows the parameter values used in the calculation of the thermal impedance for each layer. Table 5.4 shows the thermal impedance of different layers in the structure of the device module. Following the evaluation of all of the thermal parameters and designing the thermal circuit, the temperature must be derived from the equations mentioned above. Figure 5.23 shows the IGBT electro-thermal model implemented as implemented in Simulink/Matlab. This model can estimate and include the thermal effect on the electrical behavior of the IGBT.

The single chip model is simple and can predict an accurate junction temperature for a single chip. In the next section, the finite element method was utilized to verify the accuracy of the proposed model in the prediction of the temperature at different layers. Figure 5.24 shows the output characteristic waveform of the device under study when the thermal effect was considered.

Table 5.3 Device module material propoerties

material	Silicon	Solder	Copper	Isolator
Thermal conductivity	1.7×10^{6}	1.3×10^{6}	3.5×10^{6}	2.3×10^{6}
Thermal resistance	140	35	350	100

Table 5.4 Thermal Impedance of SiC IGBT

Segment	1	2	3	4	5	6
R_{dik}	0.07559	0.09061	0.01039	0.00341	0.01039	0.01039
τ_{ik}	0.06499	0.02601	0.002364	1.187e-5	0.06499	0.06499

Three-dimensional FE analysis

To verify the validity of the proposed model in the previous section, a 3D FE analysis was used to observe the thermal behavior of an IGBT module. The module structure is shown in figure 5.21 and it is coupled to a circuit model, which is operating as a single phase boost converter to supply an RL loads. The structure of the IGBT module and its corresponding mesh in the FE software is shown in figure 5.25. This model does not include the details of the heat-sink fins which act as an effective heat transfer coefficients on the base plate of the heat-sink [131].

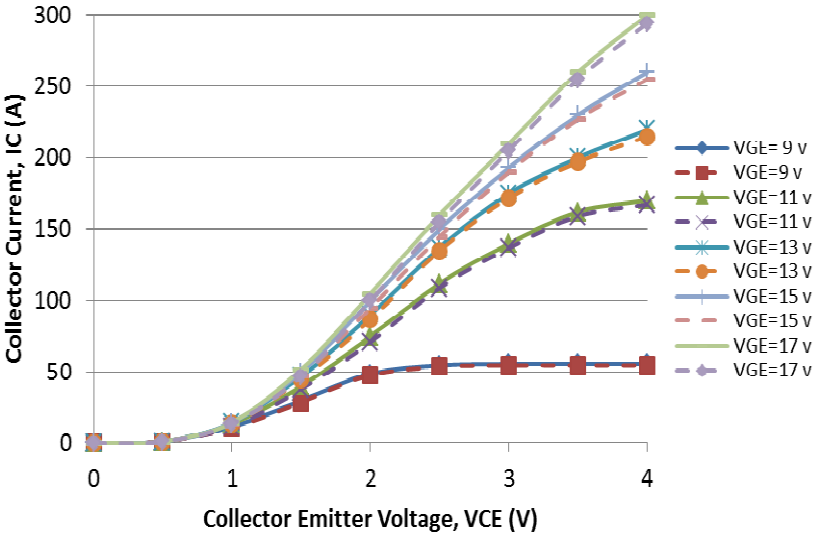

(a)

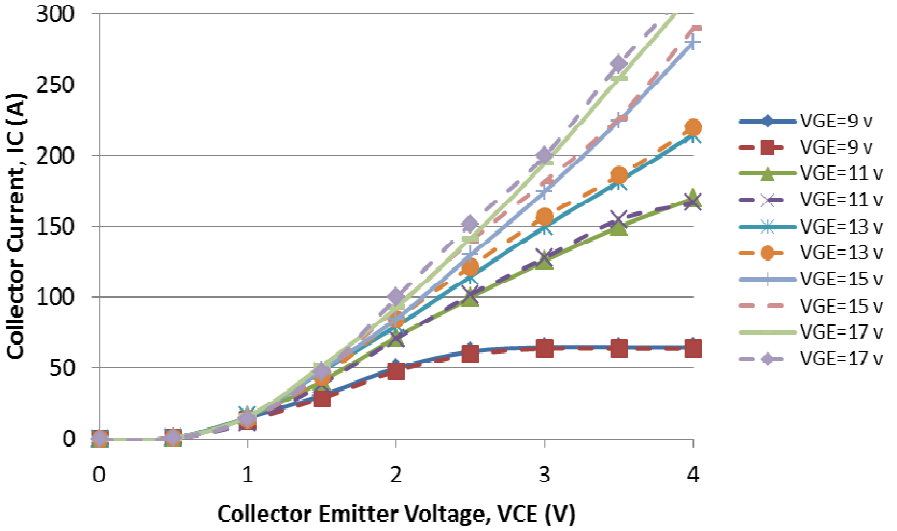

(b)

Figure 5.24 Output characteristic at a) 25 ℃ and b) 150 ℃

The measured I-V characteristic of the SiC IGBT module versus temperature is given in the manufacturer datasheet. These Data reveals a very good comparison between the results. This confirms the validity of the 3D model. The results obtained from the proposed model were compared with the results obtained by the FE analysis and the results verify the accuracy of the network model.

Figure 5.26 shows the FE algorithm procedure to indicate the temperature rise of the device in switching action. In the proposed method, this figure shows the total amount of power loss which is calculated by the following equation:

$$E_T = \frac{1}{T}\int_0^T P_T(t).dt \tag{5-53}$$

The rising temperature in the device during operation is determined by three factors; device characteristics (on-resistance, switching losses), load behavior (current) and thermal impedance of the device. These factors define an equilibrium condition between power losses and the dissipated heat. The load behavior can be modeled independently from the device characteristics. A 3D steady-state thermal behavior of the structure, shown in figure 5.25, was evaluated using FEM to solve the heat flow equation. This model is quite representative of a real power device. Hence, the heat is dissipated at the junction surface (equivalent to small region with dimensions 0.2 × 0.2 mm^2 in the semiconductor layer) as shown in figures 5.21 and 5.25. The thermal properties of the materials in the simulation are listed in Table 5.5. The finite element tool was used next to solve the following partial differential equation in each region:

$$\rho C_p \frac{\partial T}{\partial t} + \nabla.(-k\nabla T) = Q + q_s T \tag{5-54}$$

where:

k: Thermal conductivity (W/m.K)

ρ: Density (kg/m^3)

C_p: Heat capacity at constant pressure (j/Kg.K)

q_s: Absorption/Production coefficient ($W/m^3.K$)

Q: Heat source (W/m^3)

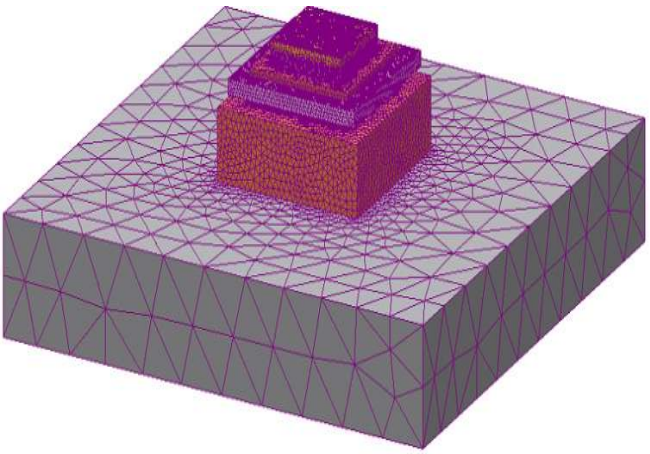

(a)

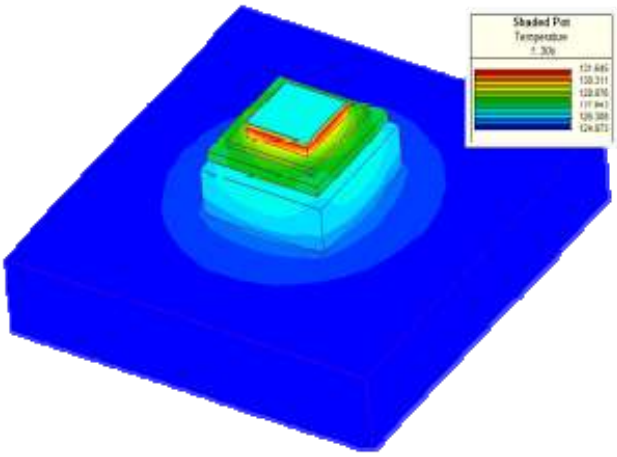

(b)

Figure 5.25 FE model of the SiC IGBT.

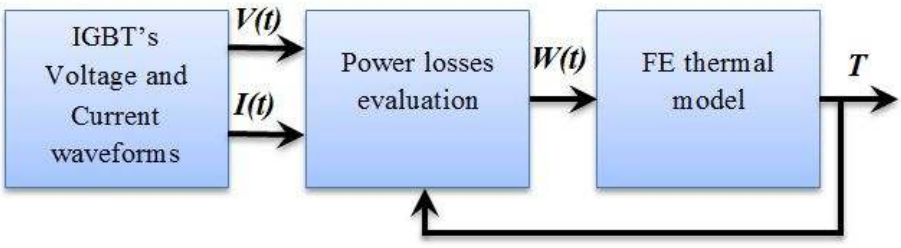

Figure 5.26 Block diagram of the FE analysis.

In the next section, the results of the FE electro-thermal model and the measurement were compared. The comparison shows the effectiveness of the performed method.

Table 5.5 Characteristics of materials used in module construction

IGBT material	Density (g/cm^3)	Specific heat (j/Kg.C)	Thermal conductivity (W/m.K)
Solder	1.85	15	1300
Copper	8.9	385	180
Silicon	2.33	700	148
Isolation	4.7	837	0.16

Figure 5.27 shows the circuit diagram of the boost converter, studied in this work, to evaluate the characteristics of SiC power module.

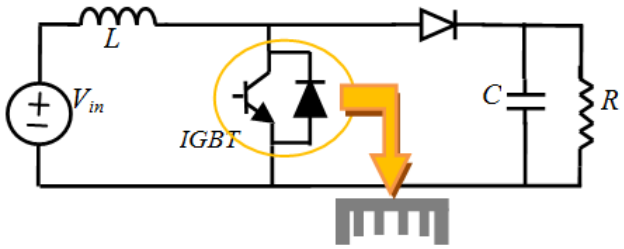

Figure 5.27 Circuit diagram of boost converter

The current from the voltage source V flows into freewheeling inductor L and store the energy for the on period of the IGBT. Also, the current flowing through the IGBT commutates to the load R though the freewheeling diode, when the IGBT turns off. The output voltage becomes higher than the input voltage with superposing the voltage across the inductor. The capacitor C, which is connected parallel to the load R, works as a filter

capacitor. The SiC IGBT was used as the switching device in the circuit while the freewheeling diode was a Si PN diode.

In this circuit, the current passing through the IGBT was changing with the changes in the load value. The case temperature of the switch was then measured and the results were compared to the results obtained from the FE approach and the analytical electro-thermal model. In this study, the switching frequency of the converter was a fixed value. Therefore, the effects of increasing the switching frequency on the thermal behavior of the device were not considered.

Figure 5.28 show a comparison of the case temperature of the IGBT obtained from the analytical electro-thermal model, FE thermal model and measurement. The results show an acceptable accuracy in predicting the temperature of the SiC switch. Note that the proposed model was only for determining the device temperature at steady-state.

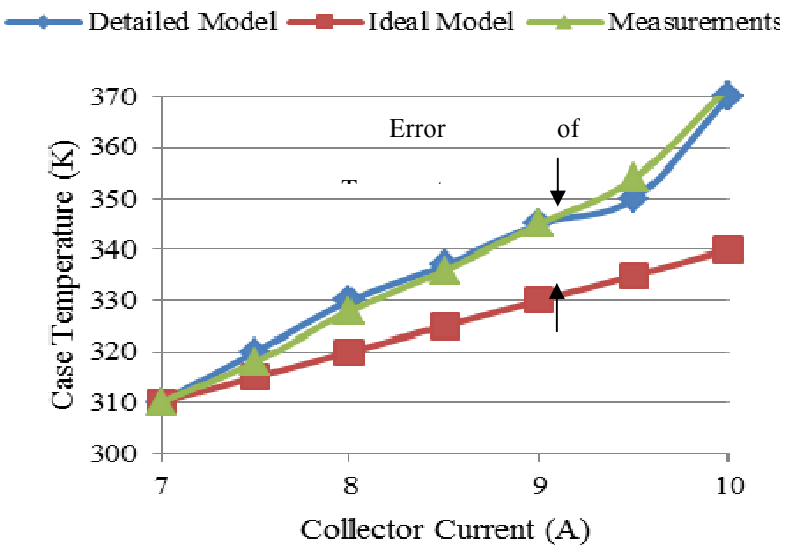

Figure 5.28 Comparison of the IGBT temperature in Si IGBT and SiC IGBT in switching state.

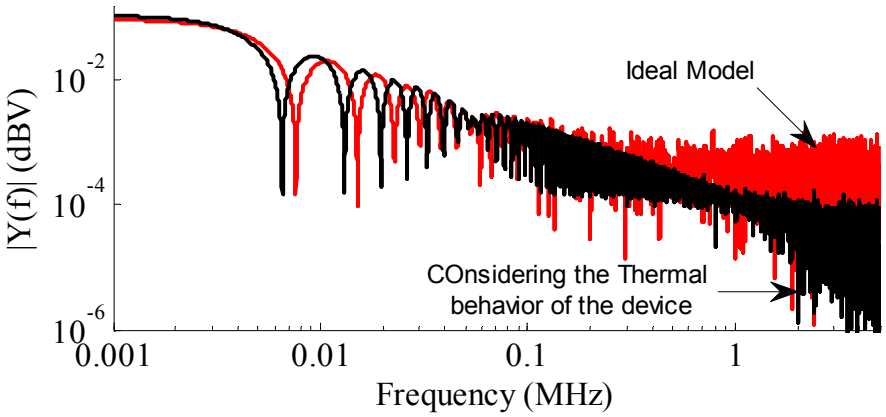

Figure 5.29 Comparing the switching harmonics when the thermal behavior is considered and when it is not considered.

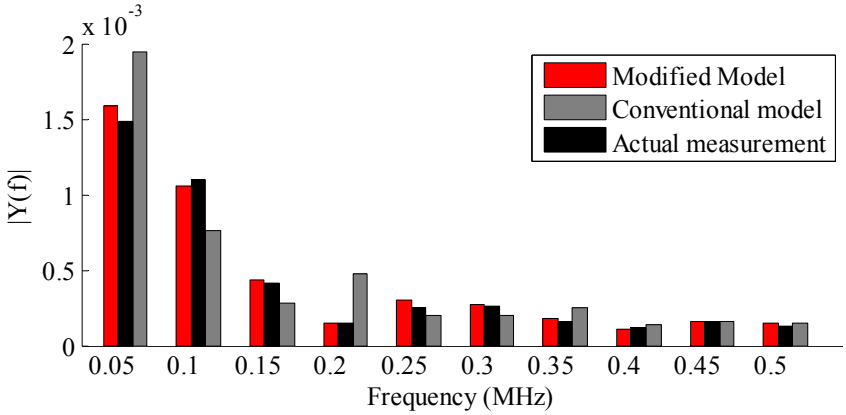

Figure 5.30 Comparison of the harmonic order in two modeling approach vs. measurement.

Also, Figure 5.29 shows a comparison of device switching harmonic between the proposed electro-thermal model and ideal model. It is observed that, the electro-thermal model of the IGBT provides a more accurate estimation of the harmonics during the switching action.

The harmonic diagram shown in Figure 5.30, confirms the higher accuracy in the proposed approach, to model the high frequency behavior in switching action.

Modeling the Power Diodes

A physics-based high-frequency (HF) model of a three-phase Diode bridge rectification system including is presented. The Diode model includes the HF stray components superimposed on the well-known Kraus's power diode model. The HF components were calculated using a three-dimensional quasi-static finite element (3D FE) analysis. The proposed complex model of the Diode was verified both numerically and experimentally. The computed Diode model was used in a low-high frequency model of cascaded power converters system and the high frequency oscillation and the frequency spectrum were experimentally verified showing excellent results.

For the design and analysis of power electronic circuits, circuit simulator programs become more and more important in order to study and predict the behavior of traditional or new proposed circuits. When the simulation study is devoted to know the EMI/EMC performance in the circuit as well as other high-frequency phenomenon, ideal model of devices are not sufficient and must be replaced by suitable models of the devices accounting for the actual behavior during its operation.

Power diodes are one of the most widely used components in power converter's circuit. Many studies have been oriented on developing diode models for different simulator packages [132]-[138]. Among them, the Diode model developed by Kraus is one of the most used in several commercial circuit simulation programs. These models although useful but many details in the models are neglected. In order to consider all those details, complete information about the geometry and physical parameters of the device is needed.

A famous approach to model the power diodes is based on the Kraus Model [139], [140]. In this method a basic structure of the Kraus model was used to model the power diodes. The two former methods are a step forward to achieve a model to describe the HF behavior of the power converters. However, these methods overlook some parasitic braches which exist in the power conversion system's layout and can provide a conductive path for the flow of HF current.

The main objective of this paper is to propose a method to model the power diodes based on the FE computational electromagnetic. In order to verify the accuracy of our proposed model, the obtained model is compared to the existing diodes. Kraus model and other related algorithms are all based on the switch parameters, which most of them are not provided in the datasheets of the product.

Physics-based modeling of the switching power converters

This section focuses on modeling the power diode with magnetic dependent features. In [140], a method based on the semiconductor device physical characteristics measurement was introduced, which demonstrate a good accuracy in predicting the transient's behavior of the device. This model also provides the noise source for excitation of system parasitic so that later can be used to predict the EMC/EMI problems in the power converters.

The model used in this study, utilized the device model which is defined in [140] and enhance the model accuracy by considering the parasitic components, which are ignored in these previous models. In this study, the object's structure and geometry was modeled using FEA to evaluate their electromagnetic characteristics. The proposed modeling method is based on coupling the analytical model of the Diode with FEM.

Diode analytical model:

In this part, the physics-based model for the model is described. The proposed model for diode is composed of the analytical model combined with the circuit model derived from FEM.

The analytical model used to model the diode is based on dynamic-charge model. The dynamic charge model realizes the dynamic nature of the charge distribution in the base region. The charge distribution in the lightly-doped base (drift) region depends not only on the instantaneous values of diode voltage and current, but also on the previous state of the diode. Several diode models based on this concept have been reported in [132-140]. In this paper, the model developed by Tseng [138] is adopted and implemented in Simulink.

Figure 5.31 shows the basic representation of the power diode model. Five components are employed, including the PN junction current I_D, junction capacitance C_j, dynamic stored charge current I_Q, leakage current I_{RB} and base-region conductivity modulation, described by the voltage V_B.

Figure 5.32 shows the content of the diode block in Simulink. The input is anode current I_A and the output is voltage V_{AK}, as the diode is considered to be a current controlled voltage source. There are two states in the model described by integrators: the base charge Q_T and the voltage across the junction capacitance V_J. A potential algebraic loop is in the interaction of I_A and V_{AK} with the whole circuit, which is eliminated by adding a stray inductance and resistance in series with the diode.

The model shown in figure 5.31 is based on the Kraus analytical model that can describe the steady-state and transient condition during the diode conducting mode of

operation. But, this model ignores most of the parasitic elements that exist in the diode layer's structure. These parasitic elements have significant impact on the propagation of noise in the circuit. To compensate this limitation, the effects of the parasitic elements should be considered. The model proposed in this paper, incorporate the model shown in figure 5.31. Subsequently, this model is expanded by adding the parasitic components that exist in the structure of the diode including the stray and mutual impedances in or between the anode and cathode terminals of the device.

The parameters and function blocks shown in figure 5.31 were implemented in Matlab/Simulink using the equations introduced in [139] and [140]. To model the diode's interlayer impedances, FE analysis is used. Next subsection explains the procedure which is followed to estimate the value of these impedances.

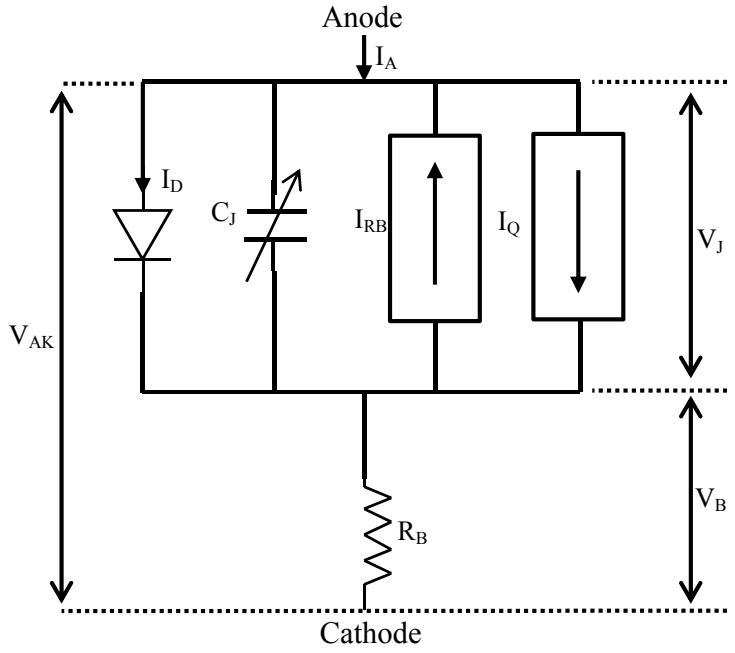

Figure 5.31 Basic representation of Dynamic charge model for diode

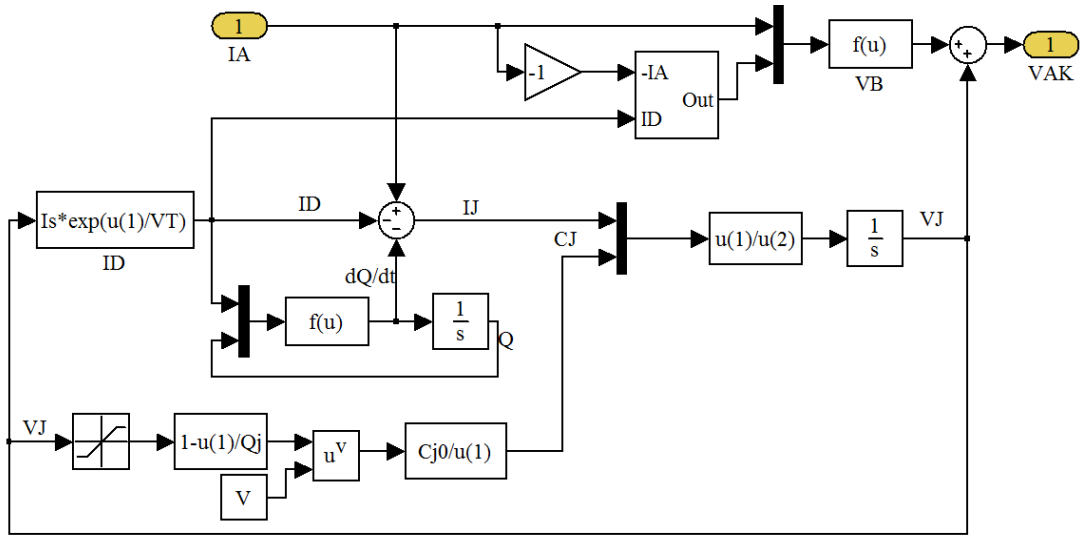

Figure 5.32 Simulink implementation of the dynamic charge model.

In the system shown in figure 5.32, the diffused current across the pn junction is calculated as follows:

$$I_D = I_S\left[\exp\left(\frac{qV_j}{kT}\right)-1\right] \tag{5-55}$$

And the junction capacitance is calculated as follows:

$$C_j = \frac{C_{j0}}{\left[1-\frac{V_j}{\varphi}\right]^v} \tag{5-56}$$

In this figure, dynamic stored charge is calculated as:

$$Q = \tau_t\left(I_D - f_s\frac{dQ}{dt}\right) \tag{5-57}$$

The avalanche breakdown is calculated as:

$$I_{RB} = I_{RBK}\exp\left[-\frac{q(V_j+V_{RB})}{\eta_{RB}KT}\right] \tag{5-58}$$

The parameter τ_t is the transit time which determines the amount of reverse recovery charge. A new parameter f_s is the softness factor which determines the reverse recovery to be hard or soft.

In the system shown in figure 5.32, the base voltage drop is calculated as follows:

$$V_B = R_B I_A = I_A \frac{2d}{qA}\left(\frac{1}{\mu_n\left(N_B + \overline{n}(t)\right) + \mu_p \overline{p}(t)}\right) \tag{5-59}$$

where the spatial average carrier concentrations *n(t)* and *p(t)* are given by:

$$\overline{n}(t) = \overline{p}(t) = \frac{Q(t)}{2dqA} \tag{5-60}$$

The total dynamic charge can be expressed as:

$$Q(t) = \tau \frac{I_D^2}{|I_A|} \tag{5-61}$$

where the absolute value of I_A is used to maintain a non-negative total stored charge in the CSR under all circumstances. Combining (5-59)-(5-61), the V_B can be expressed as:

$$V_B = \frac{I_A |I_A|}{\frac{|I_A|}{R_0} + \frac{I'^2_D}{\varphi}} \tag{5-62}$$

where R_0 and φ are given by:

$$R_0 = \frac{2d}{Aq\mu_n N_B} \tag{5-63}$$

$$\varphi = \frac{(2d)^2}{\tau(\mu_n + \mu_p)} \tag{5-64}$$

In (5-61), $-I_A$ replace I_D the second stage of reverse recovery when I_D approaches zero to maintain conductivity modulation in the CSR, as some stored charge is still left in the center of the base. This maintains a small V_B during reverse recovery and in the on-state, but still allows a large V_B during forward recovery.

$$I'_D = \begin{cases} I_D & if \quad I_D > -I_A \\ -I_A & if \quad I_D < -I_A \end{cases} \tag{5-65}$$

Table 5.6, describes the complete parameter sets, which are used in the diode model.

Table 5.6 Sequence of parameters used in the diode model

Static measurement		Dynamic measurement	
Symbol	Value	Symbol	Value
C_{j0}	4.04e-15 F	μ_p	600 cm^2/V.s
A	0.01 cm^2	q	1.602e-19
N_B	1e17 1/cm^3	V_j	1.41
τ	1e-6 s	k	1.38e-23
d	1e-2 cm	T	300 K
μ_n	1500 cm^2/V.s		

Modeling the parasitic components

To obtain the Physics-based model, the geometry of the actual diode is modeled by finite elements. A 3D quasi-static FE analysis was performed to obtain parasitic resistances and inductances of different layers in the semiconductor structure. In FE method, one approach to calculate the inductance, capacitance and resistive matrices is through calculating the energy matrix in the FE model.

Figure 5.33(a) shows a diode cell model in its FE mesh. This model consists of several layers attached together to produce a *pn* diode cell. In this structure, the silicon nitride (Si_3N_4) layer is deposited over the wafer surface. After doping the active region of the diode to form the *pn*-junction, the aluminum sheet is deposited over the entire wafer surface. Other layers arrangements are shown in figure 5.33(a) include the substrate, n and p channels. The structure and layout of the system shown in figure 5.33, is explained in [141].

To achieve the circuit model of each unit cells, the magnetostatic and electrostatic analysis were separately performed on the diode model. In the magnetostatic analysis, to obtain the inductance and resistance values, one current direction were defined within the

diode model [139]. The current directions were defined in the form of coils in the contacts of the diode's *pn* junction. The current directions are defined in figure 5.33(b). For further illustration, in this figure the diode layer's structure are depicted in 2D format. The direction of these currents was defined as follows: When the voltage on the diode exceeds the threshold voltage, minority carriers are injected from the p+ region into the n region.

Therefore, a conductive path between the p and n regions is created which can be considered in modeling the parasitic components of the device. The diode unit cells are shown in figure 5.34(b), in this figure C_d stand for diffusion capacitance and Cgeom stand for the geometric capacitance. This geometry also includes the intrinsic diode conductance G_d, the series resistance R_S (Comprised of the contact resistances and resistance in the neutral regions of the semiconductor) as well as a parasitic inductance L_S.

The electromagnetic field inside this device is governed by the following nonlinear partial differential equations:

$$\nabla\times\left(\mu_0^{-1}\nabla\times A-M\right)-\sigma\upsilon\times\left(\nabla\times A\right)+\sigma\nabla V=J^e \tag{5-66}$$

where A is magnetic vector potential , J^e is external current density, M is magnetization, V is the electric scalar potential, σ is the electric conductivity and $\boldsymbol{\upsilon}$ is the motion speed which in this case, it is equal to zero. Note that, the magnetization curve was considered in several points in the hysteresis curve.

Also, the electrostatic problem is solved for the calculation of capacitances matrix as capacitances are a function of geometry. The analysis determines the electric scalar potential distribution caused by the applied voltage.

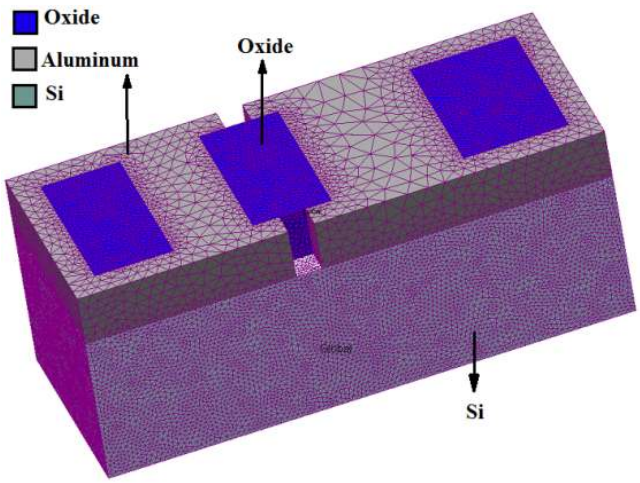

(a)

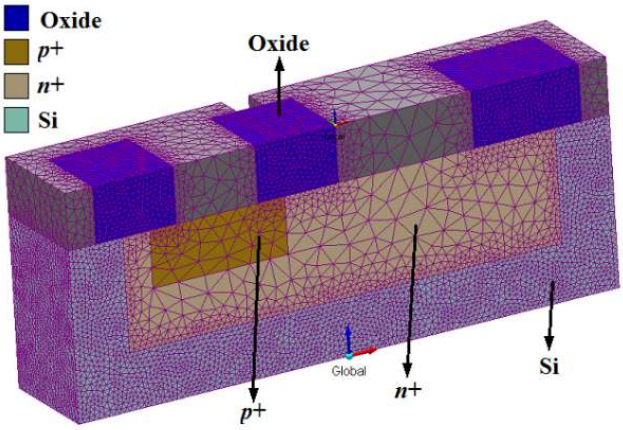

(b)

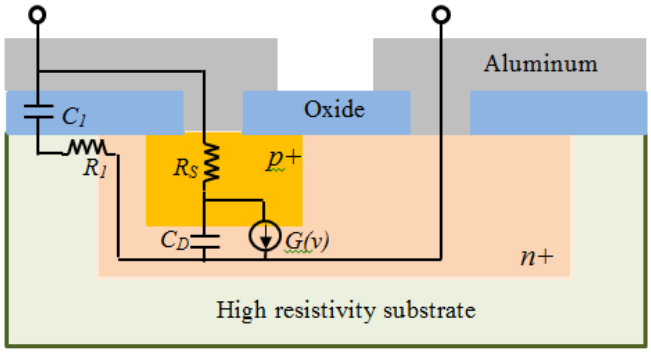

(c)

Figure 5.33 IGBT cell model, (a) 3D FEM model, (b) cutting edge of the diode structure, (b) 2D model for illustration of the current direction in the IGBT structure.

The following set of equations was solved during the electrostatic analysis:

$$E = -\frac{\partial A}{\partial t} - \nabla V = -\frac{\partial\left(\widetilde{A} - \nabla\psi\right)}{\partial t} - \nabla\left(\widetilde{V} + \frac{\partial\psi}{\partial t}\right) = -\frac{\partial\widetilde{A}}{\partial t} - \nabla\widetilde{V} \tag{5-67}$$

$$\widetilde{A} = A + \nabla\psi \tag{5-68}$$

$$\widetilde{V} = V - \frac{\partial\psi}{\partial t} \tag{5-69}$$

where ψ is magnetic flux and V is electric scalar potential.

As stated above, the parameter calculation is based on the magnetostatic and electrostatic fields. In addition to considering all electric and magnetic fields in (5-66) and (5-67), deviation of electric and magnetic fields versus time was also considered. This assumption is crucial for parameter estimation in the frequency response analysis (FRA). Since inductances and resistances change at higher frequencies, the deviation of fields should be considered for accurate results.

The power diode was created by paralleling several of those unit cells (figure 5.34(a, b)). Figure 5.34(a) shows the layout of the diode cells, paralleled together on the silicon wafer. Therefore, to obtain the power diode model, the model of each of the unit cells must be connected together, as shown in figure 5.34(b). Consequently, an electric network was obtained which can characterize the diode high-frequency behavior (Figure 5.34(c)).

Following the solution of the FE model, the inductance, capacitance and resistive matrices are obtained via calculating the energy matrix in the FE model. The magnetic energy is calculated as:

$$W = \frac{1}{2}\iiint_V \mu.Re\left(H_1.H_1^*\right)dv + \frac{1}{2}\iiint_V \mu.Re\left(H_2.H_2^*\right)dv + \frac{1}{2}\iiint_V \mu.Re\left(H_1.H_2^*\right)dv \tag{5-70}$$

where $\boldsymbol{H}_i, i = 1,2$ is the magnetic field intensity inside the model and μ is the permeability of the model.

After calculating the magnetic energy inside the FE model, using equation (5-70), all self and mutual inductances are estimated based on magnetic energy value as:

$$L_{ij} = \frac{1}{I^2} \iiint_V \mu_0 . Re\left(H_i . H_j^*\right) dv \tag{5-71}$$

The electrostatic energy was used to obtain the capacitance matrix of the model. The electrostatic is calculated by:

$$W = \frac{1}{2} \iiint_V \varepsilon . Re\left(D_1 . E_1\right) dv + \frac{1}{2} \iiint_V \varepsilon . Re\left(D_2 . E_2\right) dv + \frac{1}{2} \iiint_V \varepsilon . Re\left(D_1 . E_2\right) dv \tag{5-72}$$

where $\boldsymbol{D}_i$ is the electric displacement and $\boldsymbol{E}_i$ is the electric field inside the model. Self and mutual capacitances are calculated based on electrostatic energy value as (5-73).

$$C_{ij} = \frac{1}{V^2} \iiint_V \varepsilon_0 . Re\left(D_i . E_j\right) dv \tag{5-73}$$

The resistance matrix inside the model is calculated based on the current density in the model conductors as (5-74). The resistance between different the layers of the model is calculated by (5-75).

$$P = \iiint_V \frac{Re\left(J_1 . J_1^*\right)}{\sigma} dv + \iiint_V \frac{Re\left(J_2 . J_2^*\right)}{\sigma} dv + 2 \iiint_V \frac{Re\left(J_1 . J_2^*\right)}{\sigma} dv \tag{5-74}$$

$$R_{ij} = \frac{1}{I^2} \iiint_V \frac{Re\left(J_i . J_j^*\right)}{\sigma} dv \tag{5-75}$$

where $\boldsymbol{J}_i$ is the current density and σ shows the electric conductivity.

Figure 5.34(b) shows the electric circuit obtained from the FE model, for a single unit diode cell. In this model, all the resistors and inductors represent built-in resistances and parasitic inductances of a diode module. The diode cell within the diode module, shown

in figure 5.34(a), has the width of 36 μm. Therefore, in a device with a width of 560x4 μm, it is considered that 62 of these unit cells are in parallel (see figure 5.34(b)).

The Kraus model, shown in figure 5.31, was utilized as a block in the diode model illustrated in figure 5.34(c). This model is composed of parasitic elements, which are calculated using FEM and Kraus's analytical model. This model has the capability to represent the diode dynamic and static behaviors.

The model for the analysis of the diode in FEM contained $3.2x10^5$ degrees of freedom and $1x10^{-3}$ percent tolerance of energy. The analysis method used here is GMRES, which was used to solve nonsymmetrical systems. Since the geometry of the elements are non-uniform, geometric multi-grid method was chosen as the pre-conditioner and F-cycle as multi-grid cycle. To verify the accuracy of the diode model, a test setup, as shown in figure 5.35 was assembled. In this test, the diode was operated under different voltage and current ratings. Subsequently, the voltage waveforms were recorded to compare the high-frequency behavior of the proposed diode model with the measurement.

Figures 5.36, 5.37 and 5.38 show the results of this comparison. As it is shown in these figures, the proposed method can estimate the high frequency oscillations of the power device as well as its low frequency behavior. Figure 5.36 is illustrating the diode I-V characteristics. In this figure, the simulation results are compares with experiments. The little error is due to the measurement tools and can be compensated easily in simulation. Figure 5.37 is showing the diode's anode-cathode voltage and current in time domain. Figure 5.38 is showing the frequency spectrum of the diode current, it can be seen that the high-frequency behavior of the diode is well represented by its corresponding physics-based model.

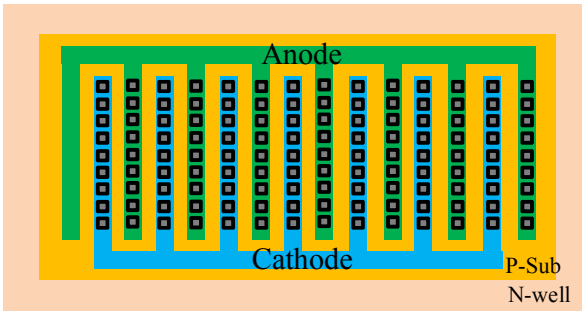

(a)

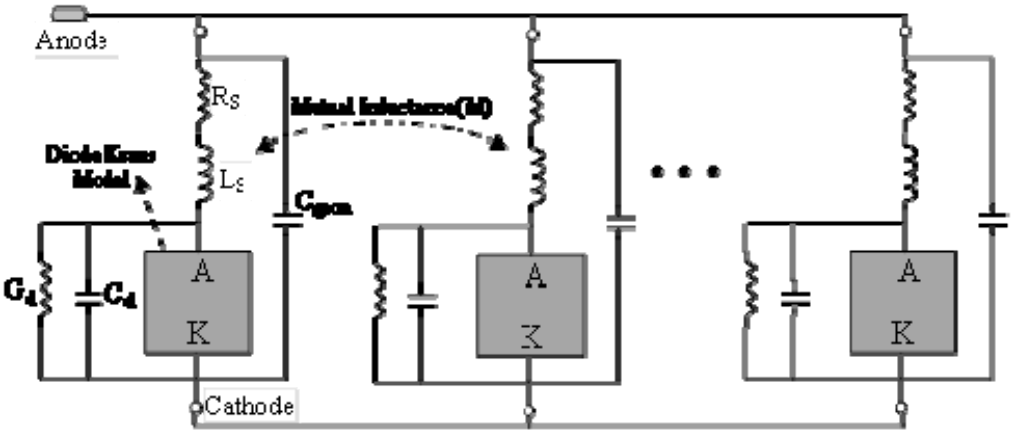

(b)

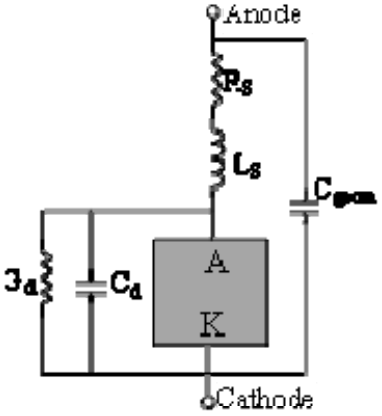

(c)

Figure 5.34 Implementation of a unit Diode cell in FE domain, (a) geometrical demonstration of the unit, (b) Diode distributed equivalent circuit network from 3DFE, (c) Lumped model reduced equivalent electrical circuit.

In these figures, the actual switching waveforms were recorded by TPS2014B Tektronix digital oscilloscope (100 MHz, 1 GS/s). Finally, the measured waveforms are compared to the waveforms which are obtained using the simulation of the proposed model for the semiconductor devices. It is noticed that the proposed model can estimate the high frequency oscillation in the switching action, which the conventional models fails to present.

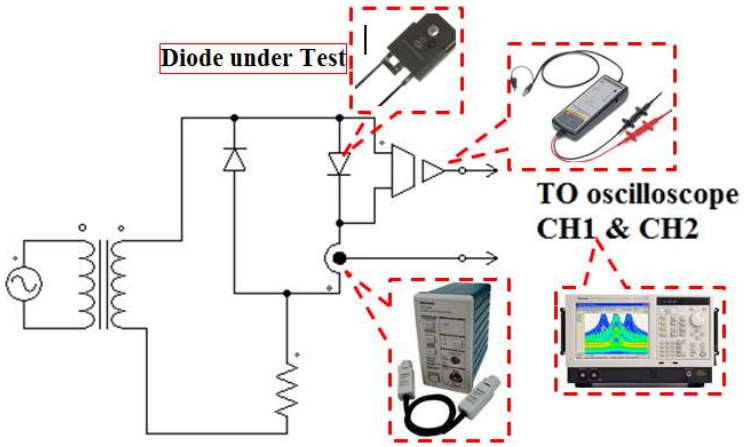

Figure 5.35 Experimental test setup.

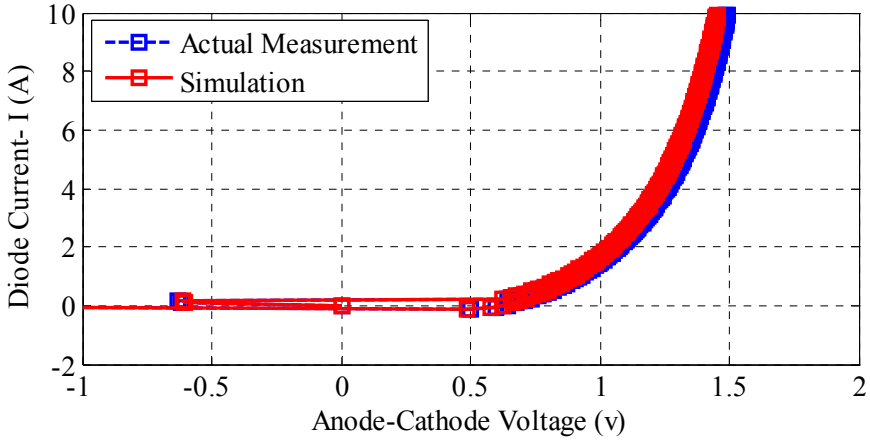

Figure 5.36 Diode I-V characteristics, comparison between the measurement and simulation

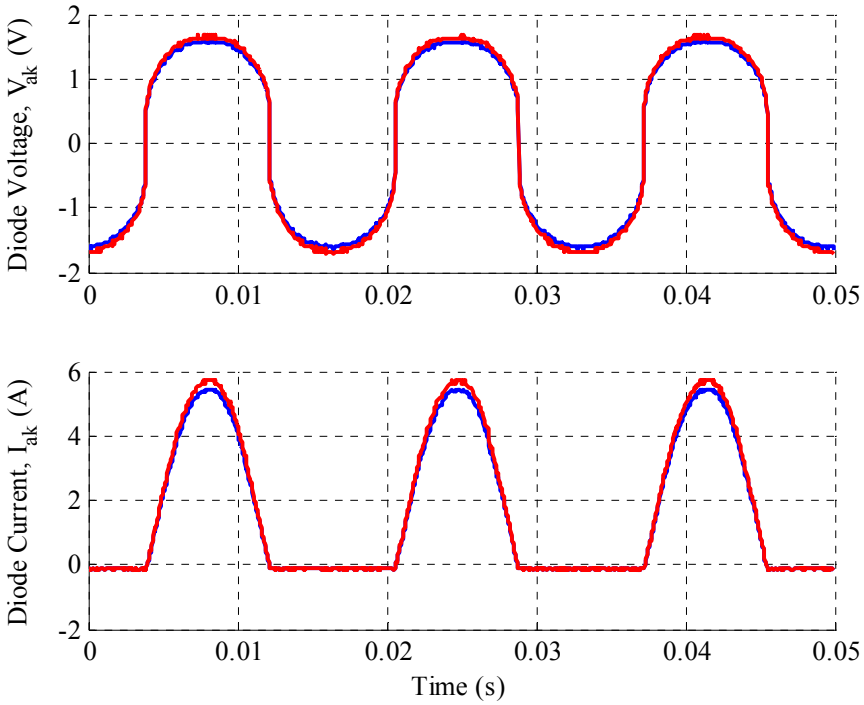

Figure 5.37 Diode I-V characteristics, comparison between the measurement and simulation in time domain

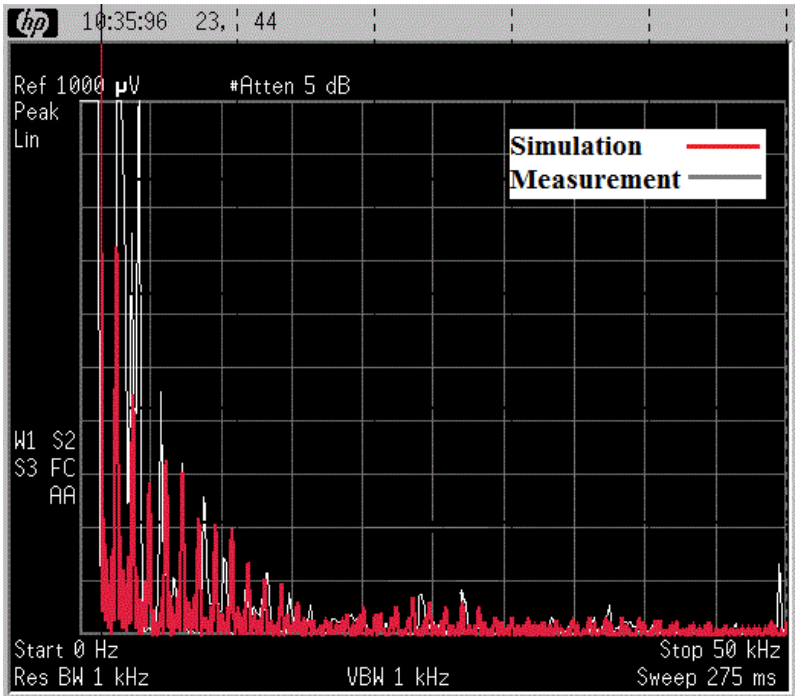

Figure 5.38 Diode I-V characteristics, comparison between the measurement and simulation in frequency domain

Chapter 6 Application of Silicon carbide devices in power electronic systems

Silicon (Si) is the most commonly used semiconductor material in manufacturing power devices because of its high availability and low production cost. However, the deficiency starts to show as for the application under high frequency, high temperature and high voltage rating condition comparing to wide band-gap compound materials (i.e. SiC). Some of the important physical properties are shown in Table 6.1 and 6.2. It can be seen from Table 6.1 that SiC offers a higher thermal conductivity, higher breakdown electric field, larger band-gap and higher saturation velocity than Si. In addition, SiC is an extremely stable material, which is considered as a more ideal material for power electronics. Silicon carbide power devices are expected to open up new markets for power conversion in high-voltage (>10 kV), high-temperature (>150^{o}C) and high-frequency (20 kHz) applications, where Si technology is fundamentally inadequate.

Recently, SiC power devices have begun to appear in the power electronics converter structure due to some of its characteristics that is superior to that of Si power devices. For a given blocking voltage, SiC minority carrier conduction modulated devices, such as a PiN diode, are expected to show an improvement in switching speed by a factor of 100 as compared to Si, while majority carrier SiC devices are expected to show a factor of 100 advantage in resistance compared to Si. Prototype devices have already demonstrated improvements over Si technology for devices of various current and voltage ratings [142], [143].

These emerging power device technologies which utilize SiC material promise to extend high frequency power conversion into the 10 kV to 25 kV range with applications in power distribution, energy storage devices and ship propulsion systems.

Table 6.1 Comparison of SiC devices [142]

SiC Schottky diode	**Si PiN diode**
Low reverse recovery charge	High recovery charge + current tailing phenomenon

SiC DMOSFET	**Si MOSFET**
Low conduction loss	Higher R_{on} resistance
No tail current at turn-off	High turn-off losses

SiC IGBT	**Si IGBT, GTO, Thyristor**
Reduction in series connected components	Increased system complexity due to cascading connected components
Higher switching frequency (up to 50kHZ)	Low switching frequencies
Immunity from thermal runaway	Facing thermal runaway due to high leakage currents
Higher efficiency	Lower efficiency
Lower conduction and switching loss	High conduction loss
Reduced maintenance cost	Increased maintenance cost

Table 6.2 Electrical properties [142]

Breakdown field	Mobility electrons	Mobility holes	Diffusion coefficient electrons	Diffusion coefficient holes	Electron thermal velocity	Hole thermal velocity
~ 106 V/cm	≤800 $cm^2\ V^{-1}\ s^{-1}$	≤320 $cm^2\ V^{-1}\ s^{-1}$	≤20 cm^2/s	≤ 8 cm^2/s	2.0×105 m/s	1.5×105 m/s

Thermal properties

Thermal conductivity	Thermal diffusivity	Thermal expansion
3.6 W cm^{-1} °C^{-1}	1.6 $cm^2\ s^{-1}$	$\alpha = 3.8 \cdot 10^{-6}$ °C^{-1}

Presently, significant efforts have been done to develop high voltage semiconductor devices needed for commercial and military high-voltage, high-frequency power conversion applications. The Electric Power Research Institute (EPRI) has reported that a solid-state distribution transformer referred to as the Intelligent Universal Transformer (IUT) is a viable replacement for conventional distribution transformers and would add significant new functional capabilities to those available from conventional copper and ion transformers. Another EPRI report identified SiC devices as a potential solution for high voltage semiconductor devices needed for the IUT. Furthermore, the goal of an ongoing Defense Advanced Research Projects Agency (DARPA) is to support the research and develop the SiC switches and diodes necessary to demonstrate the viability of the Solid State Power Substations (SSPS) for future power electronics conversion systems [142].

Physical properties of silicon carbide

Structural features

Electronic applications involve devices based on semiconductor materials with crystalline structures. The crystal structure of mono-crystalline silicon is characterized by an arrangement of Si atoms along a face centered cubic network, with a mesh parameter of 5.431 Å. The structure of crystalline silicon carbide on the other hand can be described simply by stacking compact plans, each plan being a double layer of a compact plan of C atoms on a compact plan of Si atoms. The pile of a second double layer on a first one can be in two positions, different from each other and different from the position of the first level. This is obviously the same for the next level and so on. The three possible positions

for a double layer are generally named A, B and C. According to the stacking sequence and its recurrence, the elementary mesh can be cubic (C), hexagonal (H) or rhomboid (R). Only one dimension of the grid perpendicular to the plains, which is the axis of growth, is different from one pile to another. This way, several crystallographic arrangements may exist for the same chemical composition SiC.

This uniqueness of silicon carbide is named after poly-typism (which is a polymorphism in one dimension). 170 to 200 crystallographic varieties or poly-types have been counted. Among them, few have been synthesized into the form of mono and stable materials. The poly-typism of SiC also explains the difficulties historically found and for the production of substrates and homogenous SiC films, especially since it gives to each poly-type physical properties whose ranges vary from one to another [142].

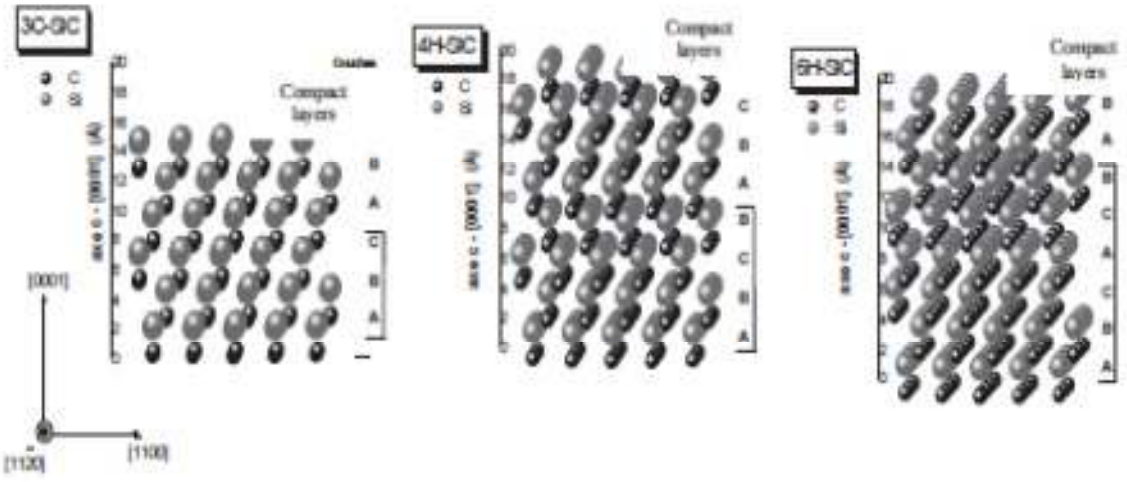

Figure 6.1 Presentation of polytypes SiC-3C, SiC-4H and SiC-6H and of Ramsdell notation. [142]

Chemical, mechanical and thermal features

The link between the Si atom and the C atom is strong; with energy equal to 6.34 eV (the binding energy between two atoms of silicon is only 4.63 eV). This simple fact makes silicon carbide a resistant material from various points of view and contributes to the interest for it, for various applications including electronics.

Firstly, SiC is high temperature resistant. Sublimating rather than melting under reasonably accessible pressure, silicon carbide cannot be synthesized from the liquid phase by conventional techniques of recrystallization. The growth of a single crystal is more delicate than that of silicon, especially as the resulting crystalline arrangement is very sensitive to the conditions of temperature and pressure.

Silicon carbide is also chemically resistant and it is very difficult for a foreign atom to penetrate the network of this material to travel inside. An input of energy (e.g. heat, photonics, electrical, or mechanical, etc.) higher than the case of silicon is necessary. In terms of temperature stability, these features are assets for operation in improper environments and for reliability, but they do not facilitate the steps of production of components based on chemical reactions (cleaning, engraving, oxidation) or diffusion of impurities.

Since development of the first manufacturing process of SiC, silicon carbide is well known for its mechanical resistance. This hardness (about three times that of silicon), which is not really a superiority for electronic applications, is reported here because it has an effect on mechanical treatments, such as cutting and polishing units in the manufacture of semiconductors for electronics.

In terms of thermal expansion, the coefficient of silicon carbide ($4x10^{-6}$ K^{-1}) is approximately two times greater than that of Si, which increases the gap with that of silica (5.5×10^{-7} K^{-1}), but reduces to that of copper ($17\times10^{-6}K^{-1}$), or aluminium (22×10^{-6} K^{-1}).

Electronic and thermal features

The attraction to the physical properties of silicon carbide for use in electronic applications is verified throughout so many studies that have been done. The huge majority of these studies concern the three most common poly-types: 3C-SiC, 6H-SiC and 4H-SiC. Many publications present measurements and modeling parameters of these materials and some properties are accurately determined (such as the forbidden energy band, or the effective masses). However, due to sensitivity to the purity of the material, or its anisotropy, some parameters are dispersed or incompletely determined (mobility and saturation speeds of load porters, especially holes; or critical breakdown field, etc.). Table 6.3 brings together the main important features for the performance of semiconductor components. The values given are trying to account for dispersions, being an average of the main results of edited measures, for a temperature of 27°C and for a doping of 1015 cm^{-3}. All three SiC polyt-ypes, with structure tests were performed, are considered here along with silicon, as a benchmark. For hexagonal poly-types, the values of mobility and speeds of load porters are provided for both parallel directions (||c) and perpendicular ($\perp$c) to the axis of growth.

Table 6.3 Main physical properties for components performances: comparison of most common SiC polytypes and silicon (at 300 K for doped materials at 1015 cm-3) [142]

	Si	3C-SiC	6H-SiC	4H-SiC
E_g (eV) Forbidden bandwidth	1.12	2.2	3.02	3.26
E_c (MV/cm) breakdown electric field	0.28	1.5	2.2	2.2
ε_r dielectric constant	11.8	9.66	9.7	10
μ_n (cm^2/Vs) intrinsic mobility of electrons	1350	900	400 (⊥c) 90 (‖c)	800 (⊥c) 1000 (‖c)
μ_p (cm^2/Vs) intrinsic mobility of holes	480	40	100 (⊥c) 20 (‖c)	110 (⊥c) 140 (‖c)
v_{sat} (10^7 cm/s) saturation speed of carriers	1	2.5	2 (⊥c) 0.2 (‖c)	2.2 (⊥c) 0.33 (‖c)
n_i (cm^{-3}) intrinsic concentration	1.4×10^{10}	6.9	2.3×10^{-6}	8.2×10^{-9}
λ_{th}(W/cm.K) thermal conductivity	1.5	4.9	4.9	4.9

Applications of silicon carbide in power electronics

EMI comparison between Si and SiC technology in a buck converter

In this part, we present a comparison of the EMI generated by a DC/DC buck converter, using silicon (Si) or silicon-carbide (SiC) switching devices. EMI was compared using Si technology as reference. The comparison parameters were the switching times and the conducted and radiated EMI. In this study three different structures (Si-buck converter, SiC-buck converter and Si-ZCS-buck converter) were compared.

In order to reduce the size of the capacitors and inductors, the switching frequency must be increased and that increases the converter emissions, sometimes causing to be out of the standard limits [144]. The major source of conducted emissions is the reverse

recovery of the semiconductor devices and the semiconductor devices based on Si technology have reached their limit in that sense [145]. Silicon technology is also in its limits regarding voltage blocking capability, operating temperature and switching frequency.

SiC semiconductor devices have near zero reverse recovery charge and time and so, they allow a considerable decrease of EMI produced by the converter. The use of SiC in power converters allows working voltages in excess of 6.5 kV, higher working temperatures, up to 350ºC [146] and higher switching frequencies. In many cases, the efficiency of the power conversion increases, as well [147].

Beside the above cited benefits of using SiC devices in power converters, there is also an important drawback consisting of an increase of EMI. The increase is due to the high switching speed (dv/dt) of SiC devices, causing high frequency currents through the converter parasitic components [148].

The other investigation is on the soft switching buck converter, which is a zero current switching buck converter. In this type of converters, the reverse recovery energy related to the switching of the Si device is eliminated. Therefore, this topology can help to reduce the amount of radiated and conducted EMI.

This part is focused on the comparison of the features of a buck converter, using different application of Si and SiC semiconductors.

Circuit and tests description

Figure 6.2 shows the schematic of the buck converter used for comparison purposes. The SiC semiconductor devices chosen for the buck converter were GA35XCP12-247 for

the IGBT and GB01SLT12-220 for the diode. For the Si based converters we choose the G30N60C3D and the 1N4148W diode. The schematic of the ZCS-buck converter is shown in Figure 6.3.

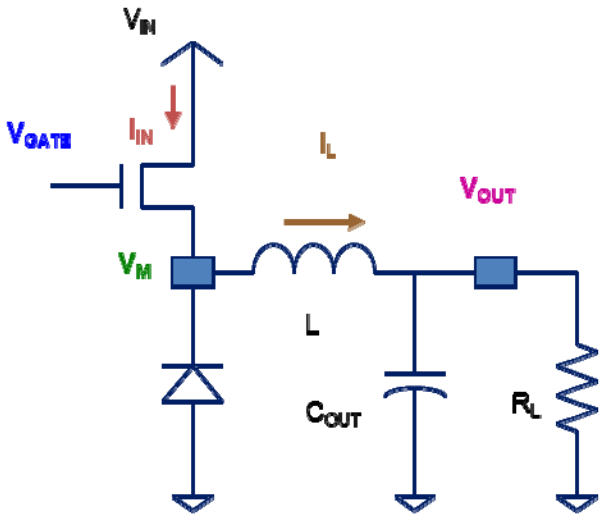

Figure 6.2 Schematic of the buck converter implemented

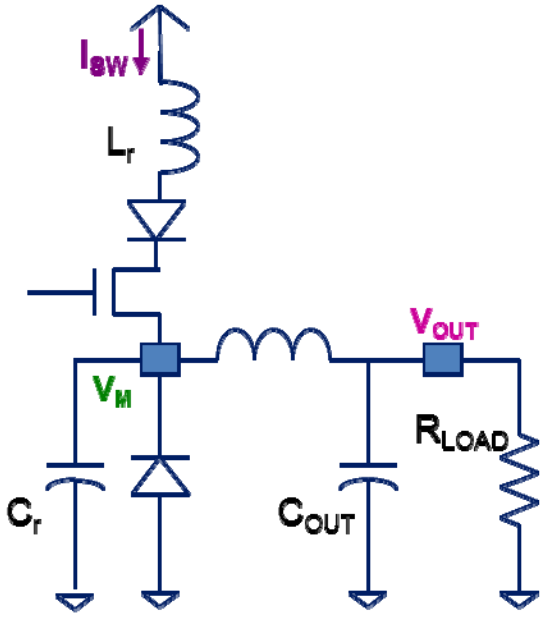

Figure 6.3 Schematic of the ZCS-buck converter

The PCB was designed with two layers. The specifications of the designed converter are summarized in Table 6.4.

Table 6.4 buck converter parameters

	Si	**SiC**
IGBT	Fairchild G30N60C3D	GeneSiC GA35XCP12-247
Diode	Si 1N4148W	SiC GB01SLT12-220
L_r	2.2 uH	N/A
L_f	1 mH	1mH
C_r	400 nF	N/A
C_f	100 uF	100 uF

In order to compare the EMI of the converter, we built a buck power converter in which we measured the conducted and radiated EMI. The measurements were performed on the Si-buck converter and SiC-buck converter and QR-ZCS-buck converter. First we measured EMI in case of using Si IGBT and diode, the second case used SiC IGBT and SiC diode, Drain-source voltage (V_{DS}), drain current (I_D), output voltage and output voltage were measured to compare the switching characteristics of the devices. The experimental setups of the converters are shown in Figs. 6.4-6.6.

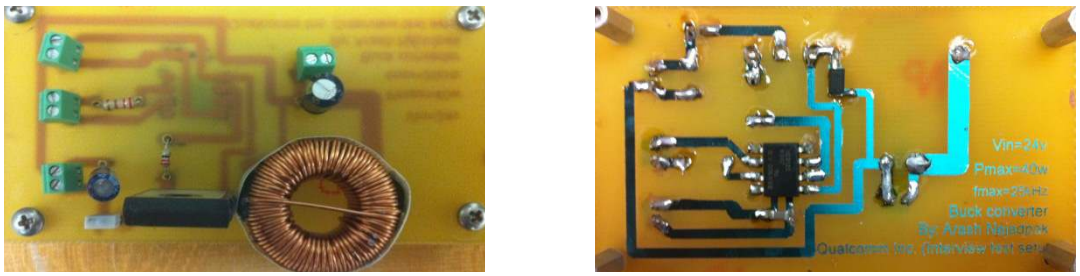

(a) (b)

Figure 6.4 Si-buck converter, (a) Top layer, (b) bottom layer.

(a) (b)

Figure 6.5 SiC-buck converter, (a) Top layer, (b) bottom layer.

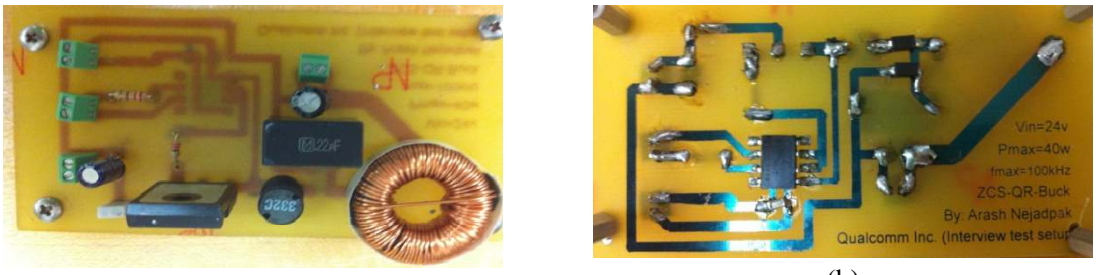

(a) (b)

Figure 6.6 ZCS-Si-buck converter, (a) Top layer, (b) bottom layer.

Experimental results

Switching characteristics

Figure 6.7 is showing the turn-on and turn-off characteristics of the IGBT for all three types of converters. In these figures the IGBT collector-emitter voltage (Drain-Source voltage) and the collector current is measure using the 150 MHz differential voltage probe and 100 MHz current probe. From the figures one can see that the reverse recovery time is much greater when using a Si diode. The turn-off times when using Si or SiC diodes are similar. Nevertheless, the use of SiC diode causes some oscillations during the turn-on switching. The output voltage and current of all three converters are shown in Figure 6.8. From this figure we can easily observe that the Voltage and current spikes will reduce when using the SiC device or applying the soft-switching algorithm.

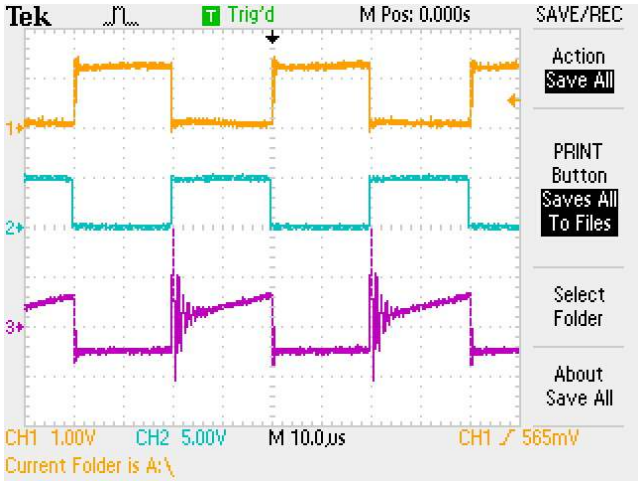

(a)

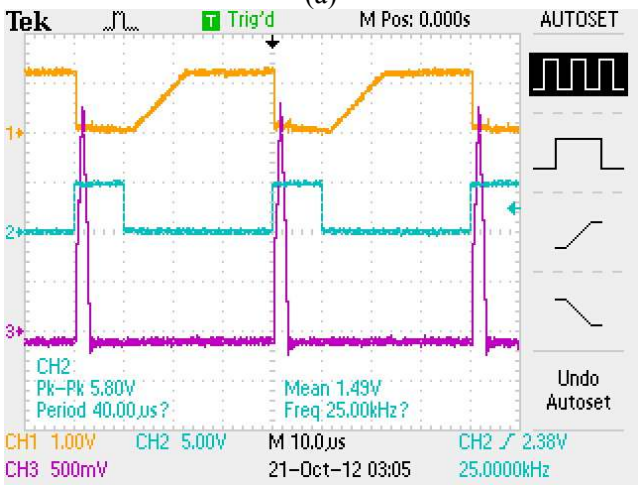

(b)

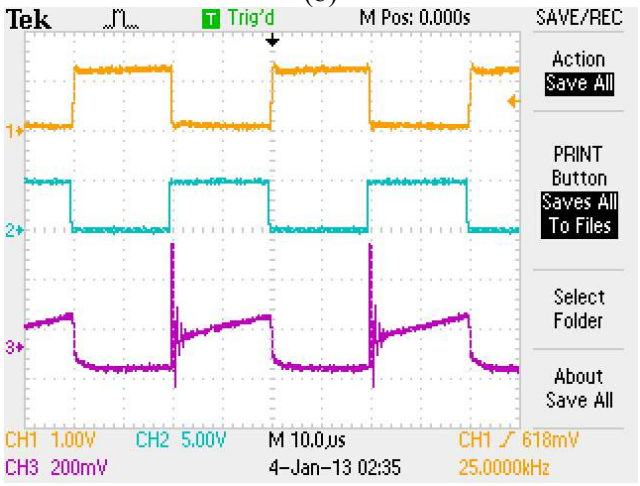

(c)

Figure 6.7 IGBT switching waveform for, (a) Si-buck converter, (b) ZCS-Si-buck converter, (c) SiC-buck converter (yellow: IGBT drain-source voltage, Blue: switching command, Red: IGBT drain current)

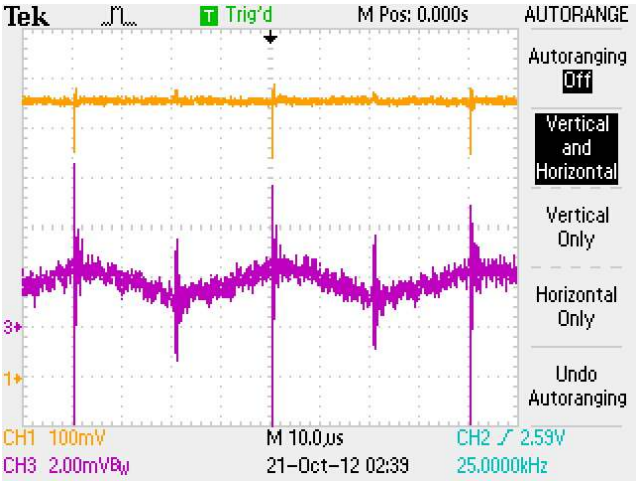

(a)

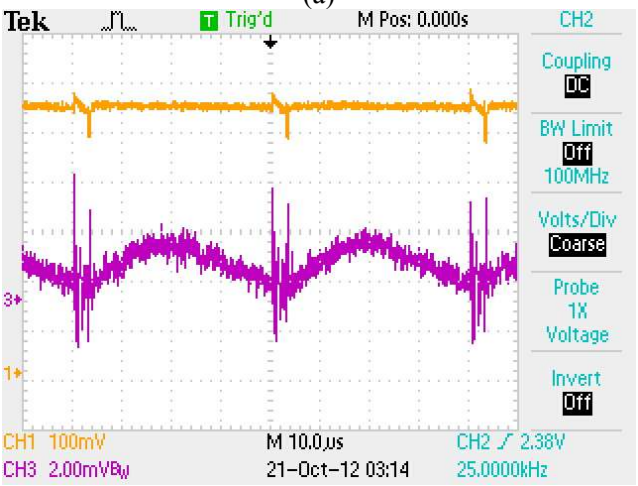

(b)

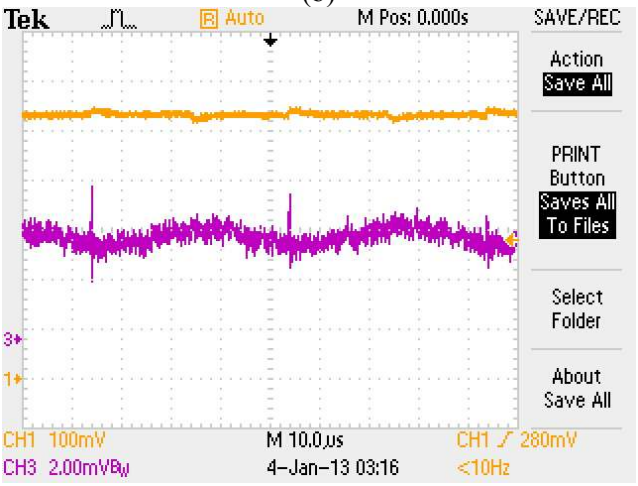

(c)

Figure 6.8 Converter output voltage and inductor current for, (a) Si-buck converter, (b) ZCS-Si-buck converter, (c) SiC-buck converter (yellow: output voltage, Red: inductor current)

Conducted EMI

Conducted EMI were measured using a line impedance stabilization network (LISN) and a spectrum analyzer as an EMI receiver. Figures 6.9 and 6.10 show the resulting spectra for the three cases described above.

From the figures it can be seen that the use of SiC devices causes a reduction of conducted EMI in the range of 10MHz to 30MHz, comparing to the same converter using Si diodes. The use of SiC IGBT causes a reduction of EMI in the range from 4 MHz to 10 MHz. In case of using soft switching technique, the conducted EMI is reduced as compared to that of the hard switching Si device, but still higher than SiC converter; this can be because of adding extra components to the converter to perform the soft switching action.

From Figs. 6.9 and 6.10, we can easily conclude that application of the Si devices in these types of switching converters may increase the noise propagation in the converter's circuit, however it can be mitigated using the soft switching techniques or using SiC devices.

Figure 6.10 shows the frequency spectrum of the converter output voltage it can be seen that in the Si-Buck converter, the noise signal covers wider ranges of frequencies as compared to that of the SiC-buck or ZCS-Si-buck converters.

In all these figures a reduction around 20 dB is observable using the either soft switching technique or SiC devices, which is a great improvement to meet the EMI standards.

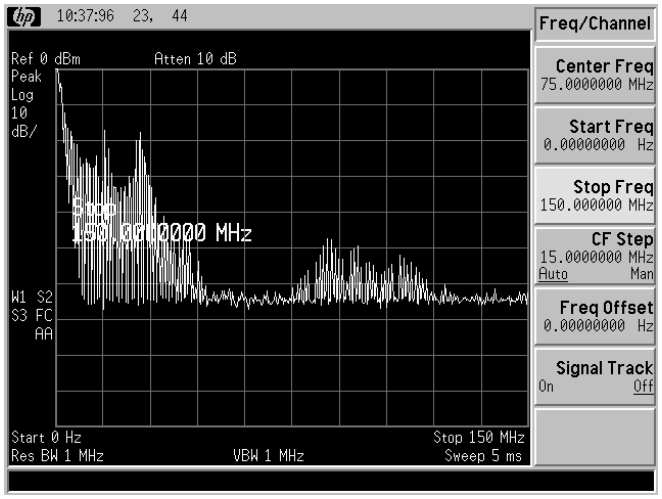

(a)

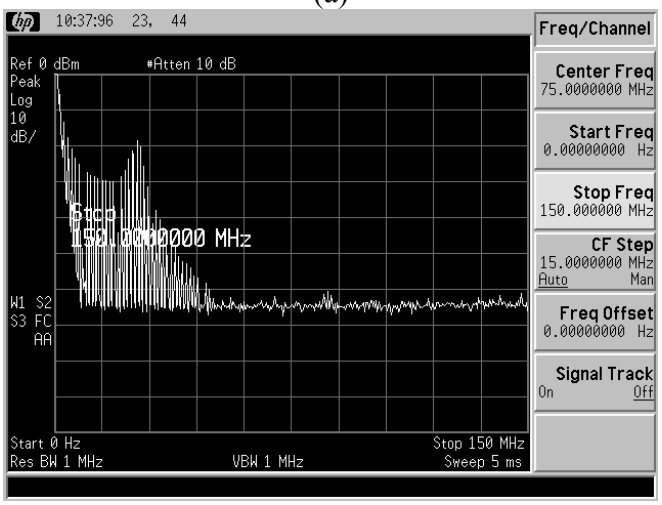

(b)

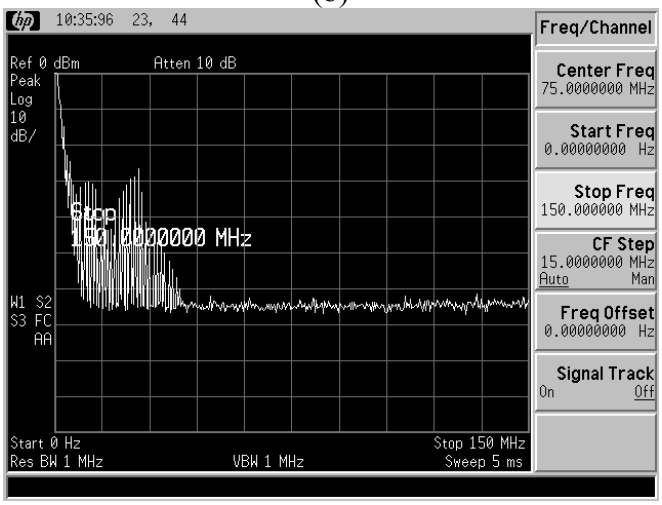

(c)

Figure 6.9 Comparison of the conducted EMI for, (a) Si-buck converter, (b) ZCS-Si-buck converter,(c) SiC-buck converter.

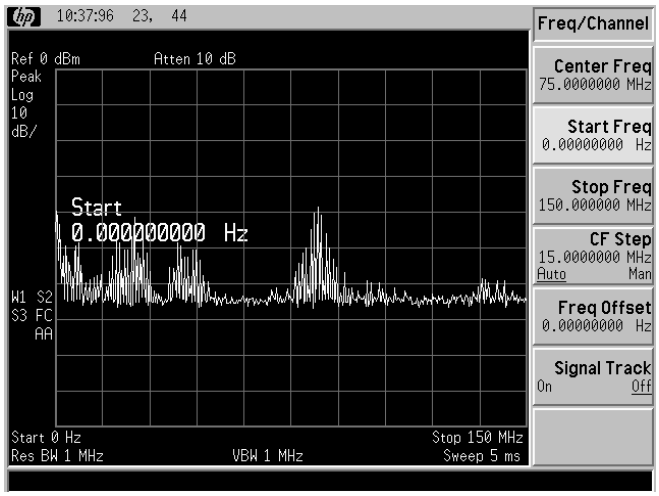

(a)

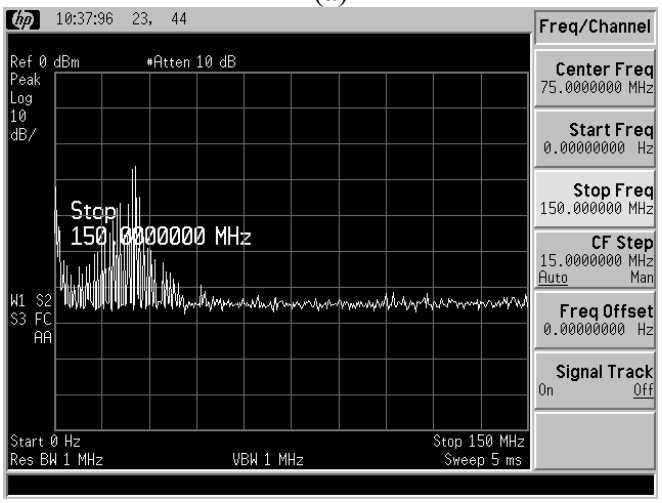

(b)

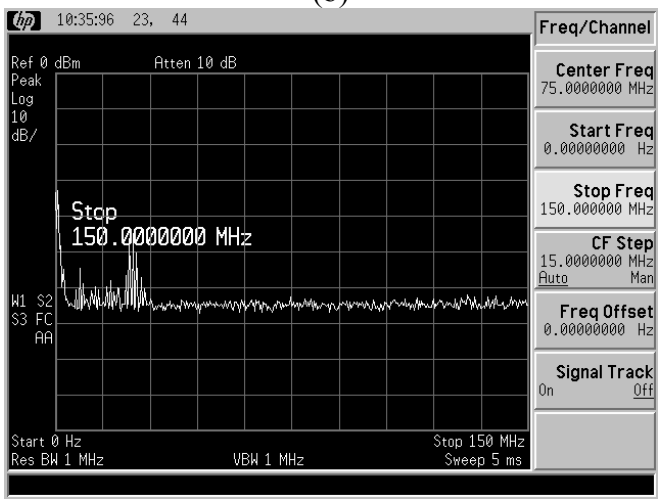

(c)

Figure 6.10 Comparison of the conducted EMI for, (a) Si-buck converter, (b) ZCS-Si-buck converter,(c) SiC-buck converter.

Radiated EMI

Radiated EMI were measured using a rod antenna to detect the radiated electric field and Tektronix spectrum analyzer, in the frequency range from DC to 50 MHz. Only vertical polarization is plotted for comparison purposes. Figure 6.11 show the radiated EMI measured. The radiated EMI using Si technology is plotted in blue in all the figures as a reference. The different cases to be compared are shown in green.

Figure 6.11 shows that the radiated EMI, in the range of 1 MHz to 2 MHz, when using SiC diode is higher than the reference values using Si. Figure 6.11 shows that radiated EMI in the whole range from 30 MHz to 1 GHz, when using SiC IGBT, are lower than the reference value using Si. When SiC is used for both, IGBT and diode, the radiated EMI are higher in the frequency band from 1 MHz to 2 MHz and lower in the rest of the spectrum.

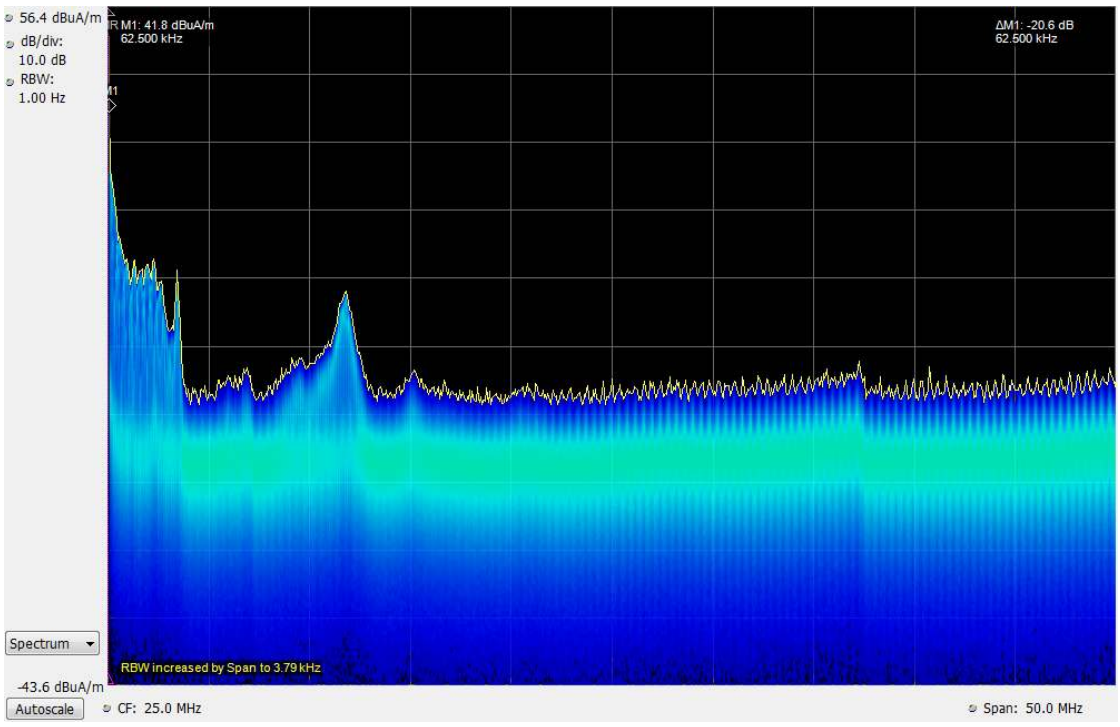

(a)

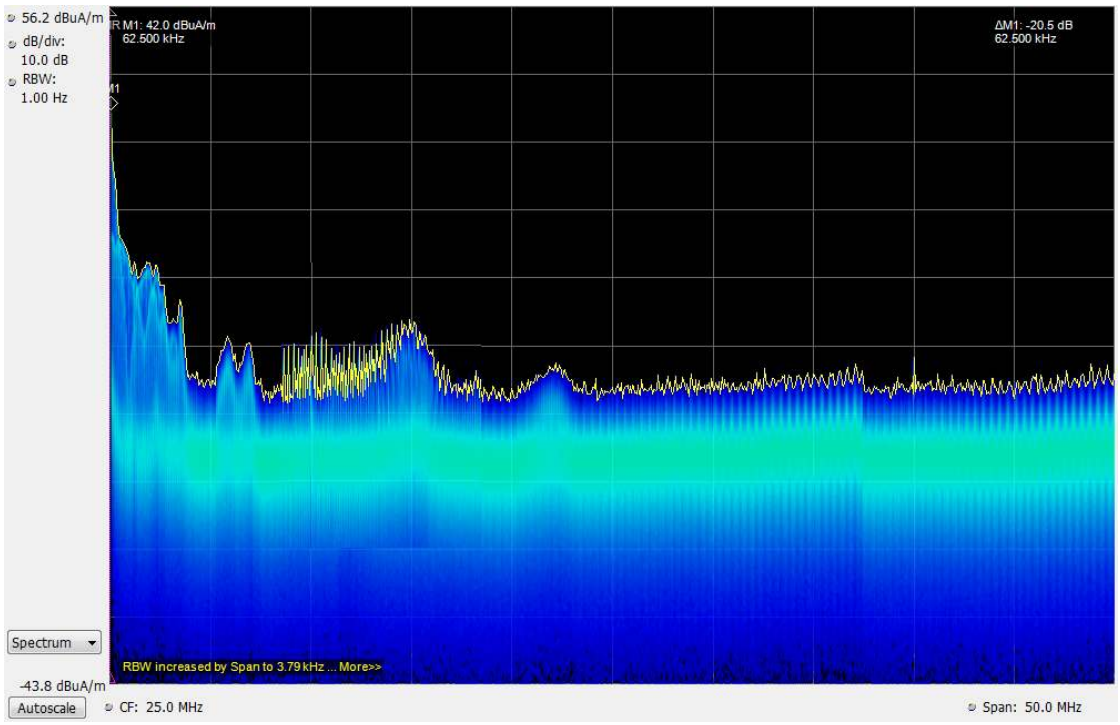

(b)

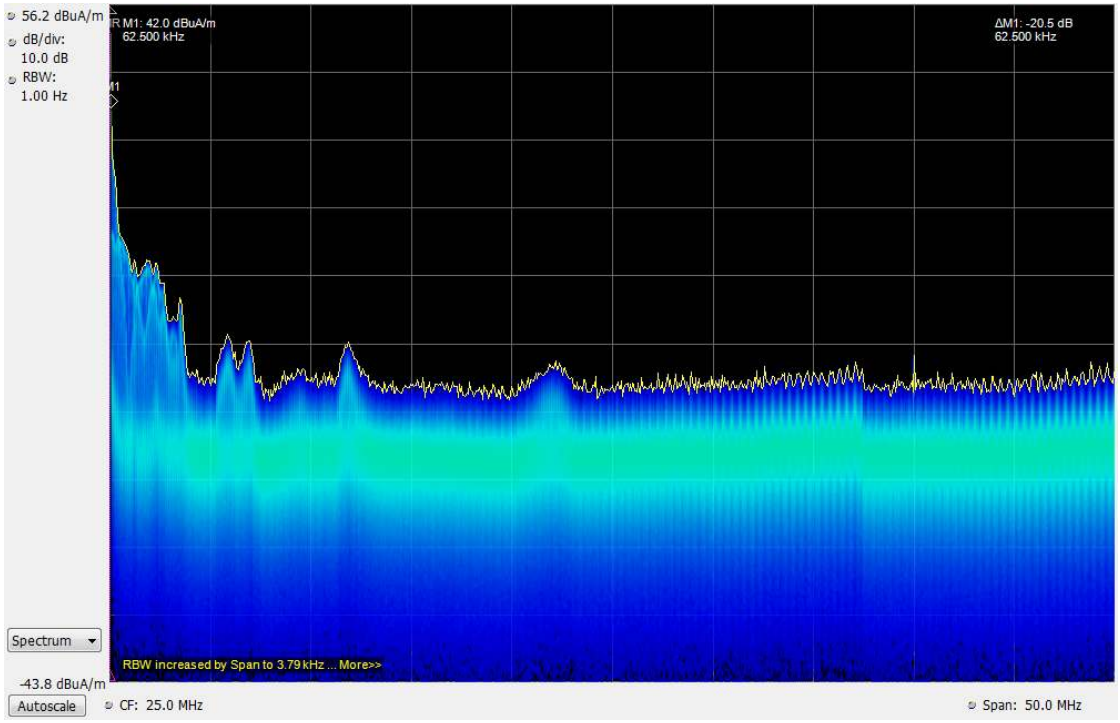

(c)

Figure 6.11 Radiated EMI for three different types of converters, (a) Si-Buck converter, (b) ZCS-Si-buck converter, (c) SiC-buck converter

The use of Si devices causes a high reverse recovery time in the IGBT, during transistor turn-on, due to high Q_{rr} of the diode. A re-bounce in the transistor turn-on can be observed for such case. The recovery time in the transistor turn-on is drastically reduced using a SiC device. These oscillations are caused, probably due to parasitic inductances and capacitances in the circuit and produce an increase in the radiated EMI. This effect remains even when the SiC IGBT is used [144].

Chapter 7 Application of physics-based modeling approach in power electronics

In a power conversion system, all components and interconnections contain parasitic circuit elements and often a combination of these elements can make EMI problems more complicated. An understanding of the magnitude of these parasitic elements and the characteristics of components over a range of frequencies will ensure the correct choice of their application. Also, the switching action excites various parasitic elements in the converter, which results in conducted and radiated energy at unpredictable frequencies. Therefore by the means of such a modeling method a more comprehensive view of the components and their interactions are obtained which later can be used in design stage. In addition to the EMI effects, temperature and heat distribution in the power conversion system components are also another issues which should be deal with.

Therefore, to model the whole power electronic converter, the first step is to model all the constitutive elements in the structure of the converter including inductors, transformers, capacitors, power semiconductor devices and copper traces. This means that we will concentrate on each of these components individually in order to obtain the exact realistic model of each component separately. We can then connect the obtained individual models together to enable the study of the effects of these components on each other under different operational condition.

This physics based model has different applications such as; design of the effective EMI filters, design the effective switching algorithms and circuit topologies for the specific application. One of the applications of the aforementioned modeling is design

and modeling of a new sets of topologies for high-frequency, high efficiency converters for variable speed drives and/or for connecting sustainable energy sources to the grid.

For example one of the challenging problems regarding to adjustable speed drives is electromagnetic interference. This phenomenon becomes much more important when a feeder with long cable is being used. Various simulation models have been developed for inverter, cable and motor. Also different simplifications degrees were adopted to ease the simulation burden. In this study a detailed model for the adjustable speed drives powertrain is obtained and analyzed.

The other example can be the inverter's switching that can be a significant source of EMI issue and also represents the source of voltage overshoot at motor terminals via long cables. Cable and motor models are added to the inverter model forming a single simulation system where the HF-phenomena are reflected accurately. Measurements comparisons are presented to prove the reliability of chosen models.

The main advantage of this modeling method is design of an inverter in high power applications with the ability to overcome the blocking voltage limitations of available power semiconductor devices. Another advantage is selection of the best matching topology with inherent reduction of switching losses which can be utilized to improve the overall efficiency.

The Physics based modeling approach can makes it possible to design any power electronic conversion system to meet packaging constrains. This includes physical characteristics such as; decreasing the size and weight of the package, optimized interactions with the neighboring components and higher power density. In addition, electromagnetic behaviors and signatures can be evaluated including the study of

conducted and radiated EMI interactions in addition to the design of attenuation measures and enclosures. In this chapter several different application of physics-based modeling is introduced.

Physics-based modeling of power inverters

The main objective of this part is to obtain a high-frequency physics-based model of IGBT-based power converters. The developed model should acts exactly as the physical device with a high level of accuracy and with little or no compromise.

In a motor-drive system, there are several components, such as the inverter, cable and motor, which need to be modeled for a comprehensive high-frequency investigation. The HF physics-based model for the armored power cable and PM synchronous motor (PMSM) were obtained, in the previous studies. This part is primarily concentrating on the HF physics-based model of active devices. The developed individual models for these active elements and the HF model of PCB copper traces in addition to other connections are used in combination to construct the whole power converter model.

Physics based modeling of the power semiconductor switches were defined in chapter 6. In this section the rest of the components of a typical power converter are modeled and connected together to construct the converter package and analyze the results.

Modeling the power converter's PCB

The power converters are usually implemented and assembled on the printed circuit boards (PCB) made of FR4 material. Poor layout of PCBs, can prepare paths for propagation of noise all over the circuit. Moreover, there is always an area embedded on the surface of the board for placement of the heat sinks. Heat-sinks need to be attached to

the switches metallic area (which is usually connected to the Source terminal of the device) for cooling purposes. Whereas, these heat-sinks are mostly connected to the ground of the system, therefore, another conductive path is created between the Source of the switch and ground. The converter's PCB and heat-sink are modeled as a part of the power conversion system, as follows:

Modeling the heat sink effects

In the manufacturing process, the IGBT is located on a ceramic substrate. This ceramic substrate can be connected to metallic plate which is connected to a heat sink. This plate is almost in close contact to the collector of the IGBT. Therefore a parasitic capacitance is produced, which can have effects on the common mode current propagation. Figure 7.1 shows the heat sink in connection with the IGBT plate in the FE model.

In this process, the electrostatic equation was solved to calculate the capacitance between the IGBT pad and the heat sink surface. The equivalent electrical network is shown in figure 7.3, where L=12 nH, R=0.002Ω and C=176pF.

Modeling the PCB copper traces

In figure 7.2, the converter's PCB is modeled. An approach to model he converter PCB is introduced in [115]. To achieve a model that can well represent the actual power electronic converter, the parasitic components of the PCB traces were also considered.

These parasitic components include the stray inductances and resistance and also the parasitic capacitances between the adjacent traces. These values are dependent on the size

and geometry of the traces and their distance from each other. To model the converter's PCB, only the power stage of the circuit is considered. This is assumed to have the most influence on the EMI characteristic of the circuit. The critical traces are designated with alphabetic letters in figure 7.2. The resistances, inductance and capacitance of the PCB traces were calculated the same way as it was explained in chapter 2.

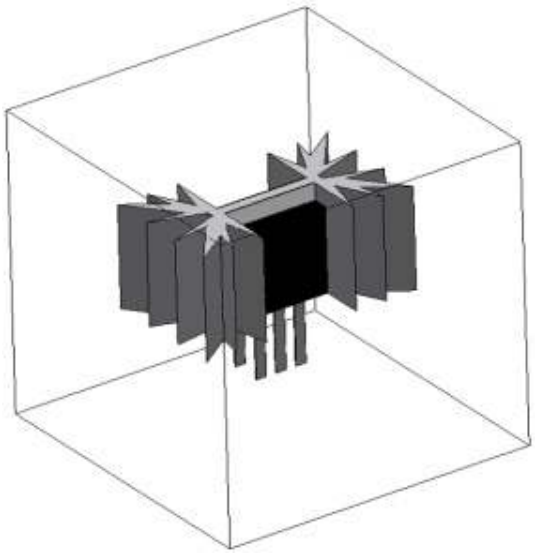

(a)

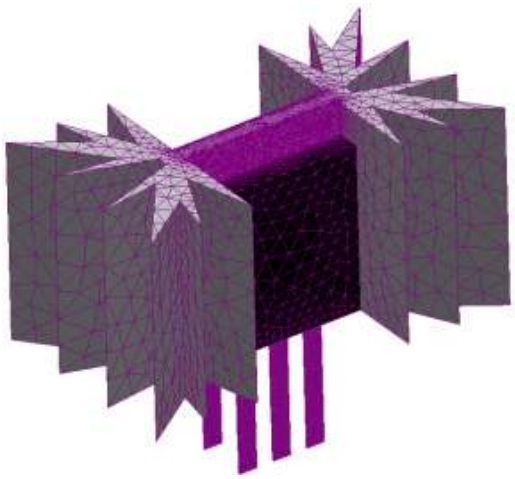

(b)

Figure 7.1 (a) IGBT to heat sink surface, (b) FE model mesh

In higher-frequencies, the resistance, inductance and capacitance behave differently from the low-frequency operation. The conductors have skin and proximity effects which cause the resistance to be much higher than the low-frequency resistance, while the inductance values decreases with the increase in the operating frequency. To obtain the accurate frequency behavior of the resistance, inductance and the capacitances matrices, these values were calculated under different PWM switching frequency.

In order to mesh the conductor's region for the high-frequency eddy current problem, care was taken such that the size of the elements used is smaller than the wavelength of the PWM excitation frequency. Table 7.1 shows the change in the values of these parameters versus frequency for different element of the PCB shown in figure 7.2.

The FR4 permittivity is considered to be a constant value and invariable with the change in the frequency, therefore, it yields a constant value for the parasitic capacitance. Table 7.1 shows the capacitance values between different traces. The values shown in Table 7.1 and 7.2 are all calculated based on the following material properties of the PCB: FR4 dielectric constant (ε_r) is equal to 4.7, relative permeability (μ_r) equal to 1 and the board thickness is 1.58 mm. Also, 2 oz. copper is used on the board, which has the thickness of 68.2 μm. The copper conductivity is equal to 59.6×10^6 S/m.

After modeling all the constitutive elements of the power train of the motor drive system, these component's models are connected together to form the converter drive system. This circuit is composed of actual switch model and lumped parasitic component in a circuit simulator such as Simulink/MATLAB. In the next section the system's model is simulated in time-domain for at least one fundamental cycle. The results were experimentally verified.

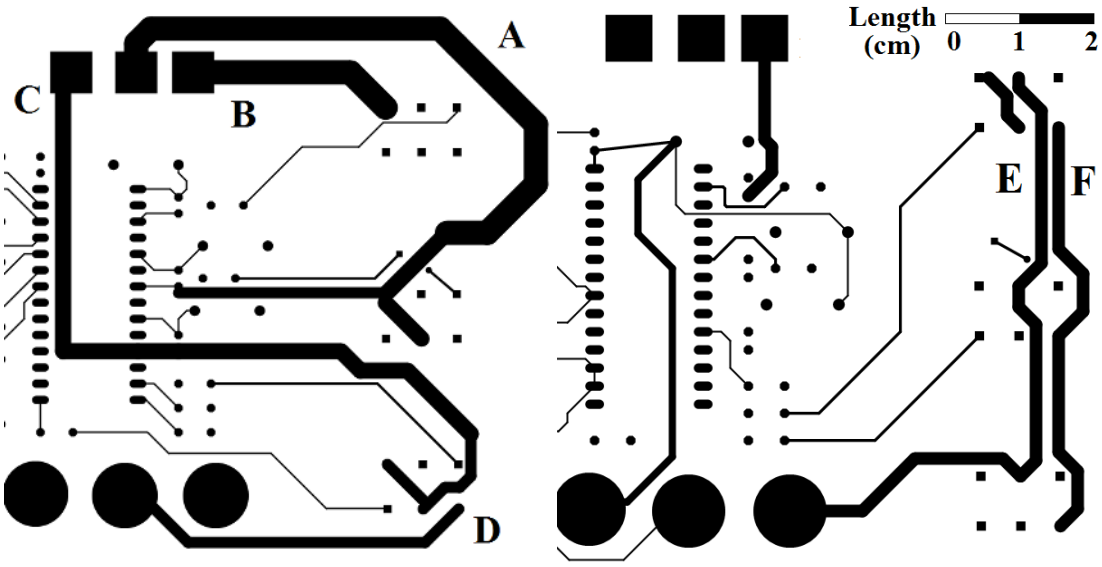

(a)

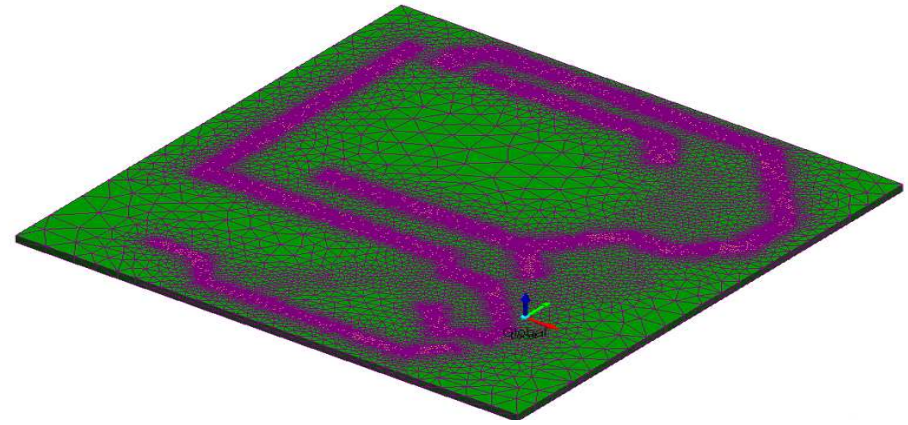

(b)

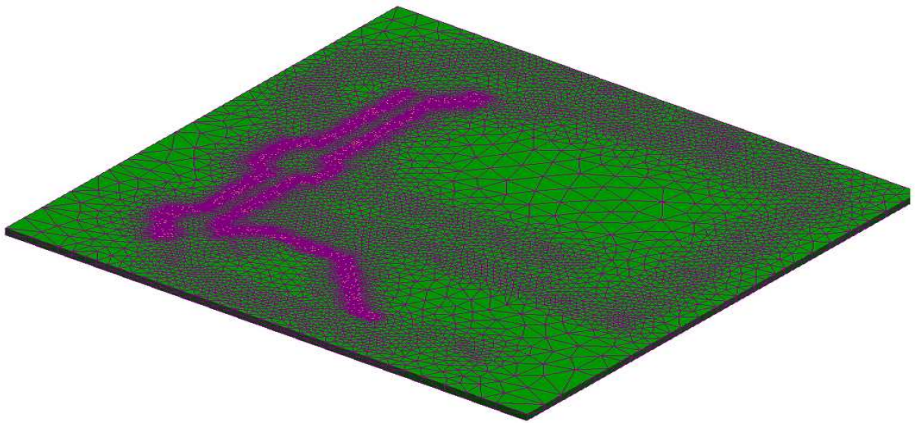

(c)

Figure 7.2 Power converter's PCB, (a)Top layer, Bottom layer, (b)Finite element model (Top layer view), (c)Finite element model (Bottom layer view).

Table 8.1 Stray inductance and resistances values in different routes.

Element:		A	B	C	D	E	F
5	R(mΩ)	15.9	7.6	23.2	18.2	25.3	20.6
kHz	L(nH)	34	16.8	65	37.1	68.3	40
10	R(mΩ)	21.8	10.3	33	26.9	36.4	29.1
kHz	L(nH)	33.6	16.2	64.8	36	67.7	39.5
20	R(mΩ)	33	16.7	47.5	38	51	41.6
kHz	L(nH)	32.8	15.5	64	35.6	67	38.7

Table 7.2 Coupling capacitances between different routes.

Elements:	A+B	A+E	A+F	E+F	C+E	C+F
C(pF)	1.88	2.96	2.96	2.15	1.37	1.33

Results and Discussion

Figure 7.3 shows the complete simulation diagram for the power converter (inverter) with inclusion of parasitic components. The time domain signals measured at the line impedance stabilization network equivalent circuit (LISN) is then converted to frequency domain through FFT. Figure 7.4 demonstrates the connection of a three-phase 42-V inverter, armored power cable and three-phase PMSM. The inverter adopts power IGBT as the switching device. In the inverter model, all the semiconductor devices are substituted with their corresponding physics-based models. To simulate such an inverter drive, the time-domain simulation approach is used. To construct the simulation model for motor-drive system, the three major components of the system (i.e. Inverter, cable and PMSM) are replaced with their corresponding physics-based models. In [106] a physics-based model is obtained for the armored power cable which is used in the system shown in figure 7.3. Also, the PMSM physics-based model is obtained in [107]. In this study, the

power circuit model is added to the system to increase the accuracy, in prediction of high-frequency behavior of the system.

The other important issue, which plays an important role in EMI propagation in the power converters, is poor layout of PCB traces. To consider the effects of PCB layout, the connections between components on the board were replaced with their equivalent circuit models. To further increase the accuracy of the simulation model, the capacitances between the semiconductor switch and heat sink surface, should be considered. The metal plate of the switch, which is usually connected to the heat sink for cooling issues, is connected to the collector of the IGBT. On the other hand, the heat sink of the switches depending on the circuit topology is connected to ground. Therefore, another parasitic capacitance between the switch metal plate and heat sink is produced.

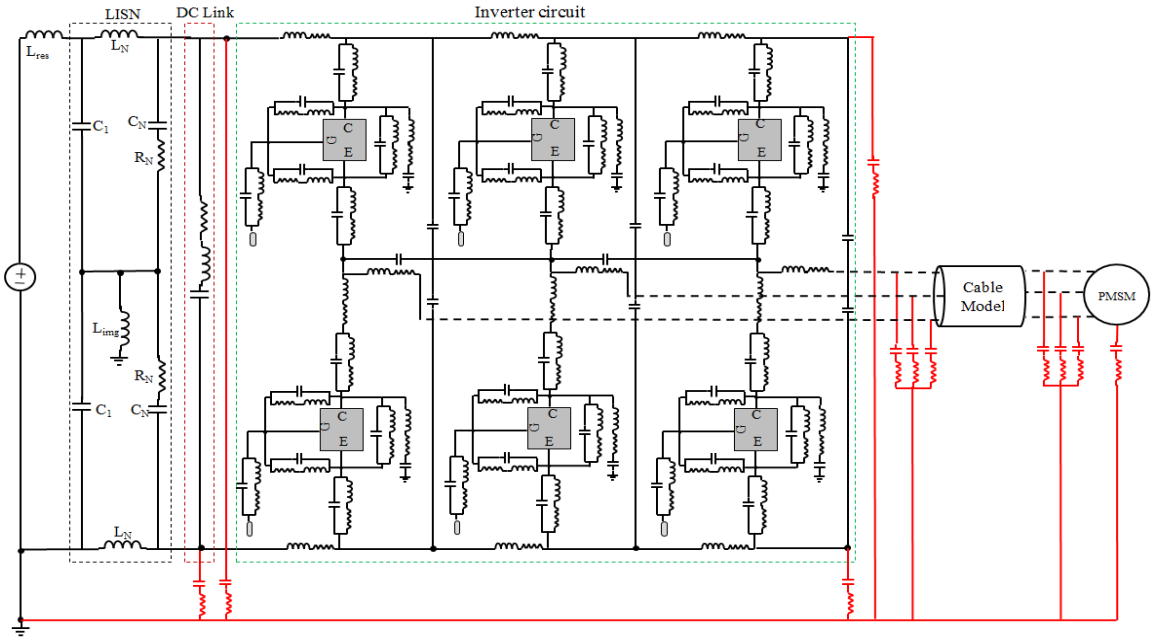

Figure 7.3 Inverter circuit of AC motor drive, used in simulation, with inclusion of parasitic components.

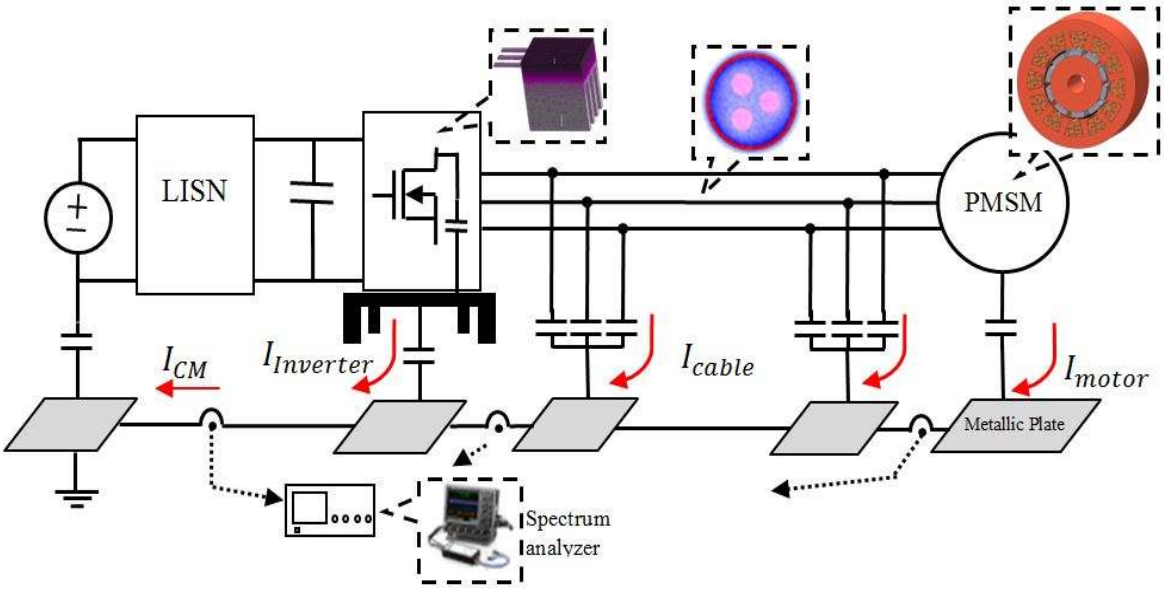

(a)

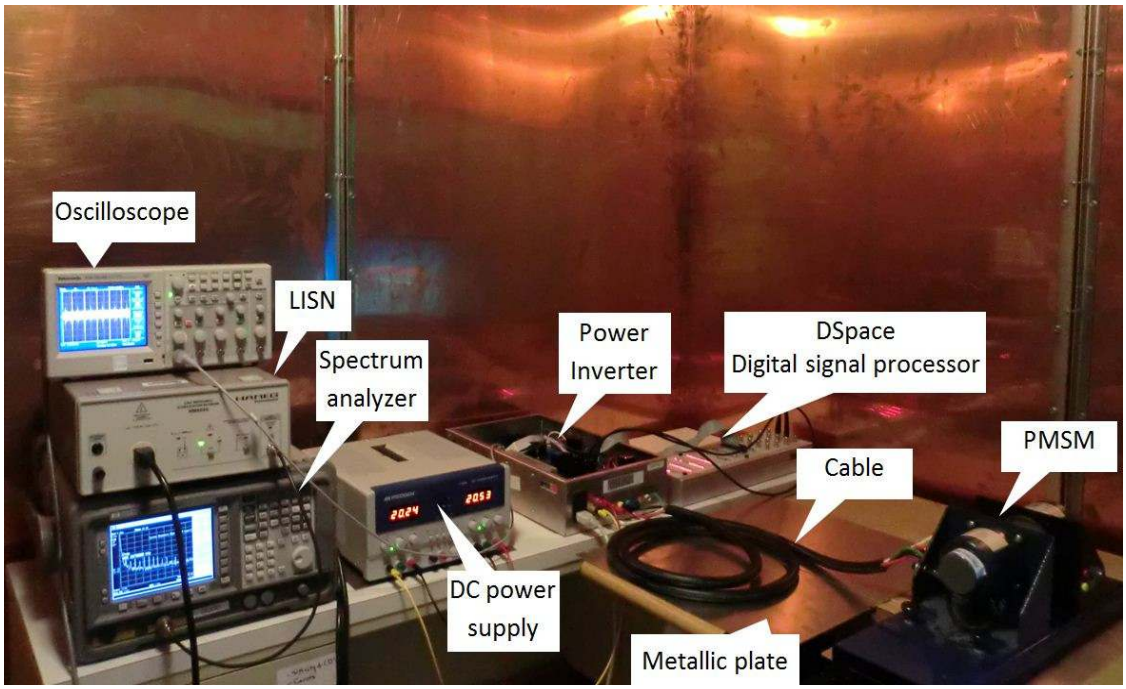

(b)

Figure 7.4 Schematic view of a motor-drive system, (a) schematic of motor-drive system used for CM measurement, (b) Experimental setup.

The test setup used to measure the frequency spectrum in different point in the drive system is shown in figure 7.4(b). The illustrated test setup is consist of a DC power supply, LISN, inverter circuit, 2m long armored power cable and a 250 Watt PMSM. To measure the common mode current, all these components are assembled on a metallic plate. Subsequently, the conducted current can be measured between these plates. The schematic of the proposed system is shown in figure 7.4(a).

The circuit diagram shown in figure 7.3 is constructed based on the experimental setup shown in figure 7.4. The circuit model shown in figure 7.3 is simulated in time domain. In order to avoid time-consuming computing process and better evaluation, the frequency domain simulation approach is used [116]. Figures 7.5 to 7.8 show comparisons between the measurements data and two modeling approaches in the frequency domain. Table 7.3 defines the LISN parameters used in the simulation model shown in figure 7.4. The experimental setup components are as follows:

- DC power supply: 42 V, 5 A.
- Line impedance stabilized network (LISN): 50 Ω 4×15 A—MN2053, Chase Electronics Ltd.;
- Variable-speed drive: It is constituted by a discrete IGBT module and its switching frequency is adjustable from 2 to 16 kHz;
- Permanent magnet synchronous motor, 250 Watt, nominal speed: 1500 r/min;
- Shielded cables: four conductors, section = 5 mm^2 + shielding braid.

Table 7.3 Values of the LISN parameters in simulation model.

Parameter	L_N (μH)	C_N (μF)	C_1 (μF)	R_N (Ω)	L_{res} (μH)
Value	50	0.1	10	50	150

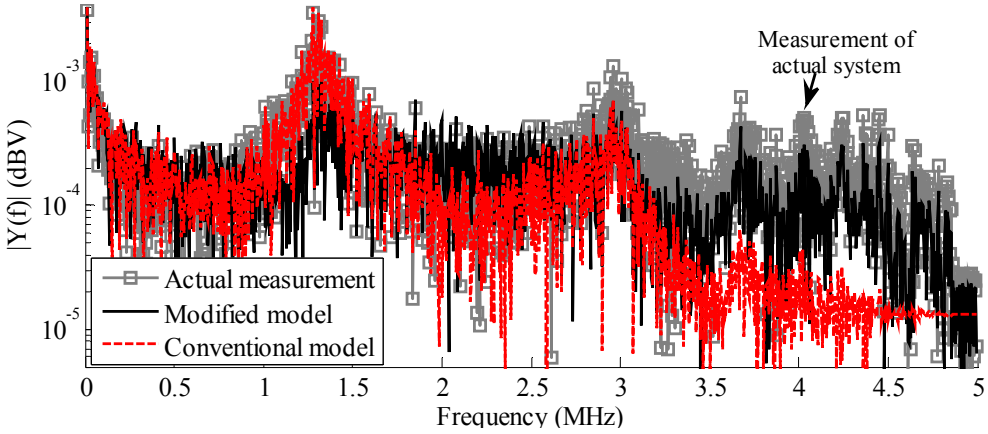

Figure 7.5 Frequency spectrum of synchronous machine's input current in Matlab.

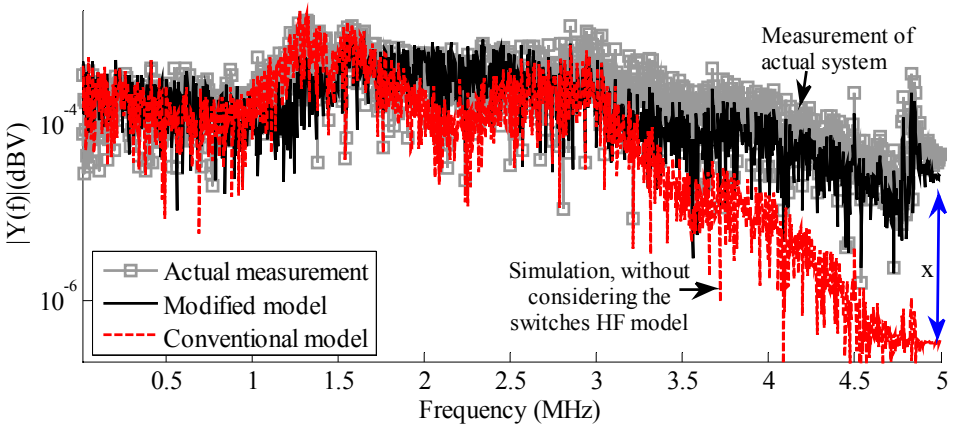

Figure 7.6 Frequency spectrum of the common mode current.

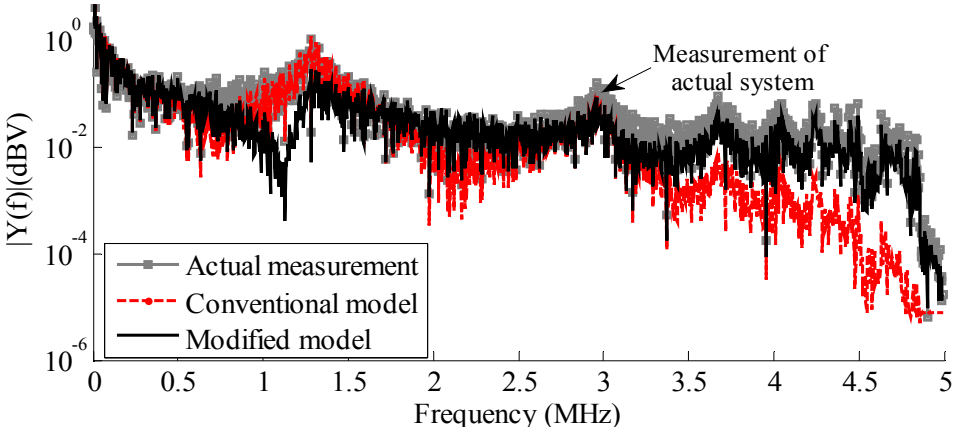

Figure 7.7 Frequency spectrum of the synchronous machine's input voltage.

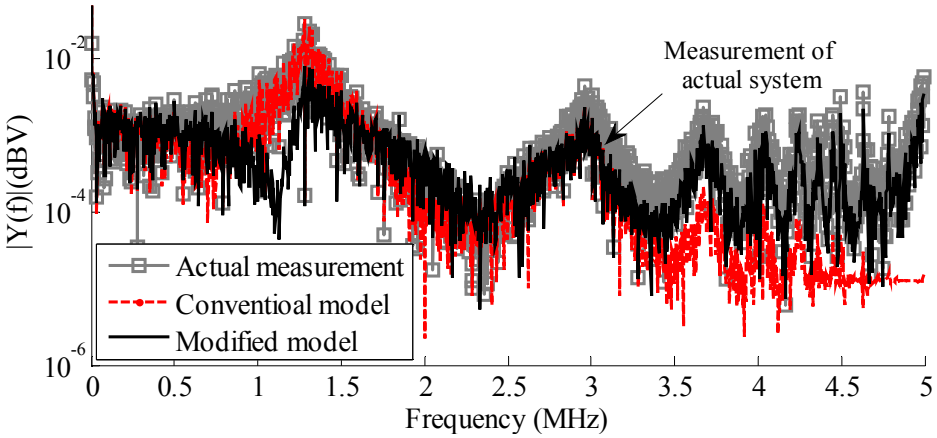

Figure 7.8 Frequency spectrum of the converter's output voltage.

As stated before, the HF models of the power cable and PMSM are reported in [106] and [107], respectively. To study the effectiveness of our models, the equivalent models for cable and PMSM were added to the inverter model and the simulation results are compared to the experimental results. To verify the accuracy of our numerical results, the common mode current of the setup in figure 7.4 was measured using the current probe with 100 MHz bandwidth.

Figure 7.5 shows the FFT spectrum of the converter input current. Also, the frequency spectrum of Common Mode (CM) current in motor drive system is demonstrated in figure 7.6. This current is measured at the ground port of the input DC power supply. In figure 7.7, the frequency spectrum of the converter input voltage is illustrated. Also, the frequency spectrum of the converter's output voltage is shown in figure 7.8. Figures 7.5-7.8 illustrate this current in two different cases; one of the cases is when the physics-based HF model for the inverter circuit is not considered (conventional model). The other case is when the converter is replaced with its corresponding physics-based model. As can be observed by considering the converter's HF model, the system

accuracy in estimating the actual power system's high-frequency behavior is improved. In the low-frequency range, where the noise is mainly caused by the switching action, the simulation matches the experimental results. In the high-frequency range where the noise is dominated by parasitic effects, the simulation was able to predict the HF behavior in frequency ranges of up to 5 MHz. However, this frequency for the conventional modeling method is up to 2 MHz. The parameter *x* (error value) in the figure 7.6 shows the difference between the conventional modeling approach and the proposed algorithm, in estimating the actual system behavior in higher frequencies. This error value at the frequency of 5 MHz is about 20 dB.

Differences between the results of the proposed model and actual measurement, in the high-frequency spectrum, may be caused by the unavailability of models of other switching noise sources and parasitic effects.

Performance Analysis of Planar Inductor Based Snubbing Circuit on EMI Effects Generated by Switching Action in DC/DC Boost Converter

In this study, a planar inductor based snubber circuit is presented for power MOSFET devices used in a Boost power converter. The proposed snubber can control the EMI effects caused by the switching actions which can affect the drive circuit. Appropriate use of the snubber and considering the parasitic elements in the switching circuits can improve the conducted EMI of the converter, eliminating the need for the bulky EMI filters. To design an effective snubber circuit, physics based model of the switch and the snubber circuit components are considered. Using impedance control method, the effects of various parasitic elements that can cause the common-mode noise can be controlled.

This effort enables the evaluation of interference issues for EMC evaluation studies early in the design process. The numerical results were validated experimentally.

This paper concentrates on the design and implementation of a customized dissipative voltage and current snubber circuit for power MOSFETs. The main contribution in this paper is that the effects of the parasitic components in the switching circuit are considered. Therefore, the snubber circuit is modified in a way to reduce the effects of these parasitic components. Initially, the parasitic components in the switching device and its corresponding snubber circuit are presented using the numerical approach. Subsequently, the proper snubber circuit is designed to cancel out the common mode current paths reducing the effects of parasitic elements.

Analysis and design of current and voltage snubber circuit

Figure 7.9 depicts the standard model of a Boost converter. One of the main problems with using this topology is the parasitic components that exist in the switching circuit. To reduce the effects of these parasitic components snubber circuit is used to protect the switch and lessen the EMI due to switching action.

The function of a current snubber is to control the rate of rise of current in the switch. The series inductance permits the switch to be fully turned on by the time the current reaches its operating value. This greatly lessens the peak power dissipation in the switch. It reduces the average dissipation in the switch and it increases the reliability [149], [150]. The current snubber also lowers the di/dt rate of switch current.

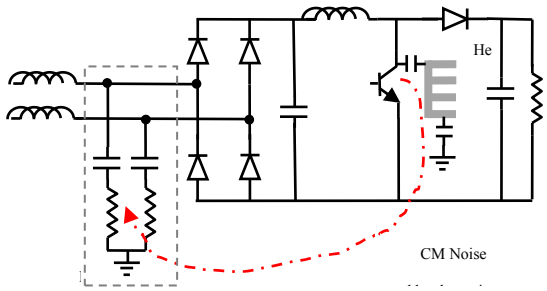

Figure 7.9 Current flow path for CM noise

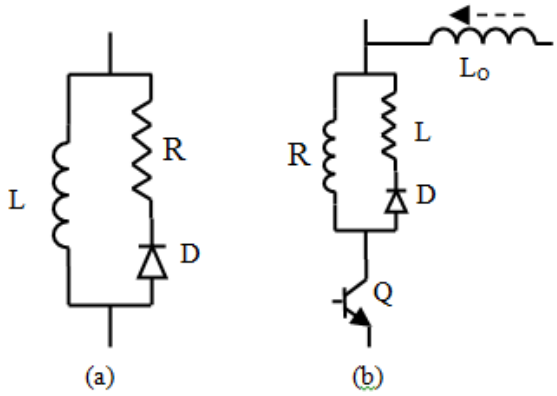

Figure 7.10 Current snubber circuit and its connection to the circuit, a) the current snubber circuit, b) its connection to the switch.

Figure 7.10 shows the current snubber and its connection to the switch. In this type of snubbers, the inductor operates normally when the switch turns on and the current only flows through the resistor when it is needed to dissipate the energy which is stored in the inductor. The amount of the power dissipated by the resistor is equal to $P = \frac{1}{2}LI^2f$ where I, is the peak current in the inductor.

To design the current snubber circuit, it is assumed that the switch is turning on into 30v. The switch current is 10 amps. An inductor of 1µH will give the diode 5ns to turn off. The power dissipation of the resistor is $W = 0.5\times10^{-6}\times10^{2}\times f_s$. With a 10 kHz switching frequency the dissipated power will be 0.5 watt. 20 Ω of resistance will give a 50 ns reset time constant which should be reasonable at 10 kHz ($\tau = \frac{L}{R}$).

The voltage snubber circuit shown in figure 7.11(a) is applicable to either rate of rise control or clamping. A typical application of a resistor-capacitor-diode snubber is to control the rate of rise of voltage on the drain or collector of a switching transistor. At turn-off, the snubber will carry a major portion of the switch current and this transfers the power dissipation of the switch into the snubber. The reliability of the switch increases since its peak power dissipation is reduced and the controlled rate of rise of the voltage also lowers the high-frequency EMI. Figure 7.11(b) shows how the snubber would be connected in the generic switch circuit [150].

The design of the snubber begins with the choice of the rise time at maximum inductor current and the supply voltage or the peak voltage of the capacitor. The relationship between the voltage and current in a capacitor allows the calculation of the necessary capacitor value. The switch current is 10 Amps and the maximum voltage is 30 V. The voltage rise time is to be 400ns. The capacitance necessary is 10nF. The time constant to discharge the capacitance is chosen to be 500 ns, which is compatible with a 10 kHz switching frequency.

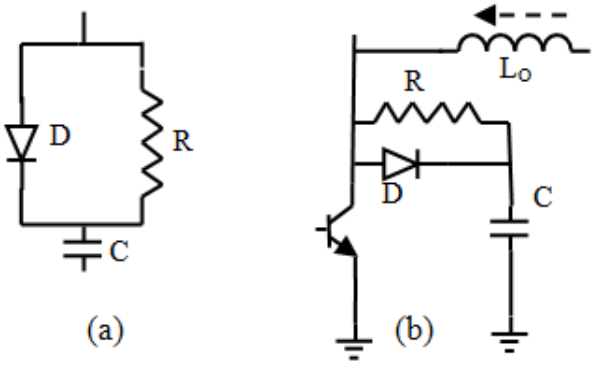

Figure 7.11 Voltage snubber circuit and its connection to the circuit, a) voltage snubber, b) its connection to the switch.

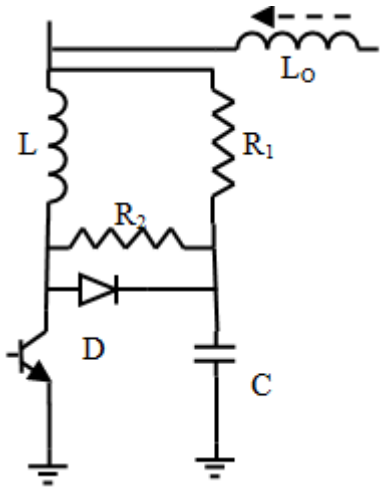

Figure 7.12 Connection of current and voltage snubber to the switch

Therefore, the discharge resistor value is 500 Ω. The amount of the power dissipated by the resistor is equal to $P = \frac{1}{2}CV^2f$, where V is the voltage that the capacitor is charged in each cycle. The power dissipated in the resistor is $P=0.5\times10^{-8}\times30^2\times f_s$ watts.

By a combination of the two proposed configuration shown above in figure 7.10 and 7.11, a type of snubber is designed that can limit the voltage or current rating. The proposed configuration is shown in figure 7.12.

In the next section, the application of the physics based modeling of the power semiconductor devices; the parasitic elements of these devices, which are the main cause for the EMI effects in the switching circuit, are modeled. The snubber circuit is modified in a way to suppress the EMI produced by these parasitic elements.

Physics based representation of the switching circuit components

In this section, the physics based model of the switching circuit is presented. The switching circuit consists of the power semiconductor device (in this case power MOSFET) and connected snubber circuit. In order to obtain the parasitic components

included in the switching circuit, the geometry and structure of the switching circuit components are modeled numerically FE, to evaluate their electrical and magnetic characteristics [151].

As presented in [152], a 2D electromagnetic FE analysis was performed to obtain resistances and inductances of the different layers in the semiconductor structure. The electrostatic problem is solved for the calculation of the capacitances. The electrostatic analysis determines the electric scalar potential distribution caused by the applied voltage in different layers then the capacitances were calculated based on the energy principle.

By applying voltage on the gate and drain, considering the source as a ground, the capacitance matrix is calculated from the stored static energy. The physics based MOSFET model is illustrated in figure 7.13. In figure 7.13(c) the low frequency MOSFET model is demonstrated as a block in which the internal parasitic components such as different layer's resistances, self-inductances, ground capacitances, the inter-layer capacitances within the device are connected.

In order to obtain the physics based representation of the whole switching circuit, it was modeled in finite element. By solving the FE model, the parasitic components of the switching circuit is obtained from low to high frequencies. The method used in this study is based on the lumped-parameter model presented in [153]. This method is used to obtain the s-domain model of the components which can be used to find the frequency response of the devices.

The other component of the proposed snubber circuit is the inductor, which also has an intrinsic effect on the EMI. Additionally, the snubber inductor can provide a path to flow the common mode current through its parasitic elements.

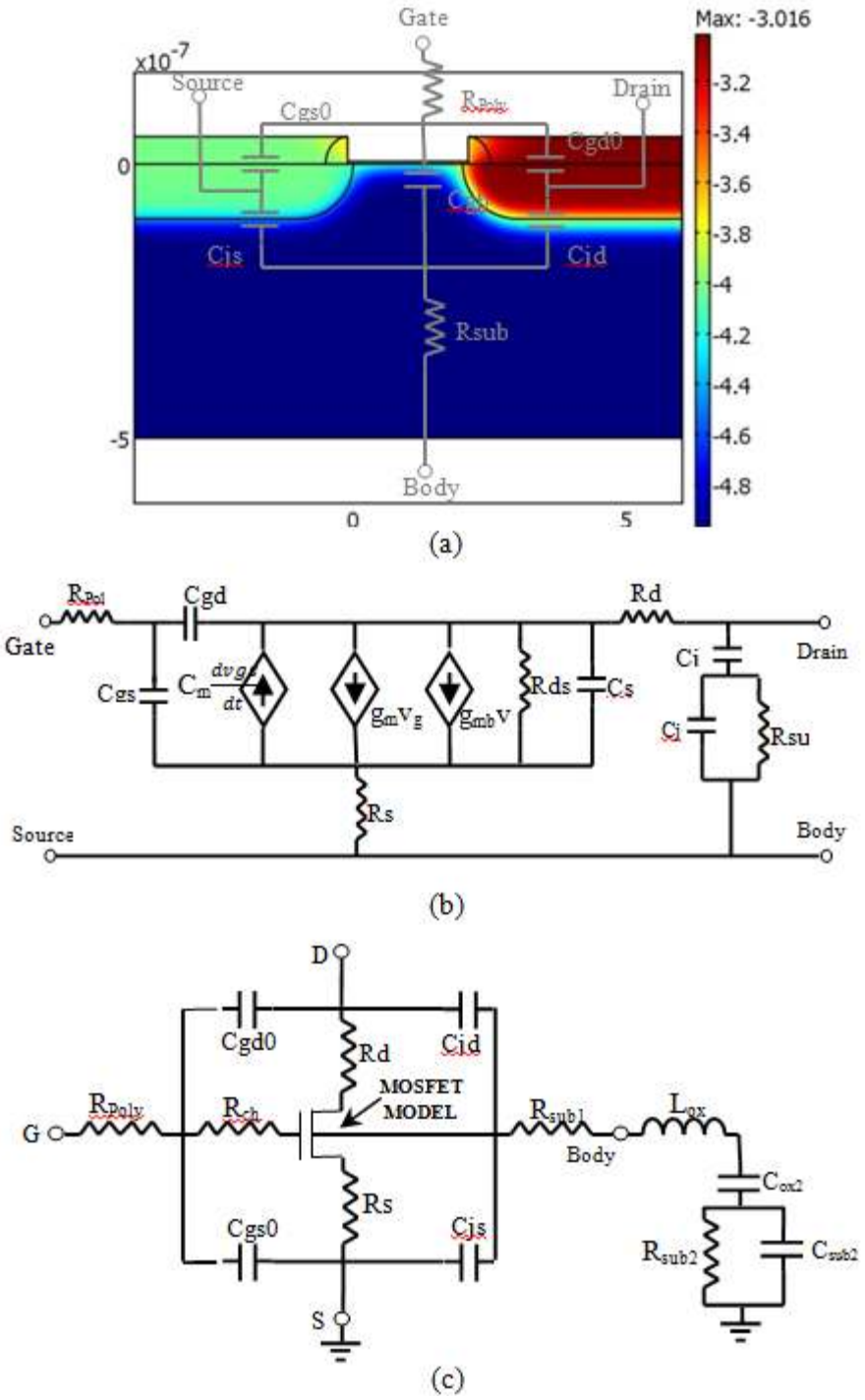

Figure 7.13 Physics based equivalent circuit of a power MOSFET, (a) Physics based model in FE software, (b) MOSFET equivalent electrical model, (c) MOSFET simplified equivalent model considering the parasitic components.

As stated in the above discussion, to meet the packaging constraints and ease of implementation, a planar inductor design is used in the design of the snubber circuit. The design and implementation of the planar inductors is described in [154], which is omitted here for sake of brevity. Based on the procedure described in [154], to implement a 1 μH inductor which can pass up to 3 A, a 2-layer winding each layer containing 5 turns was needed with a distance of 1.6 mm between the two layers.

The same procedure was used to model the planar inductor physics based model. The proposed model includes the windings' resistances, self-inductances, ground capacitances, the inter-turn capacitances within each winding. It also includes the mutual inductive and capacitive couplings between the two layers of windings. In [151], a three dimensional FE analysis model was performed on the resonant circuit components in order to calculate the parasitic elements of these components which can affect the operating condition of the converter.

The electromagnetic field inside the inductor and capacitor is governed by the following set of nonlinear partial differential equations [151]:

$$\nabla \times \left((\upsilon) \vec{\nabla} \times \vec{A} \right) = \vec{J} \tag{7-1}$$

$$\nabla . \sigma \left(\frac{\partial \vec{A}}{\partial t} + \nabla V \right) = 0 \tag{7-2}$$

where $\vec{A}$ is the magnetic vector potential, $\vec{J}$ is the total current density, υ is the magnetic reluctivity, V is the electric scalar potential and σ is the electric conductivity. By solving these equations, the resistance and inductance of the inductor are calculated as a function of frequency.

Also, the electrostatic problem is solved for the calculation of capacitances matrix as capacitances are a function of geometry rather than frequency. An electrostatic analysis is assumed to be a linear analysis which means that the electric field is proportional to the applied voltage. The analysis determines the electric scalar potential distribution caused by the applied voltage. The following Maxwell equation is solved during electrostatic analysis.

$$\nabla.(\varepsilon \nabla V) = -\rho \tag{7-3}$$

where ρ is the surface charge density, ε is permittivity, V is electric scalar potential.

Figure 7.14 shows the system structure in the FE model. This model was solved to estimate the values of the parasitic elements in the circuit model. Table 7.3 shows the number of nodes and element in the FE mesh in the different parts of the circuit.

To determine the frequency characteristics of the inductor we set $s = j\omega$ in the related equations. The input impedance of the component is calculated as (7-4) in FE software.

$$Z_{in}(j\omega) = \frac{V_{S1}(j\omega)}{I_{S1}(j\omega)} \tag{7-4}$$

Table 7.3 number of mesh in different part of the circuit.

Total number of meshes	Planar inductor Top layer	Planar inductor bottom layer	Heat sink	PCB Traces
Nodes	206438	213359	214685	182432
Edges	623845	652884	656878	607551
Faces	418534	439551	442219	391876

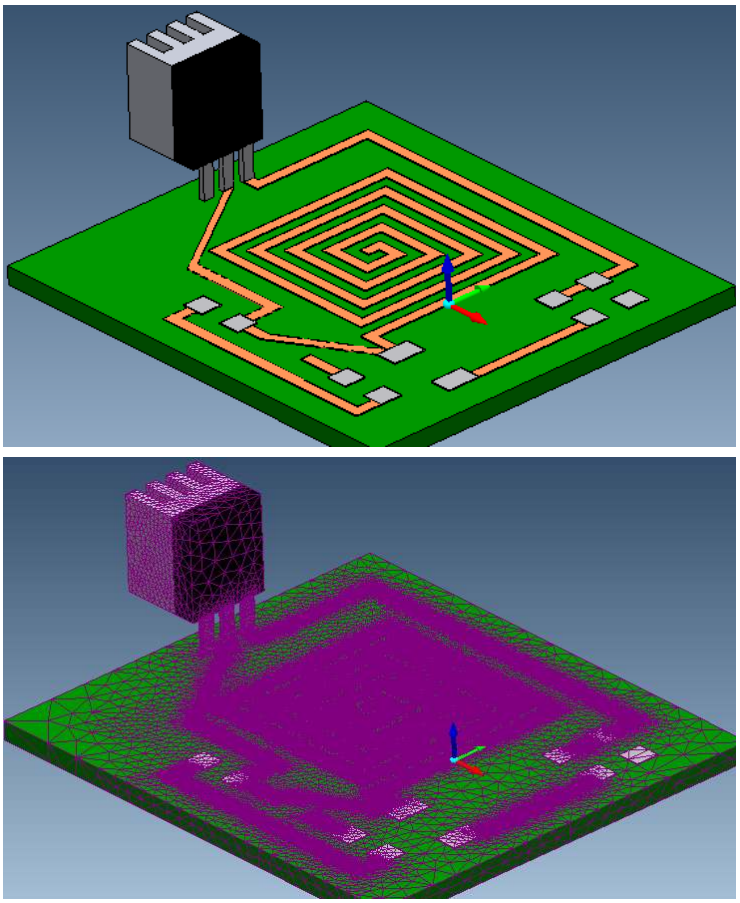

Figure 7.14 Snubber circuit model in Finite element and its corresponding mesh.

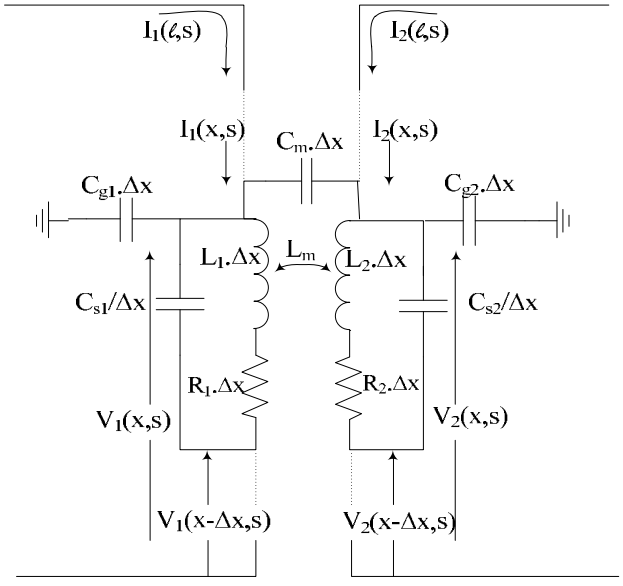

Figure 7.15 Infinitesimal section of a two-layer winding of planar inductor.

This calculation gives a rational function which can be represented by an equivalent electrical network as shown in figure 7.15. This network reflects the frequency dependence of the inductor resistance inductance and capacitance. The indices 1 and 2 in the inductor parameters stand for the first and the second layers of the inductor, respectively. Note that the neutral-end terminal point of the first layer is connected to the line-end terminal of the second layer. In figure 7.16, the drain-source voltage and current is illustrated. In this test, the MOSFET is implemented without connection of designed snubber circuit. Therefore, in the drain-source voltage there is a large tolerance in transition from on to off state. Also, a large current spike occurs in the switch's current. These voltage and current ripples can defect the semiconductor device.

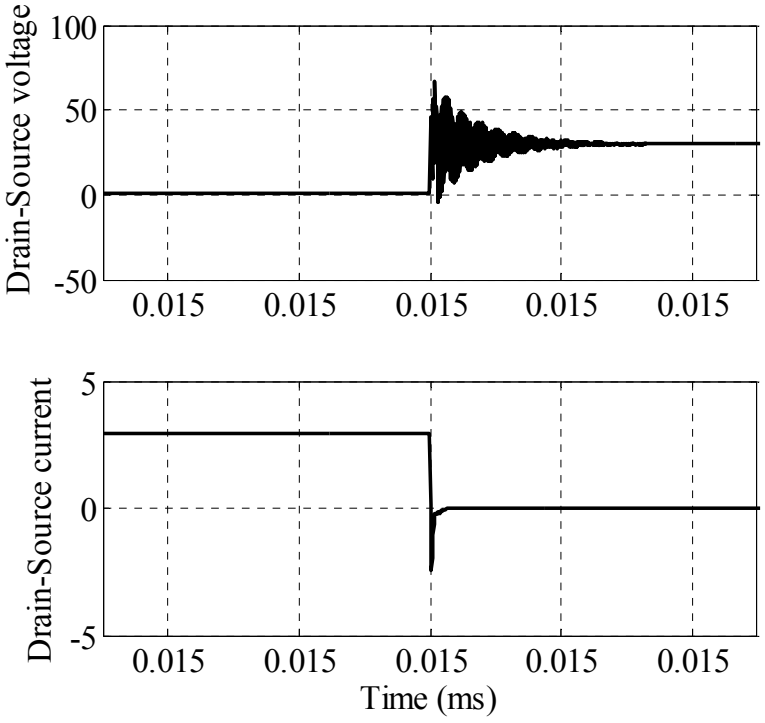

Figure 7.16 MOSFET drain-source voltage and current.

For the effective design of an EMI suppressor, the high-frequency model for the MOSFET is reduced to a simplified model. The same procedure is accomplished for the inductor circuit. Figure 7.17 shows the simplified physics based model, for the MOSFET and its connected snubber components, including the simplified lumped parameter model for planar inductor and the capacitor. In this model, the high frequency circuit model for the connection of the MOSFET to the PCB traces is also considered.

To modify the snubber circuit shown in figure 7.11, the equivalent circuit shown in figure 7.17 is used. Using the method proposed in [155], the model shown in figure 7.17 can be simplified, according to Thevenin's theorem. The simplified circuit is shown in figure 7.18. The final equivalent circuit is found by Thevenin's theorem. V_{equ} is derived as:

$$V_{equ} = -V_{ds} \cdot \frac{C_{B1}}{C_{B2}} \tag{7-5}$$

Therefore, connecting a high frequency decoupling capacitor C_{HF}, in parallel with C_{B2} the absolute value of V_{equ} will be decreased. For EM noise deduction in the semiconductor switch, the circuit shown in figure 7.17 is proposed. In this circuit, the proposed snubber circuit is connected to the MOSFET.

As mentioned earlier, the MOSFET switches are implemented in a converter supplying an RL load, with a 10 Ω resistance and 3-mH inductance. This time the MOSFET in the previous circuit is substituted with the circuit shown in figure 8.19. This model is implemented in Matlab/Simulink. The MOSFET gate is switched with a constant pulse width modulation of 2 kHz.

In figure 7.20, the drain-source voltage and current is illustrated. In this test, the proposed snubber circuit is connected to the MOSFET. Therefore, there exist lower amount of tolerances in the drain-source voltage. Also, the drain-source current has lower amount of spike as compared to the previous circuit.

Figure 7.21 shows the circuit layout for the circuit under test. This circuit contains all the components designed for the proposed circuit, in addition to the MOSFET and is used in a test Boost converter circuit.

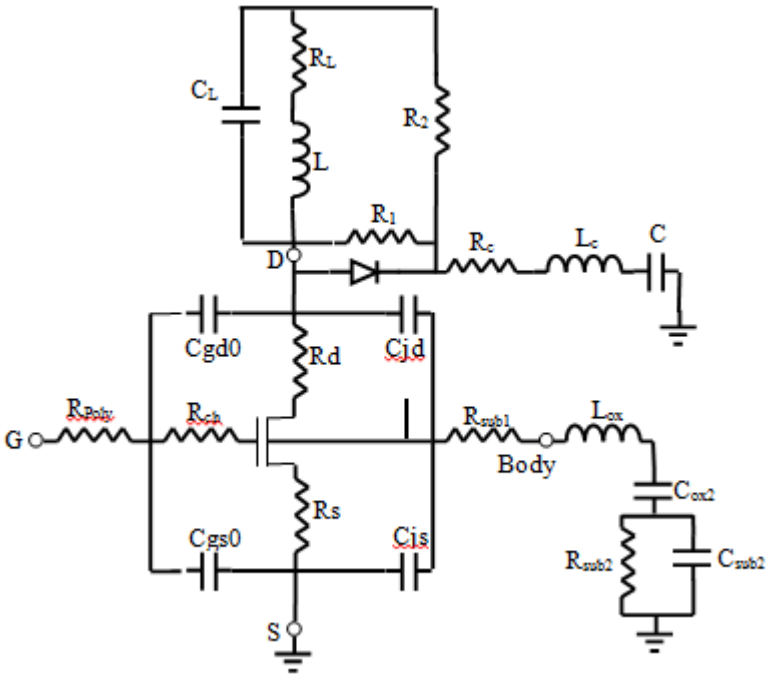

Figure 7.17 Simplified physics based model for the MOSFET and its connected snubber.

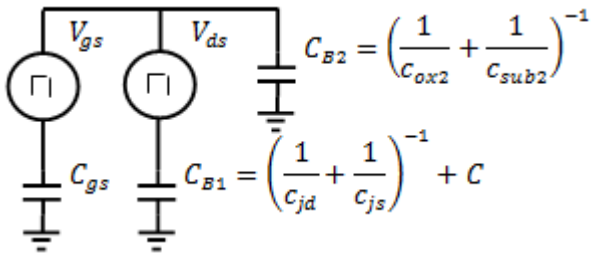

Figure 7.18 High frequency equivalent circuit.

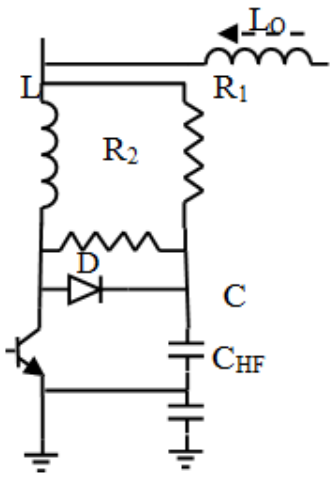

Figure 7.19 Proposed snubber circuit for power MOSFETs.

In this layout, the inductor is printed on the PC board. By proper arrangement of the components in the circuit the length of copper traces will be reduced. This leads to lower amount of trace's stray inductance and resistance which increase the reliability of the circuit. Also, the board's space occupied by the snubber circuit components is effectively reduced. This criterion must be considered when designing the printed circuit boards, because the parasitic elements in the copper traces and between the components defect the operation of the snubber circuit and will cause the propagation of EMI noises in the board. The circuit parameters are all listed in Table 7.4.

In order to verify the performance of the proposed snubber circuit, figure 7.22 and 7.23 show the experimental results, for the switch on and off time transition. Figure 7.22 and 7.23 show two cases with and without snubber circuit, respectively. As can be seen, the voltage tolerances are effectively reduced to 10 percent of the maximum voltage.

Table 7.4 Proposed snubber circuit parameters

R_1	R_2	L	C	C_{HF}
0.5	200	1μH	10nF	10μF

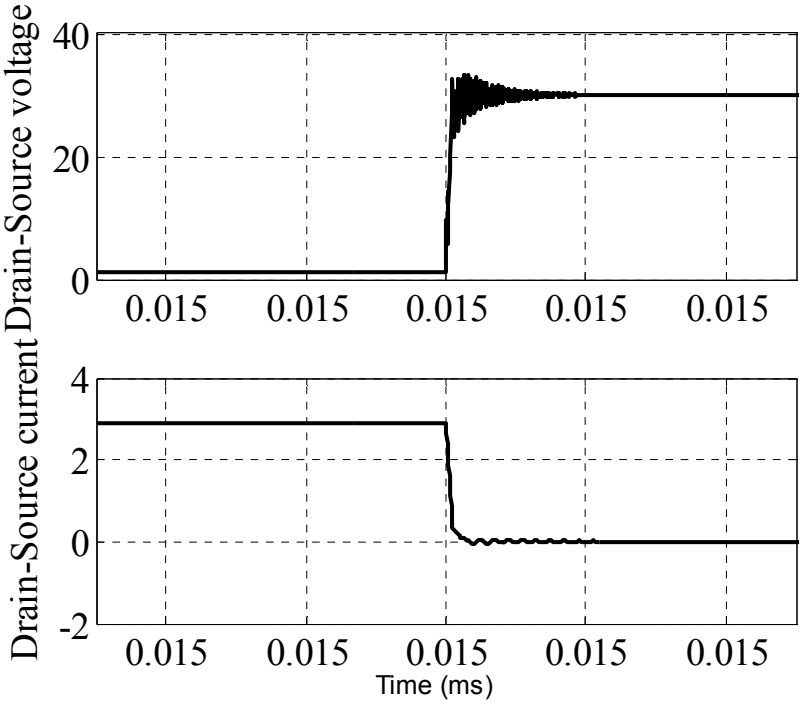

Figure 7.20 MOSFET drain-source voltage and current.

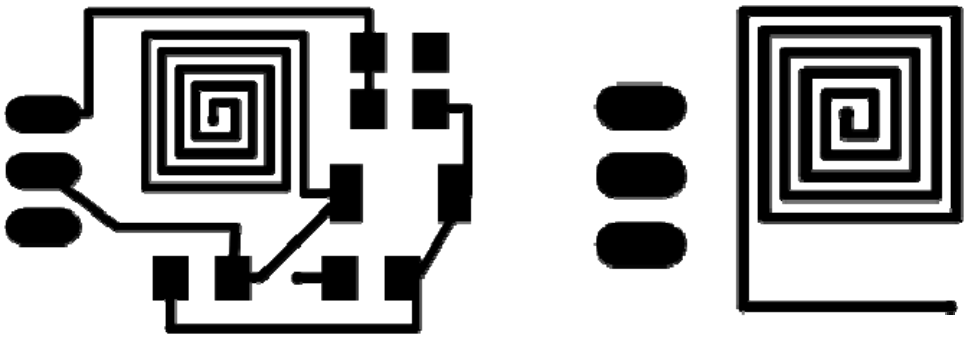

(a) (b)

Figure 7.21 Circuit layout for snubber circuit and MOSFET on PCB, (a) Top layer, (b) Bottom layer.

In this case, the maximum voltage on the switch is 30V to verify the performance of the proposed snubber circuit and the peak to peak tolerance of the voltage is 3V.

Figure 7.24(a) shows the FFT spectrum of the converter switching signal. Also, the frequency spectrum of Common Mode (CM) current in Boost converter system is demonstrated in figure 7.24(b). This current was measured at the ground port of the input DC power supply. Figure 7.24 have illustrated this current in two different cases; one of the cases is when the proposed snubber circuit is used and the other case is when the conventional snubber is being used.

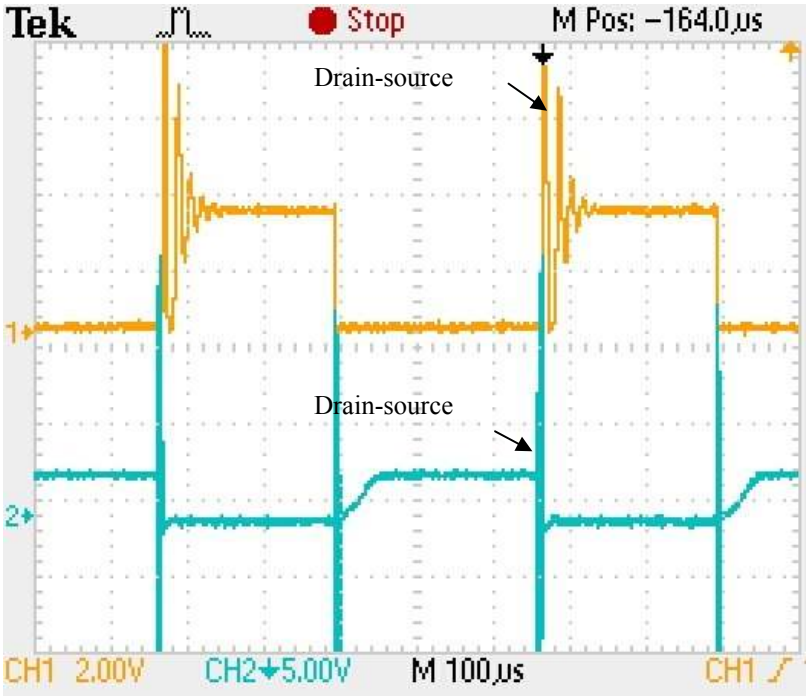

Figure 7.22 MOSFET current and voltage waveform in the circuit, f=2 kHz, $V_{DS}^{(peak\text{-}peak)}$=30 volts, $I_{DS}^{(peak\text{-}peak)}$=3 amps

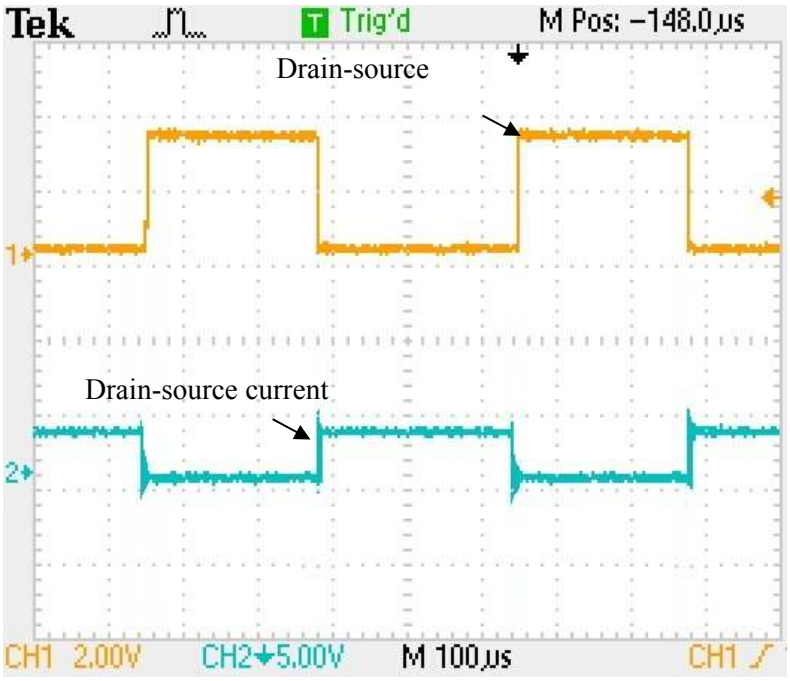

Figure 7.23 MOSFET current and voltage waveform in the circuit, f=2 kHz, $V_{DS}^{(peak-peak)}$=30 volts, $I_{DS}^{(peak-peak)}$=3 amps

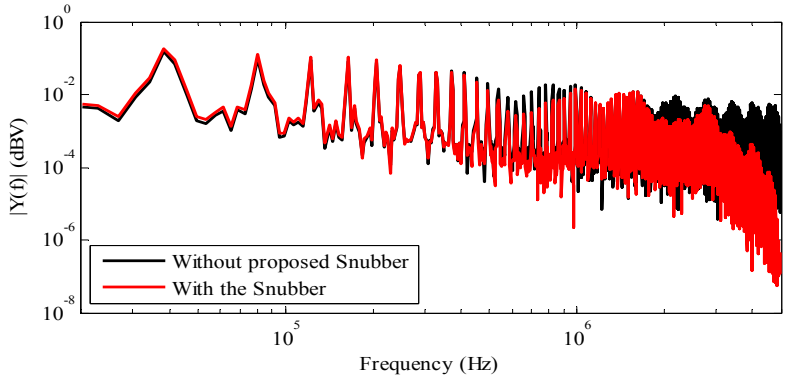

(a)

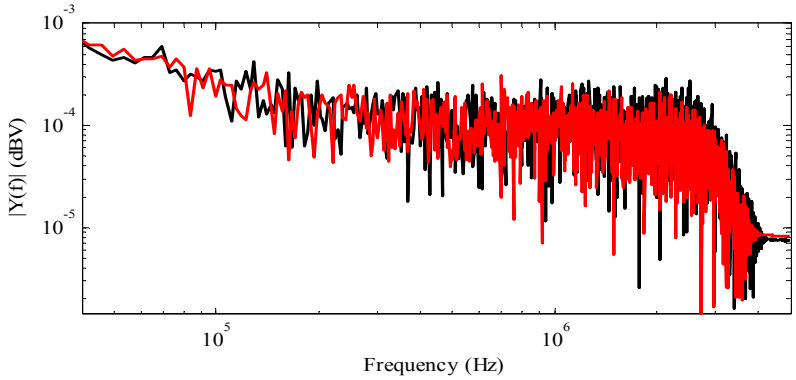

(b)

Figure 8.24 (a) Frequency spectrum of the converter switching signal, (b) CM current.

Analysis of Radiated EMI and Noise Propagation in Three-Phase Inverter System Operating Under Different Switching Patterns

In this study, a numerical model using the finite-element (FE) method was used to predict the electromagnetic interference (EMI) generated by 325V, 5kW power inverter, supplying a variable three-phase load. A comparative analysis was performed to evaluate the effects of different switching patterns on the radiated and conducted EMI levels. An experimental setup was arranged to validate the simulation results. The proposed approach is suitable for prediction of radiated and conducted EMI generated by power converters. This helps reduce the post prototype EMC testing cost by minimizing redesign and modifications of final converter product.

To mitigate the level of EMI generated in the system, in the conventional design methodologies, a costly approach of adding extra components to the inverter's circuit and proper shielding was used to limit the EMI to the EMC standards. In this study, the switching pattern of the inverter was used as a factor to control the EMI level of the system. A circuit coupled FE model was used to study the effects of three different switching patterns, 1) Hysteresis, 2) Space Vector (SVM) and Sinusoidal PWM (SPWM), on the generated electromagnetic fields and conducted noise propagated through the system. The power circuit was constructed by combining the actual switch model including the parasitic components in a circuit simulator program. Subsequently, this model was coupled to a complete converter FE model. A quasi-static transient simulation was performed, to evaluate the levels of electromagnetic fields.

Physics-based modeling of the power inverters

To obtain the Physics-based model, the geometry of the actual system was modeled in finite elements. The 3DFE based model of the inverter system is illustrated in figure 7.25. In this model, the elements which are responsible for noise propagation and field radiation are the semiconductor switches, the bus bars, the heat sink and the connection cables.

The semiconductor switches were modeled as flat iron plates in the FE model, due to their negligible effects on radiated fields as compared to the other conductors in the inverter system. The effects of semiconductor devices are only noticeable in the form of conductive noises. Therefore, a physics-based analytical model of the semiconductor devices is placed in the circuit model (Simulink) to observe the high frequency oscillation and noises produced by the switching action. The model used for the semiconductor devices was introduced in [156]. This model is composed of the device analytical model along with the parasitic components.

The aluminum heat sink and iron sheet under the inverter are connected to ground. In the other parts of the inverter, the parameters are considered to be as follows: the relative permittivity, ε_r, is 4. Its relative permeability, μ_r, is 1 and its conductivity, σ, is 0 S/m. The dimensions of the inverter package are "30×30×25 cm". The inverter system was then placed in a cube defined by an air volume.

The FE model of the inverter is coupled to the Matlab/Simulink environment as shown in figure 7.26. In this model, the semiconductor switches were modeled analytically using the approach introduced in [156]. The current direction was calculated in Simulink and was passed through the different parts of the inverter model in the FE domain. This is to calculate the propagated noise and radiated fields.

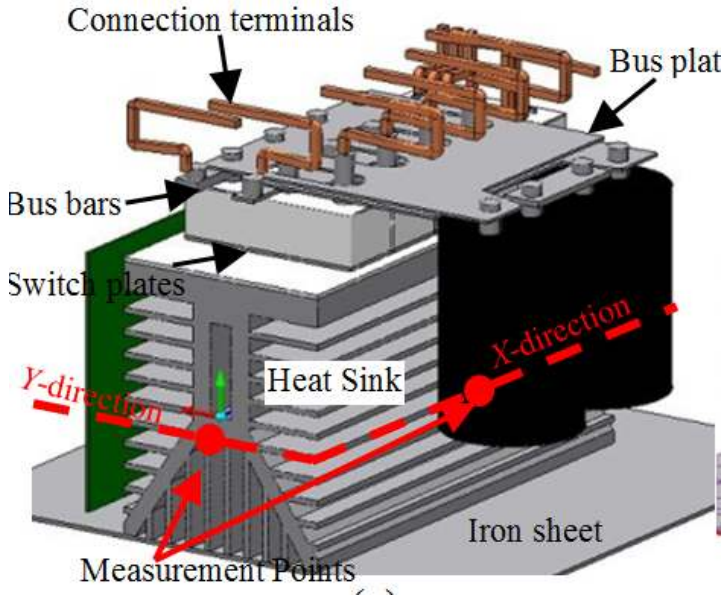

(a)

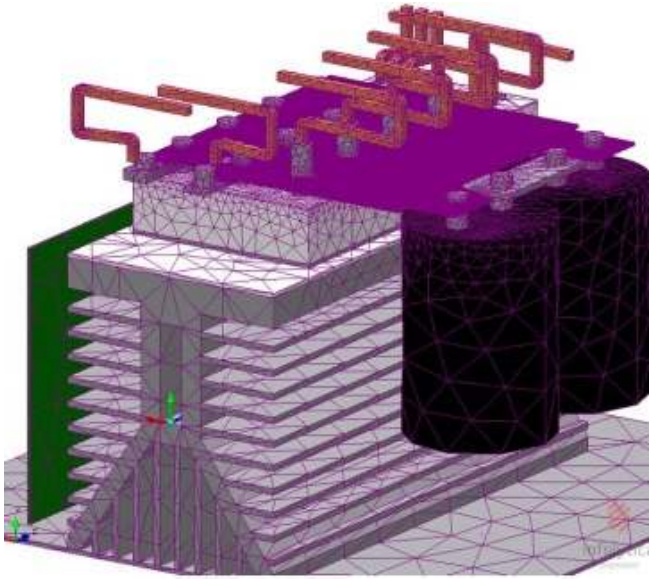

(b)

Figure 7.25 (a) Inverter package model in FE, (b) inverter meshing in FE,

Finite Element Electromagnetic Analysis

To determine the radiated EMI and propagated noise, two steps were followed. In the first step, the parasitic capacitances are calculated based on (7-6) in a static FE domain. The electrostatic problem is then solved for the calculation of the capacitances matrix, as capacitances are a function of geometry. This analysis determines the electric scalar potential distribution caused by the applied voltage. The calculated parasitic capacitance's path determines one of the propagation paths for conductive noises (the other type of paths are introduced by the coupling between the current handling conductors in the system). These capacitors are connected to the low frequency circuit model, as shown in Figure 7.26.

$$\nabla.(\varepsilon \nabla V) = -\rho \tag{7-6}$$

The calculation procedure for the parasitic capacitances is as follows:

Step 1- Solve (7-6), in static FE domain. Here, we define the different conductive parts of the inverter as an electrode with a constant voltage. The heat sink and its connected metal sheet are connected to ground. In the inverter's model, the DC bus conductors, bus bar plates, connectors to the switches, the DC bus capacitors and the semiconductor devices plates are defined as the electrodes. An 8×8 capacitance matrix was defined among all these electrodes and the ground as shown in figure 7.26.

Step 2- The electrostatic energy is used to obtain the capacitance matrix of the model. The electrostatic energy is calculated by:

$$W = \frac{1}{2}\iiint_V \varepsilon.(D_1.E_1)dv + \frac{1}{2}\iiint_V \varepsilon.(D_2.E_2)dv + \frac{1}{2}\iiint_V \varepsilon.(D_1.E_2)dv \tag{7-7}$$

where D_i is the electric displacement current and E_i is the electric field inside the model. Self and mutual capacitances are calculated based on electrostatic energy value as (7-8).

$$C_{ij} = \frac{1}{V^2} \iiint_V \varepsilon_0 . (D_i . E_j) dv \tag{7-8}$$

Table 7.5 is showing the values for parasitic capacitance between different electrodes in the model shown in figure 7.25.

Table 7.5 Coupling capacitances between different electrodes.

Capacitor:	A	B	C	D	E	F
C(pF)	6.54	7.15	3.28	917.2	5.98	6.11

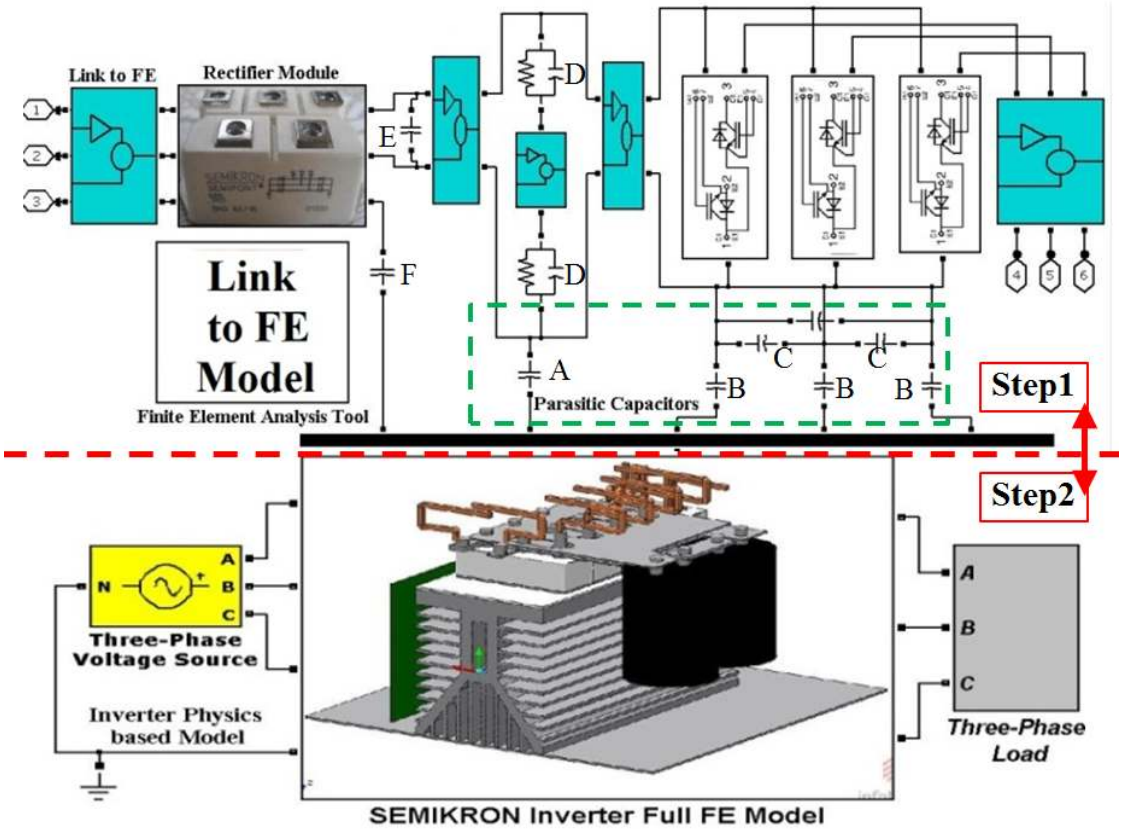

Figure 7.26 Circuit coupled FE model of three-phase inverter system.

In the second step for the evaluation of the radiated field, the implemented circuit from the first step was connected to the FE model of the inverter system using a coupled field circuit approach. The radiated EMI will propagate through all the components of the electric drive system; the model equation in the field domain is expressed as:

$$\sigma \frac{\partial A}{\partial t} + \nabla \times \left(\mu^{-1} \nabla \times A \right) = J^e \tag{7-9}$$

where σ is the conductivity, A is the vector potential, J^e is the external current density, μ is the permeability, ε is the permittivity and V is the voltage potential and ρ is the space charge density.

In the circuit-field coupled model, the sampling rate is 5μs, which is far above the maximum switching frequency. Based on Nyquist theorem, if the sampling frequency of the system is f_s, then the harmonics up to $f = f_s/2$ are observable (in this case, $f_s = 200\ kHz$). The FE model was implemented on a 16 core CPU, 190 GB of RAM server. We modeled a time period of *T/4* and the total number of elements in the model was 376684.

Results and Discussion

For simulation purposes, three switching techniques (Hysteresis, SVM and SPWM) with carrier frequency of 5 kHz applied to the inverter. In the case of the hysteresis current control mode, in which the switching frequency is variable, the hysteresis band was selected in a way that the maximum switching frequency, which is obtained at zero-crossing, is about 3 kHz. A three-phase 5 kW RL load was connected to the inverter, which makes the inverter operate at nominal power. The calculated currents were then

injected to the terminals in the 3D-FE based model. The 3D-FE solution was obtained using harmonic propagation analysis. The step time for this simulation was 5 μs. To validate the obtained numerical results, the experimental setup was implemented and the inverter's phase current spectrum is measured using a spectrum analyzer and a 100 MHz current probe. The measured and simulated frequency spectrums of the inverter's phase current for different switching techniques are shown in figure 7.27(a) to (c), respectively.

Figure 7.28 shows the comparison measurement results between three different control techniques, in simulation and experiments, respectively. It is observed that the hysteresis current control method generates larger amount of harmonics in the inverter output current as compared to SVM and SPWM.

It is observed that there is an error between the simulation and experimental results. This error is mainly due to the un-modeled current paths in the system. In terms of the current paths, there exist a lot of uncertainties for defining a general rule for the path creation for the system. These uncertainties mainly come from the unclear ground paths inside the system, relative orientation of the system, electric field and the uncertain impact of the noise currents induced by the internal field of the system. However, it can be mentioned that if a model was created, this model can be the same for all scenarios where the material properties and ground currents are the main factors that affects the radiated EMI [157].

To analyze the radiated field from the inverter, the magnetic field for different switching patterns is measured along the indicated lines in figure 7.25. The patterns of the magnetic field and magnetic flux density versus time and position were extracted from the FE solutions.

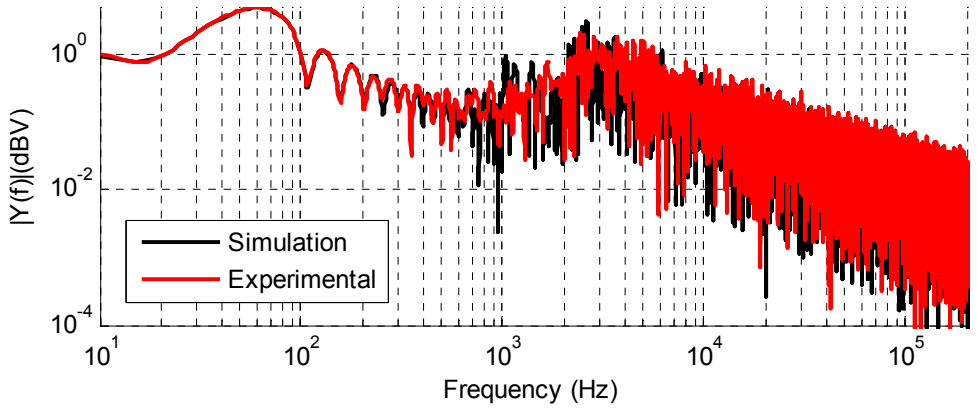

(a)

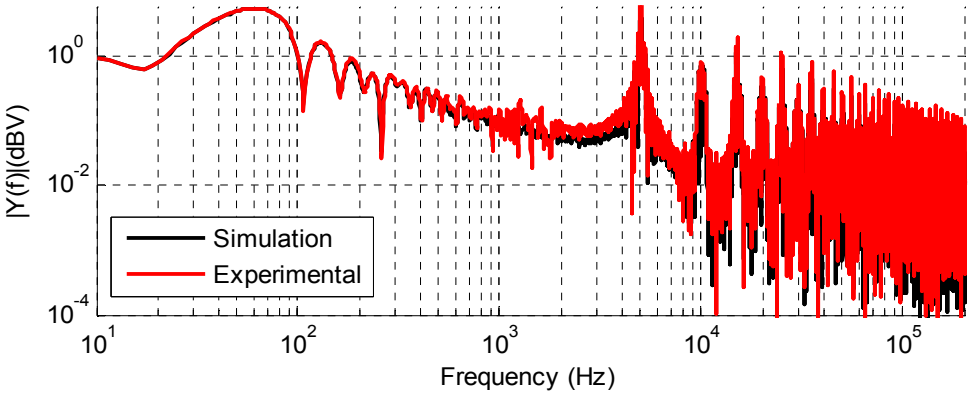

(b)

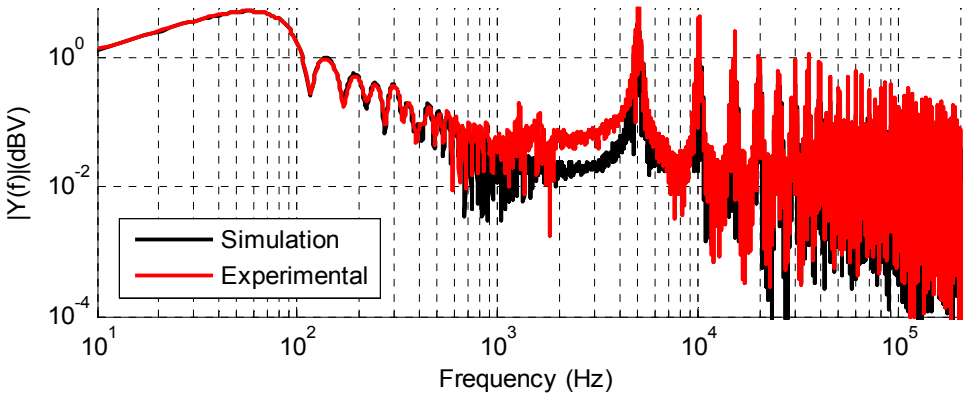

(c)

Figure 7.27 Comparison of the frequency spectrum of the inverter's phase current between circuit model and experiments, (a) Hysteresis current mode control, (b) SVM, (c) SPWM.

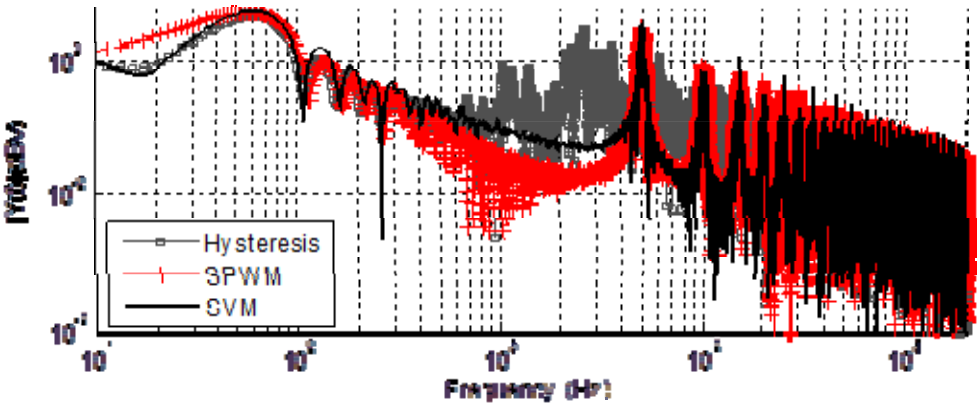

Figure 7.28 Measured frequency spectrum of the inverter's phase current.

The results of the simulation of the 3DFE model show the patterns of the radiated EMI over time at different switching techniques and at specific instances of time, in the x and y directions.

Figure 7.29 shows the test setup for measurement of the magnetic field. In this setup, the magnetic field was measured using a coil antenna. The values are plotted in the frequency domain using a spectrum analyzer in the frequency range of 10 Hz to 200 kHz.

The behavior of the radiated EMI can be shown as a function of position. The magnetic flux density was evaluated over a distance of 10 cm on either side of the inverter. The fields are shown at several instances of time that occur before, during and after switching. Figure 7.30 shows the simulation results for the magnetic flux density in three switching patterns, in *x* and *y* direction. It can be noted how the amplitude of the magnetic flux density changes with the change in switching technique.

Figure 7.31 show the experimental results for the magnetic flux density in the *x* and *y* directions. In order to understand the effects of the switching pattern on radiated field, the value of the maximum peak of the frequency spectrum of the magnetic field were

compared. As we can notice, the hysteresis current control is showing a higher peak as compared to the other switching patterns.

Figure 7.32 shows the top view of average of magnetic flux density for 0.5 ms on the *x-y* plane. The sampling frequency is 5μs and the switching frequency is 5 kHz. One can see that the intensity and propagation of the average field is higher in Hysteresis modulation than that of the SVM and SPWM. This is a good example of how the patterns of the radiated EMI fields can be analyzed using this model.

The Simulink model for the power inverter model allows us to study different aspects of the electric drive design that may affect the radiated EMI. Within this model, various parameters can be changed and studied in order to identify an EMI mitigation strategy during the design stage of these systems [157]. In the proposed model, the EMI can be analyzed at any point or plane within the simulation volume and can be solved for different switching patterns. The time dependence of the radiated EMI can also be evaluated using the model.

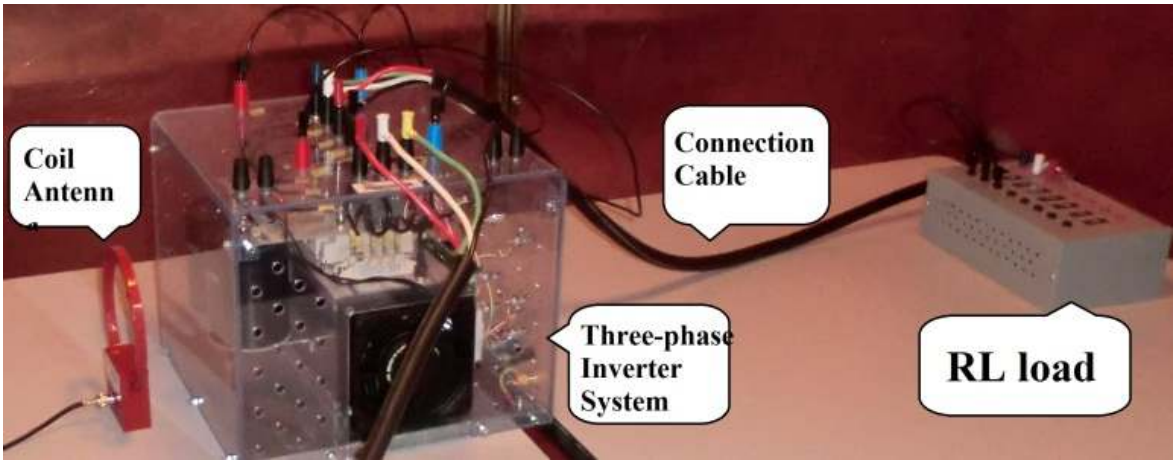

Figure 7.29 Experimental setup and measurement coil antenna in a semi-anechoic RF enclosure.

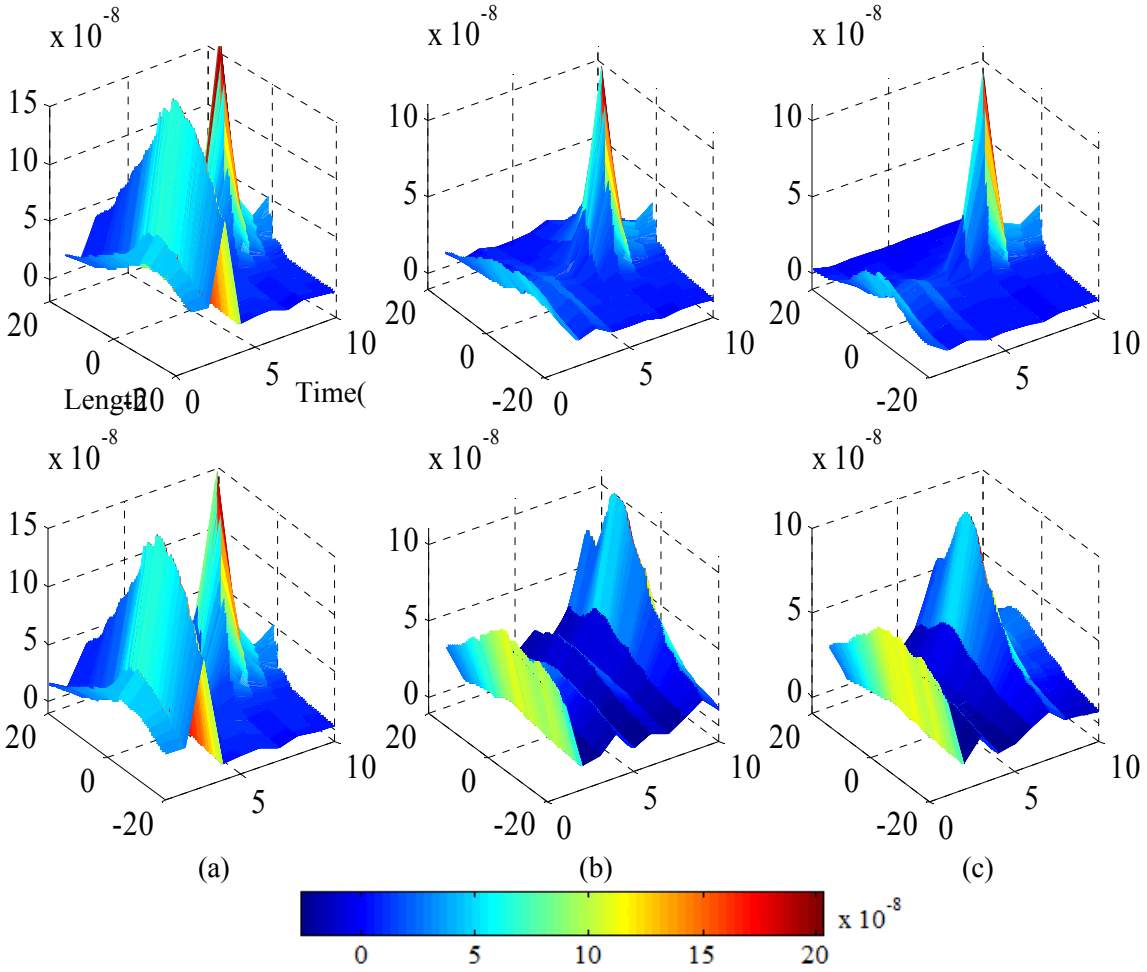

Figure 7.30 Magnetic Flux Density versus position for different switching patterns, *x*-direction (Top raw), *y*-direction (bottom raw), a) Hysteresis current control (Left column), b) SVM (Middle column), c) SPWM (Right column)

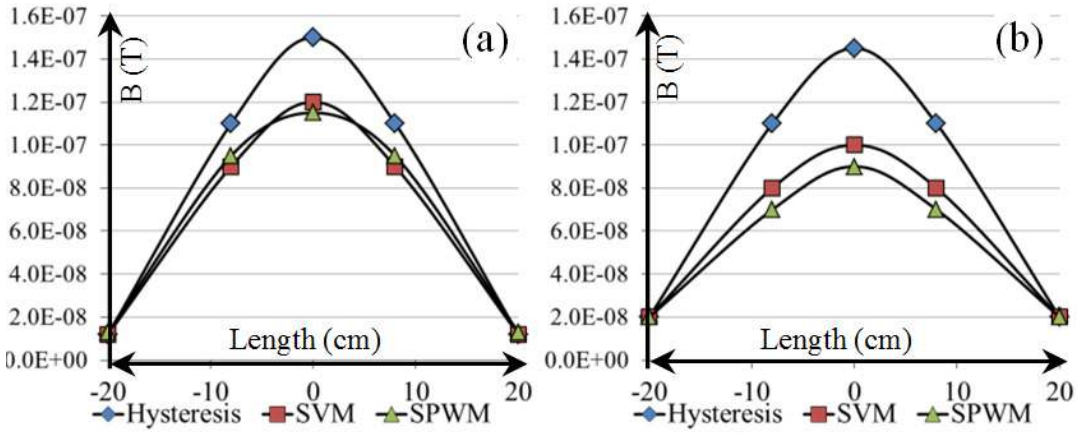

Figure 7.31 Magnetic Flux Density at different switching patterns measured using coil antenna, a) *x*-direction, b) *y*-direction.

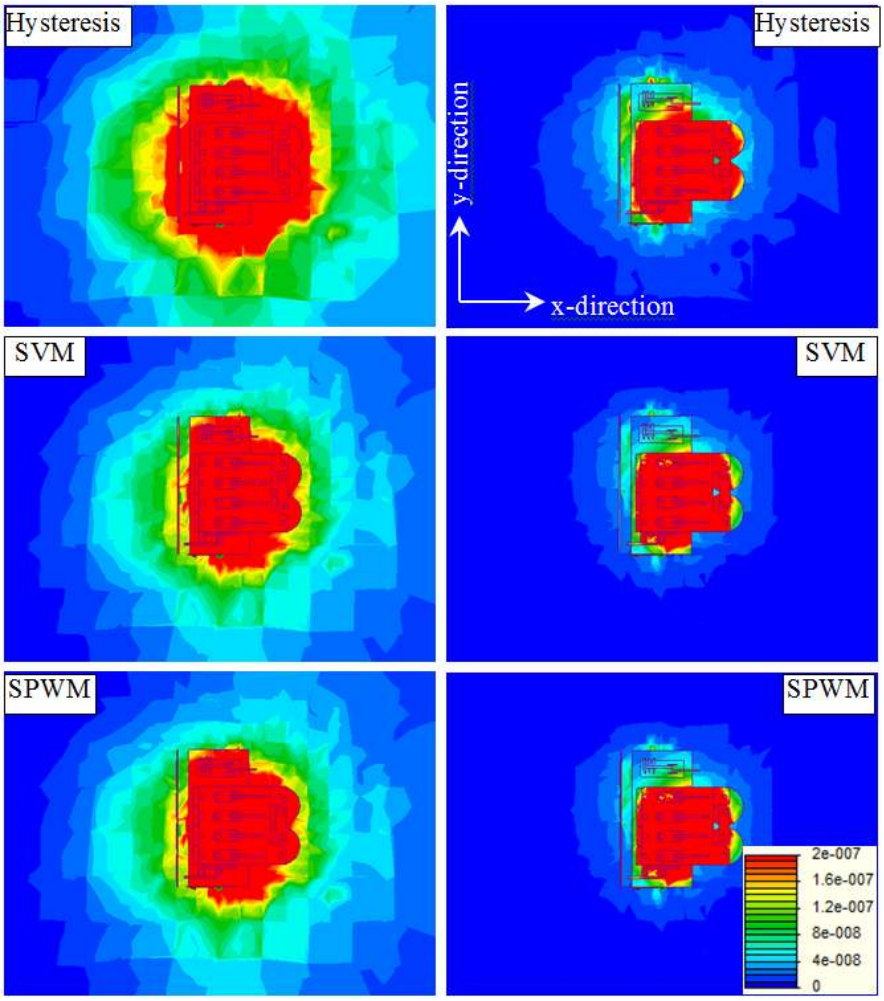

Figure 7.32 Magnetic flux density at different switching patterns before (left) and during switching (Right), a) hysteresis, b) SVM, c) SPWM

We can see how the magnetic flux density behaves over time at specific locations and at various switching patterns and frequencies. Furthermore, the field image can be obtained for various scenarios specified by the designer and provide them with information that can be obtained quickly. This would allow for efficient and effective complete design work using computational electromagnetics.

Numerical Simulation of Electromagnetic Field Correlation between Components of Power Converter-Pulse Load System

In this study, the electromagnetic field generated by a motor-drive system, consisting of an inverter, induction motor, connection cables and a AC load, is analyzed using 3D finite element (FE) model as well as experimental measurement. A new approach is proposed to model switching of the converter physically in 3DFE. Besides, the modified solution method is used for analyzing nonlinear materials. The frequency response analysis is implemented by simulation and measurement in various location and distances. The numerical simulation provides the exact field solution at a far distance and analyzes the correlation between the electromagnetic fields generated by each of these components. The implication of this study is to evaluate electromagnetic field radiation for EMC compliance at the design stage. Besides, the optimum operation of the devices for less EMI is proposed. This can be utilized in wireless monitoring of a power system.

Emission of low order harmonics can often be modeled using equivalent circuit modeling as current sources, while high order harmonics normally appear as voltage sources. In between these two simplified models there is naturally a more complex reality. Resonances may increase the complexity further. In addition, equivalent circuit modeling of power electronic drives doesn't show the radiated emission in the 3 dimensional areas around the drive. Therefore, the physics bases modeling is proposed in this paper which show the radiated field in three dimensional spaces around the device. Besides, the materials of the devices as well as accurate shape of them are investigated through this modeling. On the other hand, time-varying electric and magnetic fields generate MMFs and EMFs that can sustain the fields that compromise the flux. Also, the currents and voltages in electric power

systems are time-varying, which causes radiate electromagnetic fields. Therefore there is a need to model the EMI generated by these systems, in order to meet the EMC standards.

Several studies have been performed in the area of radiated low frequency electromagnetic field (EMF) analysis of power electronic devices [158]-[162]. Some authors have worked on the impact of radiated EMFs on environment including human being, in addition to devices [158]. Furthermore, a number of researchers have dealt with attenuation and shielding of the radiated EMF [159], [160]. In addition, physics based modeling of the PE drives in low frequency EMF is studied in [161], [162]. Various types of modeling are proposed in these papers. In this dissertation, three dimensional full finite element modeling of a typical power electronic drive in low frequency is analyzed. The frequency response of the drive is implemented in simulation and experiment and the results are compared. Finally, having these results, the application of this study is discussed.

Radiated low frequency field calculation

Due to the Hertzian dipole and Maxwell equation, the electromagnetic potential of a dipole around the z-axis at a point P (r, θ, ϕ) is given by:

$$\mathbf{A} = \frac{\mu I\, dl}{4\pi r}\mathbf{a}_z \tag{7-10}$$

However, for time variant currants, the potential in (7-10) would lead to be an inconstant field with Maxwell equation. The reason is that time-variant fields give rise to wave propagation, according to which the effect of the source current at a given value of time is felt at a distance *r* from the origin after a time delay of r/υ_p, where υ_p is the velocity of propagation of the wave. Considering this, the retarded magnetic vector potential is given by:

$$\mathbf{A} = \frac{\mu I_0 \, dl}{4\pi r} \cos(\omega t - \beta r)\mathbf{a}_z \tag{7-11}$$

where β is r/υ_p, the phase constant. The magnetic field **H** due to the Hertzian dipole is given by;

$$\mathbf{H} = \frac{\mu I_0 \, dl \sin\theta}{4\pi} \left[\frac{\cos(\omega t - \beta r)}{r^2} - \frac{\beta \sin(\omega t - \beta r)}{r} \right] \mathbf{a}_\phi \tag{7-12}$$

Equation (7-12) represents the radiated magnetic field due to the Hertzian dipole [163]. The radiated field of a complex model with thousands of dipoles, such as the proposed drive, needs calculating the field of each of these dipoles and having the whole field by using a numerical method such as the well-known finite element (FE) method. The proposed model is accurately built in FE in which the above equation is calculated.

Simulation and measurement

As mentioned above, the proposed model consists of an inverter, induction machine, connection load and an AC load. The study is divided in two cases to investigate in more details. Each study is also discussed with its application.

Case1. Converter connected to the load

The proposed model of the first case is shown in figure 7.33 This electronic drive consists of an inverter, AC load and the armored connection cable. The details of the devices are mentioned in Table 7.6.

Table 7.6 The details of the components in the tested setup

component	Characteristics
Inverter	Three-phase, 5.5 kW, switching frequency: 5kHz, , switching algorithm: SVM, length: 30cm, width: 30cm, height: 25cm, , nominal voltage: 320v, amp: 20A
Electric Load	3kW AC load
Connection cable	XLPE, Diameter: 5cm, insulated and armored PVC sheathed cable

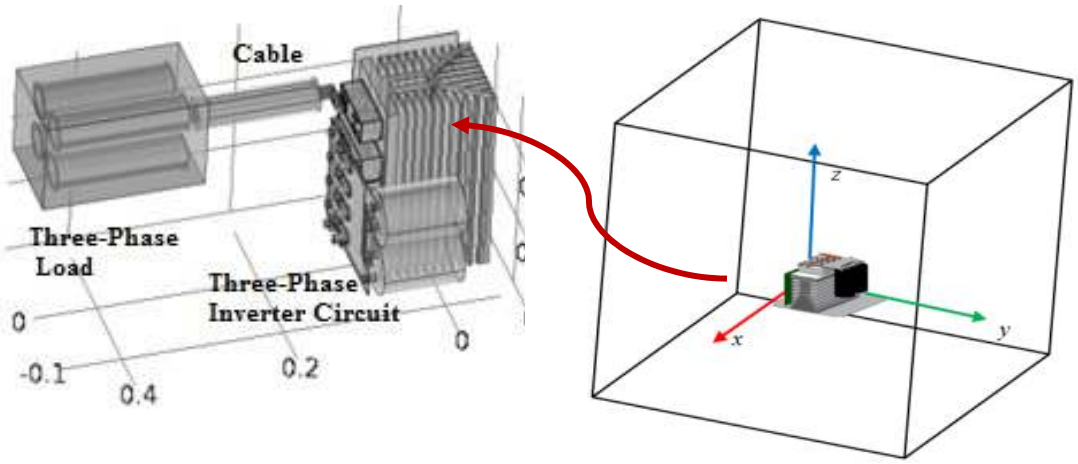

Figure 7.33 The prototype of the inverter, load and the connection cable

To model the IGBT switches of the inverter in signature study, once the switch is considered off and then it is turned on. In order to do this in FE simulation, the plate between the load and the positive bus is considered conductive plate for switch-ON case. Subsequently, this plate is considered non-conductive plate for switch-OFF case. This alteration of the conductivity of the plate happens 5000 times in a second due to the switching frequency. The simulation is implemented in 6 hours with about 6 million degrees of freedom. Since there are two cases in this study, it's decided to have two types of results. In the first case, the fields along vectors in the space are used as the result and in the second case; the harmonics of the fields and the frequency responses are investigated. Hence, in this case, the radiated fields are obtained in three dimensions at a random distance in both switching circumstances. Figure 7.34(a) and (b) show that, turning on and off the switched has the effect only on the amplitude of the magnetic field density, but the spectrum shape of the fields doesn't change significantly. On the other hand, the electric field which is shown in figure 7.35, illustrates that when the switches turns on, the electric field in two lateral planes increases while the field in the front plane

decreases. The increase in the electric field is due to the flow of the current in the converter and its reduction is because of the superposition which is suppression in this case. The suppression happens because of propagating the fields into the other conductive parts of the devices and consequently, the induced radiated fields from the imposed conductive parts. The reason of the suppression is the inverse direction of the induced field due to the Lenz law [164]. Therefore, the induced radiated field is subtracted from the main radiated field and the total field decreases as shown in figure 7.35(a).

To study the superposition phenomenon, the radiated magnetic field of each component in this setup is analyzed individually, to see their spectrum and compare it with the overall fields. The result is shown in figure 7.36(a)-(d). Comparing figure 7.36(c) with figure 7.36(a) and figure 7.36(b), the radiated magnetic field while the load is ON is more than the other components and the total field is affected from it, see figure 7.36(d). The reason is the AC load has more conductive elements including iron and copper compared to the other elements in the setup.

In order to investigate the effect of the superposition, the radiated field of a random point of the figures can be used. For instance, the values of a point of the three cases (0, 5m, 0) of figure 7.36 are aggregated. The result is $1.31e^{-3}$ (μT) while the overall maximum point is $1.10e^{-3}$ (μT) as shown in figure 7.36(d). This can be due to the dissimilarity of permeability and conductivities of the models. If the resistance of a model is less than another model in vicinity while there is no shield between them, the EMF will be induced from the component with less conductivity into the one with higher conductivity. As mentioned above, due to the Lenz law, the field radiated from this induced EMF will be the opposite of the main field, so the overall field will be less than the aggregation of the fields.

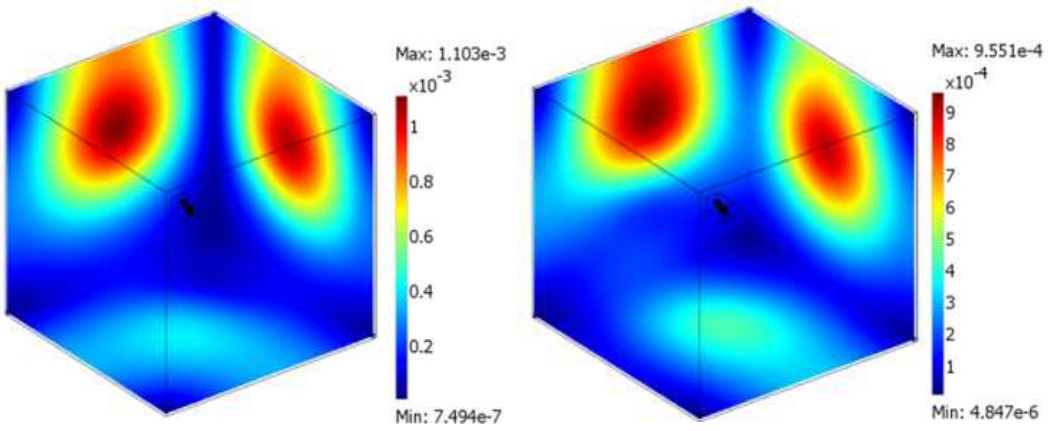

(a) (b)

Figure 7.34 Radiated magnetic field density of the system: (a) IGBT switched on (b) IGBT switched off (μT).

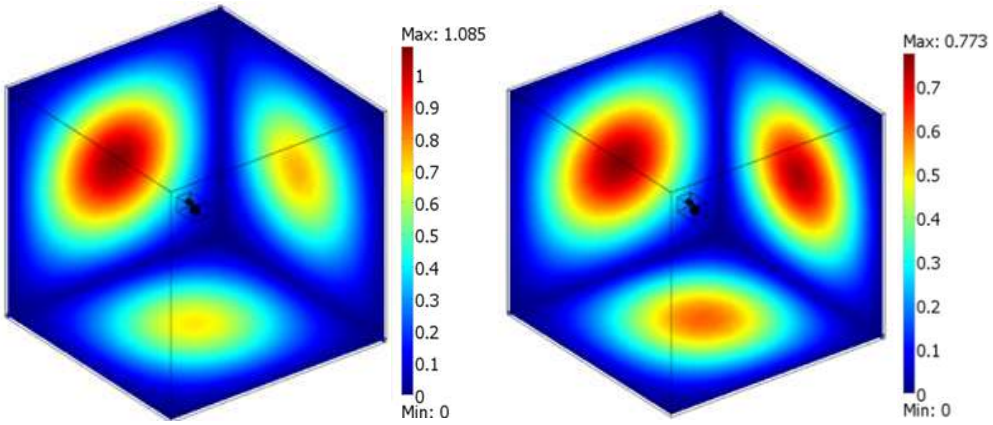

(a) (b)

Figure 7.35 Radiated electric field of the system: (a) IGBT switched on (b) IGBT switched off (μV/m).

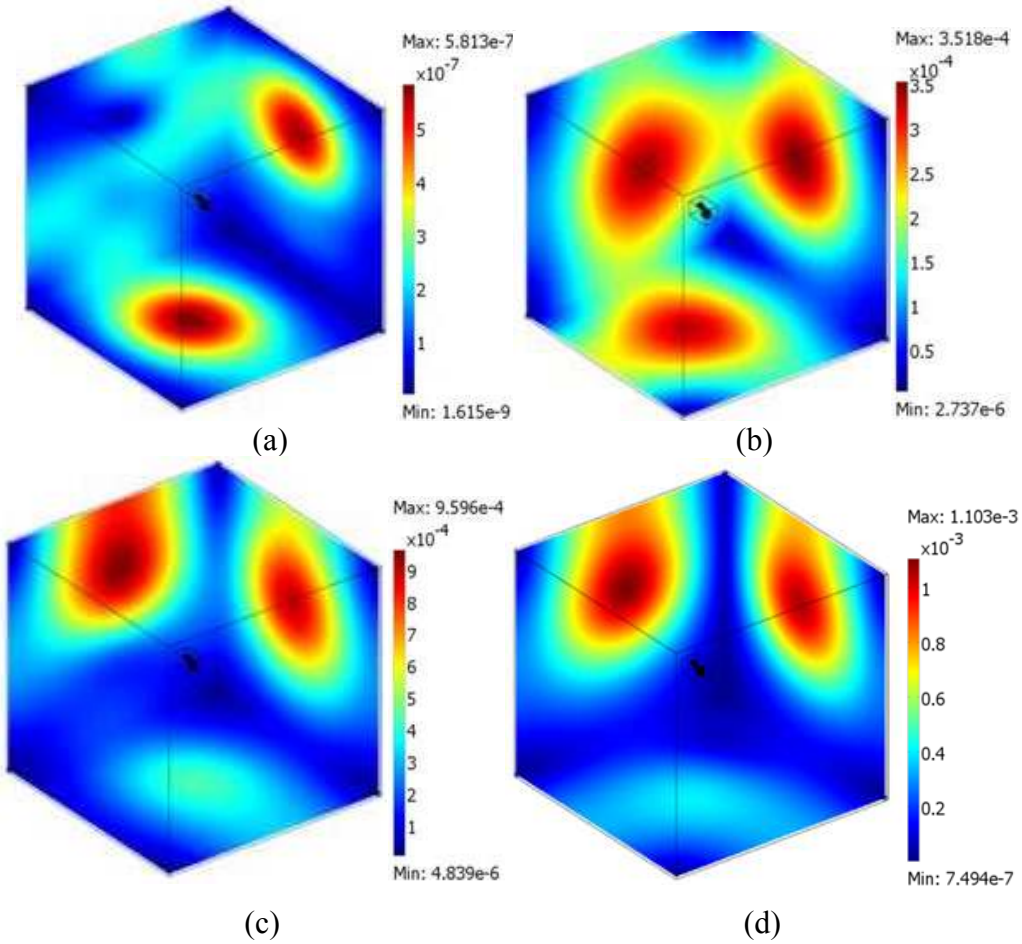

Figure 7.36 Radiated magnetic field density of the system (μT): (a) only the cable is switched on, (b) only the inverter is switched on, (c) only the load is switched on, (d) whole system in switch on.

Case2. Converter connected to the motor

In this case, the inverter is connected to an induction motor. The aim of this case is investigating the radiation of the harmonics fields from the inverter while the distance and the speed of the motor changes. The detail of the induction motor is as follows: 5.5 kW, 3phase, 208V, PF: 0.85, length: 30cm, diameter: 25cm, number of pole: 4. This case is simulated using FE shown in figure 7.37(a). The number of degrees of freedom in

meshing for this simulation was 5.7 million. That is to say the FGMRES with krylov pre-conditioner is used as the solution method. FGMRES is a variant of the GMRES method with flexible preconditioning that enables the use of a different pre-conditioner at each step of the Arnoldi process. In particular, a few steps of GMRES can be used as a pre-conditioner for FGMRES. The flexibility of this solution method is beneficial for the problem with nonlinear characteristics materials such as the core of the motor. As a result, the simulation time decreases two- three times from 8-9 hours to 3-4 hours. More explanation about the FGMRES is mentioned in. Correspondingly, the experiment is implemented in a chamber which isolated the setup from outside, shown in figure 7.37(b). The experiment is implemented based on the MIL-STD-462D. The coil antenna which can detect magnetic field from 20Hz to 30MHz is located around the inverter to get the radiated fields. The fields are transferred to an EMI receiver with a cable with 50Ω impedance. The proposed EMI receiver can detect the fields from DC to 3GHz.

The magnetic field intensity (H-field) radiated from the setup in simulation is shown in figure 7.38. The H-field is shown on a slice at 5 kHz frequency at 10 cm away from the setup. Similarly, the setup is implemented experimentally and the frequency response from DC to 20 kHz is obtained.

The unit of the simulation result is μA/m, while the unit of the experimental one is dBμA/m. the μA/m can be converted to dBμA/m by using (7-13). Using this equation, the peak at 5 kHz, -4.37 dBuA/m, would be 0.61 μA/m which is so close to the value in simulation, see figure 7.39.

$$\mu A/m = 10^{\frac{dB\mu A/m}{20}} \tag{7-13}$$

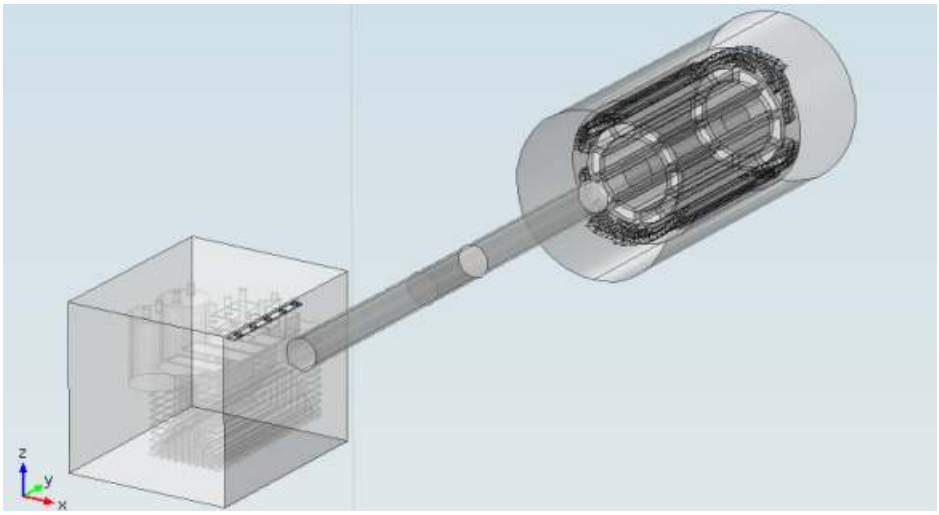

(a)

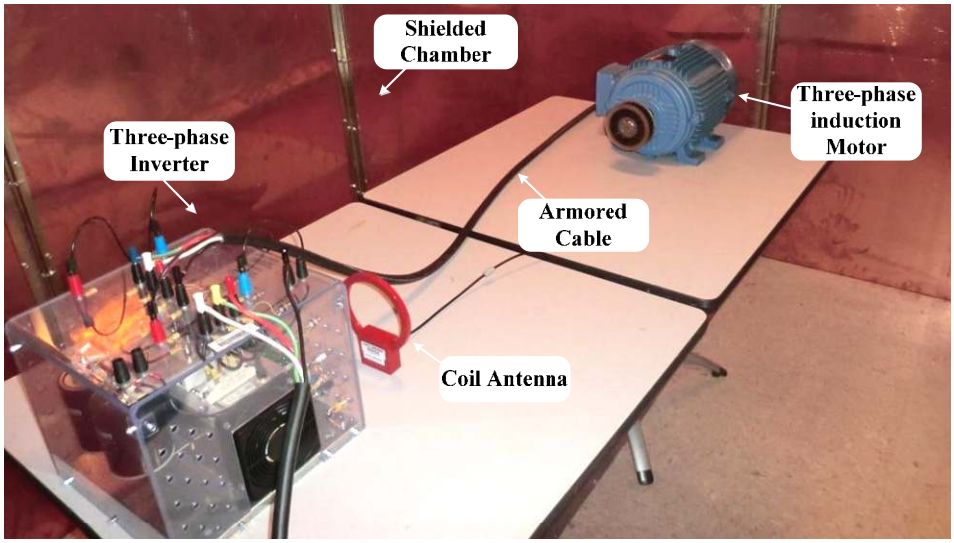

(b)

Figure 7.37 The scheme of the setup of case 2 (a) FE simulation (b) measurement

As shown in figure 7.40, the first peak located at very low frequency is propagated from the induction motor, since the motor is working at the power frequency, 60Hz. the working frequencies of the components are different and the behavior of each component can be investigating individually

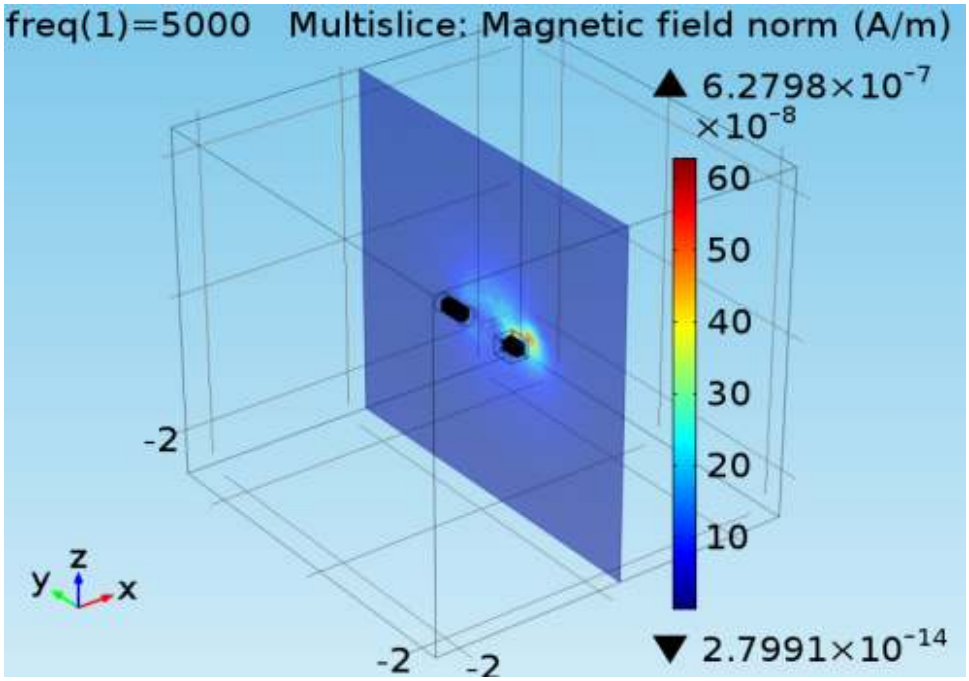

Figure 7.38 Radiated magnetic field intensity of the setup case2 at 5 kHz (μA/m)

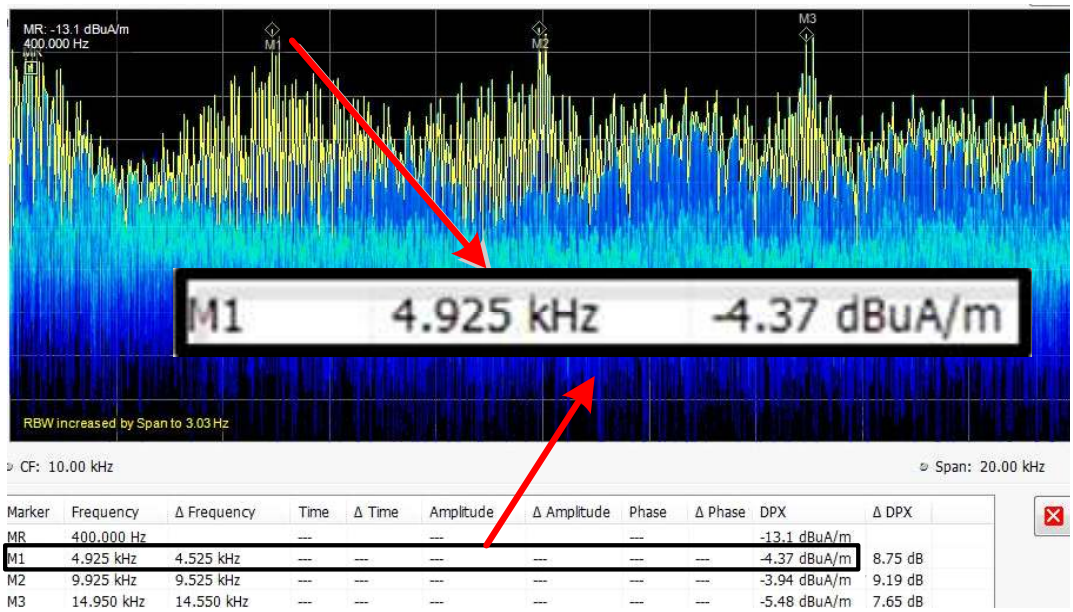

Figure 7.39 Radiated magnetic field intensity of the setup case2 from DC to 20 kHz (dBμA/m)

This can be a very useful hint in monitoring the conditions as well as detecting the faults of the motor and the inverter. Note that, the peaks at 10 kHz and 15 kHz in figure 7.40 is due to the 2^{nd} and the 3^{rd} harmonic of the inverter. The frequency responses in between harmonics are noises and sub-harmonics.

As the case study of this case, the speed of the motor is changed using the setting of the drive and the magnetic field is measured. As shown in figure 7.40, when the speed increases from 400 rpm to 700 rpm, the main peaks are more visible which is due to the increase of the field. The sub-harmonics and specially the noises generally have very insignificant changes when the speed of the motor changes. This point can be used as a hint in monitoring the conditions of the drive. For instance, while the speed of the motor is at improper rpm such as 400rpm, the main peaks are not visible; therefore, a fault or unbalance condition could not be recognized. This hint is vital in very accurate applications such as controlling high speed machines.

As another application of this case, the shielding in very vicinity of the switch, 10 cm, is tested. Figure 7.41 shows the radiated H-field with and without the shield between the switches and the antenna. It can be seen that the noises decreases dramatically. The main harmonics and sub-harmonics in between can help in selecting a shield with proper characteristics including permittivity and permeability and so on.

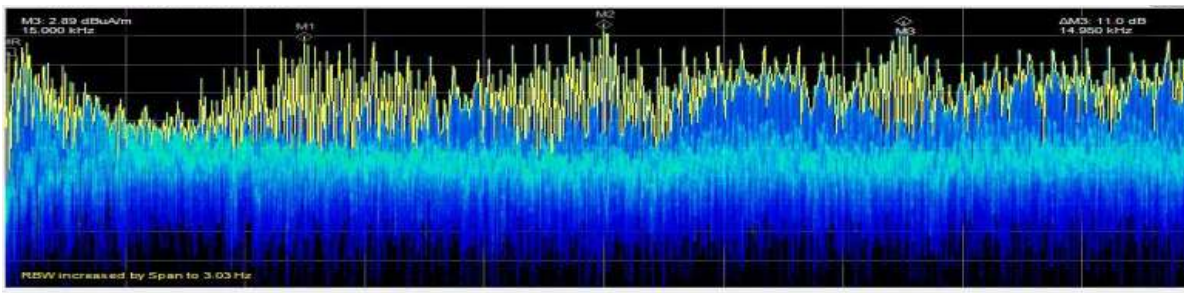

(a) At 400 rpm

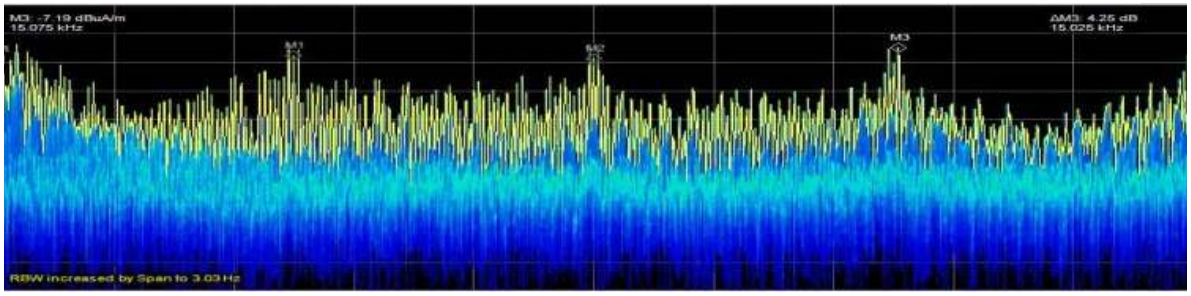

(b) At 500 rpm

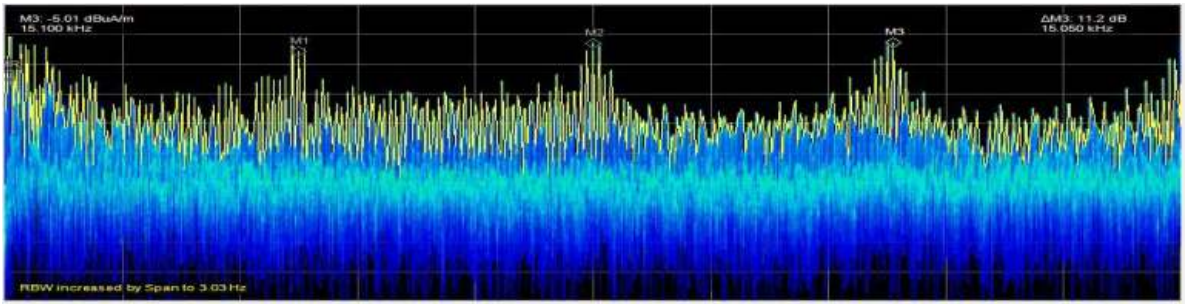

(c) At 700 rpm

Figure 7.40 Radiated magnetic field intensity of the setup case2 from DC to 20 kHz (dBμA/m) at several speeds of the motor.

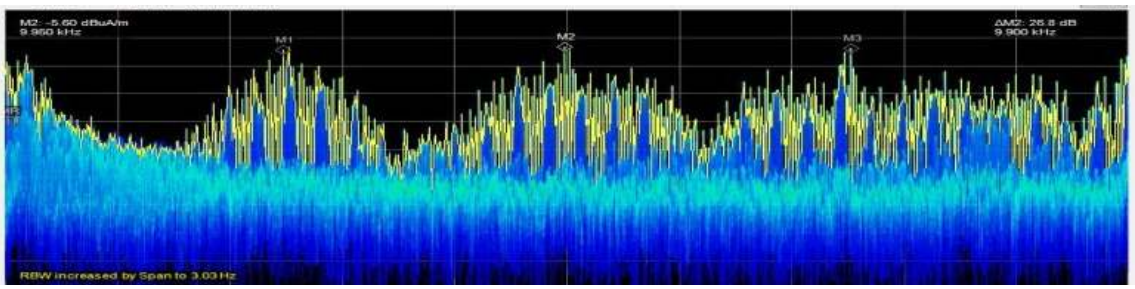

(a) Without shield

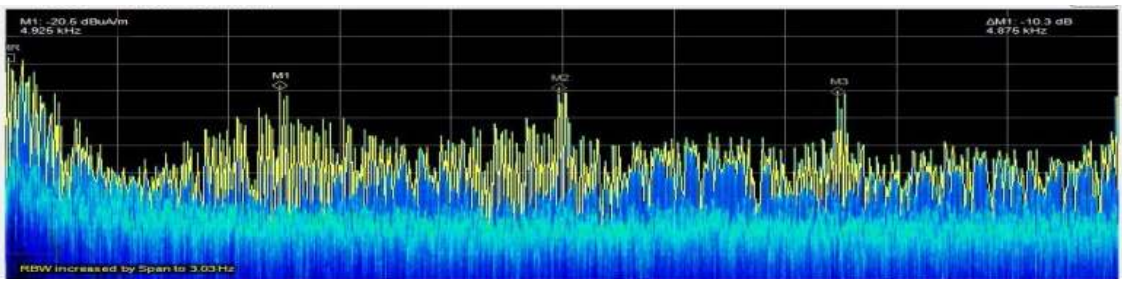

(b) With shield

Figure 7.41 Radiated magnetic field intensity of the setup case2 from DC to 20 kHz (dBμA/m) at 10 cm away from the inverter (a) with shield and (b) without shield.

Effects of Different Switching Algorithms on the Thermal Behavior of IGBT Modules under Pulse-Load Conditions

In this study the impact of pulse-loads on a six-pack IGBT power module is presented using Finite Element (FE) computations. The FE model solves the heat transfer equations which determine the thermal behavior of the six-pack IGBT module. The approach is such that the IGBT switching loss is calculated using a time domain circuit simulation model, then the results are used as input data for the FE computations. It is assumed that the IGBT module is operating as a three- phase voltage source inverter under pulse-load condition. With this model, the temperature of each chip can be directly derived from the losses of the silicon chips. The FE results can be used in order to verify the accuracy of

the NTC sensor (Negative Temperature coefficient) included in the chip. The FE computational results have been verified for some identified conditions which have been tested by the manufacturer.

To be able to estimate the chip temperature of an IGBT module, one must look at the provided manufacturer temperature sensor (NTC) and the thermal impedance of the IGBT chip. Then by calculating the IGBT losses the chip temperature can be estimated. This method was proven effective and was recommended by many authors [165-169]. However, these estimations are not accurate enough when a multichip power module is used. This is due to the fact that the distance between each chip in a power module is so small that each chip can have effect on temperature increase for the adjacent chip and consequently influences the accuracy of the IGBT temperature estimation. This is especially noticeable when an inverter operates under large pulse-load conditions. One result of this estimation error is the fact that the inverter must be de-rated in order to be protected. This limits the maximum loading of the inverter and requires that a larger power module to be chosen for a safe operation [170]. Therefore, it is critical to have accurate temperature estimations for an IGBT multi-chip module under large pulse-load conditions.

During normal operation, an IGBT may experience a short-circuit, which is a more pleasant object of study when it is possible to estimate the device failure by means of simulation at the circuit level. Although an NTC might be used to measure the temperature of an IGBT switch, the NTC measures the average temperature of the whole IGBT module. However, the difference between the actual IGBT/Diode temperature and the NTC temperature is a function of many parameters. Notice that a part of the heat generated in

each IGBT and diode is dissipated in the surrounding space through convection and ventilation. Accordingly, there is an error in the measured temperature of NTC [165].

A Finite Element tool is used to study the effect of pulse-load on the chip temperatures for a six-switch IGBT inverter module operating at different switching algorithms. Based on this method, each chip temperature can be directly calculated by the power switching losses and their corresponding locations in the module. In order to perform this investigation, first the power losses need to be model in MATLAB/Simulink to obtain the magnitudes of the power dissipated in each chip. This data can then be entered into Comsol Multi-physics Software, which is used to evaluate the data for accurate calculation of the temperatures at the IGBT junction points.

Electro-thermal analysis of PWM inverter

High voltage power converters with the ability to deal with pulse-loads are commonly used in radar power supplies. The performance specifications in these types of power supplies are very important. These supplies require fixed regulation and high efficiency. Figure 7.42 shows an inverter model developed in MATLAB with which the study of the electro-thermal effects of the IGBT on the overall performance of the inverter is performed. In this section, the principal operation of the inverter circuit is described along with the simulation results.

A. Electrical Operation

For sake of simplicity, the simulation of the IGBT module shown in figure 7.42 was performed for a relatively low IGBT switching frequency to illustrate the behavior of the circuit. In the PWM inverter of figure 7.42, the duty cycle ratio of the input signal to the

IGBT gate drivers is varied using the space vector PWM technique to produce a 60 Hz sinusoidal variation of the RL load current.

The operation of the inverter is divided into six sections. During the first $\frac{\pi}{3}(rad)$ of 60 Hz inverter operation, IGBTs S_{ap}, S_{an} and S_{bn} are switched on while the others are in the off state. This process changes in a way to track the reference voltage as [166]:

$$V_{ref} = \frac{3}{2}\left(V_a + \alpha V_b + \alpha^2 V_C\right), \alpha = e^{j\frac{2\pi}{3}}$$

The inverter operation during other sequences of the 60-Hz reference sine wave is similar to the aforementioned sequence, except that the opposite phase of the bridge is switched on and off. The sinusoidal variations of the duty cycle ratios for each phase are specified by comparing triangle waveforms to the magnitude of the sinusoidal reference signal. When the value of the reference sine wave is larger than the value of the upper triangle wave, S_{ap} is switched on; otherwise, it must be off. The same procedure goes on the other IGBTs as well [166].

In this switching algorithm, a significant amount of heat is dissipated in the IGBTs due to the on-state losses for the large load current and the switching losses that occur for the typical 10 kHz switching frequency.

Figure 7.43 shows the simulated load current for the space vector PWM inverter operation and figure 7.44 shows the power loss waveforms in each IGBT under a pulse-load. In this study it is assumed that the pulse-load has the following condition: 1) Duration of the pulse is less than the line frequency, 2) The pulse-load is exerted at half of the line frequency. The pulse-load causes a noticeable temperature rise in the second leg of the IGBTs.

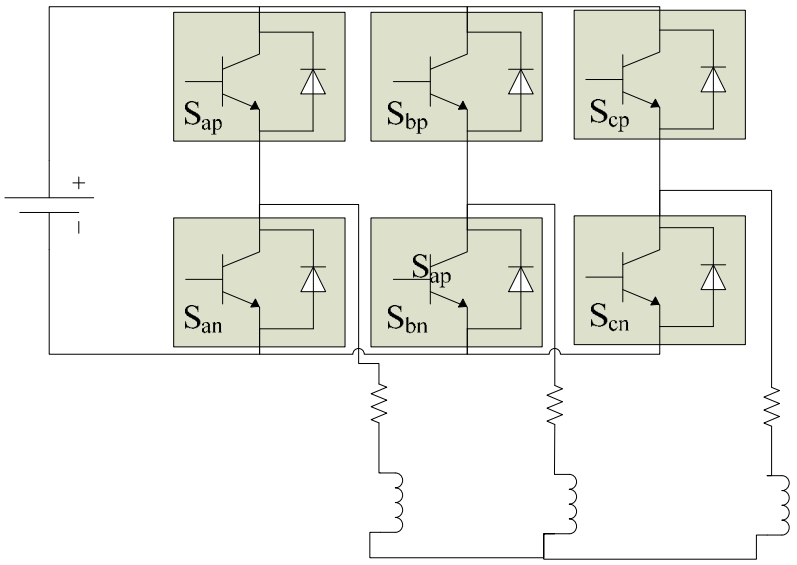

Figure 7.42 Schematic of six switches inverter circuit

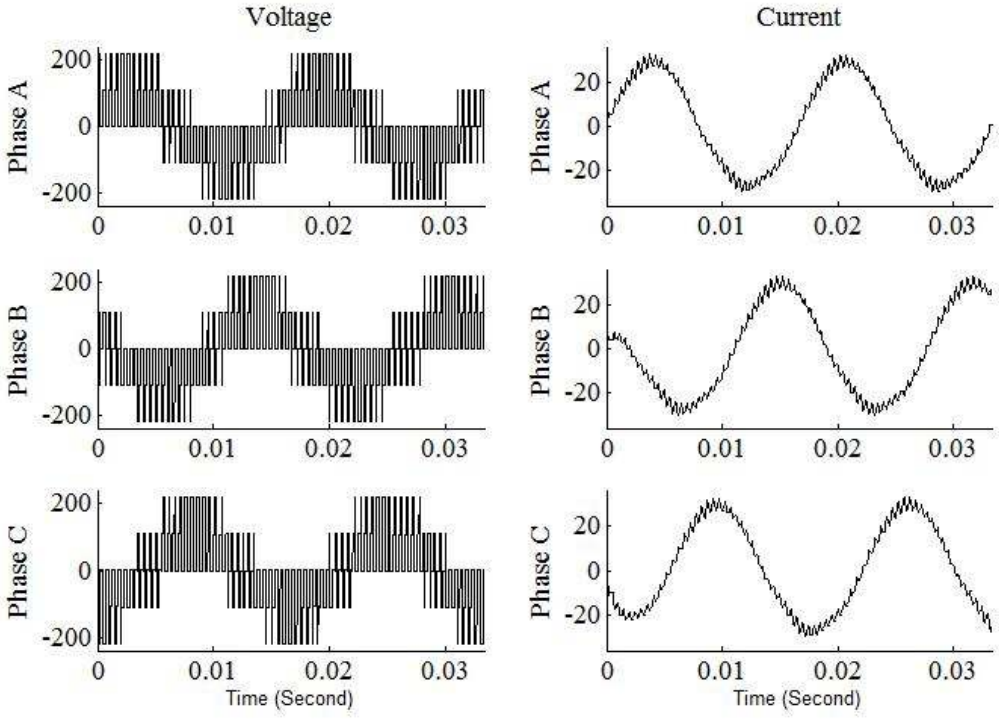

Figure 7.43 Line Current and Voltage in the case of SVPWM

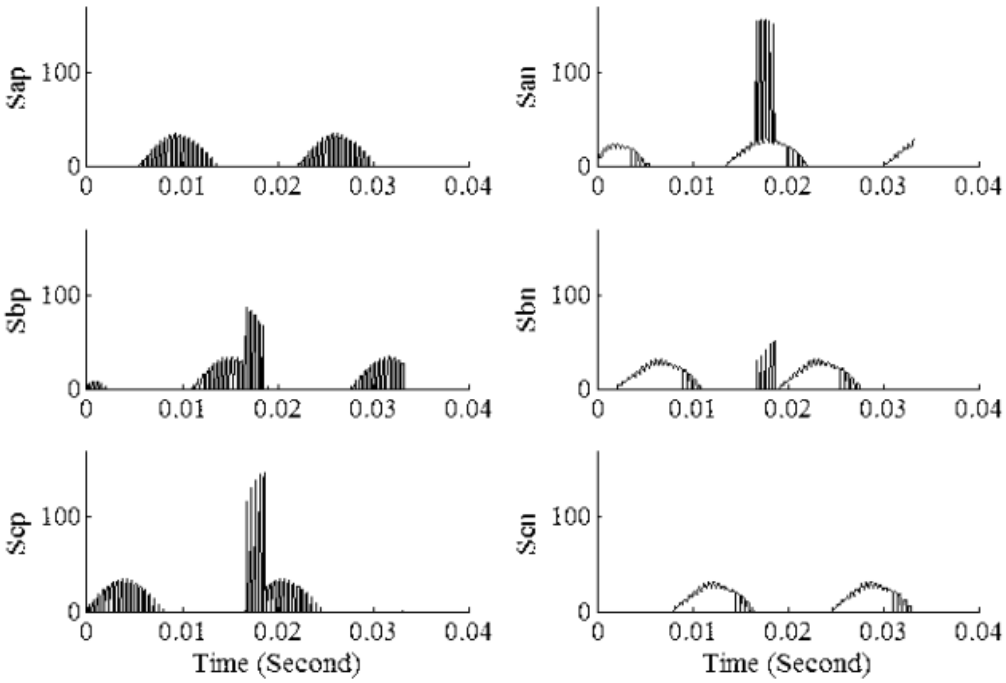

Figure 7.44 Pulse-load effect on each of the inverter phases in case of SVM

Notice that the silicon chip surface temperature varies due to the change in the current waveform and this change is related to the method of switching, also notice that the chip surface temperature cools after the peak in load current and during the phase in which the device is off. However, in this process the maximum rated temperature of the chip is detected, therefore, this particular example could lead to failures of the chip [166].

As the load switches at high frequency, the output voltage may collapse totally over a period of time if the converter is not regulated properly. The converter should switch at least at twice the load switching frequency for good regulation and stable operation.

In figure 7.43 and figure 7.44 the case in which the duration of the pulse-load is smaller than line frequency are shown when inverter is controlled by Space Vector PWM,

in these figures it is assumed that the pulse-load duration is 1/8 of the main frequency the model is also analyzed for 1/4 and 1/2 of the line frequency; The simulation results are given in Table 7.7.

In these figures, the DC input voltage to the inverter is 325 V and fed a three-phase RL load(R=3Ω, L=4 mH). Also, a pulse-load is applied within a specific cycle which affects the second leg of the inverter; figure 7.45 shows the output line voltages and currents when the inverter was controlled by Hysteresis switching algorithm method. It can be seen that the current is falling at the instant when the pulse is applied. Figure 7.46 shows the inverter's IGBT power losses and Table 7.7 compare the total power losses in each cycle for the inverter when it is operating under different switching algorithms and when the pulse-load duration is lower than line frequency.

Figures 7.47 and 7.48 show the output voltage and current and instant power loss waveforms of the inverter, respectively, when it is controlled via the SPWM (Sinusoidal PWM) switching method. From Table 7.7, it can be concluded that the Hysteresis method causes more losses as compared to the other two and the SVPWM creates the least amount of power loss.

Figs. 7.44, 7.46 and 7.48 shows the instantaneous power dissipated as heat during one 10 kHz switching cycle of the simulation. The switching cycle was chosen so that the details of both the turn-on and the turn-off waveforms can be observed on the same figure (the on-time is much longer at the peak load current). The dissipated energy waveform is readily obtained using MATLAB to integrate the dissipated power waveform.

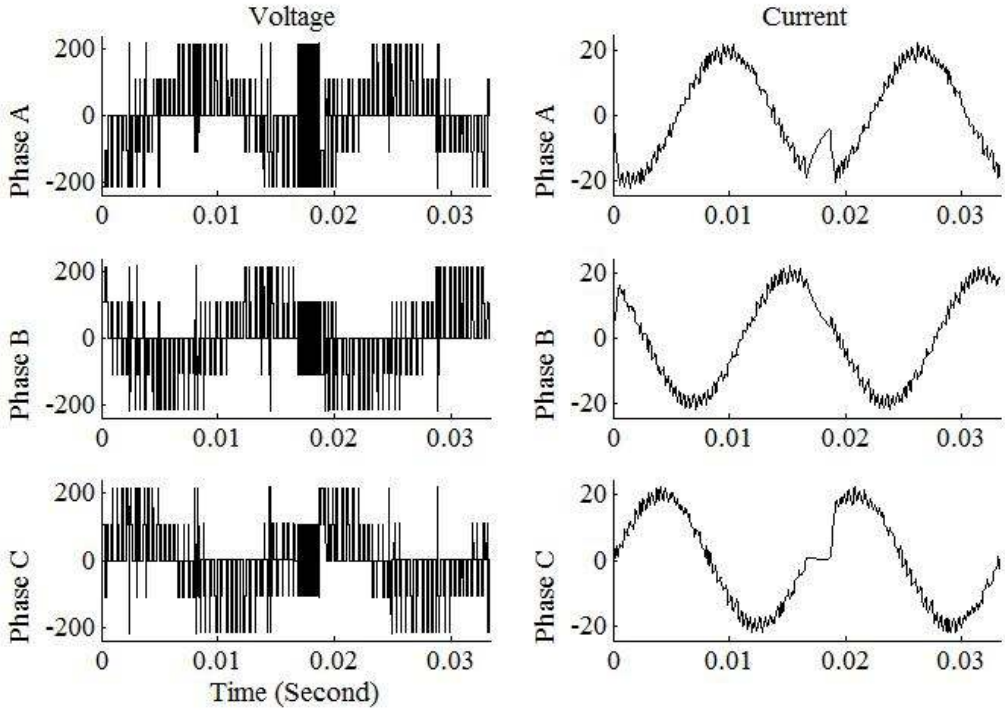

Figure 7.45 Line Current and Voltage in the case of Hysteresis Current Control method

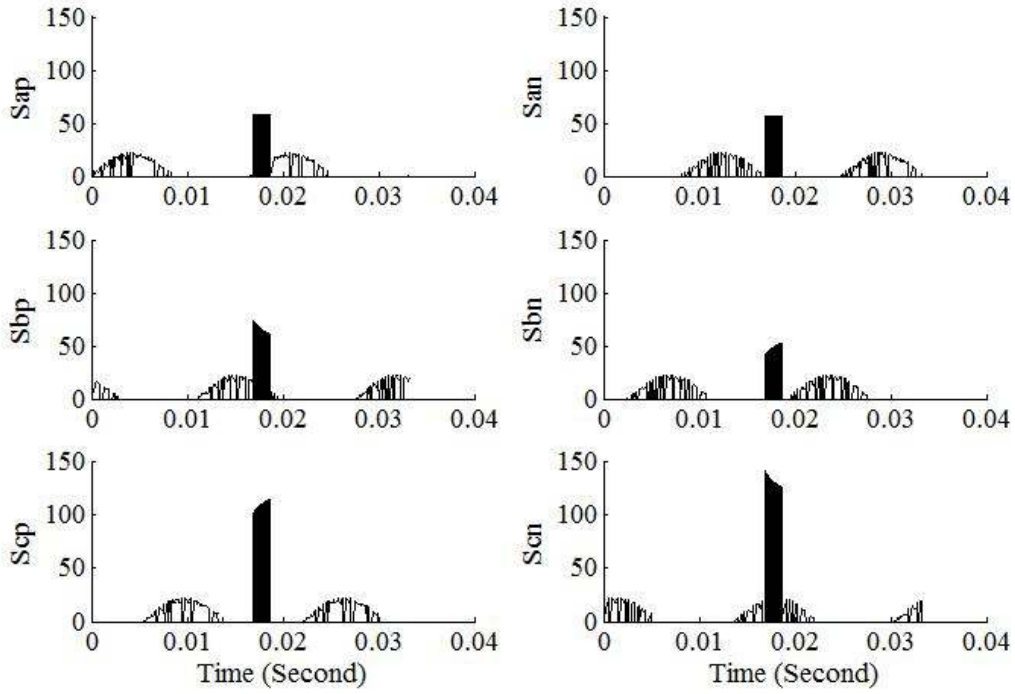

Figure 7.46 Pulse-load effect on each of the inverter phases in case of Hysteresis Current Controlled inverter

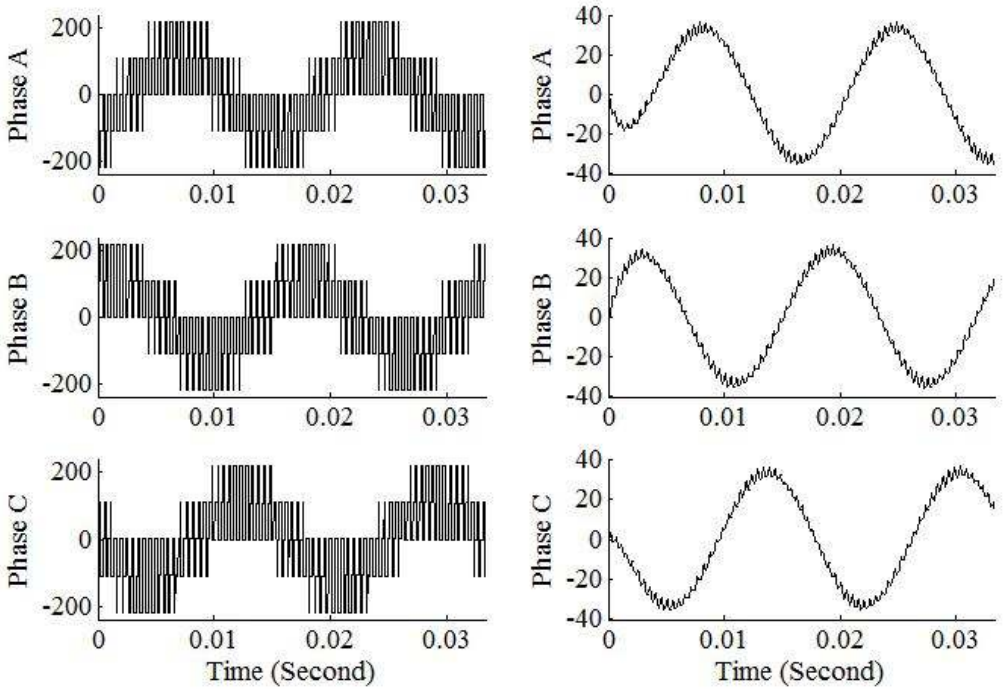

Figure 7.47 Line current and voltage in the case of Sinusoidal PWM method

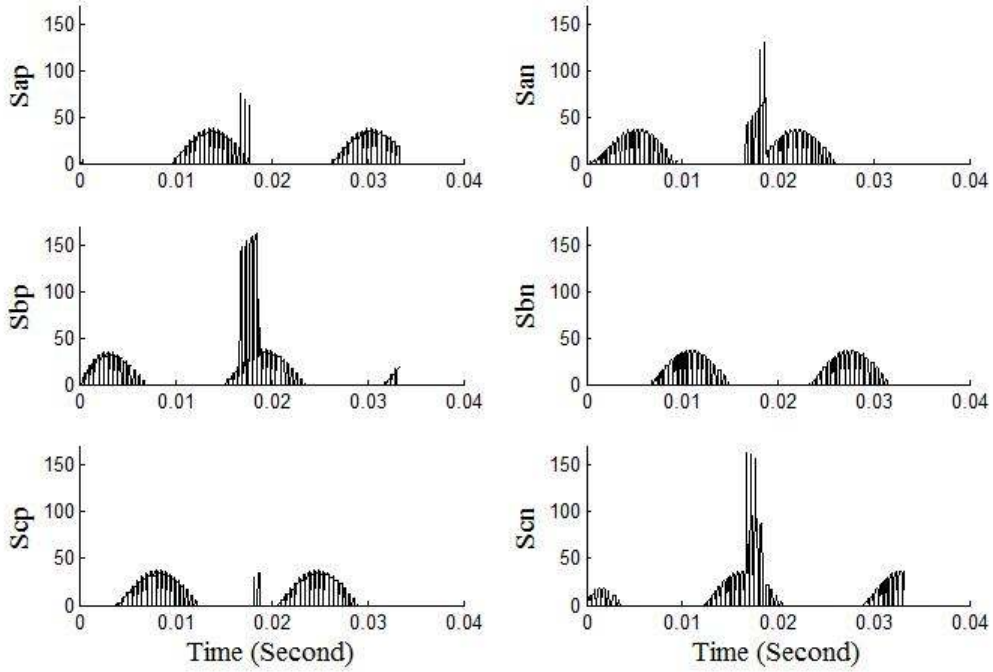

Figure 7.48 Pulse-load effect on each of the inverter phases in case of Sinusoidal PWM method

As can be seen from the previous figures, the hysteresis switching method is performed in such a manner so as to maintain the output current in close proximity to the reference current. Therefore, when an instantaneous pulsed current is drawn from each phase, the control algorithm keep all upper switches off, thus the inverter output current collapses. However, in SVPWM and SPWM, this pulse does not affect the output waveforms.

Table 7.7 Total power loss of the six switch inverter in one cycle in the vicinity of 120 Amps Pulse-load

Control Method	Total Power Loss(Watt)
Hysteresis Current Control	86.82
SPWM	92.59
SVM	80.56

B. Electro-thermal Interactions

To obtain accurate data about the thermal behavior of the system the thermal model of the chip must be first be acquired. For this purpose, the following process is used to determine the temperature distribution for the model shown in figure 7.49:

1) First, an electro-thermal simulation of the inverter is performed over a few 60 Hz cycles (for each switching algorithm).

2) The average dissipated power is determined for each device using MATLAB to integrate the dissipated power over a complete 60 Hz cycle.

3) The calculated value of the average dissipated power is then used as a power source into the corresponding model of figure 7.49 (a).

4) Finally, by utilizing the FE tool, the average temperatures are used as an initial condition for the next cycle, this process is repeated iteratively, in order to reach to a steady state result.

Principle of electro-thermal modeling of multiple chip modules

A picture of the total system and its electrical connections are shown in figure 7.49(a). In figure 7.49(b), the die and substrate of an IGBT module are represented. The module has three substrates with two IGBTs and two diodes on each of them. A temperature sensor (NTC) was located inside a corner of the IGBT module to predict the junction temperature [2].

A. Measurement of the chip temperatures

Two measurement methods were used to measure the chips temperature. One method was an infrared camera (IR) which recorded both steady and dynamic temperatures for different IGBT chips. The other measurement method was based on the thermal network of the IGBT module which will be briefly discussed in next subsection, in this method the thermal resistance of the each part of the module is determined by the manufacturer [170].

Recently, many other approaches for thermal modeling of IGBT modules have been proposed, from which it was decided that using FEM was the most common one. This will be discussed in more detail in next section.

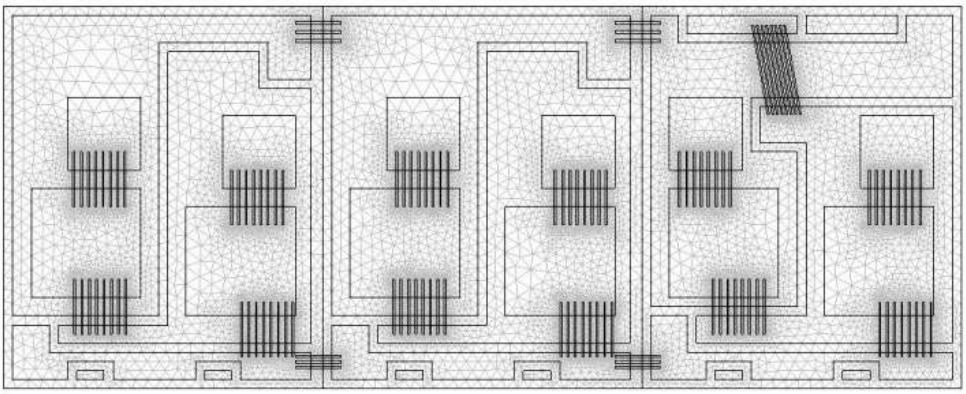

(a)

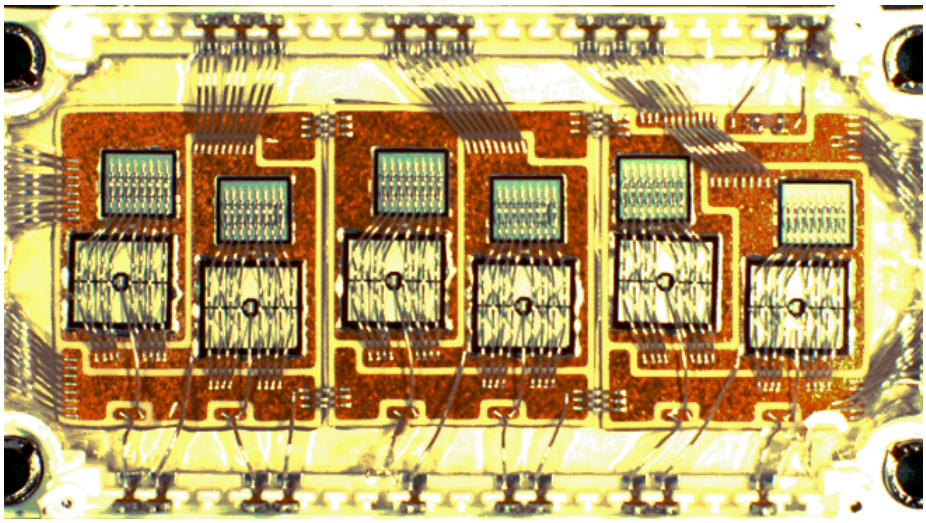

(b)

Figure 7.49 (a) Diagram of heat transfer in a six switch IGBT module, (b) IGBT open module

B. Thermal impedance using single chip model

Generally, the thermal impedance between the junction and case layer of each IGBT/Diode chip was provided by the manufacture as shown in figure 7.50. The thermal resistance and time constant for each parallel segment are shown in Table 7.8. From this figure, the thermal impedance of one chip in the module can be expressed by the following equation [168], [170]:

$$ZI_{jc} = \sum_{k=1}^{4} \frac{R_{ik}}{1 + s\tau_{ik}} \quad ; \tau_{ik} = R_{dik} C_{dik}$$

$$ZD_{jc} = \sum_{k=1}^{4} \frac{R_{dk}}{1 + s\tau_{dk}} \quad ; \tau_{ik} = R_{dk} C_{dk}$$

where, ZI_{jc} and ZD_{jc} are the junction to case thermal impedances of the IGBT and the diode chips respectively; R_{ik}/C_{ik} and R_{dk}/ C_{dk} k ∈ (1, 4) are the k_{th} layer thermal resistance/capacitance of each IGBT and diode chip respectively; τ_{ik} and τ_{dk} are the time constants of IGBT and diode chips under the k^{th} layer.

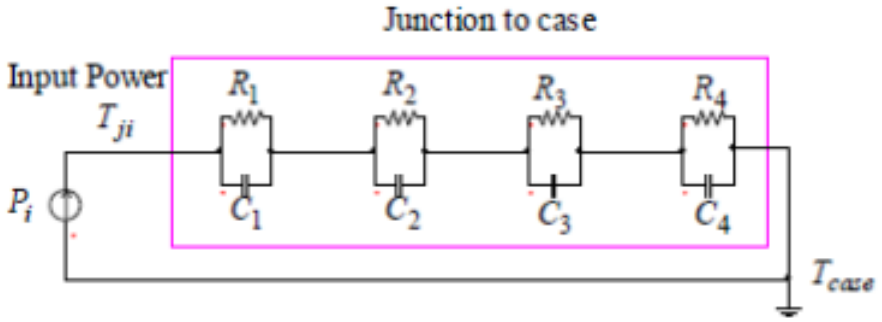

Figure 7.50 Equivalent diagram of the thermal impedance between junction and case layer from the manufacture

Table 7.8 Thermal Impedance of Tested IGBT

Segment	1	2	3	4
R_{dk}(K/W)	014283	0.17143	0.01931	0.00341
τ_{dk}(S)	0.06499	0.02601	0.002364	1.187e-5
R_{dik}(K/W)	0.07559	0.09061	0.01039	0.00341
τ_{ik}(S)	0.06499	0.02601	0.002364	1.187e-5

After obtaining all of the thermal parameters and designing the thermal circuit, the temperature must be derived from the equations mentioned above. The single chip thermal model is made directly by making the following assumptions; (1) the case temperatures under S_x and D_x in a same substrate are uniform and (2) no coupling exists between IGBTs and Diode chips in the same substrate.

The Single chip model is simple and can predict an accurate junction temperature for a single chip; however, it cannot predict the junction temperature well when the drive operates at a pulse-load condition because the three assumptions are not accurate anymore. Furthermore, this simple model induces a large amount of errors because of heat convection through the large distance between Diodes and IGBTs. To overcome these limitations in [170] a thermal network model was introduced which takes into consideration the interactions of nearby semiconductors in the module. Another method introduced is to apply FE method in order to inspect the thermal behavior in the module.

According to above reasons, the single chip IGBT module cannot accurately predict the IGBT and Diode junction temperatures for multiple chip modules. In order to provide an accurate prediction of junction temperature, a more precise temperature prediction model is needed.

Two-dimensional FE simulation

In order to verify the validity of the approach that extends the thermal network, 3D simulation using Comsol is used to predict the thermal behavior of an IGBT module. The module is part of a package shown in figure 7.49 and used as a three-phase inverter to supply a three phase RL load. As described before, six IGBT modules are used to supply

the load. Taking into account the limit on the maximum number of nodes that can be used in the FEM software and the limitations in the CPU and the data storage requirements, one needs to simplify the system before building the model. The structure inside of the IGBT module is presented in detail on figure 7.49 IGBT and Diode chips are typically soldered to the ceramic substrate and the base plate provides the mechanical support for the whole power module. The simplified model does not include the details of the heatsink fins which act as effective heat transfer coefficients on the base plate of the heatsink.

The measured temperature of the six-pack IGBT module is shown in the datasheet. These Data reveals a very good match between the results which confirms the correctness of the 3D model and justifies our reliance on it. The temperature data obtained from [170] is compared with the results obtained by FE analysis and the results verify the accuracy of the network model extracted from the experimental data in predicting the junction temperature of the IGBT module. For instance, as mentioned in the IGBT module data sheet by the manufacturer, in the case of a 1200 VDC link voltage and a current of 150 amperes the junction temperature will reach to 175 degrees Celsius. After comparing this value to the results of the FEM, the results validate the accuracy of the model. In the proposed method in this figure the total amount of power loss is calculated by

$$E_T = \frac{1}{T}\int_0^T P_T(t).dt$$

In order to obtain the total loss with respect to the volume, this parameter must be divided by the volume of each module, in order to obtain the amount of power loss in Joules per cubic meter ($\frac{joule}{m^3}$)

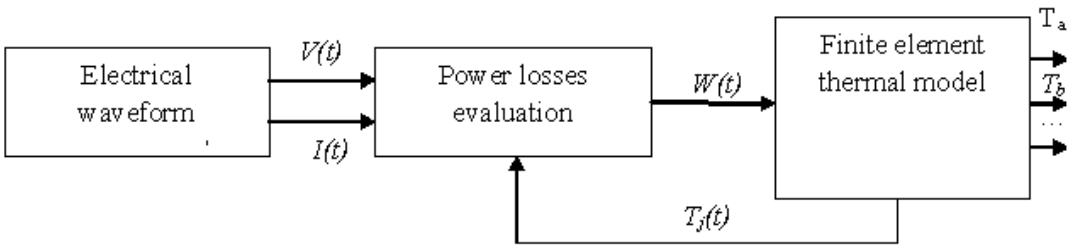

Figure 7.51 Block diagram of the applied algorithm

As is demonstrated in the Figure 7.51, in the pulse-load condition each IGBT chip acts differently. The rising temperature in the device during operation is determined by three factors: device characteristics (on-resistance, switching losses), load behavior (current) and thermal impedance of the device. These factors define an equilibrium condition between power losses and dissipated heat. The load behavior can be modeled independently from the device characteristics. A 3D steady-state thermal analysis of the structure (69.6 mm thick and 27.6 mm wide) shown in Figures 7.52 through 7.55 has been implemented in the Comsol Multiphysics simulator which uses FEM to solve the heat flow equation. Furthermore, thermal properties of each material have been supposed to be dependent of the temperature. This model is quite representative of a real power device. Hence, heat is dissipated at the junction surface (equivalent to small region with dimensions 0.2×0.2 mm^2) as shown in figures 7.52 and 7.53. The thermal properties of the materials in the simulation are listed in Table 7.9.

The Finite element tool is next used to solve the following partial differential equation in each region:

$$\rho C_p \frac{\partial T}{\partial t} + \nabla.(-k\nabla T) = Q + q_s T$$

Table 7.9 Characteristics of materials used in module construction

IGBT material	Density (kg/m^3)	Specific heat (j/Kg.K)	Thermal conductivity (W/m.K)
Aluminum	25.02	25.07	25.2
Comer	25.9	21.3	35.6
Silicon	26.5	30.2	41.3
Bonding	30	39.5	64.7

where:

k: Thermal conductivity (W/m.K)

ρ: Density (kg/m^3)

C_p: Heat capacity at constant pressure (j/Kg.K)

q_s: Absorption/Production coefficient (W/m^3.K)

Q: Heat source (W/m^3)

As mentioned in the datasheet from the manufacturer, the junction temperature in the case while it is handling 150A DC current is about 175 degree Celsius. In figure 7.52, this condition was tested with the FE computation and reached the same results.

Under normal conditions, when the power module is conducting a 20 ampere current, figure 7.53 shows the thermal distribution over the entire chip.

Now, under pulse-load currents the following figures show the results; the first case is when the duration of the pulse is $\frac{1}{8}$ of the period. This can be seen in figure 7.54. In all of the cases it is assumed that the peak of the pulse current load is 120 amperes.

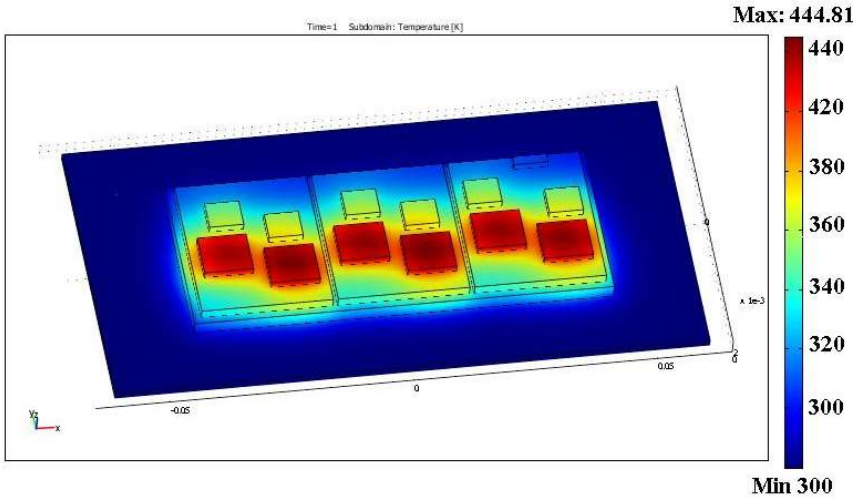

Figure 7.52 FE model under DC condition

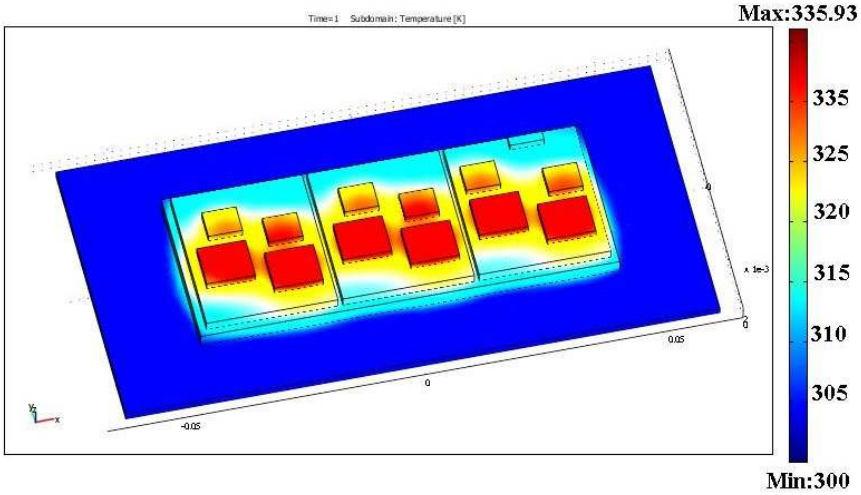

Figure 7.53 FE model carrying 20 ampere AC current, operating under normal condition

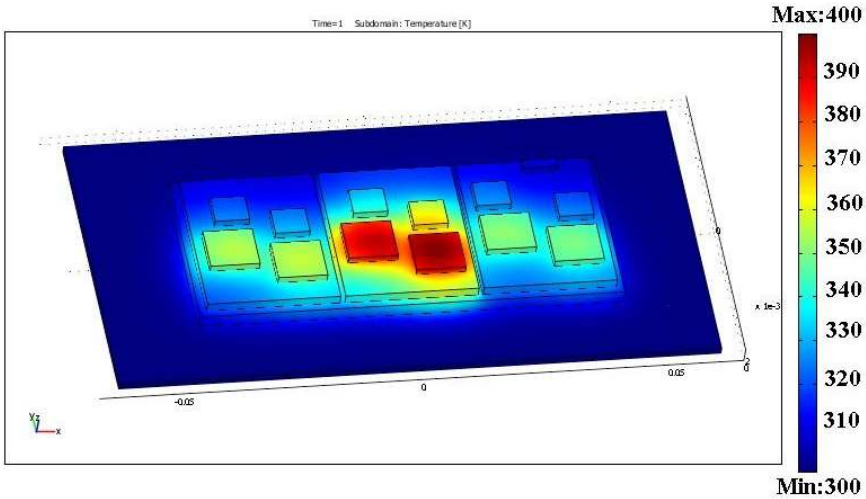

Figure 7.54 FE model carrying 20 ampere Ac current plus a 120 ampere pulsed current

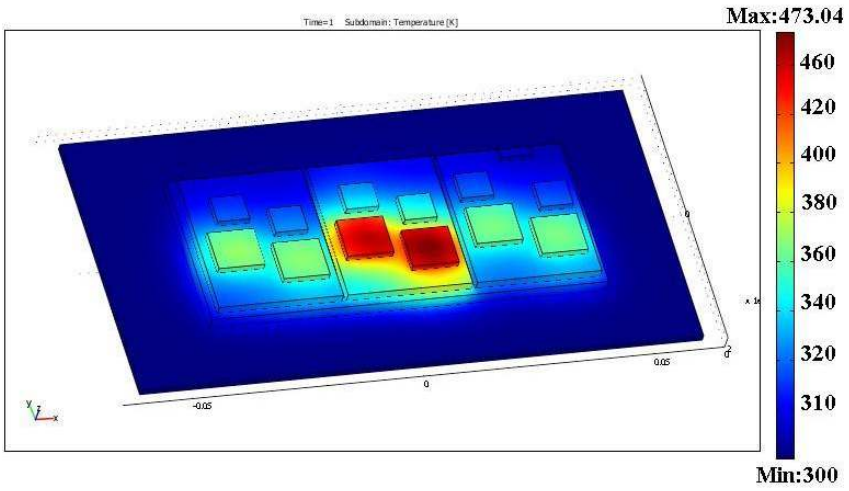

Figure 7.55 FE model carrying 20 ampere Ac current plus a 120 ampere pulsed current

In figure 7.55, the case is shown where the pulse-load width is $\frac{1}{4}$ of the main period, so the total loss increases.

These analyses were also performed on the other switching methods; Table 8.10 shows the results of these analyses.

Table 7.10 (Units are in $Kelvin^{\circ}$)

Switching Algorithm	Normal condition	Pulse-load with 1/8 period width	Pulse-load with 1/4 period width
Hysteresis Current Control	340	423	498
SPWM	335	400	473
SVM	310	378	415

Chapter 8 Design optimization of power electronic converters using physics-based models

We can consider optimization as a methodology that requires two fundamental elements: adaptation and purpose. Strictly speaking, we can define optimization as: (1) a systematic change, modification, adaptation of a process that aims to (2) achieve a pre-specific purpose. This purpose can be the maximum/minimum of a numerical function defined by the user. In other words, optimization must involve an element of knowing what needs to be achieved (maximize a function) but insufficient information on how to get there. A practical resolution of this situation is the essence of optimization theory.

Based on this understanding, an optimization algorithm can be defined as a set of clear instructions specifying how to proceed, starting from certain initial conditions, until we reach the final goal imposed before. An important point to add here is that most of the time the algorithm fails to achieve the exact pre-specified goal, arriving instead at an approximation of the goal. In engineering applications, there is always a degree of tolerance allowing us to accept certain margins of errors. This means that an optimization goal is always ideal, or a purely mathematical condition, which can be realized in nature only through a certain model that tries to mimic the physical or mathematical process under consideration.

This chapter introduces genetic algorithms. The genetic algorithm (GA) based optimization is adopted to improve the dynamic and steady state response of estimated position and estimated speed of the algorithm. The optimization problem is first formulated and then solved offline using genetic algorithms. The parameters for optimization are chosen to minimize the value of the objective function which can vary

by the application. The optimization process details are given, followed by the simulation results.

The optimization of the power electronic converter is considered to be necessary before designing the overall system. This is due to the fact that if the steady state accuracy and dynamic performance of the system are poor, it will cause instability in the system. Which means that even on tuning the controllers and sensors, one cannot meet the desired control objectives. Using optimization, one can find the optimal values of the components and operating condition of the converters, before designing the controllers for the converter control system and performing the real time control with the actual system.

Genetic algorithms

The GA is a population based global search procedure inspired by natural selection and genetics law [171, 172]. GA starts with an initial population of individual solutions and keeps modifying the population at each generation or iteration following a set of rules. In each of the iterations, the GA chooses a random set of individual solutions from current population and uses them to reproduce to form a new set of individual solutions. In this way after certain generations or iterations, population evolves towards an optimal solution. Selection, crossover and mutation are three set of rules followed by GA to create new generation from existing one. For more details about genetic algorithm and various types of genetic operators, the reader may consult literature [171].

After a careful consideration of available parameters, some parameters are chosen for our optimization problem; value of the components, their geometry, their location on the

power electronic converter's PC-board operating frequency and filters. The GA evolves the given population of individuals.

In the following sections, some examples are discussed in which the physics-based model is used to perform the optimization task.

Evaluation of High Frequency Electromagnetic Behavior of Planar Inductor Designs for Resonant Circuits in Switching Power Converters

In this study, a planar inductor based resonant circuit is designed for zero-current switching (ZCS) buck converter. In order to evaluate the factual behavior of the converter at the design stage, a numerical model of the inductor was created and implemented using the finite element (FE) analysis. Using the numerical model, a high frequency physics based circuit model was obtained for the converter's resonant circuit. The acquired physics based circuit model was used to approximate the electrical behavior of the resonant circuit. The operating condition of the half-wave ZCS buck converter was verified both numerically and experimentally. It was shown that by using the proposed high frequency model, it is possible to evaluate realistic waveforms of voltages and currents including the effects of parasitic elements. This is essential step for studying conducted electromagnetic field emissions in power converters for the evaluation of their EMI interactions for EMC compliant designs.

Resonant circuits appear in various converter topologies. Soft-switching converters have lower loss and noise characteristics than pulse width modulation (PWM) converters. In practice, resonance is a major contributor to the creation of EMI. It can cause unexpected current noise flow in the common mode path.

Generally, in order to control the conducted emissions (CE) noise in a switching power supply, the issue of parasitic elements during the design stage must be considered. These parasitic elements are circuit elements (resistance, inductance or capacitance) that are possessed by an electrical component but are not desirable for its intended purpose. So far, various algorithms were introduced to eliminate or minimize the effects of these unwanted elements. Previously, methods based on the parallel-plate waveguide and FEM analyses were introduced to solve the PCB unwanted coupling problems. Poor layout of the PCB is usually the main source of high levels of conducted emission. All components and interconnections contain unintentional (parasitic) circuit elements which often a combination of them can make a change in the operating condition of the power converter. This makes the EMI issues more complicated. An understanding of the magnitude of these parasitic elements and the characteristics of the components over a range of frequencies will ensure the correct choice of their application. Also, the switching action causes various parasitic elements in the converter and result in conducted and radiated energy at unpredictable frequencies. In practice, these parasitic oscillation frequencies are most difficult to filter out. They often cause the most interference with signal processing circuitry. Therefore, comprehension of the source of resonance is vital in achieving EMC compliance when solving an EMI problem. Hence, it is important to investigate the effects of switching-frequency control on EMI generation.

The operating principle of the Quasi-resonant converters is described in [173]. These converters are obtained by adding the resonant elements L_r and c_r to the PWM switching converters. Figure 8.1 shows the simplified circuit model for ZCS-Buck converter.

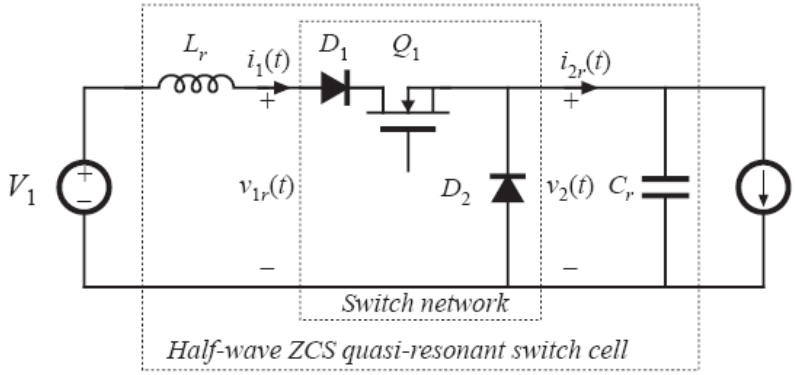

Figure 8.1 Half wave zero current switching buck converters' circuit model [173].

The parasitic elements in the configuration of the resonant components can affect the operating condition of the whole converter. In order to have a more precise study on the converter behavior, a distributed model should be obtained for each of the elements.

In this study, a planar inductor based resonant circuit is designed for the converter's resonant inductor (shown by L_r in figure 8.1). This design can meet the packaging constraints in power electronic converters in addition to the required EMI compliance levels. Design and characteristic optimization of the planar inductor is studied in references [174-177]. The electromagnetic radiation of a PCB planar inductor is discussed in [177], [178]. As an example, based on the procedure in reference [173], the inductance value is selected to be $L_r = 1\mu H$ and the resonant capacitor is selected to be $C_r = 400\,nf$. With this selection, the resonant frequency will be $f_0 = \frac{1}{2\pi\sqrt{L_r C_r}} = 251.65kHZ$.

Subsequently, in order to find the parameters of the converter, a finite element analysis is performed on the resonant part of the converter. After obtaining the high frequency physics based model of the resonant circuit, the resonant behavior of the

proposed planar inductor based resonant circuit is compared with the ideal resonant circuit. The FE analysis is used to study the electromagnetic behavior of the proposed resonant circuits. As a result, a high frequency model is obtained for the resonant circuit under a wide range of switching frequencies. Finally, the resonant circuit design was optimized in order to compensate the destructive effects of parasitic elements in the operation of the converter. The results were verified through simulations and experimentation.

Resonant circuit design optimization

As shown in figure 8.4(a), the first resonance frequency in figure 8.4(b) is much lower than the expected resonance frequency (the first resonance frequency shown in figure 8.4(a)). This phenomenon may deteriorate the operation of the converter. Because the resonance part of the converter is designed to resonate in 250 kHz (in this example) but in practice, it's resonating at lower frequencies.

In order to solve this problem, an optimization procedure is used in the design of the planar inductor. The main objective in the procedure of the optimization is to set the resonance frequency to desired value (i.e. 250 kHz) while reducing the amplitude of higher order harmonics. To achieve this goal, through the optimization process the planar inductor trace thickness and voltage clearance is changed as well as the number of turns. Therefore a multi-objective function is formed as a combination of each of these single objectives. The first part of this multi-objective function is calculated from a transient non-linear FE analysis to calculate the value of the inductor. Moreover, the second part of this multi-objective function is calculated from the circuit simulation of the resonant

circuit which is implemented in Pspice environment. A classic genetic algorithm multi-objective optimization scheme is utilized to do the optimization task automatically. The variable of the genetic algorithm are indeed the inductance value of the planar inductor and magnitude of the harmonics in the resonant circuit output.

Figure 8.2 depicts the flowchart of the parameter optimizing procedure using GA. GA is a population based global search procedure which is inspired by natural selection and genetics law. Parameters for optimization are number of turns in each layer (N) and inductor's trace dimensions. The GA evolves the given population of individuals.

The objective function is as follows:

$$Objective\ function = \alpha_1.|\Delta f|^2+\alpha_2.|Z_{in}(s)|^2$$

where, $\alpha_{1,2}$=Weights signifying the importance of the objective function (taken as 1 in our case), Δf: frequency of the main resonance (resonant circuit first natural frequency) and $Z_{in}(s)$: input impedance of the resonant circuit.

The main purpose of GA is to find the minimum for objective function.

The fitness function computes the error of the simulated and specified reference signal at each time point. The errors are then squared and added together to give a single scalar objective value.

The fitness values shown in figure 8.3, illustrate that after about 10 number of iteration the error reaches to an acceptable value. Table 8.1 shows the results of the GA-algorithm and it is compared to the conventional inductors. Note that the optimization procedure is mainly applied on the design of the planar inductor and the resonance capacitor is not considered in the design optimization.

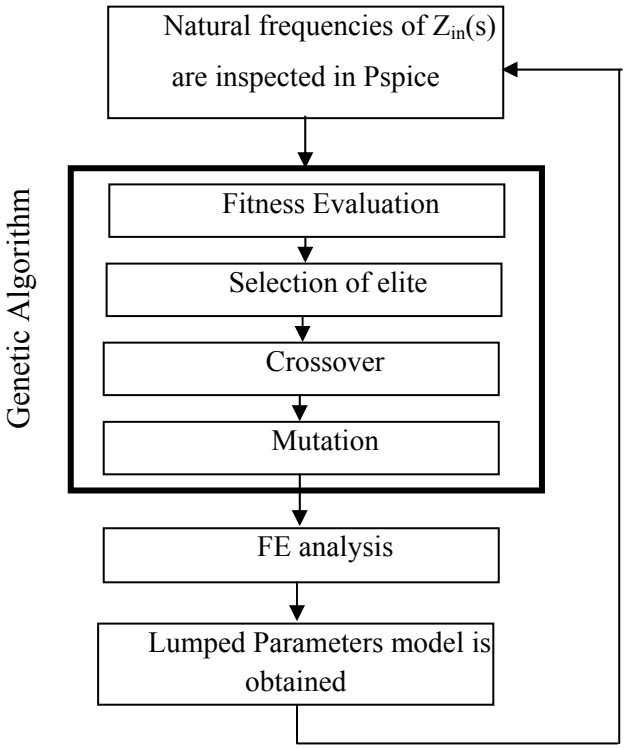

Figure 8.2 The optimization process.

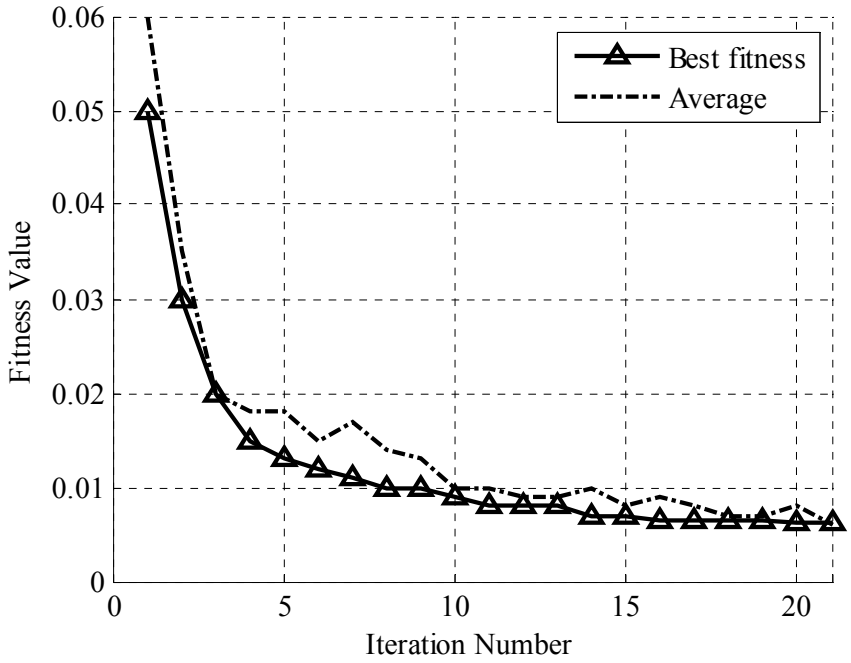

Figure 8.3 Iteration accomplished by GA to minimize the objective function.

Figure 8.4(c) shows the frequency spectrum of the optimized resonant circuit. In this figure, compared to figure 8.4(b), the unwanted higher frequency resonances are reduced. Also the main resonance frequency is set to its desired value. (i.e. 250 kHz)

Results and discussion

Figure 8.5, shows the experimental setup used to test and verify the results. As shown in this figure, to inspect and record the results, a 600 MHz, 10 Gsample/s oscilloscope was used. The bandwidth for both the voltage and current probes were 100 MHz. The converter should operate in zero-current switching condition. Therefore, the switching frequency and duty cycle is set by the digital function generator.

Figure 8.6 shows the effects of high-frequency operating conditions on the zero current switching of the MOSFET in the converter of the example circuit. In this configuration, it was expected to increase the output voltage of the converter by increasing the operating frequency of the MOSFET, while keeping the zero current switching sequence as shown in the ideal case (without considering all parasitic elements) given in figure 8.6(a). The simulation results show that the zero-current switching behavior of the converter is completely lost as a result of using the high-frequency circuit model for the resonance circuit as shown in figure 8.6(b). The parameters in these circuits were evaluated from the FE implementation described in the previous section.

Table 8.1 Optimal values for designed inductor resulted from GA.

Planar inductor	Inductance (μH)	Trace width	Number of turns
Initial design	1	40 (mil)	8
Optimized design	0.76	29.75 (mil)	6

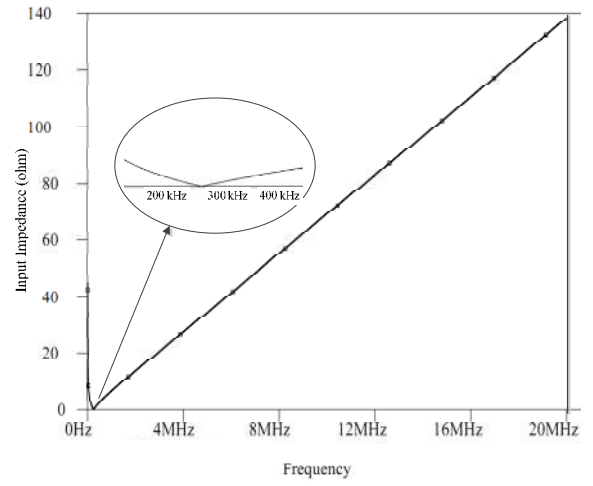

(a)

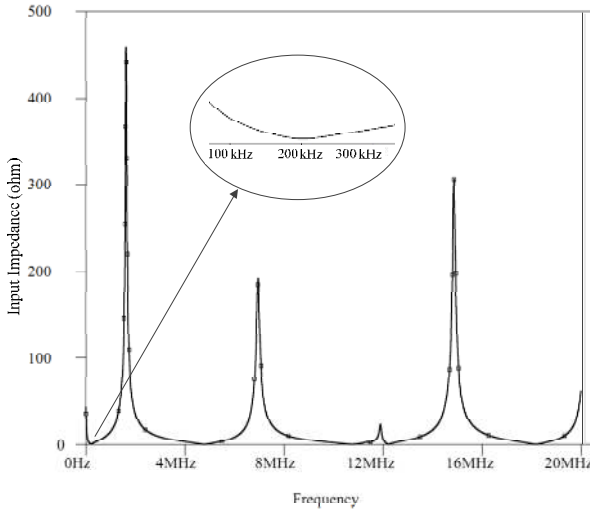

(b)

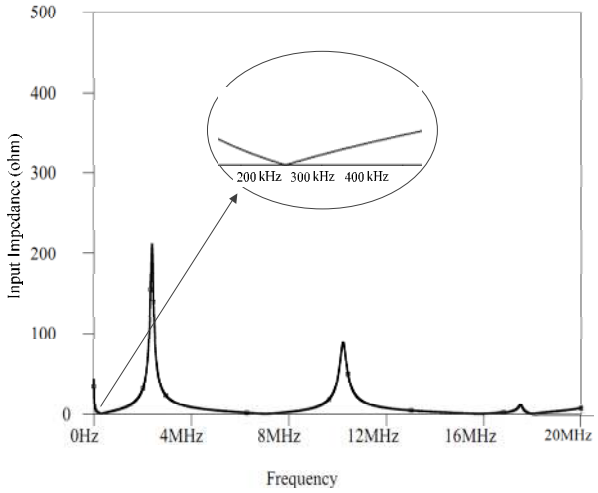

(c)

Figure 8.4 Frequency response analysis of the ZCS buck converter. (a) Simple model (b) Distributed-parameter frequency model, (c) Optimized distributed-parameter frequency model.

To keep the desired performance of the converter, the switching frequency of the converter should be kept below the value shown in figure 8.4(b).

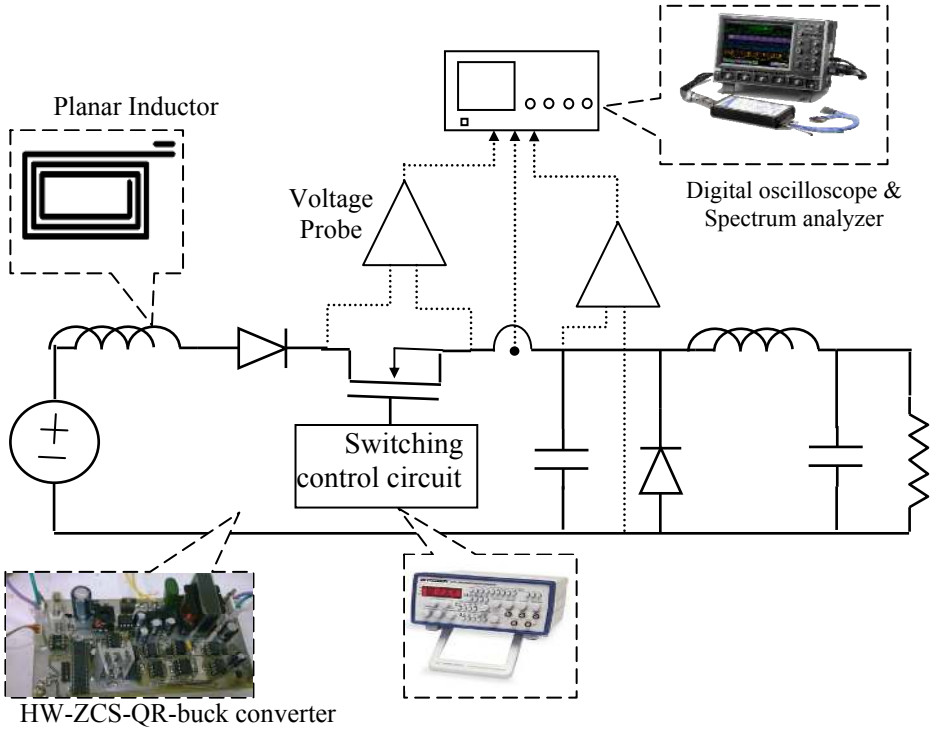

Figure 8.5 Schematic of the converter's experimental setup.

In an actual case (distributed-parameter frequency model), it can be observed from figure 8.4(b) that the next resonant frequencies, happen at the frequencies starting from 4.5 MHz and above. Figure 8.7 shows a comparison between two different designs of the resonant circuit. Figure 8.7(a) shows the FFT analysis of the primary design of the resonant circuit and Figure 8.7(b) shows the FFT of the optimized resonant circuit output signal. It is noticed that, by design optimization the number and amplitude of harmonics is reduced. To verify the simulation results in figure 8.6, an experimental test was carried

out. Figure 8.8 shows the measured voltage and current of the semiconductor switch, which is located in series with the resonance inductor (see figure 8.1). As it is illustrated in figure 8.8(a), in the primary design (non-optimized) of the resonance circuit, by increasing, the switching frequency above a certain value the unwanted resonances will appear. These resonances can harm the proper zero-current switching operation of the converter.

Figure 8.8(b) shows the switch's voltage and current, in the circuit with the optimized resonance circuit. As it is illustrated in this figure the converter is operating in zero-current switching condition as it was expected.

In figure 8.8(a), some distortions are observed in the switch's voltage waveform. These distortions are mainly because of the parasitic elements of the circuit and poor layout of the PCB, which are not considered in this study.

In this section, a method for the high frequency model of the converter's components is presented using coupled circuit/ electromagnetic FE computations. FE analysis was performed to obtain the frequency behavioral model of the converter. The natural frequencies computed from the proposed s-domain model, was used to analyze the circuit's electrical behavior and operation. The results show that the s-domain model of the converter has the ability to reveal the behavior of parasitic elements as well as higher resonances which has critical impact in studying EMI problems. This model can also be implemented for other types of converters making it practical for the evaluation on EMI/EMC issues in the design and development stages.

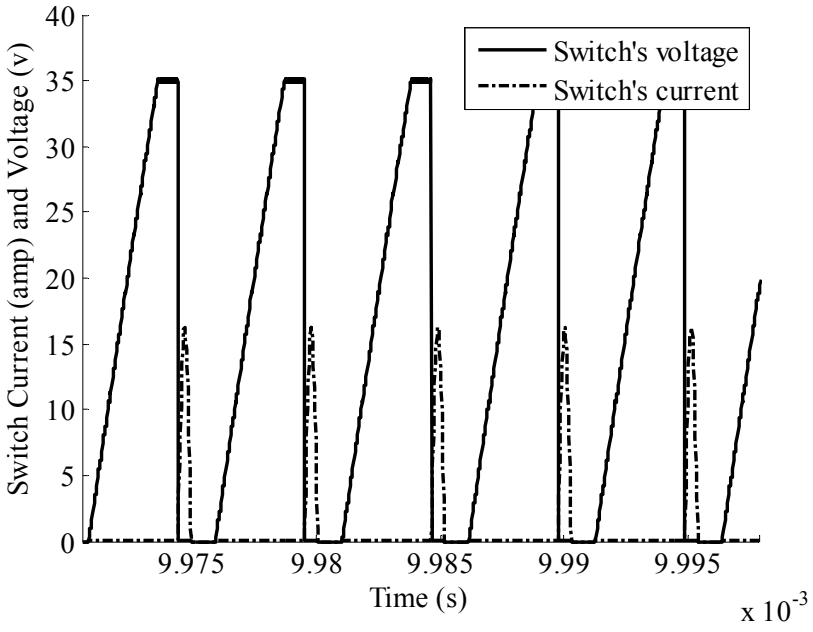

(a)

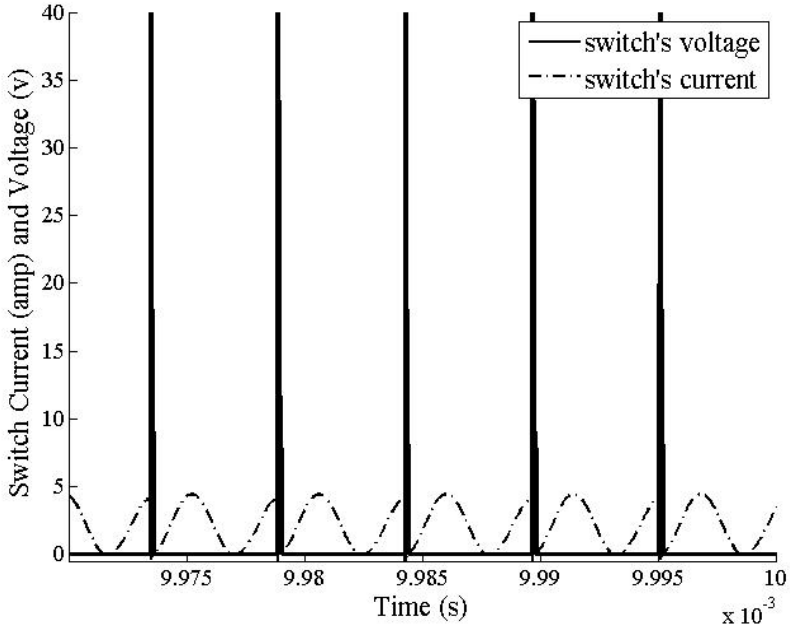

(b)

Figure 8.6 Voltage and current of the switches in ZCS-Buck converter, (a) ideal case, (b) actual case.

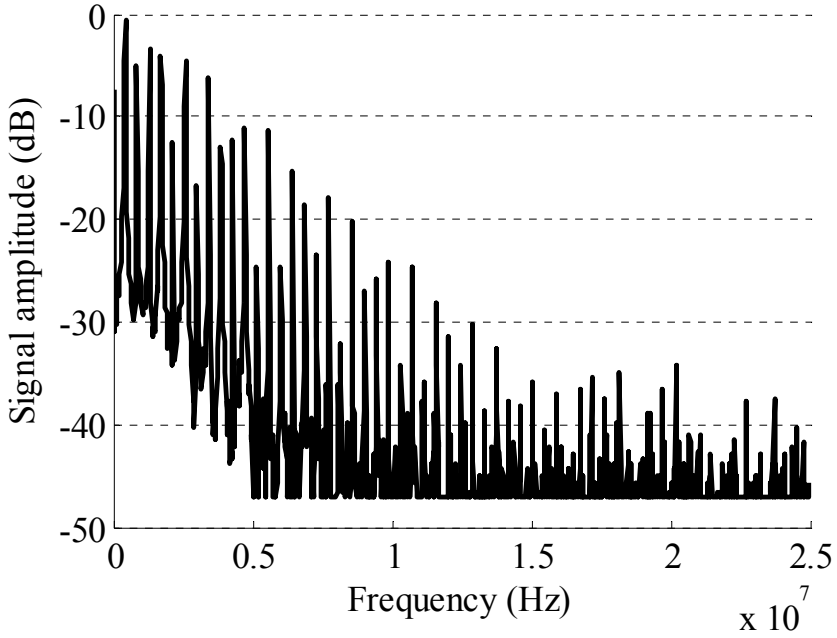

(a)

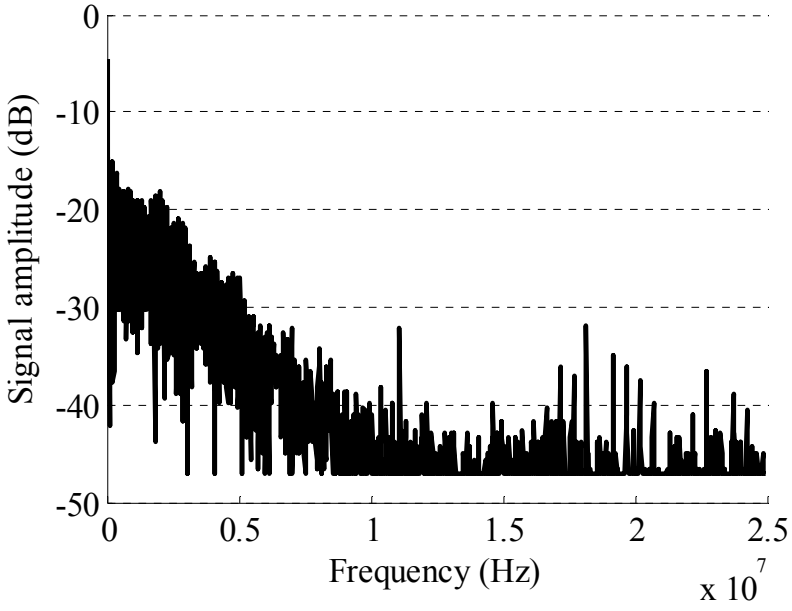

(b)

Figure 8.7 FFT spectrum of the resonant circuit, a)Initial design, b) Modified design.

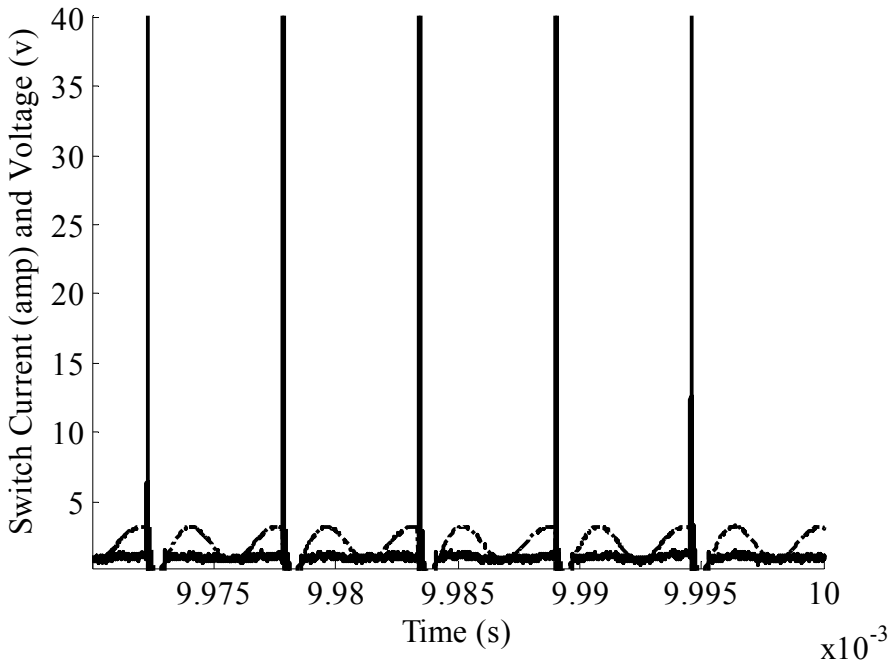

(a)

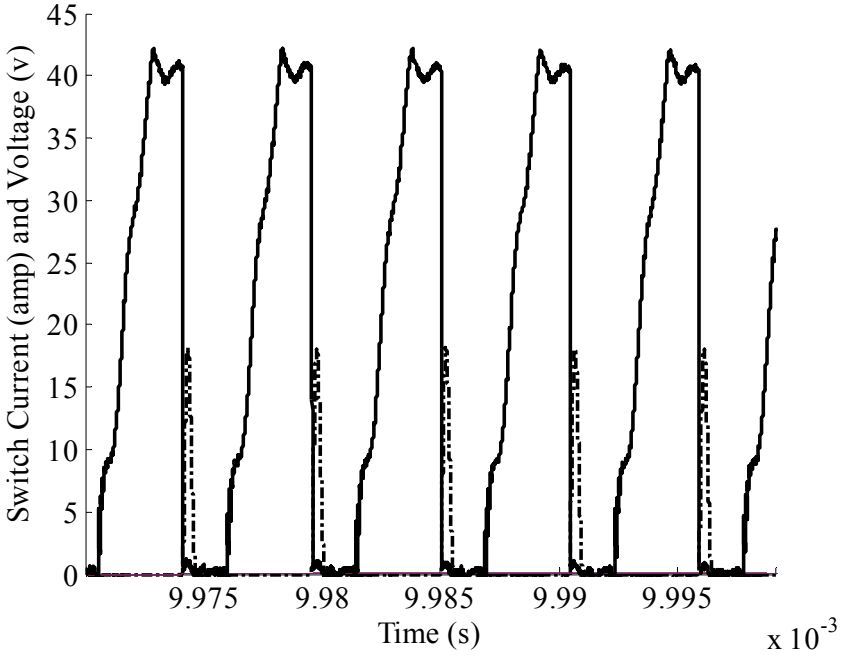

(b)

Figure 8.8 Measured voltage and current of the switches in ZCS-Buck converter, (a) optimized circuit, (b) primary designed circuit.

Design of Planar Inductor Based Z-source Inverter for Residential Alternate Energy Sources

This study deals with a planar inductor design for optimal size reduction of z-source inverters. The smallest possible inductor size is realized through the utilization of the Finite Element method (FEM) and genetic algorithms. Operating condition of the Z-source inverter was set to a point such that it works with a smaller inductance value. We studied the reduction of radiated electromagnetic field as a result of size reduction from the planar inductor design. The resulting planar inductor was co-fired on a ceramic substrate and placed in the inverter circuit. The test results were compared to standard circuit with a normal coil design. The behavior characteristics of the optimally designed planar inductor were verified through experiments.

Currently, circuit packaging has become an important issue in design and manufacturing process of power electronic converters. The reason behind this idea are the rising demand for low profile and portable devices on the customer side and manufacturing of power converters that are cheaper, more reliable and have a better electromagnetic and thermal characteristics in addition to the ascending power density[179]. To design a specific circuit for a certain application in its minimum size, some points are notable, 1-for a specific application; there exist several different circuit topologies which possess its own benefits and drawbacks. Thus, the densest and most compact topology which is compatible with the predefined application should be selected, 2-circuit operational parameters should be set in a manner to make these parameters compatible and efficient when the circuit is comprise of or combined with the low profile components, 3-application of planar devices such as inductors and capacitors

which decrease the volume and increase the power density is another gateway for this intention [180].

When utilizing alternate energy sources, a single stage converter which is controlled in a simpler and more efficient way is of interest. Therefore, z-source inverters have attracted much attention. Traditional inverters, such as the VSI (voltage source inverters) and the CSI (current-source inverters) require one more separate DC/DC converter, resulting in two stage power conversions which increases not only the complexity of the circuitry and control but the cost and the space requirement. Z-Source inverters (ZSI) have a unique impedance network. Through this network it can decrease or increase the input voltage using the shoot-through state in a single stage [181].

Planar inductors are mostly being used in power electronic converters due to favorable cooling and ease of fabrication [183]. Compared to the conventional counterparts, planar magnetic components demonstrate good performance with respect to Coupling among the windings, size, repeatability and thermal management [183]. Currently, various studies are being conducted on the development of design technology to apply planar magnetic to the core of transformer that occupies the largest volume among the components of Switching Power Supplies [182].

Z-Source Inverter

Figure 8.9 shows the general Z-source converter structure, which consists of inductors *L1*, *L2* and capacitors *C1*, *C2* connected in X shape coupling the inverter to the dc voltage source which may be a battery, or any type of alternate energy source such as a PV cell or a Fuel cell. If the alternate energy sources are used as a dc voltage source,

their output voltage is widely varied with a current drawn from them. The boost dc-dc converter is applied due to limitations on the inverter which does not allow the ac voltage produced to be greater than the dc voltage. The Z-source converter can produce a desired ac voltage regardless of the dc source voltage. To design a Z-source inverter for residential loads, a single phase topology with four numbers of switches is selected, which has 2 active states and 2 zero voltage states. One of the zero voltage states occurs when all the switches are in off state and the other zero voltage state takes place when the load terminals are shorted through both the upper and lower switches of any phase legs [184, 185].

The Z-source inverter is an appropriate choice for residential applications because its common mode EMI is low. It is a single stage circuit which has lower switching loss due to Zero-Voltage switching for switches Q3 and Q4. Also, it becomes a proper choice for high-frequency applications [181].

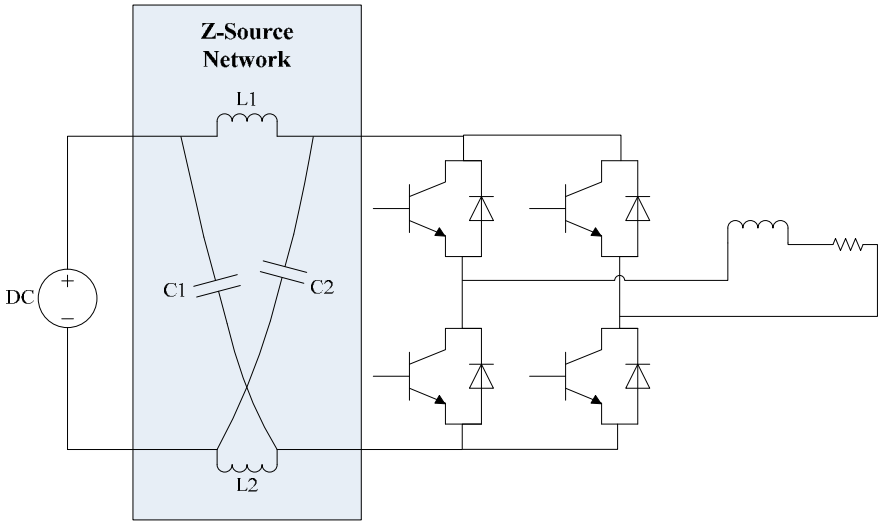

Figure 8.9 General Configuration of ZSI

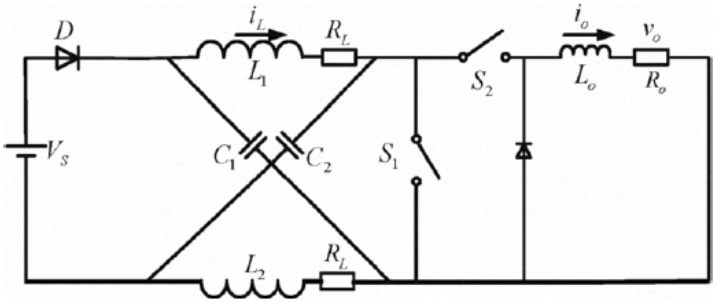

Figure 8.10 Equivalent circuits of ZSI, [184]

The ZSI has two operating modes: non shoot-through mode and shoot-through mode [186].The equivalent circuit has two switches; S_1 is switching at a duty ratio of $d = \frac{T_0}{T}$ *and* S_2 is switching at a duty ratio of S_2 is $m = \frac{T_1}{T}$ and $d + m \leq 1$. [188]

To design the Z-source impedance network the inductors and capacitors are assumed to have the same value, therefore (8-1) holds true [188]:

$$V_{C1} = V_{C2} = V_C \quad , \quad V_{L1} = V_{L2} = V_L \tag{8-1}$$

Assuming that the converter is working in discontinues conduction mode, three conduction modes are considered. Shoot through with the time length ofT_0, active state with the time length ofT_1 and traditional zero states with the length of T-T_0-T_1. All the elements in the circuit are assumed to be ideal by taking the average voltage of the inductor over one switching period (T) The system model can be in the form shown in (8-2).[188]

$$\begin{bmatrix} \dot{I}_L \\ \dot{v}_C \\ \dot{I}_0 \end{bmatrix} = \begin{bmatrix} 0 & \frac{2\frac{T_0}{T}-1}{L} & 0 \\ -\frac{2\frac{T_0}{T}-1}{C} & 0 & -\frac{\frac{T_1}{T}}{C} \\ 0 & \frac{2\frac{T_1}{T}}{L_0} & -\frac{R_0}{L_0} \end{bmatrix} \cdot \begin{bmatrix} I_L \\ v_C \\ I_0 \end{bmatrix} + \begin{bmatrix} \frac{V_{in}}{L}\left(1-\frac{T_0}{T}\right) \\ 0 \\ -\frac{v_{in}}{L_0}\frac{T_1}{T} \end{bmatrix} \tag{8-2}$$

The steady state equation based on the characteristic of the inductor and capacitor are shown in equations (8-3, 8-4, 8-5)

$$-\left(2\frac{T_0}{T}-1\right)V_C-\left(1-\frac{T_0}{T}\right)V_{in}=0 \tag{8-3}$$

$$\left(2\frac{T_0}{T}-1\right)I_L+\frac{T_1}{T}I_0=0 \tag{8-4}$$

$$2\frac{T_1}{T}V_C-R_0I_0-\frac{T_1}{T}V_{in}=0 \tag{8-5}$$

From (8-3) the voltage across capacitors C1 (and C2) is obtained as (8-6).

$$\frac{V_C}{V_{in}}=\frac{1-\frac{T_0}{T}}{1-2\frac{T_0}{T}} \tag{8-6}$$

where, V_{in} is the input voltage to the Impedance network and V_c is the voltage across each of the capacitors which is equal to the output of the impedance network (called DC link).

In proposed application, it is assumed that the PV-array is working in the nominal voltage of 75 V, the peak output voltage of inverter is 110 V and the converter switching frequency is 50 kHz. By considering the M=0.65 as modulation index of the inverter, the RMS voltage of the capacitor has the value of 169.23 v and T_0 is calculated by (8-6), which T0=7.15 µs. Considering the converter is feeding a resistive load, using (8-5) T1 is obtained as 12.85 µs. Consequently, the inductor RMS current can be obtained using (8-4).

In boundary conduction mode, when there is no shoot-through, the capacitor voltage is always equal to the input voltage; therefore, there is no voltage across the inductor and only a pure dc current going through the inductors. The purpose of the inductors is to

limit the current ripple through the devices during boost mode with shoot-through. During shoot-though, the inductor current increases linearly and the voltage across the inductor is equal to the voltage across the capacitor. On the contrary, during non-shoot-through modes, the inductor current decreases linearly and the voltage across the inductor is the difference between the input voltage and the capacitor voltage [189]. Using the (8-4), the RMS current through the inductor is calculated as follows:

$$\bar{I}_L = \frac{T_1 / T}{1 - 2\,T_0 / T} I_0 \tag{8-7}$$

where I_o is the inverter output RMS current.

Therefore, the average current through the inductor is: $\bar{I}_L$=5.9 Amps. As the converter is assumed to work in boundary conduction mode the$\Delta I_L = \sqrt{3} * 5.9 = 10.22$

D_{Boost} of the converter according to (9-1) is D_{boost}=0.642 and the voltage across the capacitor is 169.23 V. Thereafter, we can calculate the approximate inductance value for Impedance network which is designed for boundary conduction mode:

$$V_L = L.\frac{\Delta I}{\Delta t} \Rightarrow L = \frac{V_L.\Delta t}{\Delta I} \tag{8-8}$$

The inductance value should be L≈ 52 μH. Capacitance value of the Impedance network capacitor is calculated in a similar manner;

$$\Delta V_C = \frac{I_{avg}.T_0}{C} \Rightarrow C = \frac{I_{avg}.T_0}{\Delta V_C} \tag{8-9}$$

In order to have 10% of ripple in capacitor voltage, the capacitance value should be C=185 μF. Note that these values guarantee that the operation of the converter is boundary conduction mode. If the converter tends to work in discontinues conduction mode with similar power and current rating, the inductance value must be less.

For proposed application it is considered that L=20 μH and C=185 μF. The proper operation of the converter under specified design is verified through simulation as it is shown in Figure 8.9.

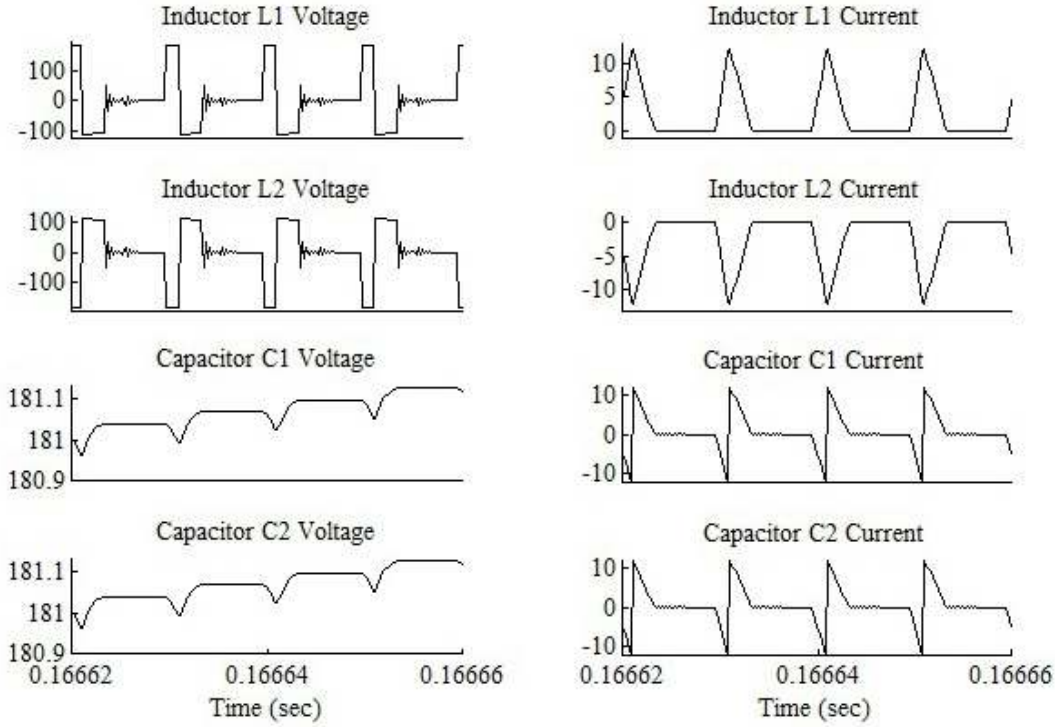

Figure 8.11 Impedance network component's voltage and current waveform

Planar Inductor Design

The planar inductor is a low profile device that covers a large area; whereas, conventional inductors are devices which are more cubical in volume. Planar inductors are designed in the same manner as conventional inductors. Planar inductors use the same planar cores and PC winding board techniques. It is normal to operate planar magnetic circuits at a little higher temperature than conventional designs. Furthermore, the current density can be higher as compared to a normal round wire.

In this section, two different designs for inductor used in Z-source converter are analyzed and compared. One is conventional inductors which uses EI core and the other is planar inductor with spiral windings which clearly will have less volume.

After the initial design of the planar inductor, in order to reduce the size and improve the characteristic of a spiral inductor, a combination of genetic algorithm and FE method are used to check the flux density and required inductance. The experimental process for the planar inductor design and evaluation of characteristics carried out in this study is shown in figure 8.12. Here two types of inductors designed in both configurations: Planar and non-planar; and then the results of our design are compared with the Finite element method. First the non-planar configuration is designed.

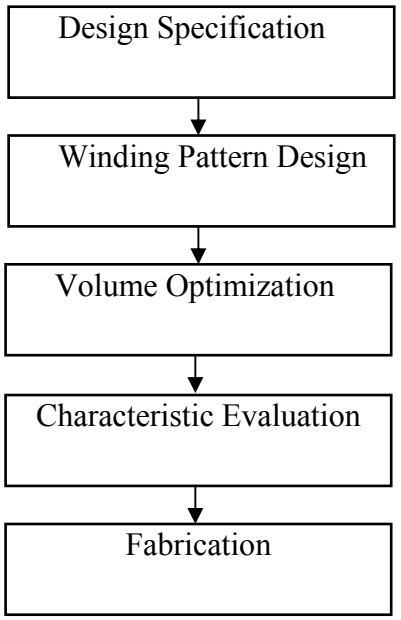

Figure 8.12 Fabrication process for planar transformer

The design specification is shown in Table 9.2; the converter parameter is designed due to these parameters,

Table 8.2 Inductor parameters

Parameters	Values
Inductance	20 μH
Peak current	10 amps
RMS current	5.9 amps
Frequency	50 kHz
Permissible temperature rise	30 ℃

Input inductor: in order to design the inductor we have to first define the diameter of the wire which is going to be used in inductor construction.

$I_{rms}=5.9\ A$

$$J_{wire}=5\,{}^{A}\!/_{mm^2}\Rightarrow A_{wire}=\frac{I_{rms}}{J_{wire}}=1.18mm^2 \tag{8-10}$$

Now considering the maximum operation frequency of the inductor we can calculate the skin effect of the conductor

$$\delta=\frac{6.6\times10^{-2}}{\sqrt{f}}=\frac{6.6\times10^{-2}}{\sqrt{50\times10^{3}}}=2.9\times10^{-4}=0.294mm \tag{8-11}$$

As it is noted in (8-11) the skin depth at the given frequency is more than the required cross sectional area of the wire that is calculated in (8-10).Therefore, there is an essential need to use Litz wire in order to reduce the current density. For such a cross sectional area, the wire of the size AWG-28 was used which has the diameter of 0.321mm and a cross sectional area of 0.081mm^2. Therefore, approximately 14 wires of AWG-28 should be Litz. Accordingly, the appropriate core will be chosen. For the design of this inductor, we consider PC40EI28-Z with its appropriate bobbin which is BE28-1110CPLFR. This type of bobbin can contain around 26 turns of the specified wire. Now The maximum

length of air gap is $l_g = \frac{\sqrt{A_e}}{10} = \frac{\sqrt{86\times10^{-6}}}{10} = 0.927\times10^{-3} \cong 0.927mm$. Then the total reluctance is obtained:

$$R_{mid} = \frac{l_g}{\mu_0 A_e} = \frac{0.927\times10^{-3}}{4\pi\times10^{-7}\times86\times10^{-6}} = 8.581\times10^{6} \Rightarrow R_{tot} = 2R_{mid} = 1.716\times10^{7}$$

By considering this reluctance we can calculate the number of turns in inductor:

$$N = \sqrt{R_{tot} \times L} = \sqrt{1.715 * 10^7 * 20 * 10^{-6}} = 18.52 \approx 19$$

Now, this design can satisfy the design criterion. The other criterion is saturation of the PC40 core. As TDK Company stated, 450mT in 60 degree of Celsius is the maximum flux density for these types of cores.

$$B_{max} = \frac{NI_{max}}{R_{tot}A_e} = \frac{19 \times 10}{1.716 \times 10^7 \times 86 \times 10^{-6}} = 0.125\ T$$

As it can be seen, the maximum flux density is less than the maximum valid flux density. Now, by twisting 19 turns around the bobbin BE28-1110CPLFR,the inductor resistance is then calculated as follows:

$$R = \frac{l}{\sigma_{cu}A} = \frac{Nl_w}{\sigma_{cu}A} = \frac{19 \times 4 \times (14) \times 10^{-3}}{5.96 \times 10^7 \times 0.205 \times 10^{-6}} = 0.0148\ \Omega$$

To design the planar inductor, the first step is to calculate the trace width. For calculating the width of external and internal traces, on PCB ANSI/IPC-2221/IPC-2221A design standards for calculation of trace width can be used which approximate the traces width as follows.

$$A[mils^2] = (\frac{I}{KT^b})^{\frac{1}{c}} \quad (PCB\ trace\ area) \tag{8-12}$$

$$l\ [mils] = \frac{A}{my}\ (PCB\ trace\ width) \tag{8-13}$$

where, I [A] is the current which passes through the trace, T [°C] is the temperature rise and m [oz] is mass of copper. Y, b, c and k are also constants that are shown in table 8.3.

Therefore, a trace which can pass current of 5.9 RMS amperes should be at least 96.7 mils (2.45 mm) for internal and 70.2 mils (1.78 mm) for external traces with20 mils of clearance.(If the maximum allowable temperature rise is 30 degree of Celsius and a copper thickness of 1 Oz/ft^2 is used) .

Table 8.3 Constants

y *[mils/oz]*	b	c	k	
1.378	0.44	0.725	0.048 external layer	0.024 internal layer

The other design for inductor is the air core planar inductor. In this part, an air core spiral winding inductor is designed and the characteristic of this inductor is compared to the previous designs. For this design, it is assumed that the inductor must pass a current of 5.9RMS amps. Hence, the trace needs to have a width of 1.783 mm according to (8-12) and (8-13).Therefore, to obtain an inductor of 20 μH we can use (8-14);

$$L = \frac{\mu_0 N^2 D_{AVG} C_1}{2} . \left(\mathrm{Ln}\left(\frac{C_2}{\rho}\right) + C_3\rho + C_4\rho^2 \right) \tag{8-14}$$

where:

$$\rho = \frac{D_{out} - D_{in}}{D_{out} + D_{in}} \tag{8-15}$$

$$D_{AVG} = \frac{D_{in} + D_{out}}{2} \tag{8-16}$$

And $C_1 \sim C_4$ depending on the layout, in which for the square type of winding are as follows: *C_1=1.27, C_2=2.07, C_3=0.18, C_4=0.13. D_{Out}* is calculated such as (8-17);

$$D_{out} = D_{in} + 2W + (W + S) \times (2N - 1) \tag{8-17}$$

where D_{in} is the internal diameter, W is the trace width and S is the distance between two adjacent trace. For a multiple layer inductor the total inductance is$L_{total} = L_1 + L_2 \pm 2M$where $M = 2K_c\sqrt{L_1 L_2}$.The coupling factor K_c in this equation is a function of distance between layers and winding style, which is calculated by (8-18):

$$K_c = \frac{N^2}{(Ax^3 + Bx^2 + Cx + D)(1.67N^2 - 5.84N + 65) \times 0.64} \tag{8-18}$$

where Parameters A to D are estimated through as: A=0.184, B=-0.525, C=1.038, D=1.001.

These calculations were carried out on a 2 layer winding and the following data was obtained. When 14 turns were completed in each winding and a distance of 0.2 mm between the layers was achieved, an inductance of 20 μH was obtained. (In this case W=1.78mm, S=0.5mm and the distance between each layer is 0.2 mm)

In a design with more than two layers, there would be more coupling factors. The same method can be used to obtain each coupling factor and the total inductance per the mutual-inductance connection formulas could be used.

In the next section, this initial design is optimized in order to satisfy the design criterion. One of these criteria is fringing flux, which can be severe in any gapped ferrite inductor. Nevertheless, this would be more noticeable on planar construction because of the printed winding board as shown in figure 8.15.

FE Analysis Design Optimization of Planar Inductor

The main objective in the design of the planar inductor is to reduce the total volume. On the other hand, when the volume is reduced, the power density capability of the inductor will reduce as well as the voltage clearance and the value of the inductance. In this study, in order to find a compromise between the value of the inductor, the radiated electromagnetic field to the surrounding environment and the minimum volume of the inductor and power quality of the Z-source inverter, a multi-objective function is formed as a combination of each of these single objectives. The first part of this multi-objective function is calculated from a transient non-linear FE analysis to calculate the value of the inductor and measure the radiated electromagnetic field. Moreover, the second part of this multi-objective function is calculated from the circuit simulation of the Z-source inverter which is implemented in Simulink environment. A classic genetic algorithm multi-objective optimization scheme is utilized to do the optimization task automatically. The variable of the genetic algorithm are indeed the geometrical dimension of the planar inductor and the inductance value and magnetic flux density around the inductor.

Figure 8.13 depicts the flowchart of the parameter optimizing procedure using GA. For more details about genetic algorithm and various types of genetic operators see [171].

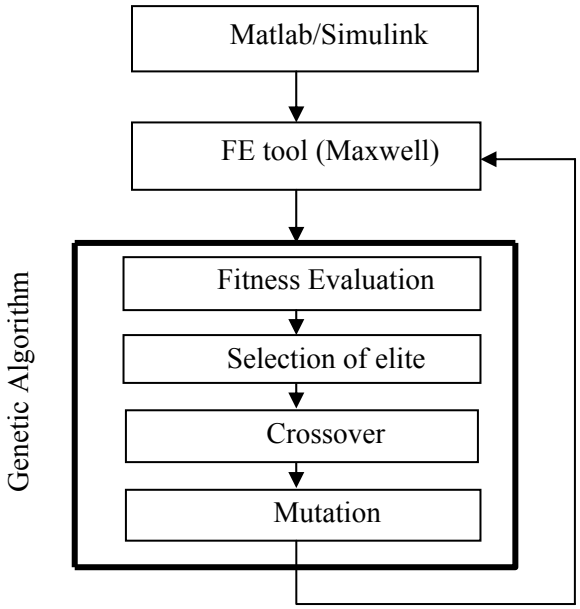

Figure 8.13 The GA optimization procedure

GA is a population based global search procedure which is inspired by natural selection and genetics law. Parameters for optimization are number of layers (n) and number of turns in each layer (N). The GA evolves the given population of individuals.

Each individual of the population represents a trial solution to the problem of minimizing fitness function given by:

$Objective\ function = A + \alpha_1.|B|^2 + \alpha_2.|\Delta L|^2$

where,$\alpha_{1,2}$=Weights signifying the importance of the objective function (taken as 1 in our case), A: surface occupied by planar inductor, B: radiated magnetic field outside the inductor surface and ΔL: inductance value error. The main purpose of GA is to find the minimum for objective function. The fitness function computes the error of the simulated and specified reference signal at each time point. The errors are then squared and added together to give a single scalar objective value. In our case, there are three signals- geometry, magnetic flux in

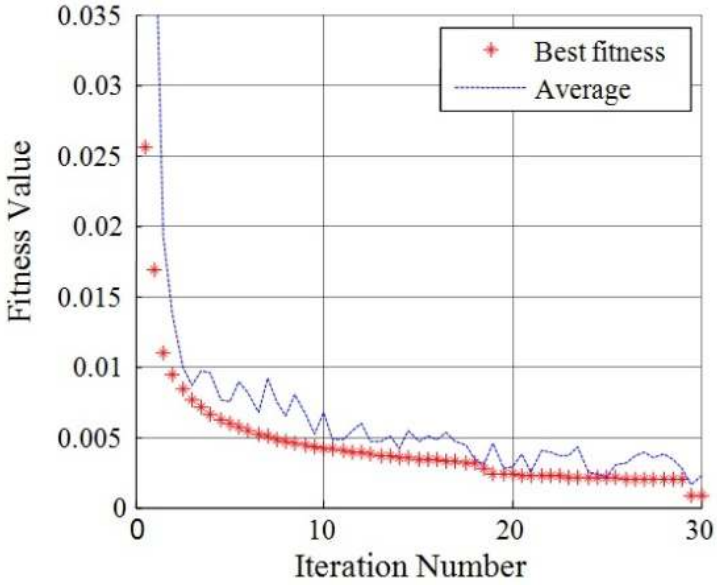

Figure 8.14 Iteration accomplished by GA to minimize the objective function

the adjacent area of the inductor and inductance. The fitness function is the sum of the squared errors for each signal again resulting in a single scalar value.

The fitness values shown in figure 8.14, illustrate that after about 10 number of iteration the error reaches to an acceptable value. Table 8.4 shows the results of the GA-algorithm and it is compared to the conventional inductors. Figure 8.15 shows the radiated electric field in a planar inductor excited by the current waveforms shown in figure 8.9 by Z-source converter. The magnetic field around the conventional inductor used in the circuit is also shown in figure 8.16. As it is illustrated in figure 8.15 and 8.16, by performing the optimization techniques the electromagnetic fields around the inductor is decreased. By comparing Figures 8.15 and 8.16, it is clear that the amount of the magnetic field in the edge of the cubic space in planar inductor is at least 5 times less than conventional inductor shown in figure 8.16; so it can cause less magnetic interference in the adjacent components on the circuit board.

Table 8.4 Optimal values for designed inductor resulted from GA

Style		Planar(optimized)	Planar	Traditional
Total window area		47.9 mm^2	66.1 mm^2	112.7 mm^2
Inductance (μH)		23	20.2	21
Minimum Weight		25g	*Less than 15g*	50 g
Resistance(Ω)		0.8	0.5	0.3
Core Dimension	No. of turns	10	14	19
	No. of layers	4	2	3

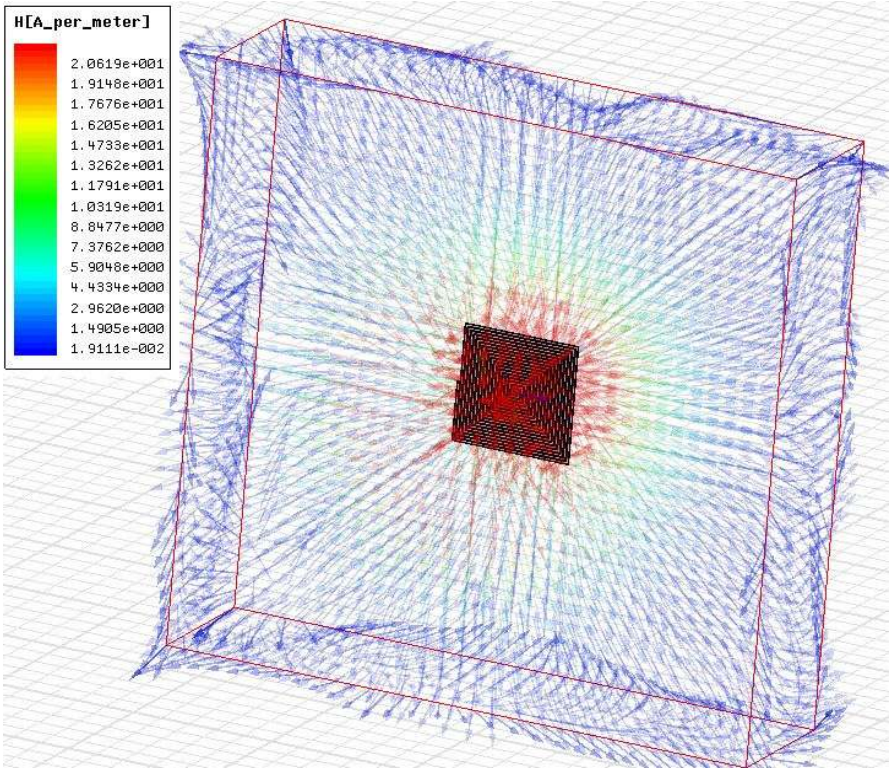

Figure 8.15 Electromagnetic model of planar inductor

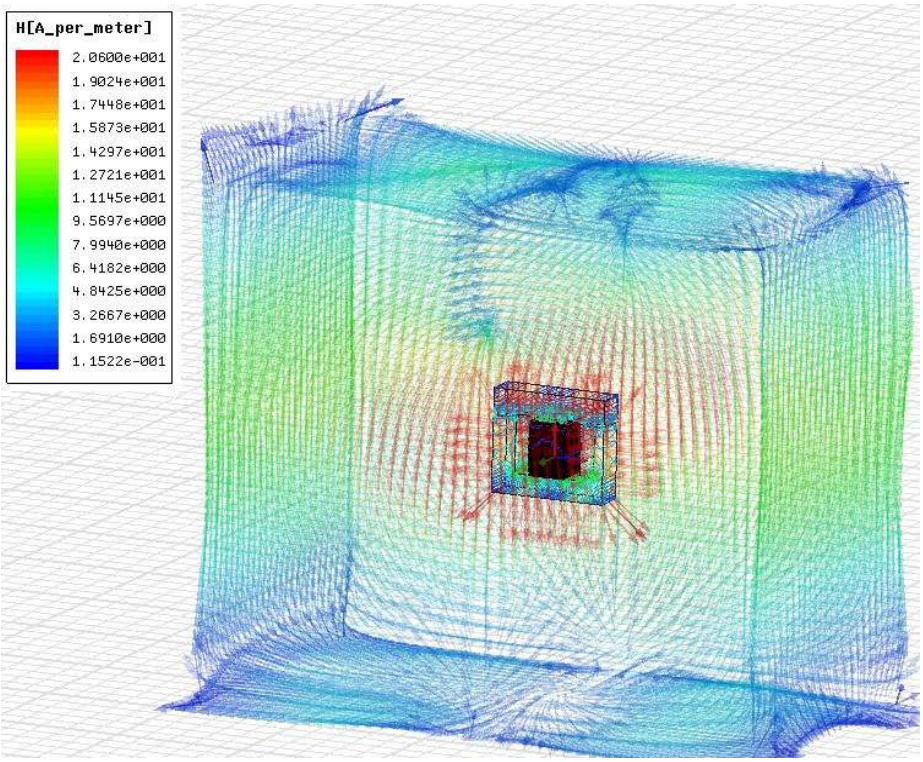

Figure 8.16 Electromagnetic model of inductor with EI-core

Figure 8.17 shows a schematic view and photograph of the fabricated inductor. The inductor consisted of four LTCC layers and Ag spiral coil winding created on the LTCC's surface. The coil in figure 8.17 has 14 turns and a dimension of 1.78*mm*in width, 30μm in thickness and 0.5 *mm* in pitch. 951 Green Tape is used as a LTCC substrate [190].

Experimental Results

The experimental results are presented for prototype planar inductor based Z-source inverter with sinusoidal modulation index, m=0.65 and shoot through duty ratio of *d*=0.2 in open-loop condition. Parameters used for experiment are given in Table 9.5.

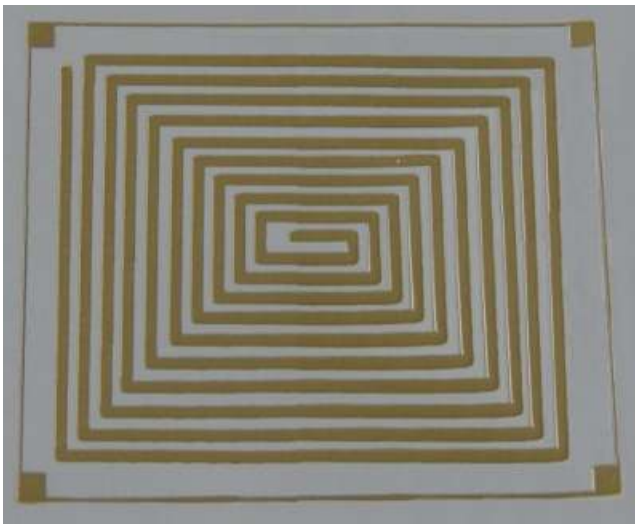

Figure 8.17 Implementation of Inductor windings on LTCC

Figure 8.18 shows the Z-source component L_1 current and voltage. In figure 8.18 the scale of the oscilloscope is 100 volts/div which means that V_{p-p} of the inductor is equal to 300 volts and the inductor peak current is 12 amps. Figure 8.19, also shows the converter output current and voltage. In figure 8.19, the scale of the oscilloscope in CH2 which shows the output current is 5 v/div which means that I_{p-p} of the inductor is equal to 6 amps and the output voltage V_{p-p} is 250 volts.

Table 8.5 Experimental setup parameters

Parameter	Value
Input Voltage	75 V
Z-source Inductor	20 μH
Z-source Capacitor	185μF
Shoot through Duty ratio	0.2
Filter Inductance	3.8 mH
Switching Frequency	50 kHz
R-Load	42 Ω

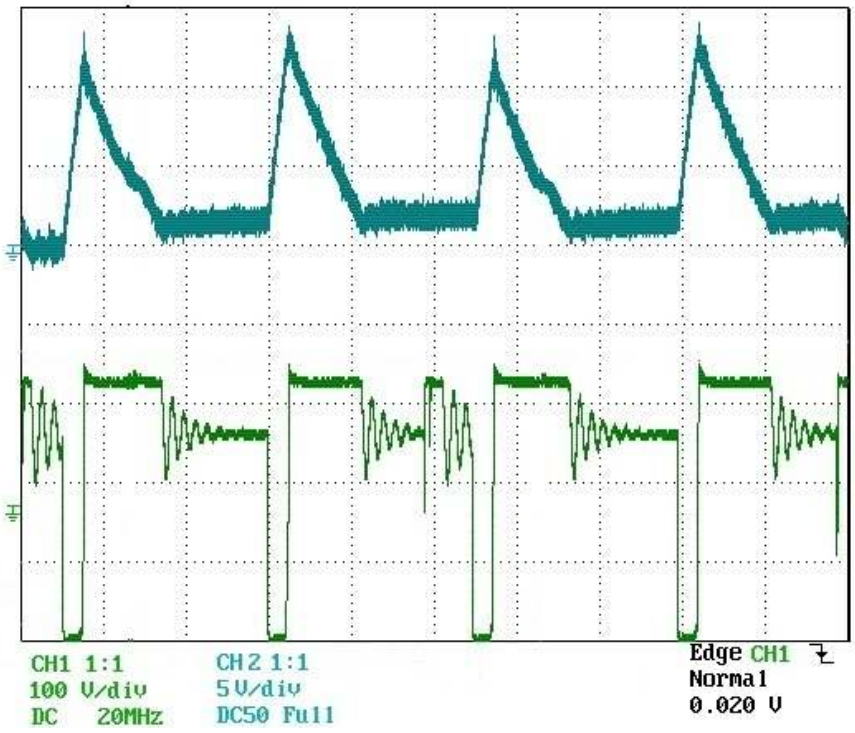

Figure 8.18 Z-source impedance network's inductor current and voltage waveforms

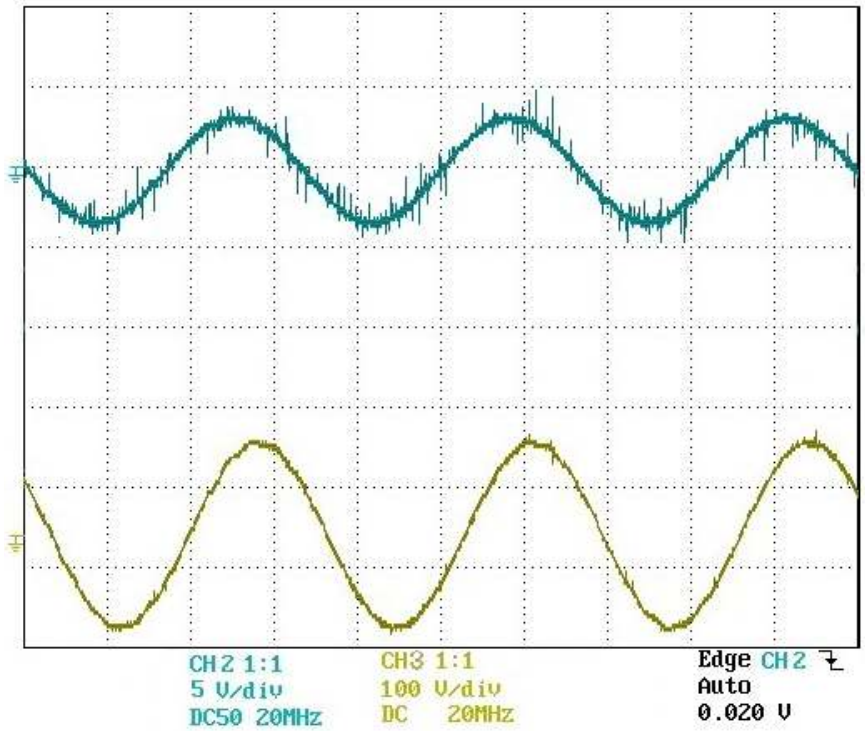

Figure 8.19 Load current and voltage waveforms

Figure 8.20, shows the simulation results for Z-source Impedance network's inductor's voltage and current, which shows the same results as compared to the experimental results in figure 8.20. Figure 8.21, also shows the converters output current and voltage in simulation which was verified through experimentation in figure 8.20.

Planar inductor is designed for Impedance network of Z-source inverter and it is optimized in order to obtain the minimum size of the inductor in addition to keep the operational characteristic. Electromagnetic behavior of magnetic components of Z-source impedance network was analyzed via FE methods and planar spiral inductor was designed to create less amount of EMI as compared to the conventional inductors. Finally Spiral Planar inductor was fabricated on the LTCC in Multilayer. The design was confirmed numerically as well as experimentation.

Physics-Based Optimization of EMI Performance in Frequency Modulated Switch Mode Power Converters

In this study, a physics-based representation of a frequency modulated switch mode converter is presented. The proposed physics based model can be used to evaluate the electromagnetic interference in the structure of the converter. In this method the power converter magnetic components and their position on the circuit board are modeled numerically using finite element analysis (FEA). Subsequently, the placement of the components and also the electrical and operating parameters of the converter are optimized in a way to limit the propagated electromagnetic field of the components. This is an essential fact in design of the power converters and the evaluation of their EMI interactions for EMC compliance.

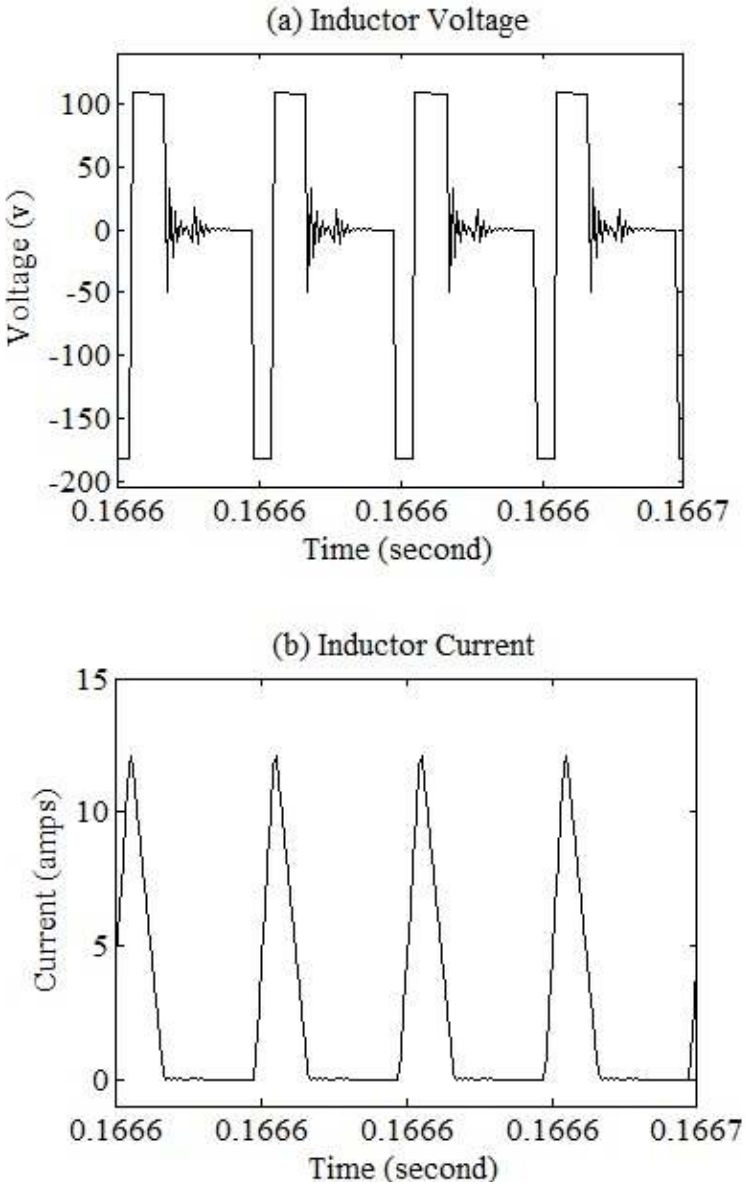

Figure 8.20 Simulation results for Z-source inductor voltage and current

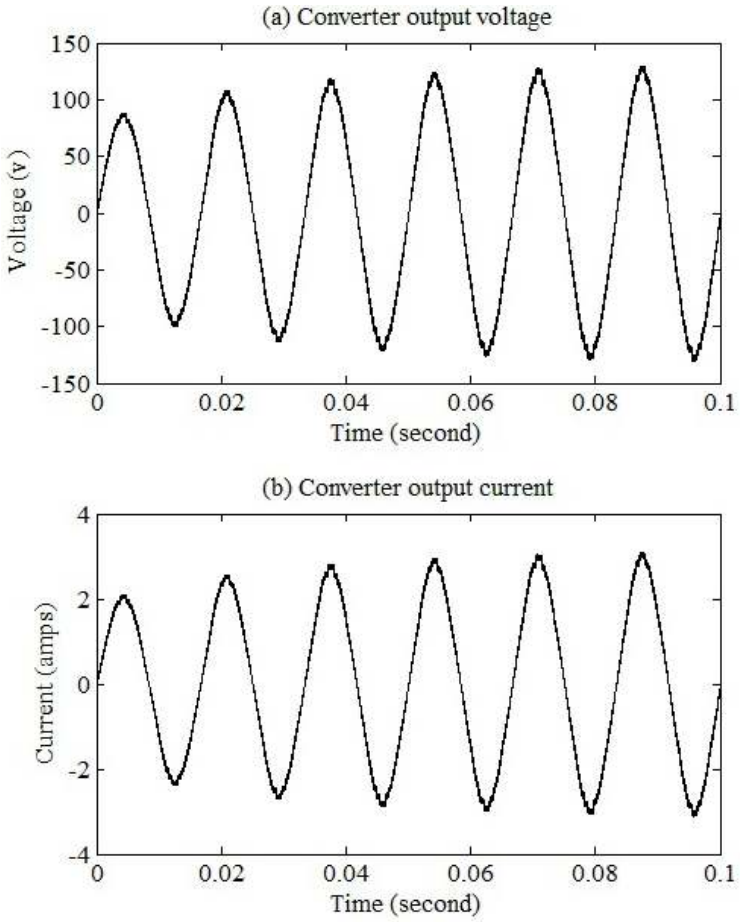

Figure 8.21 Simulation results for converter output voltage and current

Electromagnetic compatibility (EMC) is becoming an important feature in the design of modern power electronic systems [191]. High power processed at high switching frequency in a switching power supply causes electromagnetic interference (EMI), which may interfere with the normal operation of the power electronic conversion systems. Also, the Federal Communication Commission (FCC) and International Special Committee on Radio Interference (CISPR) have introduced strict protocols for power electronic designers, regarding to constraining the EMI.

So far many studies have been dedicated to the reduction of the EMI effects in power electronic converters. In [192], a method based on the proper filter design for EMI reduction was reported. The other algorithms to suppress the EMI are through using a improved modulation technique, [193], [194] and modifying the circuit board and structure of the circuit, [195-198]. In the former technique, the peak of the electromagnetic spectrum is suppressed through the spectral spreading algorithms or specific modulation techniques. These methods can spread the energy over the entire frequency band, which in turns reduce the EMI.

In all the conventional design methodology, EMC issues are addressed only after a prototype is built. At that stage, the only applicable approach to limit the EMI unpredictable problems are restricted to adding extra components or even redesigning the entire system, with a large impact on the cost of the products. It is, therefore, recognized that EMC must be addressed during the early design stages and not after.

In this study, a numerical approach is used to study the field effects in the power electronic converter's circuit, altering the values of the components and their relative positions and arriving at the best possible setting with respect to EMI performance. However, so many setting combinations are feasible. Therefore, an optimum setting is probably impossible to achieve. This paper, more concentrates on how to use the FE software to develop an appropriate guidelines to understand and reduce EMI.

Electromagnetic Field Computation

To investigate the EMI in the power electronic converters, there is a need to visualize the components which are the main contributor to the EMI problem in the power circuit.

These components are considered as a source of conducted and radiated EMI. Consequently, using simulation software the relative position of the components with respect to each other as well as the field effects in the circuit can be studied.

In this study, finite element analysis software is used to develop strategies to achieve the best EMI performance. 2D electromagnetic FE analysis is used as a tool to have an accurate physics-based simulation. The electromagnetic field inside this device is governed by the following nonlinear partial differential equations:

$$\nabla\times\left(\mu_0^{-1}\nabla\times A-M\right)-\sigma v\times\left(\nabla\times A\right)+\sigma\nabla V=J^e \tag{8-19}$$

where **A** is magnetic vector potential , $\mathbf{J}^e$ is external current density, **M** is magnetization, V is the electric scalar potential, σ is the electric conductivity and $\boldsymbol{v}$ is the motion speed which in this case, it is equal to zero. Note that, the magnetization curve was considered in several points in the hysteresis curve.

The power electronic system which was modeled in this paper is a quasi-resonant ZCS-Buck converter. The topology of the converter is shown in figure 8.22. In this circuit the switching frequency is of the order of 100 kHz. Hence the wavelength is of the order a few millimeters. Therefore, the generated electromagnetic field inside the circuit is coupled to the other components of the circuit. This phenomenon may leads to poor EMI performance of the system. By performing simulation, the intra-system EMI is observed.

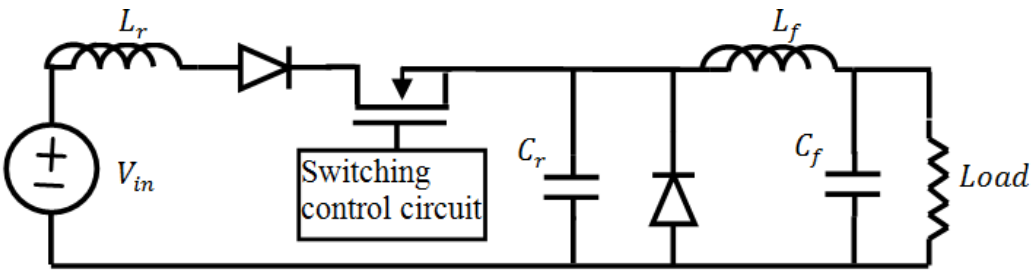

Figure 8.22 Schematic of the Quasi-resonant ZCS-Buck converter.

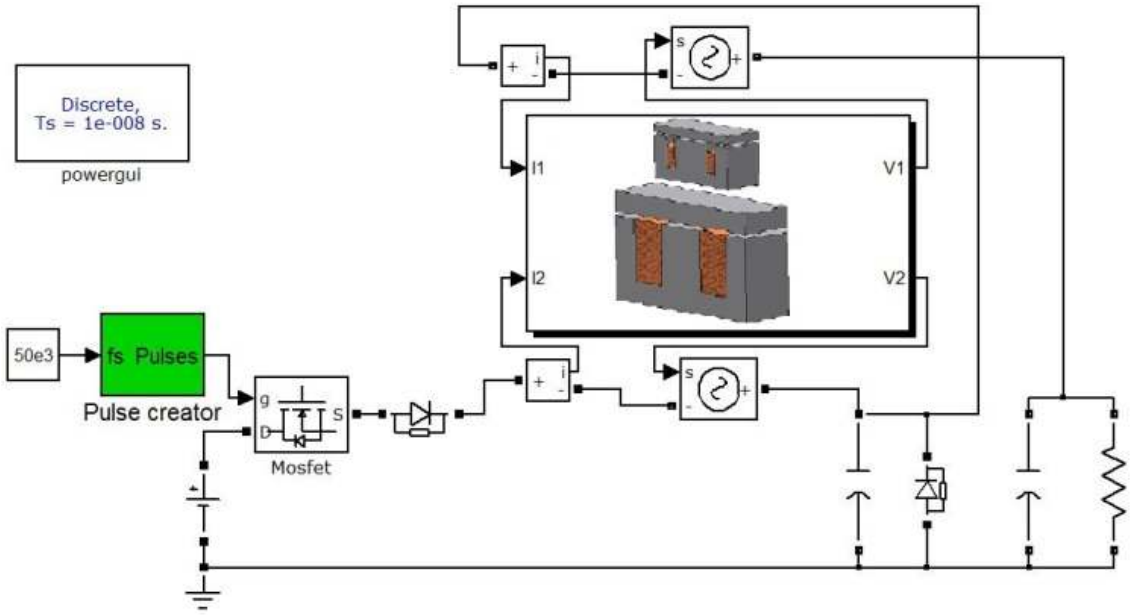

Figure 8.23 Schematic of the physics-based Quasi-resonant ZCS-Buck converter.

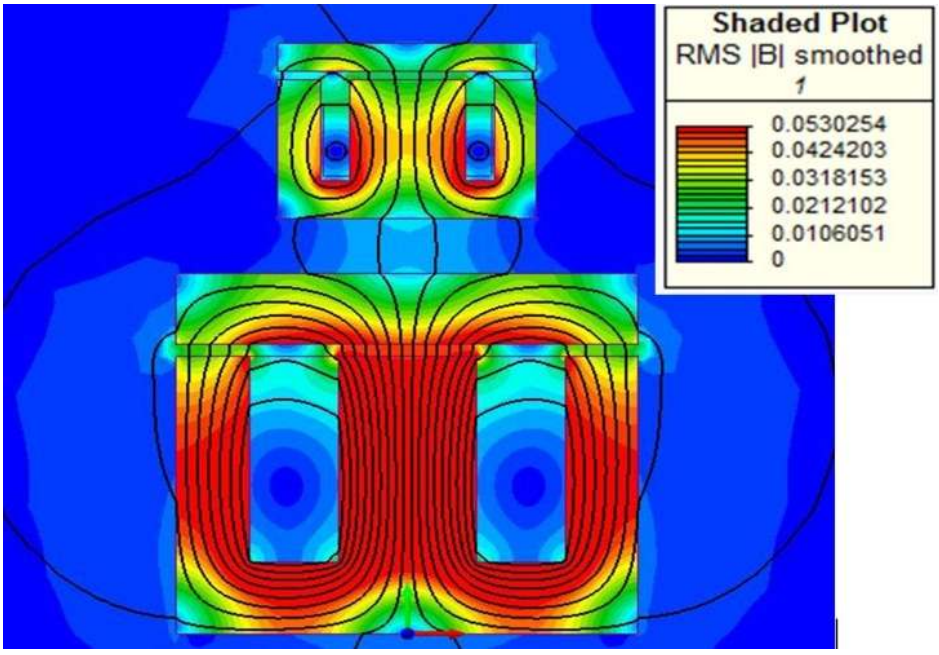

Figure 8.24 Magnetic component's structure and placement in finite element.

Figure 8.23 shows the schematic of the physics-based quasi-resonant converter. In this case, magnetic components have the most impact on the high-frequency behavior of the converter as well as the EMI effects inside the circuit. Therefore, in this structure, only the magnetic components are modeled numerically in finite element and the other components are remaining unchanged as ideal case. Modeling the magnetic components is entirely described in [199], which for sake of brevity is omitted here.

Figure 8.24 shows the relative placement and location of the two power inductors with respect to each other, inside the converter's layout. It is noticed that, passing the high frequency current through these components, generates electromagnetic fields, which can propagated all around the circuit PC-board. This high frequency electromagnetic field, not only affects the self-inductance of the inductor, by forming the saturation in some areas of the ferrite core, but also can affect the other components which are surrounded by this field. This phenomenon is shown in figure 8.24, where the electromagnetic fields, generated by the two inductors, are interfered with each other. Therefore, the parasitic elements of these two components are excited by the abovementioned high-frequency electromagnetic field. Inappropriate placement of the magnetic components in a circuit may cause unwanted effects in the behavior of the converter and deteriorating the EMI performance of the converter.

The FFT spectrum of the converter's current and voltages at different points are shown in figure 8.25. Figure 8.25(a), (b) and (c) compares the input current spectrum, filter inductor's current spectrum and output voltage spectrum of the converter in the ideal case and physics-based mode (non-optimized case), respectively. This FFT spectrum was depicted up to 5 MHz. It is noticed that almost 0.99 dBV difference

between these two spectrums in the frequency range of lower than 10 kHz. The low frequency effects may be due to the saturation in the inductor's core and leakage inductances, which was not considered in the ideal case. Also, it is observed that using the physics-based model, some high-frequency oscillations can be detected, which could not be seen in the ideal case. These high-frequency oscillations can cause EMI problem as well as radio frequency noises in the power converter.

In the next section, an optimization method is introduced, which can reduce the EMI effects. In this method, the converter's operational parameters (such as switching frequency) and the magnetic components value and placement are used as the optimization variables. Therefore, by proper placement of the components and setting the operating frequency the interference between the two components are limited. Consequently, this may leads to reduction in the EMI effects in the converter.

Design and Optimization Procedure

As it was shown in figure 8.25, inappropriate placement of the components in the circuit deteriorates the EMI performance of the system. In order to solve this problem, an optimization procedure is used to design the magnetic components and their location on the board. The main objective is to minimize the size of the board confining the two magnetic component of the converter, as illustrated in (8-20), while satisfying the EMC standards. The optimization variables are the inductance value, operating frequency of the system and the energy of the output voltage signal. The first two variables are calculated from a pre-defined table characterize the converter operating parameters. The

third variable is calculated from the circuit simulation of the converter's circuit, which is implemented in Simulink/MATLAB environment.

To solve the optimization problem a multi-objective function is defined as equation (8-20). The first part of this multi-objective function is the area confined the two magnetic components. Moreover, the second part of this multi-objective function is the energy of the signal. A classic genetic algorithm multi-objective optimization scheme is utilized to do the optimization task automatically.

$$Objective\ function = \alpha_1.|Area|^2+\alpha_2.\left|E_f\right|^2 \quad (8\text{-}20)$$

where, $\alpha_{1,2}$=Weights signifying the importance of the objective function (taken as 1 in our case), $Area$: Area, confining the two magnetic components and E_f: Energy of the output voltage signal.

Figure 8.26 depicts the flowchart of the parameter optimizing procedure using GA. GA is a population based global search procedure which is inspired by natural selection and genetics law [200]. Parameters for optimization are the converter's operating parameters and placement of the magnetic components with respect to each other. The GA evolves the given population of individuals. The main purpose of GA is to find the minimum for objective function. The object function as states in (8-20) is consisting of the area of the circuit board and energy of the output voltage signal. In order to change the area which confines the two inductors, the filter inductor's position is considered as a reference and the resonant inductor placement is changing all around the reference point (filter inductor). Figure 8.27 illustrates the process of changing the placement of the two inductors as with respect to each other.

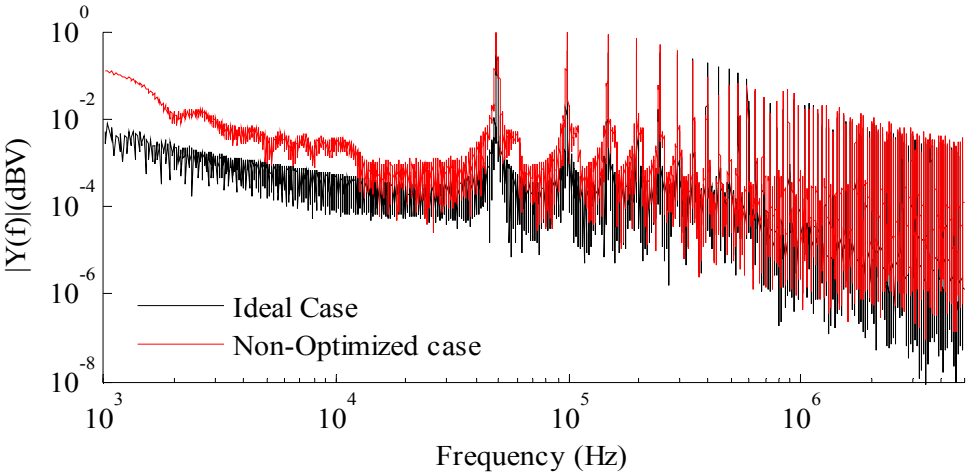

(a)

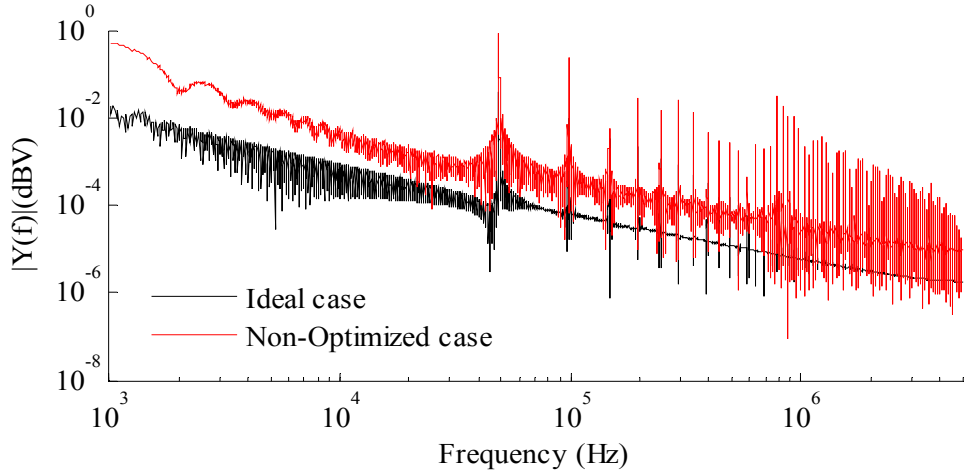

(b)

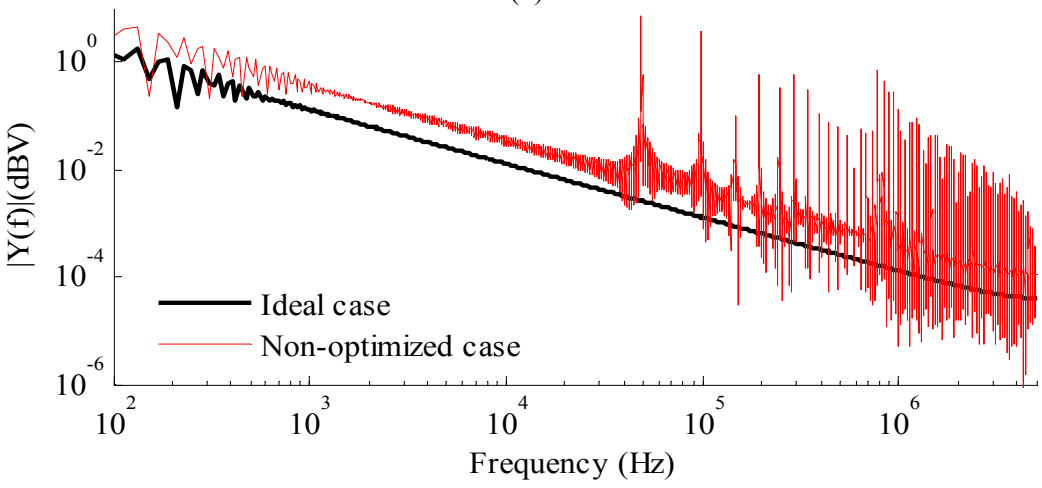

(c)

Figure 8.25 Comparison of FFT spectrum between ideal quasi-resonant converter and its corresponding physics-based model, a) Resonant inductor's current, b) filter inductor's current, c) output voltage.

The other important factor in the objective function is the energy of the signal (E_f). This parameter can be used as a criterion to measure the EMI performance of the system. The lower value for this parameter can be a representative for a better performance of the whole system's EMI performance. The energy of the signal is calculated based on the following equation:

$$E_x =< x(t), x(t) > = \int_{-\infty}^{\infty} |x(t)|^2 dt \tag{9-21}$$

In which based on the Parseval's theorem for energy signals, we have:

$$\int_{-\infty}^{\infty} |x(t)|^2 dt = \frac{1}{2\pi} \int_{-\infty}^{\infty} |X(\omega)|^2 d\omega \tag{9-22}$$

where $X(\omega)$ is the Fourier transform of $x(t)$.

The optimization results illustrate that after about 18 number of iteration the error reaches to an acceptable value.

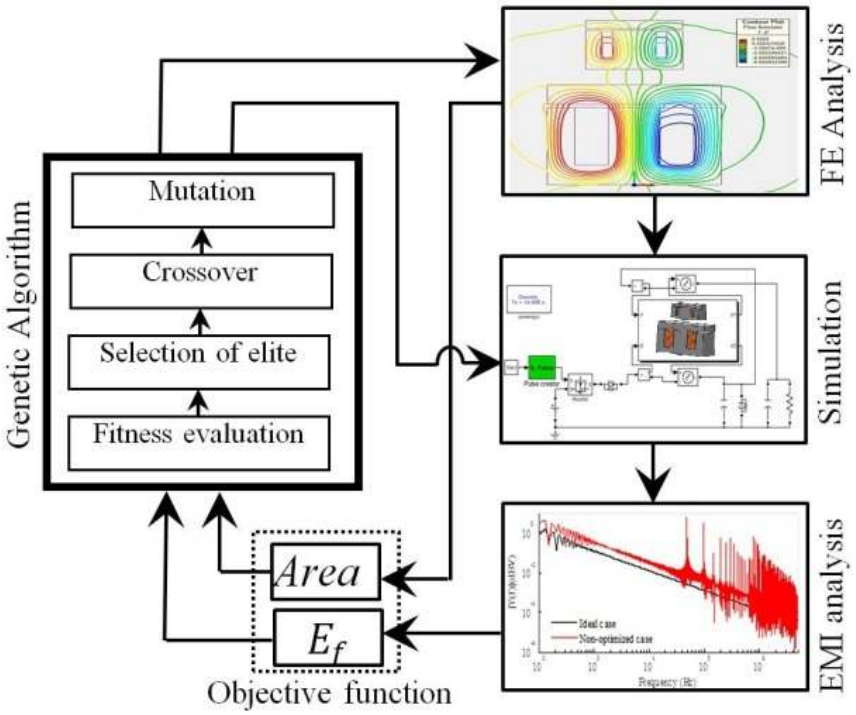

Figure 8.26 The optimization process diagram.

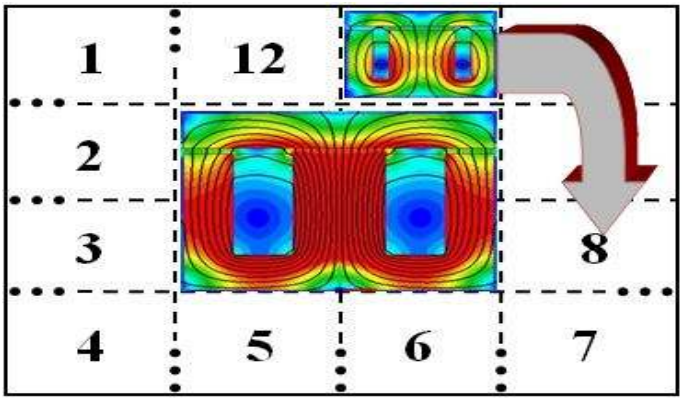

Figure 8.27 Iteration accomplished by GA to minimize the objective function.

Results and Discussion

Table 8.6 shows the results from the optimization process. The magnetic component positions of this converter are shown in figure 8.28. It is clear that this power converter is showing a poor EMI performance at initial design stage (figure 8.28(a)). FE analysis is performed observe the near-field effects for the given layout. Further, we performed repeated simulations to determine the best EMI performance versus geometry of the board and the frequency (figure 8.28(b)).

Figure 8.29 compares the input current spectrum, filter inductor's current spectrum and output voltage spectrum of the converter in the ideal case and physics-based mode (non-optimized case), respectively. It is noticed that in the optimized case the pick of the frequency spectrum is decreased, as compared to the non-optimized case.

Figure 8.30 shows the circuit layout of the converter in the optimized case. In this case, the magnetic components are placed, somehow, that the magnetic field generated by each one has the less interference with the other.

Table 8.6 Optimization results

Parameters	L_r (μH)	f (kHz)	Area (mm^2)
Initial design	120	50	3360
Optimized design	45	90	11000

Simulation results shown in figure 8.29 are also verified experimentally. Figure 8.31, shows the FFT spectrum of the actual converter input current and output voltage, recorded by using the spectrum analyzer. It is observed that the amplitude of the FFT spectrum is decreased in the optimized case.

A method for improving the EMI performance of the power electronic converters was presented. This method is mainly based on the optimization of the converter at the design stage and proper placement of the components on the circuit board. The converter's components are modeled using coupled circuit/electromagnetic FE computations.

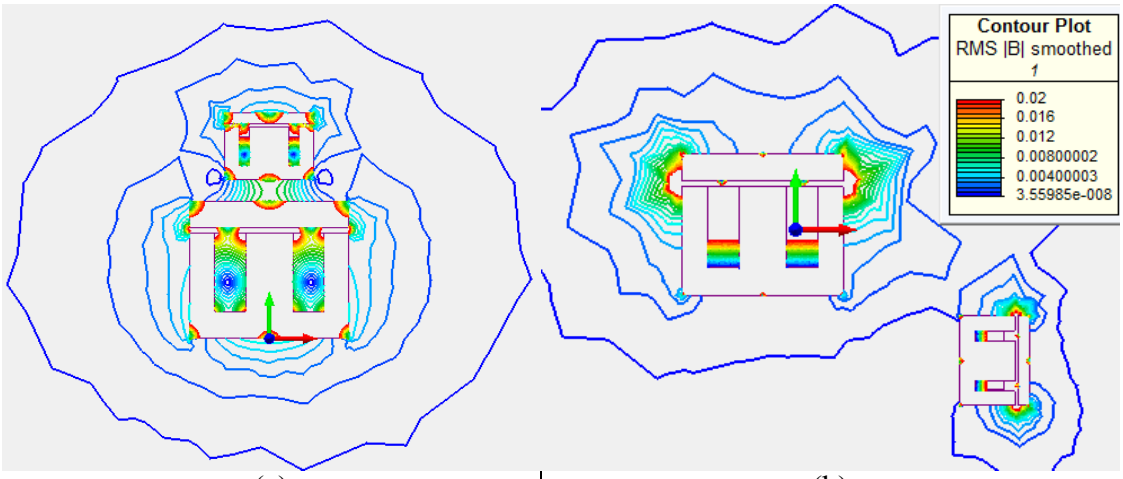

(a) (b)

Figure 8.28 Layout of the system, a) Before Optimization, b) After optimization

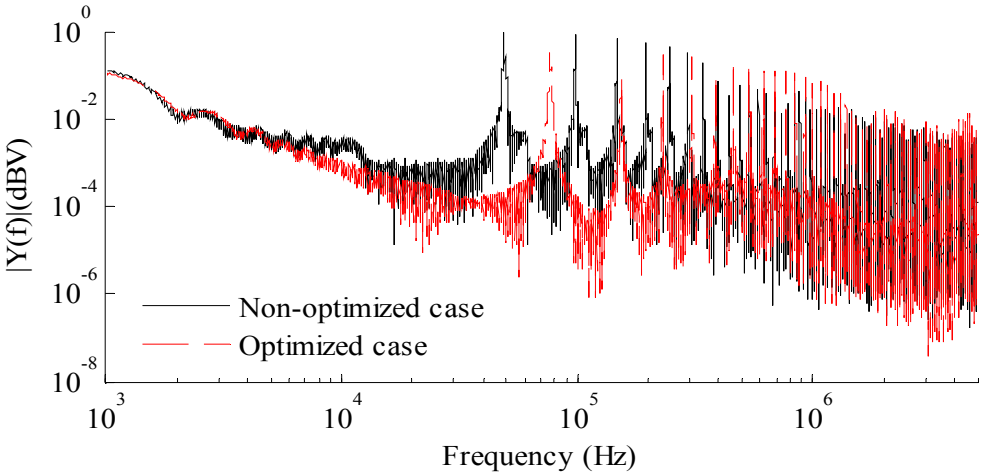

(a)

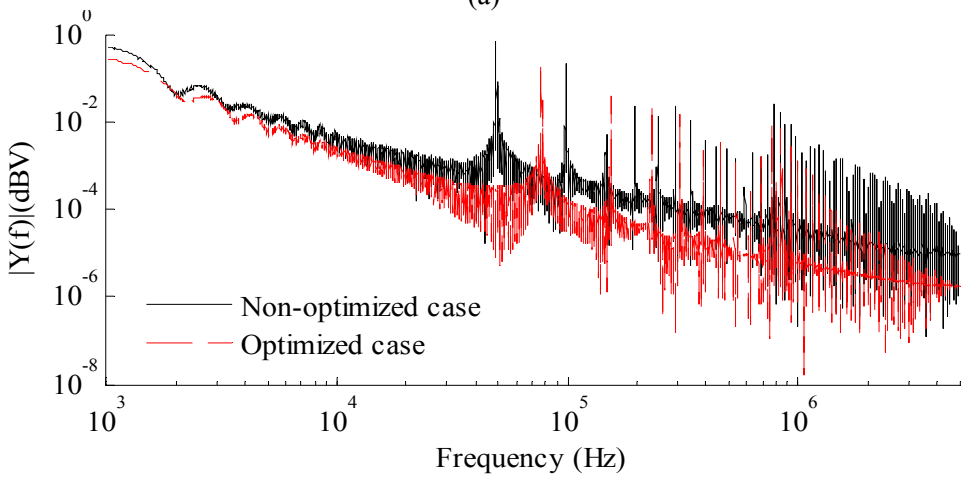

(b)

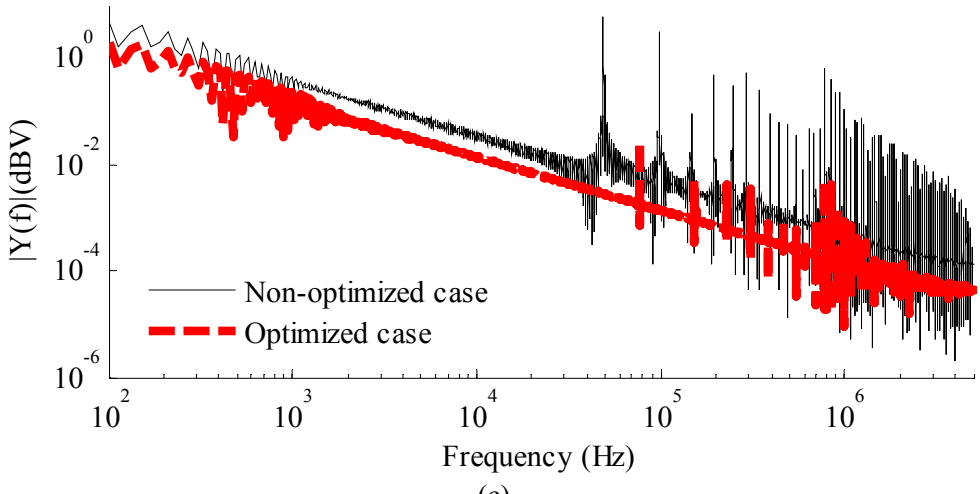

(c)

Figure 8.29 Comparison of FFT spectrum between optimized and non-optimized quasi-resonant converter, a) Resonant inductor's current, b) filter inductor's current, c) output voltage.

FE analysis was performed to obtain the physics-based behavioral model of the converter. The converter's operating parameters and components placement are optimized using genetic algorithm.

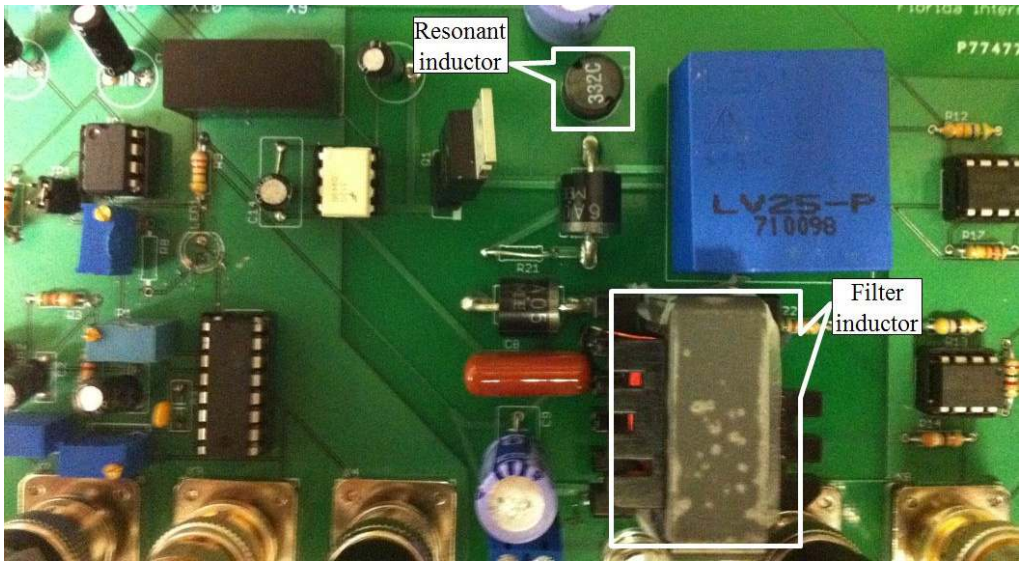

Figure 8.30 ZCS quasi-resonant buck converter's circuit in the optimized layout.

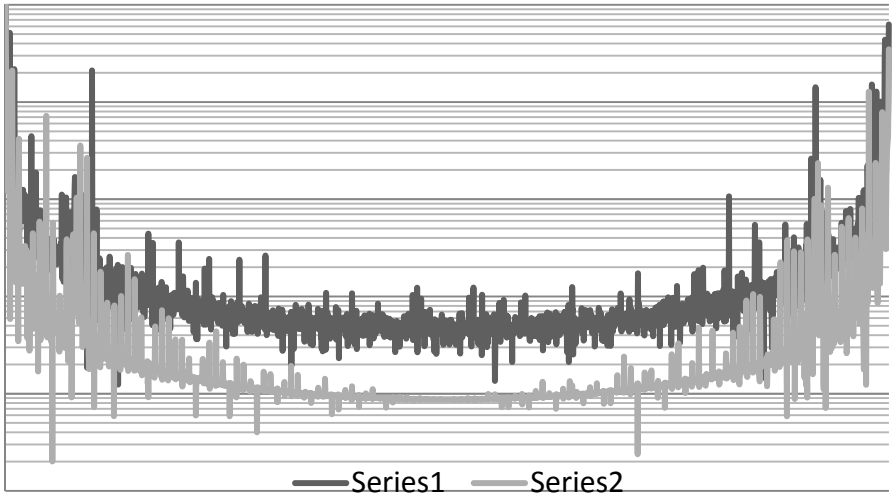

Figure 8.31 FFT spectrum of the ZCS-QRC Buck converter's output voltage, a) input current, b) output voltage.

The results show that using this method, we can evaluate the EMI performance of the converter before it is actually built. This algorithm can, also, be implemented for the other types of power electronic converters, making it practical for the evaluation on EMI/EMC issues at the development stages.

Chapter 9 Conclusion

This work presented development of physics-based models and design optimization of power electronics conversion systems. This was done numerically rather than experiments. The parameters used to build different components models were obtained from coupled–FE analyses. This technique is significance because the FEA methodologies to extract high frequency parameters were shown to be accurate and eliminates costly machine testing. Different models were built for low and high frequency studies. These models were used to investigate different low and high frequency operation issues in some typical power electronics system.

Coupled Field-Circuit analysis was used to model the high-frequency behavior of the converter. Modeling components with internal connections represent a challenge because of alter of the magnetic field which will change the components parameters which usually are calculated during testing. In addition, the complete drive model is developed for EMI analysis. It consists of lumped parameter models for different system components, which enable faster simulations.

A methodology for high-frequency parameters extraction and harmonic behavior evaluation for different power electronic components using FEM was developed. The results show the ability of this algorithm to extract harmonics and to capture the high-frequency behavior of the systems.

This modeling methodology can be utilized to evaluate and predicate the power electronics system components future behavior at early design stages which will reduce the development cycles, cut overall cost, prevent failures, develop operational strategies and test a subsystem exhaustively before integrating it into the system.

A change in the converter operating conditions and its influence on the system's high-frequency behavior has also been investigated. It shows a difference in the parameter values and in the system's high-frequency behavior.

The prediction of accurate ground currents and overvoltage in the design stages of drive system would reduce the time required for design modifications as well as for evaluation of EMC compliance issues. The model can be utilized in design optimization of the converter package during design process. Use of this procedure could prove economical, as it would help designers develop new designs for high frequency operating conditions numerically. With the proposed model, this can be done without the need for repeated build and test procedures in the development stage.

.

Chapter 10 Recommendations and Future Works

The main focus of this dissertation is on physics-based modeling of power electronic conversion systems, to predict the high-frequency conducted and radiate noise from these systems. The other advantage of this approach is that, it enables of with a proper diagnostics and prognostics tools that can help us to improve our design.

However, to further improve the quality of the power conversion system sthe following recommendation is proposed:

Through the physics-based modeling a stability analysis can be performed on the power conversion systems in-order to verify the validity and effectiveness of the control system. Once this has been achieved, the optimization of the whole system for stability can be tackled.

The transient behavior of the IGBT module has been investigated with respect to theoretical parameter variations. It may be possible to make measurements on production chips to verify the expected variations across a wafer; in combination with finite-element simulation, future improvements in production methodology and control can be targeted for maximum gains in device performance.

A future topic of research would be to expand and apply the ideas used in these models to new device structures and then implement them in SABER software simulation to confirm the validity of the developed model.

Moreover, regarding the magnetic components of the system the following researches can be performed: The gate drive transformers are essential part of the electronic circuits. Including the parasitic capacitance effect in the modeling and analysis can help in better understanding of the transformer operation and improve the performance of the

transformer. Also, having more accurate expressions for determining the geometrical parameters for required inductance both in the case of PCB would help in designing a better transformer. Also, implementing multiple versions in different electromagnetic softwares to strive for better match between the simulated data and the physically measured data, is suggested.

Furthermore, the following suggestions can be considered for future study and can be extended in different ways:

- Used the real time distributed environment to perform system study such as stability and reconfiguration.
- To further refine and develop the models and parameter estimation methods developed here.
- To model different type of nonlinear materials and their effect on the system overall harmonic behavior.
- Develop robust control algorithms for noisy environments to minimize the interference and to keep them in service as long as possible. And then use the real time shell to evaluate the developed control algorithm.
- Using the tools and models developed to perform system studies such as stability and reconfiguration.
- Effect of replacing power electronics building blocks on the system performance. To include the dc system into the study

REFERENCES

1. Nagy Abed, ”Physical Dynamical Simulation of Shipboard Power Systems in a Distributed Computational Environment”, PhD. Dissertation, Electrical Engineering dept., Florida International University, 2007.

2. Shreerang Ganu, ” High Frequency Electric Machine Models for the Evaluation of Operational Impacts in Integrated Drives”, PhD. Dissertation, Electrical Engineering dept., Florida International University, 2007.

3. M. L. Heldwein, J. W. Kolar, “Design of Minimum Volume EMC Input Filters for an Ultra Compact Three-Phase PWM Rectifier”, to be published at COBEP’07, Sept. 30-Oct. 4, 2007.

4. D. Sullivan, “Electromagnetic Simulation using the FDTD Method”, John Wiley & Sons, Inc., 2000.

5. D. Cottet, M. Paakkinen, “Scalable PEEC-SPICE modeling for EMI analysis of power electronic packages and subsystems”, Proc. EPTC’06, Singapore, Dec. 6-8, 2006.

6. E. Wolfgang, W. Gerling, U. Drofenik, “Reliability of Power Electronic Systems”, ECPE-Tutorial, Nuremberg, Germany, April 19-20, 2007.

7. D. Cottet, S. Hartmann, U. Schlapbach, “Numerical Simulations for Electromagnetic Power Module Design”, Proc. ISPSD’06, Naples, Italy, June 4-8, 2006.

8. M. L. Heldwein, T. Nussbaumer and J. W. Kolar, ”Differential Mode EMC Input Filter Design for Three-Phase AC-DC-AC Sparse Matrix PWM Converters”, Proc. PESC’04, pp. 284-291, 2004.

9. P. Musznicki, J.-L. Schanen, B. Allard and P. Chrzan, “Accurate Modeling of Layout Parasitics to Forecast EMI Emitted from a DC-DC Converter”, Proc. PESC’04, vol.1, pp. 278-283, 2004.

10. Müsing, M. L. Heldwein, T. Friedli, J. W. Kolar, “Steps Towards Prediction of Conducted Emission Levels of an RB-IGBT Indirect Matrix Converter”, Proc. PCC’07, Nagoya, Japan, pp. 1181-1188, 2007.

11. U. Drofenik, D. Cottet, A. Müsing, J. W. Kolar, “Design Tools for Power Electronics: Trends and Innovations“, Ingenieurs del'automobile, No. 791, pp. 55 – 62, Dec. 2007

12. Ruehli, G. Antonini, J. Esch, J. Ekman, A. Mayo, A. Orlandi, “Nonorthogonal

PEEC Formulation for Time- and Frequency-Domain EM and Cirucit Modeling “, IEEE Trans. Electromagnetic Compatibility, vol.45, no.2, pp. 167-176, 2003

13. J. Ekman, “Electromagnetic Modeling Using the Partial Equivalent Circuit Method”, Ph.D. thesis, EISLAB, Luleå University of Technology, Sweden, 2003.

14. J. W. Kolar, U. Drofenik, J. Biela, M. L. Heldwein, H. Ertl, T. Friedli, S. D. Round, “PWM Converter Power Density Barriers”, Proc. PCC'07, Nagoya, Japan, April 2-5, 2007.

15. C. Martin, J. L. Schanen, R. J. Pasterczyk, “Inside a power module”, Proc. IAS’04, vol.3, pp. 1519-1525, Oct. 3-7, 2004.

16. M. Ciappa, “Selected failure mechanisms of modern power modules”, Microelectronics Reliability 42, pp. 653-667, 2002.

17. Ali Davoudi, “Reduced-Order Modeling of Power Electronics Components and Systems”, PhD. Dissertation, Electrical and Computer Engineering Dept., University of Illinois at Urbana-Champaign, 2010

18. F. Witulski, “Introduction to modeling of transformers and coupled inductors,” *IEEE Trans. Power Electron.*, vol. 10, pp. 349–357, May 1995.

19. A. Massarini and M. K. Kazimierczuk, “Self-capacitance of inductors,” *IEEE Trans. Power Electron.*, vol. 12, pp. 671–676, Jul. 1997.

20. W. J. Sarjeant, “Capacitors,” *IEEE Trans. Ind. Electron.*, vol. 25, pp. 861–922, Oct.

21. Palmer, P.R.; Santi, E.; Hudgins, J.L.; Xiaosong Kang; Joyce, J.C.; Poh Yoon Eng; , "Circuit simulator models for the diode and IGBT with full temperature dependent features," *Power Electronics, IEEE Transactions on* , vol.18, no.5, pp. 1220- 1229, Sept. 2003

22. Xiaosong Kang; Caiafa, A.; Santi, E.; Hudgins, J.L.; Palmer, P.R.; , "Characterization and modeling of high-voltage field-stop IGBTs," *Industry Applications, IEEE Transactions on* , vol.39, no.4, pp. 922- 928, July-Aug. 2003

23. Cacciato, M.; Consoli, A.; Scarcella, G.; De Caro, S.; Testa, A.; , "High frequency modeling of DC/AC converters," *Power Electronics and Applications, 2005 European Conference on* , vol., no., pp.10 pp.-P.10, 0-0 01990.

24. Dongsheng Zhao; Ferreira, B.; Roch, A.; Leferink, F.; , "New Common Mode EMI filter for motor drive using a fourth leg in the inverter," *Electromagnetic Compatibility - EMC Europe, 2008 International Symposium on* , vol., no., pp.1-6, 8-12 Sept. 2008

25. Konstantinou, G.S.; Agelidis, V.G.; , "Bidirectional rectifier-inverter multilevel topology without DC-link passive components," *Energy Conversion Congress and Exposition (ECCE), 2010 IEEE* , vol., no., pp.2578-2583, 12-16 Sept. 2010

26. Mazumder, S.K.; Rathore, A.K.; , "Performance evaluation of a new hybrid-modulation scheme for high-frequency-ac-link inverter: Applications for PV, wind, fuel-cell and DER/storage applications," *Energy Conversion Congress and Exposition (ECCE), 2010 IEEE* , vol., no., pp.2529-2534, 12-16 Sept. 2010

27. E. Ruehli, "Equivalent Circuit Models for Three-Dimensional Multi-conductor Systems", IEEE Trans. on Microwave Theory and Techniques, Vol. 22 No. 3, pp. 216-221, 1974.

28. J. Jin, "The Finite Element Method in Electromagnetics", John Wiley & Sons, NY, USA, 1993.

29. U. Drofenik, D. Cottet, A. Müsing, J.-M. Meyer, J. W. Kolar, "Computationally Efficient Integration of Complex Thermal Multi-Chip Power Module Models into Circuit Simulators", Proc. PCC'07, Nagoya, Japan, April 2-5, 2007.

30. U. Drofenik, D. Cottet, A. Müsing, J.-M. Meyer, J. W. Kolar, "Modeling the Thermal Coupling between Internal Power Semiconductor Dies of a Water-Cooled 3300V/1200A HiPak IGBT Module", Proc. PCIM'07, Nuremberg, Germany, May 22-24, 2007.

31. U. Drofenik, G. Laimer, J. W. Kolar, "Theoretical Converter Power Density Limits for Forced Convection Cooling", Proc. PCIM'05, Nuremberg, Germany, June 7-9, pp. 608-619, 2005.

32. U. Drofenik, J. W. Kolar, "A General Scheme for Calculating Switching- and Conduction-Losses of Power Semiconductors in Numerical Circuit Simulations of Power Electronic Systems", Proc. IPEC'05, Niigata, Japan, April 4-8, 2005.

33. G. Burke, A. Poggio, "Numerical electromagnetics code (NEC) – Method of Moments", Research Report, Lawrence Livermore Laboratory, Livermore, CA, 1981.

34. R. Saleh, J. White, "Fast-Cap: A Multipole-Accelerated 3-D Capacitance Extraction Program", IEEE Trans. on Computer- Aided Design, vol.10, no.10, pp. 1447-1459, 1991.

35. M. Kamon, M. J. Tsuk, J. K. White, “FastHenry: a multipole- accelerated 3-D inductance extraction program”, IEEE Trans. Microwave Theory and Techniques, vol.42, no.9, pp.1750-1758, 1994.

36. Z. Zhu, B. Song, J. White, “Algorithms in FastImp: A Fast and Wide-Band Impedance Extraction Program for Complicated 3D- Geometries”, IEEE Trans. Computer-Aided Design of Integrated Circuits and Systems, vol.24, no.7, 2005.

37. A.E. Ruehli, H. Heeb, “Circuit Models for Three-Dimensional Geometries Including Dielectrics”, IEEE Trans. Microwave Theory Technology, vol.40, no.3, pp. 1507-1516, 1992.

38. J. Biela, J. W. Kolar, “Cooling Concepts for High Power Density Magnetic Devices”, Proc. PCC'07, Nagoya, Japan, April 2- 5, 2007.

39. T. Franke, G. Zaiser, J. Otto, M. Honsberg-Riedl, R. Sommer, “Current and Temeprature Distribution in Multi-Chip Modules under Inverter Operation”, Proc. EPE’99, Lausanne, Switzerland, 1999.

40. S. Munk-Nielsen, L. N. Tutelea, U. Jaeger, “Simulation with Ideal Switch Models Combined with Measured Loss Data Provides a Good Estimate of Power Loss”, Conf. Record of IAS’2000, Roma, Italy, Oct. 8-12, vol.5, pp. 2915-2927, 2000.

41. J. Chen and S. Downer, “MOSFET Loss and Junction Temperature Calculation Model in MATLAB”, Proc. PCIM’04, Nuremberg, Germany, May 23-27, 2004.

42. U. Drofenik, “Embedding Thermal Modeling in Power Electronic Circuit Simulation”, ECPE Power Electronics Packaging Seminar, Baden-Dättwil, Switzerland, June 7-8, 2004.

43. J. W. Kolar, F. C. Zach, “A Novel Three-Phase Utility Interface Minimizing Line Current Harmonics of High-Power Telecommunications Rectifier Modules”, Record of INTELEC’04, Vancouver, Canada, Oct. 30-Nov. 3, pp. 367-374, 1994.

44. C. Martin, J. M. Guichon, J. L. Schanen, “Gate circuit layout optimization of power module regarding transient current imbalance”, Proc. PESC’05, Recife, Brazil, pp. 541-546, June 12-16, 2005.

45. D. Cottet, A. Hamidi, “Numerical Comparison of Packaging Technologies for Power Electronics Modules”, Proc. PESC’05, Recife, Brazil, June 12-16, 2005.

46. T. Wikström, T. Stiasny, M. Rahimo, D. Cottet, P. Streit, “The corrugated p-base IGCT - a new benchmark for large area SOA scaling”, Proc. ISPSD’07, Jeju, Korea, May 27-30, 2007.

47. T. Friedli, M. L. Heldwein, F. Giezendanner, J. W. Kolar, “A High Efficiency Indirect Matrix Converter Utilizing RB-IGBTs”, Proc. PESC’96, 1199-1205, 2006.

48. J. Tichenor, S. Sudhoff and J. Drewniak, “Behavioral IGBT Modeling for Predicting High Frequency Effects in Motor Drives”, IEEE Trans. Power Electronics, vol.15 (2), pp. 354-360, 2000.

49. K. M. Muttaqi, M. E. Haque, “Electromagnetic Interference Generated from Fast Switching Power Electronic Devices”, International Journal of Innovations in Energy Systems and Power, Vol. 3, no. 1 (April 2008), ss. 19-26.

50. G. L. Skibinski, R. J. Kerkman and D. Schlegel, “EMI emissions of modern PWM AC drives,” In IEEE Industry Applications Magazine, vol. 5, Issue: 6, pp. 47 - 80, 1999.

51. Bozzi, M.; Georgiadis, A.; Wu, K.; , "Review of substrate-integrated waveguide circuits and antennas," Microwaves, Antennas & Propagation, IET , vol.5, no.8, pp.909-920, June 6 2011.

52. V. Naumanen, J. Korhonen, P. Silvetoinen and J. Pyrhönen, "Multilevel modulation method for mitigation of high du/dt-originated oscillating overvoltages at motor terminals," IET Power Electron., 2010.

53. V. Naumanen, "Multilevel converter modulation: implementation and analysis," Ph.D. dissertation, Lappeenranta University of Technology, 2010.

54. John C. Joyce, “Current Sharing and Redistribution in High Power IGBT Modules”, PhD dissertation, University of Cambridge, May 2001.

55. P. Zhou, W. N. Fu, D. Lin, S. Stanton and Z. J. Cendes, “Numerical modeling of magnetic devices,” IEEE Transactions on Magnetics, Vol. 40, pp. 1803-1809, July 2004.

56. G. Meunier, D. Shen, J. L. Coulomb, “Modelisation of 2D and axisymmetric magnetodynamic domain by the finite elements method,” IEEE Transactions on Magnetics, Vol.24, No.1, 1988, pp.166-169.

57. P. Lombard and G. Meunier, “A general purpose method for electric and magnetic combined problems for 2d, axisymmetric and transient systems,” IEEE Transactions on Magnetics, Vol. 29, No. 2, March 1993, pp. 1737–1740.

58. F. Piriou and A. Razek, “Coupling of saturated electromagnetic systems to non-linear power electronic devices,” IEEE Transactions on Magnetics, Vol. 24, No. 1, January 1988, pp.274–277.

59. F. Piriou and A. Razek, “A model for coupled magnetic-electric circuits in electric machines with skewed slots,” IEEE Transactions on Magnetics, Vol. 26, No. 2, March 1990, pp. 1096–1100.

60. F. Piriou and A. Razek, “Numerical simulation of a non-conventional alternator connected to a rectifier,” IEEE Transactions on Energy Conversion, Vol. 5, No. 3, September 1990, pp. 512–518.

61. O. A. Mohammed, Electromagnetic field formulations and the finite element method, lecture notes, FIU.

62. D.J. Wilcox, M. Conlon and W.G. Hurley, “Calculation of self and mutual impedances for coils on ferromagnetic core,” IEE Proceedings, Vol. 135, Pt. A, No.7, Sept. 1988, pp. 470-476.

63. F. De Leon, A. Semlyen, “Efficient calculation of elementary parameters of transformers,” IEEE Transactions on Power Delivery, Vol.7, No. 1, Jan. 1992, pp.376-383.

64. R. Asensi, J. A. Cobos, O. Garcia, R. Prieto and J. Uceda, “A full procedure to model high frequency transformer windings,” IEEE Power Electronics Specialists’ conference proceedings, 1994.

65. R. Prieto, R. Asensi, J. A. Cobos, O. Garcia, J. Uceda, “Model of the capacitance effects in magnetic components,” IEEE Power Electronics Specialists’ conference proceedings,1995.

66. V. A. Niemela, G. R. Skutt, A. M. Urling, Y. N. Chang et al., “Calculating the short circuit impedances of a multi winding transformer from its geometry,” IEEE Power Electronics specialists’ conference proceedings, 1989.

67. P. R. Wilson, “Advanced modeling and simulation techniques for magnetic components,” Power Electronics and Variable Speed Drives, 21-23 Sept.1998, conference publication no.456, IEE 1998, pp.187-193.

68. J. Pleite, R. Prieto, R. Asensi, J. A. Cobos, E. Olias, “Obtaining a frequency dependent and distributed effects model of magnetic components from actual measurements,” IEEE Transactions on Magnetics, Vol. 35, No. 6, Nov. 1999, pp. 4490-4502.

69. J. Lammeraner and M.Stafl, “Eddy currents,” Cleveland, Ohio, CRC, 1966.

70. P. L. Dowell, “Effects of eddy currents in transformer windings,” Proceedings of IEEE, Vol.113, pp.1387-1394, Aug.1966.

71. J. P. Vandelac and P. D. Ziogas, “A novel approach for minimizing high frequency transformer copper losses,” IEEE Transactions on Power Electronics, Vol.3, pp. 266-277, July 1988.

72. J. D. Lavers and V Bolborici, “Loss comparison in the design of high frequency inductors and transformers,” IEEE Transactions on Magnetics, Vol. 35, pp. 3541-3543, Sept. 1999.

73. F. Tourkhani and P. Viarouge, “Accurate analytical model of winding losses in round litz wire winding,” IEEE Transactions on Magnetics, Vol.37, pp.538-543, Jan. 2001.

74. A. Podoltsev, I. N. Kucheryavaya, B. Lebedev, “Analysis of effective resistance and eddy current losses in multiturn winding of high frequency magnetic components,” IEEE Transactions on Magnetics, Vol.39, No.1, Jan. 2003.

75. J. Yunas, N.A. Rahman, Lem Tien Chai and B.Y. Majlis, "Study of coreless planar inductor at high operating frequency," *Semiconductor Electronics, 2004. ICSE 2004. IEEE International Conference on* , vol., no., pp. 5 pp., 7-9 Dec. 2004.

76. A. Renko, T. Von Rauner, "EMI-Suppression Design in Flexible Printed Circuit Design in Small Electronic Devices," Electronics System integration Technology Conference, 2006. 1st , vol.1, no., pp.73-79, 5-7 Sept. 2006

77. J.D. Van Wyk, F.C. Lee, "Power electronics technology at the dawn of the new millennium-status and future," Power Electronics Specialists Conference, 1999. PESC 99. 30th Annual IEEE , vol.1, no., pp.3-12 vol.1, Aug 1999

78. Y. Kayano, M. Tanaka, J.L. Drewniak, H. Inoue, "Common-mode current due to a trace near a PCB edge and its suppression by a guard band," Electromagnetic Compatibility, IEEE Transactions on , vol.46, no.1, pp. 46- 53, Feb. 2004

79. M. Boris Levin, “Calculation of Electrical Parameters of Two-Wire Lines in Multiconductor Cables,’’ IEEE Trans.EMC, vol. 50, pp. 697-703, 2008.

80. Rolfes L and B. Schiek, ‘‘Methods for the calibrated measurement of the scattering parameters of planar multi-port devices,” Adv. Radio Sci, vol. 5 pp.439-445, 2007.

81. M. R. Barzegaran, A. Nejadpak, O. A. Mohammed, “High Frequency Electromagnetic Field Model for the Evaluation of Parasitic Elements in Power Converters,” The Applied Computational Electromagnetics Society, ACES 2011, The 27th Annual International, vol., no., pp. March, 2011

82. A. Marvin, ‘‘Shielding Measurements of Equipment Enclosures in the Radiating Near Field,” IEEE Trans.EMC, vol. 49, pp. 860-867, Nov 2007.

83. L. Wang, C.N.-M. Ho, F. Canales, J. Jatskevich, "High-Frequency Modeling of the Long-Cable-Fed Induction Motor Drive System Using TLM Approach for Predicting Overvoltage Transients," Power Electronics, IEEE Transactions on , vol.25, no.10, pp.2653-2664, Oct. 2010.

84. S. Amarir, K. Al-Haddad, "A Modeling Technique to Analyze the Impact of Inverter Supply Voltage and Cable Length on Industrial Motor-Drives," Power Electronics, IEEE Transactions on , vol.23, no.2, pp.753-762, March 2008.

85. C. Purcarea, P. Mutschler, O. Magdun, A. Rocks and A. Binder, "Time domain simulation models for inverter-cable-motor Systems in Electrical drives," Power Electronics and Applications, 2009. EPE '09. 13th European Conference on , vol., no., pp.1-10, 8-10 Sept. 2009.

86. O.A. Mohammed, S. Ganu, "FE-Circuit Coupled Model of Electric Machines for Simulation and Evaluation of EMI Issues in Motor Drives," Magnetics, IEEE Transactions on , vol.46, no.8, pp.3389-3392, Aug. 2010.

87. V. Ardon, J. Aime, O. Chadebec, E. Clavel, J.-M Guichon and E. Vialardi, "EMC Modeling of an Industrial Variable Speed Drive With an Adapted PEEC Method," Magnetics, IEEE Transactions on , vol.46, no.8, pp.2892-2898, Aug. 2010.

88. A.C. Baisden, D. Boroyevich and J.D. van Wyk, "High Frequency Modeling of a Converter with an RF-EMI Filter," Industry Applications Conference, 2006. 41st IAS Annual Meeting. Conference Record of the 2006 IEEE , vol.5, no., pp.2290-2295, 8-12 Oct. 2006.

89. A. M. Sitzia, A.E. Baker, T.W. Preston, A. Puzo and A. Pons, "Finite element analysis for power electronics EMC applications," Magnetics, IEEE Transactions on , vol.32, no.3, pp.1517-1520, May 1996.

90. H. D. Paula, D.A. de Andrade, M.L.R. Chaves, J.L. Domingos and M.A.A. de Freitas, "Methodology for Cable Modeling and Simulation for High-Frequency Phenomena Studies in PWM Motor Drives," Power Electronics, IEEE Transactions on , vol.23, no.2, pp.744-752, March 2008.

91. G. Antonini, S. Cristina and A. Orlandi, "A prediction model for electromagnetic interferences radiated by an industrial power drive system," Industry Applications, IEEE Transactions on , vol.35, no.4, pp.870-876, Jul/Aug 1999.

92. D. Labrousse, B. Revol and F. Costa, "Common-Mode Modeling of the Association of N-Switching Cells: Application to an Electric-Vehicle-Drive System," Power Electronics, IEEE Transactions on , vol.25, no.11, pp.2852-2859, Nov. 2010.

93. Z. Wang, K.T. Chau, L. Chunhua, "Improvement of Electromagnetic Compatibility of Motor Drives Using Chaotic PWM," Magnetics, IEEE Transactions on , vol.43, no.6, pp.2612-2614, June 2007.

94. F. Costa, C. Vollaire and R. Meuret, "Modeling of conducted common mode perturbations in variable-speed drive systems," Electromagnetic Compatibility, IEEE Transactions on , vol.47, no.4, pp. 1012- 1021, Nov. 2005.

95. M. Moreau, N. Idir and P. Le Moigne, "Modeling of Conducted EMI in Adjustable Speed Drives," Electromagnetic Compatibility, IEEE Transactions on, vol. 51, no. 3, pp. 665-672, Aug. 2009.

96. A. F. Moreira, T. A. Lipo, G. Venkataramanan and S. Bernet, "High-Frequency Modeling for Cable and Induction Motor Overvoltage Studies in Long Cable Drives," Industry Applications, IEEE Transactions on , vol. 38, no. 5, pp. 1297-1306, 2002.

97. E. Gubia, P. Sanchis, A. Ursúa, J. López and L. Marroyo, "Frequency Domain Model of Conducted EMI in Electrical Drives," Power Electronics Letters, IEEE , vol. 3, no. 2, pp. 45-49, 2005.

98. L. Xing, F. Feng and J. Sun, "Behavioral modeling methods for motor drive system EMI design optimization," Energy Conversion Congress and Exposition (ECCE), 2010 IEEE , vol., no., pp. 947-954, Sep. 2010.

99. J. Kotny, N. Idir, "Time domain models of the EMI sources in the variable speed drives," Energy Conversion Congress and Exposition (ECCE), 2010 IEEE , vol., no., pp. 1355-1360, 2010.

100. B. Revol, J. Roudet, J.-L. Schanen and P. Loizelet, "EMI Study of Three-Phase Inverter-Fed Motor Drives," Industry Applications, IEEE Transactions on , vol. 47, no. 1, pp. 223-231, 2011.

101. Q. Liu, F. Wang and D. Boroyevich, "Conducted-EMI Prediction for AC Converter Systems Using an Equivalent Modular – Terminal – Behavioral (

MTB) Source Model," Industry Applications, IEEE Transactions on , vol. 43, no. 5, pp. 1360-1370, 2007.

102. Y. Saad, *Iterative Methods for Sparse Linear Systems*, 2nd edition, Society for Industrial and Applied Mathematics, 2003.

103. J.-sheng Lai, S. Member, X. Huang, E. Pepa, S. Chen and T. W. Nehl, "Inverter EMI Modeling and," vol. 53, no. 3, pp. 736-744, 2006.

104. C.S. Mitter, A.R. Hefner, D.Y. Chen and F.C Lee, "Insulated gate bipolar transistor (IGBT) modeling using IG-SPICE ," *Industry Applications, IEEE Transactions on* , vol.30, no.1, pp.24-33, Jan/Feb 1994.

105. R. Withanage, N. Shammas, S. Tennakoorr, C. Oates, W. Crookes, "IGBT Parameter Extraction for the Hefner IGBT Model", Universities Power Engineering Conference, 2006. UPEC '06. Proceedings of the 41st International, vol. 2, pp. 613-617, Sept. 2006.

106. N.Y. Abed and O.A. Mohammed, "Frequency-Dependent Coupled Field-Circuit Modeling of Armored Power Cables Using Finite Elements," *Magnetics, IEEE Transactions on* , vol.47, no.5, pp.930-933, May 2011.

107. O.A. Mohammed, S. Ganu, N. Abed, S. Liu and Z. Liu, "High frequency PM synchronous motor model determined by FE analysis," *Magnetics, IEEE Transactions on* , vol.42, no.4, pp.1291-1294, April 2006.

108. Y. Weens, N. Idir, R. Bausière and J. J. Franchaud, "Modeling and Simulation of Unshielded and Shielded Energy Cables in Frequency and Time Domains," *Magnetics, IEEE Transactions on* , vol.42, no.7, pp. 1876- 1882, July 2006.

109. K. Gulez and A. A. Adam, "High-Frequency Common-Mode Modeling of Permanent Magnet Synchronous Motors," *Electromagnetic Compatibility, IEEE Transactions on* , vol. 50, no. 2, pp. 423-426, May 2008

110. J. L. Tichenor, S. D. Sudhoff and J. L. Drewniak, "Behavioral IGBT modeling for predicting high frequency effects in motor drives," *Power Electronics, IEEE Transactions on* , vol. 15, no. 2, pp. 354-360, Mar. 2000.

111. F. Frisinao, C. Leonardio, A. Raciti and S. Torrisi, "Physics based model of punch through IGBTs simulated by PSpice," *Computers in Power Electronics, 1998. 6th Workshop on* , vol., no., pp.27-35, 1998.

112. V. Pathirana, E. Napoli, F. Udrea and S. Gamage, "An Analytical Model for the Lateral Insulated Gate Bipolar Transistor (LIGBT) on Thin SOI," Power Electronics, IEEE Transactions on , vol. 21, no. 6, pp. 1521-1528, 2006.

113. J. C. Joyce, “Current sharing and redistribution in high power IGBT modules”, PhD thesis, University of Cambridge, UK, May 2001.

114. Mitsubishi semiconductors power modules MOS, “Using IGBT Modules”, Mitsubishi Electric, Sep. 1998.

115. L. Beghou, B. Liu, L. Pichon and F. Costa, “Synthesis of Equivalent 3-D Models from Near Field Measurements — Application to the EMC of Power Printed Circuit Boards,” Magnetics, IEEE Transactions on , vol. 45, no. 3, pp. 1650-1653, 2009.

116. J. L. Schanen, L. Jourdan and J. Roudet, “Layout optimization to reduce EMI of a switched mode power supply,” in Proc. IEEE PESC, Cairns, Australia, pp. 2021–2026, Jun. 2002

117. Cotorogea, M.; Claudio, A.; Rodriguez, M.A.; , "Parameter extraction method for the Pspice model of the PT- and NPT-IGBT's by electrical measurements," Power Electronics Congress, 2002. Technical Proceedings. CIEP 2002. VIII IEEE International , vol., no., pp. 101- 106, 20-24 Oct. 2002

118. A.R. Hefner Jr., D.M. Diebolt, "An experimentally verified IGBT model implemented in the Saber circuit simulator," Power Electronics, IEEE Transactions on , vol.9, no.5, pp.532-542, Sep 1994, doi: 10.1109/63.321038

119. A.T. Bryant, P.R. Palmer,E. Santi, J.L. Hudgins, "Simulation and Optimization of Diode and Insulated Gate Bipolar Transistor Interaction in a Chopper Cell Using MATLAB and Simulink," Industry Applications, IEEE Transactions on , vol.43, no.4, pp.874-883, July-aug. 2007

120. A.T. Bryant, Wanying Kang, E. Santi, P.R. Palmer, J.L. Hudgins, "Two-step parameter extraction procedure with formal optimization for physics-based circuit simulator IGBT and p-i-n diode models," Power Electronics, IEEE Transactions on , vol.21, no.2, pp. 295- 309, March 2006

121. S. Musumeci, A. Raciti, M. Sardo, F. Frisina, R. Letor, "PT-IGBT PSpice model with new parameter extraction for life-time and epy dependent behaviour simulation," Power Electronics Specialists Conference, 1996. PESC '96 Record., 27th Annual IEEE , vol.2, no., pp.1682-1688 vol.2, 23-27 Jun 1996

122. Wanying Kang, Hyungkeun Ahn, M.A.E. Nokali, "A parameter extraction algorithm for an IGBT behavioral model," Power Electronics, IEEE

Transactions on , vol.19, no.6, pp. 1365- 1371, Nov. 2004, doi: 10.1109/TPEL.2004.836635

123. Claudio, M. Cotorogea, M.A. Rodriguez, "Parameter extraction for physics-based IGBT models by electrical measurements," Power Electronics Specialists Conference, 2002. pesc 02. 2002 IEEE 33rd Annual , vol.3, no., pp. 1295- 1300 vol.3, 2002

124. L. Ljung, System Identification: Theory for the User. Second edition. PTR Prentice Hall, Upper Saddle River, NJ, 1999.

125. Gustavsen and A. Semlyen, "Rational approximation of frequency domain responses by vector fitting," IEEE Trans. Power Delivery, vol. 14, No. 3, July 1999, pp. 1052-1061.

126. M. Q. Phan, J. N. Juang and R.W. Longman, "Markov Parameters in System Identification: Old and New Concepts," Structronic Systems: Smart Structures,Devices and Systems (Part 2), Tzou, H.-S. and Guran, A. (Eds.), World Scientific,Singapore, 1998, pp. 263-293.

127. R. Johansson, I. Verhaegen, C.T. Chou, "Stochastic theory of continuous-time state-space identification," Decision and Control, 1997., Proceedings of the 36th IEEE Conference on , vol.2, no., pp.1866-1871 vol.2, 10-12 Dec 1997

128. T. Takagi and M. Sugeno, "Fuzzy identification of systems and its applications to modeling and control," IEEE Trans. Syst., Man, Cybern., vol. SMC-15, pp. 116–132, Jan./Feb. 1985.

129. Hyeong-Seok Oh, Mahmoud El Nokali, "A new IGBT behavioral model, Solid-State Electronics", Volume 45, Issue 12, December 2001, Pages 2069-2075.

130. Ammous, A.; Allard, B.; Morel, H.; , "Transient temperature measurements and modeling of IGBT's under short circuit," Power Electronics, IEEE Transactions on , vol.13, no.1, pp.12-25, Jan 1998

131. Nejadpak, A.; Mirafzal, B.; Mohammed, O.; Lixiang Wei; , "Effects of different switching algorithms on the thermal behavior of IGBT modules under pulse-load conditions," IECON 2010 - 36th Annual Conference on IEEE Industrial Electronics Society , vol., no., pp.451-456, 7-10 Nov. 2010

132. P.O. Lauritzen "Power semiconductor device models for use in circuit simulators", Proc of Conf on Industry Applications, pp.1559 -1563 1990

133. A.A. Barna and D. Horelick "A simple diode model including conductivity modulation", IEEE Trans on Circuit Theory, vol. CT-18, no. 2, pp.233 -240 1971

134. Î—. Benda and î•. Spenke "Reverse recovery processes in silicon power rectifiers", Proc of the IEEE, vol. 55, no. 8, pp.1331 -1354 1967

135. Y. Liang and V.J. Gosbell "Diode forward and reverse recovery model for power electronic SPICE simulations", IEEE Trans on Power Electronics, vol. 5, no. 3, pp.346 -355 1990

136. P.O. Lauritzen and C.L. Ma "A simple diode model with reverse recovery", IEEE Trans on Power Electronics, vol. 6, no. 2, pp.188 -191 1991

137. Î¥. Jin , Îš Hoffmann and W. Kiffe "A forward recovery model of power diodes", Proc of European Power Electronics Conf, pp.339 -342 1991

138. Tseng, K.J.; Foo, C.F.; Palmer, P.R.; , "Implementing power diode models in SPICE and Saber," *Power Electronics Specialists Conference, PESC '94 Record., 25th Annual IEEE* , vol., no., pp.59-63 vol.1, 20-25 Jun 1994

139. Kraus, R.; Hoffmann, K.; Mattausch, H.J.; , "A precise model for the transient characteristics of power diodes ," *Power Electronics Specialists Conference, 1992. PESC '92 Record., 23rd Annual IEEE* , vol., no., pp.863-869 vol.2, 29 Jun-3 Jul 1992

140. Kraus, R.; Turkes, P.; Sigg, J.; , "Physics-based models of power semiconductor devices for the circuit simulator SPICE," *Power Electronics Specialists Conference, 1998. PESC 98 Record. 29th Annual IEEE* , vol.2, no., pp.1726-1731 vol.2, 17-22 May 1998

141. Yan Yan, “Silicon-Based Tunnel Diode Technology”, PhD dissertation, University of Notre Dame, July 2008.

142. Robert Perret, “Power Electronics Semiconductor Devices”, John Wiley Inc., March 2009.

143. Planson, D.; Tournier, D.; Bevilacqua, P.; Dheilly, N.; Morel, H.; Raynaud, C.; Lazar, M.; Bergogne, D.; Allard, B.; Chante, J.-P.; , "SiC power semiconductor devices for new applications in power electronics," *Power Electronics and Motion Control Conference, 2008. EPE-PEMC 2008. 13th* , vol., no., pp.2457-2463, 1-3 Sept. 2008

144. Bogonez-Franco, P.; Sendra, J.B.; , "EMI comparison between Si and SiC technology in a boost converter," *Electromagnetic Compatibility (EMC*

EUROPE), 2012 International Symposium on , vol., no., pp.1-4, 17-21 Sept. 2012.

145. T. P. Chow and M. Ghezzo, “SiC power devices,” Proc. Materials Research Society Symp., vol. 423, 1996, pp. 9-21.

146. R. Wang, P. Ning, D. Boroyevich, M. Danilovic, E. Wang, R. Kaushik, “Design of high-temperature SiC three-phase AC-DC converter for >100ºC ambient temperature,” Proc. Energy Conversion Congress and Exposition ECCE, Atlanta, USA, 2010, pp. 1283-1289.

147. C.N.M. Ho, F. Canales, S. Pettersson, G.Escobar, A. Coccia and N. Oikonomou, "Performance evaluation of full SiC switching cell in an interleaved boost converter for PV applications," Energy Conversion Congress and Exposition (ECCE), 2011 IEEE , vol., no., pp.1923-1927, 17-22 Sept. 2011

148. M. Adamowicz, S. Giziewski, J. Pietryka and Z. Krseminski, “Performance comparison of SiC Schottky ultrafast recovery diodes,” Compatibility and Power Electronics (CPE), 2011 7th International Conference-Workshop, pp. 144-149, 1-3 June 2011.

149. Pressman, Abraham I.; Billings, Keith; Morey, Taylor (2009), Switching Power Supply Design (Third ed.), McGraw-Hill, ISBN 0-07-148272-5

150. C. P. Todd, "Snubber circuits: Theory, design and application", Unitrode-Power Supply Design Seminar, pp. 1993.

151. M. R. Barzegaran; A. Nejadpak; O. A. Mohammed;, “High Frequency Electromagnetic Field Model for the Evaluation of Parasitic Elements in Power Converters,” The Applied Computational Electromagnetics Society, ACES 2011, The 27th Annual International, vol., no., pp. March 27th-31st, 2011

152. Alfuhaid, A.S.; , "Frequency characteristics of single-phase two-winding transformers using distributed-parameter modeling," Power Delivery, IEEE Transactions on , vol.16, no.4, pp.637-642, Oct 2001

153. Jonsener Zhao; , “A new calculation for designing multilayer planar spiral inductors,” Electronics Design Strategy, News. EDN, July 29, 2010

154. Myounggon Kang; In Man Kang; Hyungcheol Shin; , "Extraction and modeling of physics-based gate resistance components in RF MOSFETs," Silicon Monolithic Integrated Circuits in RF Systems, 2006. Digest of Papers. 2006 Topical Meeting on , vol., no., pp.4 pp., 18-20 Jan. 2006

155. Haoyi Ye; Zhihui Yang; Jingya Dai; Chao Yan; Xiaoni Xin; Jianping Ying; , "Common mode noise modeling and analysis of dual boost PFC circuit," Telecommunications Energy Conference, 2004. INTELEC 2004. 26th Annual International , vol., no., pp. 575- 582, 19-23 Sept. 2004

156. A. Nejadpak, O.A. Mohammed, "Physics-Based Modeling of Power Converters from Finite Element Electromagnetic Field Computations," Magnetics, IEEE Transactions on , vol.PP, no.99, pp.1, 0

157. A. Rosales, A. Sarikhani, O.A. Mohammed, "Evaluation of Radiated Electromagnetic Field Interference Due to Frequency Switching in PWM Motor Drives by 3D Finite Elements," Magnetics, IEEE Transactions on , vol.47, no.5, pp.1474-1477, May 2011

158. L. Satish, S.K. Sahoo, "An effort to understand what factors affect the transfer function of a two-winding transformer," Power Delivery, IEEE Transactions on , vol.20, no.2, pp. 1430- 1440, Apr. 2005

159. Reduction of a ship's Magnetic Field Signature, John J. Claypool, published by Morgan & Claypool 2008.

160. G. Coat, A. Foggia, JP. Bongiraud, P. Thiec, "Electromagnetic Signature of Induction Machines" Energy Conversion, IEEE Transaction on, Vol. 14, No. 3, Sep. 1999.

161. M. Degano, P. Zanchetta, J. Clare, L. Empringham, "HF induction motor modeling using genetic algorithms and experimental impedance measurement," Industrial Electronics (ISIE), 2010 IEEE International Symposium on , vol., no., pp.1296-1301, 4-7 Jul. 2010.

162. A. Boglietti, E. Carpaneto, "An accurate high frequency model of AC PWM drive systems for EMC analysis," 2001 IEEE IAS Annual Meeting., vol.2, no., pp.1111-1117, vol.2, 30 Sep-4 Oct. 2001.

163. V.C. Gungor, Bin Lu; Hancke, G.P.; , "Opportunities and Challenges of Wireless Sensor Networks in Smart Grid," Industrial Electronics, IEEE Transactions on , vol.57, no.10, pp.3557-3564, Oct. 2010.

164. M F. Ubeid, M. M. Shabat, M. O. Sid-Ahmed, "Effect of negative permittivity and permeability on the transmission of electromagnetic waves through a structure containing left-handed material," natural science magazine, Vol.3, No.4, 328-333, 2011.

165. Ammous, A.; Allard, B.; Morel, H.; , "Transient temperature measurements and modeling of IGBT's under short circuit," Power Electronics, IEEE Transactions on , vol.13, no.1, pp.12-25, Jan 1998 doi: 10.1109/63.654955

166. Mantooth, H.A.; Hefner, A.R., Jr.; , "Electrothermal simulation of an IGBT PWM inverter," Power Electronics, IEEE Transactions on , vol.12no.3, pp.474-484, May 1997, doi: 10.1109/63.575675

167. J.J Rodriguez, Z Parrilla, M. Velez-Reyes, A.Hefner, J. Reichl and J.S Lai, "Thermal Component Models for Electro Thermal Analysis of Multi-chip Power Modules", In Proceedings of IEEE Industry Application Society Annual Meeting, October, 2002, pp. 234-241

168. Yunsu Chan, "Thermal component model for electrothermal analysis of IGBT module systems", IEEE Transactions on Advanced Packaging, Vol.24, No.3, August, 2001.

169. Steve Clemente, "Transient thermal response of power semiconductors to short power pulses", IEEE Transactions on power electronics, Vol.8, no.4, 1993, pp..337-341

170. Lixiang Wei; Kerkman, R.J.; Lukaszewski, R.A.; Brown, B.P.; Gollhardt, N.; Weiss, B.W.; , "Junction Temperature Prediction of a Multiple-chip IGBT Module under DC Condition," Industry Applications Conference, 2006. 41st IAS Annual Meeting. Conference Record of the 2006 IEEE , vol.2, no., pp.754-762, 8-12 Oct 2006 doi: 10.1109/IAS.2006.256611

171. J.H. Holland, Genetic Algorithms, Scientific American,1992, pp 66-72

172. MATLAB Genetic algorithm toolbox manual.

173. R. W. Erickson, D. Maksimovic, *Fundamentals of Power Electronics, Springer,* 912 p., 2nd ed., 2001.

174. Tin-ho Li, Jianjing Wang and H.S.-H. Chung, "Effect of parasitic elements in a power converter on the switching performance of a MOSFET-snubber-diode configuration," Applied Power Electronics Conference and Exposition (APEC), 2011 Twenty-Sixth Annual IEEE , vol., no., pp.364-371, 6-11 March 2011

175. M.R. Abdul-Gaffoor, H.K. Smith, A.A. Kishk and A.W. Glisson, "Simple and efficient full-wave modeling of electromagnetic coupling in realistic RF multilayer PCB layouts," Microwave Theory and Techniques, IEEE Transactions on , vol.50, no.6, pp.1445-1457, Jun 2002.

176. Jong-Gwan Yook, L.P.B. Katehi, K.A. Sakallah, R.S. Martin, L. Huang and T.A. Schreyer, "Application of system-level EM modeling to high-speed digital IC packages and PCBs," Microwave Theory and Techniques, IEEE Transactions on , vol.45, no.10, pp.1847-1856, Oct 1997.

177. W. Chen, X. Yang and Z. Wang, "Application of Wavelets and Auto-Correlation-Function For Cancellation of High-Frequency EMI Noise," ACES Journal, vol. 24, no.3, pp. 332 - 336, June 2009.

178. A. Bhargava, D. Pommerenke, K.W. Kam, F. Centola and C. Lam, "DC-DC Buck Converter EMI Reduction Using PCB Layout Modification," Electromagnetic Compatibility, IEEE Transactions on , vol.53, no.3, pp.806-813, Aug. 2011

179. Van Wyk, J.D.; Lee, F.C.; , "Power electronics technology at the dawn of the new millennium-status and future," Power Electronics Specialists Conference, 1999. PESC 99. 30th Annual IEEE , vol.1, no., pp.3-12 vol.1, Aug 1999

180. Zhang, Y.E.; Sanders, S.R.; , "Design, manufacture and application of in-board magnetic devices," Power Electronics and Motion Control Conference, 2004. IPEMC 2004. The 4th International , vol.3, no., pp. 1791- 1798 Vol.3, 14-16 Aug. 2004

181. Farhangi, B.; Farhangi, S.; , "Comparison of z-source and boost-buck inverter topologies as a single phase transformer-less photovoltaic grid-connected power conditioner," Power Electronics Specialists Conference, 2006. PESC '06. 37th IEEE , vol., no., pp.1-6, 18-22 June 2006.

182. Yong-Hee Shin; Yong-Seung Oh; Kang-Soon Ahn; Chang-Sun Kim; , "Adapter design using planar transformer for aircraft," Telecommunications Energy Conference, 2009. INTELEC 2009. 31st International , vol., no., pp.1-5, 18-22 Oct. 2009

183. S. Wang, “Modeling and Design of Planar Integrated Magnetic Components,” M.S. Thesis, Virginia Tech, Blacksburg, VA, July 2003.

184. Fang Zheng Peng; , "Z-source inverter," Industry Applications, IEEE Transactions on , vol.39, no.2, pp. 504- 510, Mar/Apr 2003

185. Xupeng Fang; , "Modeling of voltage-fed Z-source inverter by switching functions," Industrial Technology, 2008. ICIT 2008. IEEE International Conference on , vol., no., pp.1-6, 21-24 April 2008

186. Quang-Vinh Tran; Tae-Won Chun; Jung-Ryol Ahn; Hong-Hee Lee; , "Algorithms for Controlling Both the DC Boost and AC Output Voltage of Z-Source Inverter," Industrial Electronics, IEEE Transactions on , vol.54, no.5, pp.2745-2750, Oct. 2007

187. Jonsener Zhao; , "A new calculation for designing multilayer planar spiral inductors," Electronics Design Strategy, News. EDN, July 29, 2010

188. Cheng Ruqi; Zhao Gengshen; Guo Tianyong; Zhao ergang; Zhao yao; Qi chao; , "Modeling and state feedback control of Z-source inverter," Power Electronics and Intelligent Transportation System (PEITS), 2009 2nd International Conference on , vol.3, no., pp.125-129, 19-20 Dec. 2009

189. Shen, M.; Joseph, A.; Yi Huang; Peng, F.Z.; Zhaoming Qian; , "Design and Development of a 50kW Z-Source Inverter for Fuel Cell Vehicles," Power Electronics and Motion Control Conference, 2006. IPEMC 2006. CES/IEEE 5th International , vol.2, no., pp.1-5, 14-16 Aug. 2006

190. 951 Green TapeTM, DuPont Microcircuit Materials; http://www.dupont.com/mc

191. M. Joshi, V. Agarwal, "Component placement for improved EMI performance in power electronic circuits," Applied Power Electronics Conference and Exposition, 1998. APEC '98. Thirteenth Annual , vol.2, no., pp.911-917 vol.2, 15-19 Feb 1998

192. Fang Luo; Boroyevich, D.; Mattavelli, P.; , "Improving EMI filter design with in circuit impedance mismatching," Applied Power Electronics Conference and Exposition (APEC), 2012 Twenty-Seventh Annual IEEE , vol., no., pp.1652-1658, 5-9 Feb. 2012

193. Gosavi, A.; , "Application of Spread Spectrum technique for EMI reduction in boost converter - A case study," Electromagnetic Interference & Compatibility, 2008. INCEMIC 2008. 10th International Conference on , vol., no., pp.145-148, 26-27 Nov. 2008

194. Li, H.; Li, Z.; Halang, W.A.; Tang, W.K.S.; , "A chaotic soft switching PWM Boost converter for EMI reduction," Industrial Electronics, 2008. ISIE 2008. IEEE International Symposium on , vol., no., pp.341-346, June 30 2008-July 2 2008

195. H.F. Blanchette, K. Al-Haddad, "Solving EMI-Related Problems for Reliable High-Power Converters Design With Precomputed Electromagnetic Models," Power Electronics, IEEE Transactions on , vol.25, no.1, pp.219-227, Jan. 2010

196. Zeineddine, K.; Uan-Zo-li, A.; Chung-hao Chen; Jaehong Hahn; Dong-ho Han; , "A power-efficient method to mitigate the EMI of Switched-Mode Power Supplies," Power Electronics and ECCE Asia (ICPE & ECCE), 2011 IEEE 8th International Conference on , vol., no., pp.453-459, May 30 2011-June 3 2011

197. Lee, F.C.; Shuo Wang; Pengju Kong; Chuanyun Wang; Dianbo Fu; , "Power architecture design with improved system efficiency, EMI and power density," Power Electronics Specialists Conference, 2008. PESC 2008. IEEE , vol., no., pp.4131-4137, 15-19 June 2008

198. Britto, K.R.A.; Dhanasekaran, R.; Vimala, R.; Saranya, B.; , "EMI analysis and evaluation of an improved flyback converter," Computer Communication and Informatics (ICCCI), 2012 International Conference on , vol., no., pp.1-7, 10-12 Jan. 2012

199. Abed, N.Y.; Mohammed, O.A.; , "Physics-Based High-Frequency Transformer Modeling by Finite Elements," Magnetics, IEEE Transactions on , vol.46, no.8, pp.3249-3252, Aug. 2010

200. D. E. Goldberg, Genetic Algorithms in Search, Optimization and Machine Learning, Addison-Wesley Longman Publishing Co., Inc. Boston, MA, USA, 1989

VITA

ARASH NEJADPAK

1983	Born, Karaj, Iran
2001-2006	Bachelor of Engineering in Electrical Engineering, Bu-Ali-Sina University, Iran
2007-2009	M.S. in Electrical Engineering, Sharif University of Technology, Tehran, Iran
2010-2013	PhD. in Electrical Engineering, Florida International University, Miami, Florida, USA

PUBLICATIONS AND PRESENTATIONS

JOURNAL PAPERS

A. Nejadpak, M.R Barzegaran, O.A. Mohammed, "Evaluation of High Frequency Electromagnetic Behavior of Planar Inductor Designs for Resonant Circuits in Switching Power Converters," Applied Computational Electromagnetic Society (ACES) Journal, vol. 26, no. 9, pp. 737-748, 2011

Nejadpak, A., Mohammed, O. A., "Physics-Based Modeling of Power Converters from Finite Element Electromagnetic Field Computations," *Magnetics, IEEE Transactions on*, vol.49, no.1, pp.567-576, Jan. 2013

Arash Nejadpak, Ali sarikhani, Osama A. Mohammed, "Analysis of Radiated EMI and Noise Propagation in Three-Phase Inverter System Operating Under Different Switching Patterns", *Magnetics, IEEE Transactions on* , vol. PP, no., pp.1, 0.

Ali Sarikhani, **Arash Nejadpak**, Osama A. Mohammed, "Estimation of Operational Inductance in Permanent Magnet Synchronous Machines by a Real-time Physics-based inductance Observer", *Magnetics, IEEE Transactions on* , vol. PP, no., pp.1, 0.

Arash Nejadpak, Mohammadreza Barzegaran, Osama A. Mohammed, "Numerical Simulation of Far-field Electromagnetic Field Correlation between Components of Power Converter-Pulse Load System", *Magnetics, IEEE Transactions on* ,[In Press]

CONFERENCE PAPERS

Nejadpak, A.; Mirafzal, B.; Mohammed, O.; Lixiang Wei, "Effects of different switching algorithms on the thermal behavior of IGBT modules under pulse-load conditions," IECON 2010 - 36th Annual Conference on IEEE Industrial Electronics Society , vol., no., pp.451-456, 7-10 Nov. 2010

Nejadpak, A.; Barzegaran, M.; Mohammed, O. A.; , "Design of the high frequency electromagnetic behavior of planar inductor for resonant circuits in switching power converters," Computation in Electromagnetics (CEM 2011), IET 8th International Conference on , vol., no., pp.1-2, 11-14 April 2011

Nejadpak, A.; Barzegaran, M.R.; Sarikhani, A.; Mohammed, O.A.; , "Design of planar inductor based Z-source inverter for residential alternate energy sources," Applied Power Electronics Conference and Exposition (APEC), 2011 Twenty-Sixth Annual IEEE , vol., no., pp.1698-1703, 6-11 March 2011

Mohammadreza Barzegaran, **Arash Nejadpak**, Osama A. Mohammed, "High Frequency Electromagnetic Field Model for the Evaluation of Parasitic Elements in Power Converters," 27th Annual Review of Progress in Applied Computational Electromagnetics March 27-31, pp 623-629 2011 – Williamsburg, Virginia

Arash Nejadpak; Osama Mohammed; , "Physics Based Modeling of Power Converters from Finite Element Electromagnetic Field Computations," 18th International Conference on the Computation of Electromagnetic Fields, COMPUMAG 2011, vol., no., pp. , July 2011– Sydney, Australia

Nejadpak, A.; Mohammed, O.A.; , "Functional ON/OFF behavioral modeling of power IGBT using system identification methods," Applied Power Electronics Conference and Exposition (APEC), 2012 Twenty-Seventh Annual IEEE , vol., no., pp.1826-1832, 5-9 Feb. 2012

A. Nejadpak, O.A. Mohammed, "Finite Element Physics Based Modeling of Cross-Talk Effect on PCB Traces", Conference on Applied Computational Electromagnetics, ACES 2012, Ohio from April 10-14, 2012.

Nejadpak, A. Mohammed, O.A., "Physics-Based Optimization of EMI Performance in Frequency Modulated Switch Mode Power Converters," *Electromagnetic Field Problems and Applications (ICEF), 2012 Sixth International Conference on* , vol., no., pp.1-4, 19-21 June 2012

Arash Nejadpak, Osama A. Mohammed, "Performance Analysis of planar inductor based snubbing circuit on EMI effects generated by switching action in DC/DC Boost converter," *Electromagnetic Compatibility (EMC EUROPE), 2012 International Symposium on* , vol., no., pp.1-6, 17-21 Sept. 2012